HAL
open science

Energy management of a solar thermodynamic micro power plant

Mustapha Amine Rahmani

To cite this version:

Mustapha Amine Rahmani. Energy management of a solar thermodynamic micro power plant. Automatic. Université de Grenoble, 2014. English. NNT : 2014GRENT077 . tel-01147143

HAL Id: tel-01147143

https://theses.hal.science/tel-01147143v1

Submitted on 29 Apr 2015

HAL is a multi-disciplinary open access archive for the deposit and dissemination of scientific research documents, whether they are published or not. The documents may come from teaching and research institutions in France or abroad, or from public or private research centers.

L'archive ouverte pluridisciplinaire **HAL**, est destinée au dépôt et à la diffusion de documents scientifiques de niveau recherche, publiés ou non, émanant des établissements d'enseignement et de recherche français ou étrangers, des laboratoires publics ou privés.

UNIVERSITÉ DE GRENOBLE

THÈSE

pour obtenir le grade de

DOCTEUR DE L'UNIVERSITÉ DE GRENOBLE

Spécialité : **Automatique**

Arrêté ministériel : 7 août 2006

Présentée par
Mustapha Amine RAHMANI

Thèse dirigée par **Mazen ALAMIR** et
coencadrée par **David GUALINO**
préparée au sein du
laboratoire GIPSA-lab
dans **l'école doctorale EEATS**
et **Schneider Electric/Strategy & Technology**

Gestion de l'énergie d'une micro centrale solaire thermodynamique

Energy management of a solar thermodynamic micro power plant

Thèse soutenue publiquement le **04 Décembre 2014**,
devant le jury composé de:

Alain GLUMINEAU
Professeur des Universités, Ecole Centrale de Nantes, Président du jury
Pascal DUFOUR
Maitre de conférences HDR , Université Claude Bernard Lyon 1, Rapporteur
Yann CHAMAILLARD
Professeur, Université d'Orléans , Rapporteur
Mazen ALAMIR
Directeur de recherche, CNRS, Examinateur
David GUALINO
Schneider-Electric / Strategy & Technology, Grenoble, Examinateur
Stéphane COLASSON
CEA, Grenoble, Examinateur

Remerciements

Je tiens avant toute chose à remercier mon directeur de thèse Mazen ALAMIR-Directeur de recherche CNRS- et mon encadrant de thèse David GUALINO-chef de service Mécatronique et Automatique chez Schneider Electric-. Ainsi, je remercie Mazen pour avoir dirigé cette thèse avec succès en faisant face avec moi aux divers (nombreux !!!) obstacles scientifiques que j'ai rencontrés pendant ces 3 années : ses conseils et ses idées venus d'ailleurs m'ont été d'une grande aide pour débloquer des situations difficiles. Je remercie David, pour son intérêt et son implication au travail que j'ai mené, pour m'avoir toujours poussé vers l'expérimental en me donnant les ressources qu'il fallait.

Je tiens aussi à remercier toutes les personnes de Schneider Electric que j'ai côtoyé et avec qui j'ai eu la chance de travailler. Je commencerais par remercier Mr Frédéric VAILLANT, qui a dirigé le pôle Stratégie et Innovation chez Schneider Electric, pour m'avoir fait confiance en acceptant de m'accueillir au sein du pôle Innovation. Je remercie également tout les anciens et actuels membres de l'équipe Mécatronique et Automatique aussi bien pour la bonne humeur et la formidable ambiance qui règne dans le service mais aussi pour m'avoir accueilli parmi eux et faciliter grandement mon intégration à mes débuts. Je remercie particulièrement Benoit GRAPPE-chef du Projet MICROSOL- et Sylvain LECHAT SANJUAN-Ingénieur de recherche chez Schneider Electric- avec qui j'ai eu la chance de travailler pour mettre en œuvre le banc moteur Stirling au CEA Grenoble. A cet effet, j'adresse aussi des remerciements à Stéphane COLASSON- Responsable du Laboratoire des Systèmes Thermiques et Thermodynamiques (LS2T) au CEA-, pour avoir participé à mon jury de soutenance et avoir contribué avec Amélie MAISSE-Technicienne au CEA-, que je remercie également, à mettre en œuvre le banc moteur Stirling.

Je tiens à remercier Alain GLUMINEAU d'avoir accepté de présider le jury de thèse et remercie également Yann CHAMAILLARD et Pascal DUFOUR pour m'avoir fait l'honneur d'être les rapporteurs de cette thèse et pour leurs remarques et questions pertinentes qui ont aidé à améliorer la qualité de ce travail et du manuscrit.

Un grand merci également à tous les membres du GIPSA-lab, permanents et doctorants, que j'ai eu la chance de côtoyer et avec qui j'ai passé d'agréables moments. Je remercie en particulier Emmanuel WITRANT- Maître de conférences UJF- pour m'avoir donné la chance d'effectuer mon stage de master au CERN dans le service de Paolo PETAGNA que je remercie également. Ce fut pour moi une première expérience très enrichissante dans le monde de la recherche.

Des remerciements sincères vont à tous mes amis pour leur soutien et leur écoute et pour m'avoir remonté le moral à chaque fois que j'en avais besoin.

Enfin, je voudrais remercier toute ma famille et plus particulièrement mon frère Abdelhak et mes parents: ma mère Hassiba et mon défunt père Mohamed Said, qui ont toujours été là pour moi, aussi bien pendant les périodes de joie que pendant les moments difficiles et qui m'ont toujours soutenu dans mes choix et encouragé à donner le meilleur de moi-même.

Résumé — Cette thèse s'inscrit dans le cadre du projet collaboratif MICROSOL, mené par Schneider Electric, et qui œuvre pour le développement de micros centrales solaires thermodynamiques destinées à la production d'électricité en sites isolés (non connectés au réseau électrique) en exploitant l'énergie thermique du soleil. Le but de cette thèse étant le développement de lois de commande innovantes et efficaces pour la gestion de l'énergie de deux types de micros centrales solaires thermodynamiques : à base de moteur à cycle de Stirling et à base de machines à Cycle de Rankine Organique (ORC).

Dans une première partie, nous considérons une centrale solaire thermodynamique à base de machine à cycle de Stirling hybridée à un supercondensateur comme moyen de stockage d'énergie tampon. Dans ce cadre, nous proposons une première loi de commande validée expérimentalement, associée au système de conversion d'énergie du moteur Stirling, qui dote le système de performances quasi optimales en termes de temps de réponse ce qui permet de réduire la taille du supercondensateur utilisé. Une deuxième loi de commande qui gère explicitement les contraintes du système tout en dotant ce dernier de performances optimales en terme de temps de réponse, est également proposée. Cette dernière loi de commande est en réalité plus qu'un simple contrôleur, elle constitue une méthodologie de contrôle applicable pour une famille de systèmes de conversion de l'énergie.

Dans une deuxième partie, nous considérons une centrale solaire thermodynamique à base de machine à cycle de Rankine Organique (ORC) hybridée à un banc de batteries comme moyen de stockage d'énergie tampon. Etant donné que ce système fonctionne à vitesse de rotation fixe pour la génératrice asynchrone qui est connectée à un système de conversion d'énergie commercial, nous proposons une loi de commande prédictive qui agit sur la partie thermodynamique de ce système afin de le faire passer d'un point de fonctionnement à un autre, lors des appels de puissance des charges électriques, le plus rapidement possible (pour réduire le dimensionnement des batteries) tout en respectant les contraintes physiques du système. La loi de commande prédictive développée se base sur un modèle dynamique de la machine ORC identifié expérimentalement grâce à un algorithme d'identification nonlinéaire adéquat.

Mots clés : Centrales solaires thermodynamiques, moteurs Stirling, machines à cycle de Rankine Organique (ORC), contrôle des systèmes de conversion de l'énergie, contrôle prédictif, contrôle par mode glissant, identification de modèles non linéaires.

Abstract — This Ph.D thesis was prepared in the scope of the MICROSOL project, led by Schneider Electric, that aims at developing Off-grid solar thermodynamic micro power plants exploiting the solar thermal energy. The aim of this thesis being the development of innovative and efficient control strategies for the energy management of two kinds of solar thermodynamic micro power plants: based on Stirling engine and based and Organic Rankine Cycle (ORC) machines.

In a first part, we consider the Stirling based solar thermodynamic micro power plant hybridized with a supercapacitor as an energy buffer. Within this framework, we propose a first experimentally validated control strategy, associated to the energy conversion system of the Stirling engine, that endows the system with quasi optimal performances in term of settling time enabling the size reduction of the supercapacitor. A second control strategy that handles explicitly the system constraints while providing the system with optimal performances in term of settling time , is also proposed. This control strategy is in fact more than a simple controller, it is a control framework that holds for a family of energy conversion systems.

In a second part, we consider the Organic Rankine Cycle (ORC) based thermodynamic micro power plant hybridized with a battery bank as an energy buffer. Since this system works at constant speed for the asynchronous generator electrically connected to a commercial energy conversion system, we propose a model predictive controller that acts on the thermodynamic part of this system to move from an operating point to another, during the load power demand transients, as fast as possible (to reduce the size of the battery banks) while respecting the physical system constraints. The developed predictive controller is based upon a dynamic model, for the ORC power plant, identified experimentally thanks to an adequate nonlinear identification algorithm.

Keywords: Solar thermodynamic power plants, Stirling engines, Organic Rankine Cycle (ORC) machines, control of energy conversion systems, model predictive control (MPC), sliding mode control, nonlinear model identification.

Contents

Table of symbols and acronyms **xix**

1 General Introduction **1**

1.1 Context of the thesis 1

1.2 Aims of the thesis 4

2 Solar thermodynamic micro power plants **7**

2.1 Introduction 7

2.2 General description of a solar thermodynamic micro power plant 9

2.3 Conclusion 13

I Modeling, Simulation and control of an Off-Grid Stirling based Solar Thermodynamic Micro Power Plant. **15**

3 Nonlinear Static Model of the Stirling Engine **19**

3.1 Generalities about Stirling engines 20

3.2 Model with losses of an alpha type Stirling engine 24

3.3 Stirling engine parameter identification 33

3.4 Optimal Stirling engine motor torque controller 38

3.5 Conclusion 39

4 Dynamic Model of the Energy Conversion System associated with the Stirling Engine **43**

4.1 Energy conversion system architecture 43

4.2 Dynamic modeling of the energy conversion system 44

4.3 State Space representation of the energy conversion system and control objectives 51

4.4 Conclusion 52

5 Development of a first control strategy for the Energy Conversion System associated to the Off-Grid Stirling based power Plant. 53

5.1 Analysis and control of the energy conversion system 54

5.2 Experimental Validation on a dedicated electrical motor testbed 65

5.3 Experimental Validation on the Stirling engine based power system 69

5.4 Conclusion 79

6 Constrained control framework for the Energy Conversion System associated to the Off-Grid Stirling based thermodynamic power Plant 81

6.1 Deeper in the system analysis 82

6.2 Constrained Sliding Mode control of the energy conversion system 85

6.3 The State Feedback law 92

6.4 Simulation-based validation 94

6.5 Conclusion 100

II Modeling, Simulation and control of an Off-Grid Organic Rankine Cycle (ORC) based Solar Thermodynamic Micro Power Plant. 105

7 Nonlinear Dynamic Model Identification of an ORC power plant 109

7.1 Presentation of the ORC power plant prototype 110

7.2 Control objectives and system constraints 113

7.3 Brief state of the art on physical and semi physical ORC power plants dynamic models 115

7.4 Wiener Models based Identification Structure 117

7.5 State Space representation of the ORC power plant identified dynamic models . 122

7.6 Conclusion 133

8 Constrained Optimal Control of the ORC based power plant 135

8.1 Study of the admissible steady states 135

8.2 Constrained Model Predictive Control of the ORC power plant 140

8.3 Conclusion 145

Conclusion **147**

A Résumé en français **149**

A.1 Introduction 149

A.2 Micro Centrale solaire thermodynamique à base d'une machine Stirling 150

A.3 Micro Centrale solaire thermodynamique à base d'une machine ORC 161

A.4 Conclusion générale 172

B Average modeling of the DC/DC converters of the energy conversion system associated to the Stirling based power plant **173**

B.1 Average modeling of the DC/DC full bridge converter 173

B.2 Average modeling of the bidirectional DC/DC converter 176

C Starting procedure for the Stirling based power system **181**

C.1 Case where (Mode_Regule_FB)=1 181

C.2 Case where (Mode_Regule_FB)=2 184

C.3 Case where (Mode_Regule_FB)=3 184

D Proofs related to chapter 6 **185**

D.1 Proof of Lemma 6.1 185

D.2 Mathematical conditions to check items 5), 6) and 7) of Assumption 6.5 186

D.3 Proof of proposition 6.1 187

Bibliography **189**

List of Figures

1.1 BipBop program axes 2

2.1 Representation of the needed Saharian surfaces to produce the currently consumed energy in MENA (Middle East and North Africa), EU (European Union) and the World. (provided by the German Aerospace Center (DLR), 2005.) . . . 8

2.2 Schematic of a solar thermodynamic micro power plant 10

2.3 SCHOTT PTR 70 solar absorber 10

2.4 Parabolic trough mirrors constituting the solar collector field of the ORC based power generation system 11

2.5 Stirling engine provided by "Cool Energy" 12

2.6 ORC prototype provided by "EXOES" 13

3.1 Diagram of an alpha type Stirling engine (`http://www.ohio.edu/mechanical/stirling/`) 21

3.2 Diagram of a beta type Stirling engine (`http://www.ohio.edu/mechanical/stirling/`) 22

3.3 Diagram of a gamma type Stirling engine (`http://www.ohio.edu/mechanical/stirling/`) 23

3.4 Pressure-Volume (P-V) diagram of the Stirling Cycle and pistons position for an alpha-type Stirling engine during a complete cycle 23

3.5 temperature distribution for an alpha type Stirling engine in the ideal isothermal model (`http://www.ohio.edu/mechanical/stirling/`). 25

3.6 Sinusoidal volume variation (Schmidt analysis) for an alpha type Stirling engine (`http://www.ohio.edu/mechanical/stirling/`). 28

3.7 Overview of the Stirling based power system 34

3.8 Zoom on the Stirling engine and the cooling loop 35

3.9 Identification procedure for the Stirling engine unknown parameters 36

3.10 Comparaison between the measured and the theoretical output electrical power, absorbed and rejected heat powers 36

3.11 Comparaison between the measured and theoretical output hot and cold temperatures . . . 37

3.12 Comparison between the fitted Stirling engine torque equation and the torque derived from the experimental data. each point in the figure corresponds to an operating condition defined by N_{rot}, $\dot{m}_h$, $\dot{m}_c$, Th_{in} and Tc_{in} . . . 38

3.13 Stirling engine optimal torque controller . . . 39

3.14 Isolines of the optimal hot side mass flow rate $\dot{m}_h^{ref}$ for P_{elec}^{ref}=100 W and P_{elec}^{ref}=200. . . . 40

3.15 Isolines of the optimal cold side mass flow rate $\dot{m}_c^{ref}$ for P_{elec}^{ref}=300 W and P_{elec}^{ref}=400. . . . 40

3.16 Optimal hot and cold mass flow rates references for the following operating conditions : $Th_{in} = 170°C$ and $Tc_{in} = 20°C$. . . . 41

4.1 Overview of the Stirling based thermodynamic power plant and its associated power conversion system . . . 45

4.2 Behn-Eshenbourg simplified model for the PMSG . . . 45

4.3 Full wave diode bridge. . . . 47

4.4 DC/DC Full Bridge converter. . . . 48

4.5 bidirectional DC/DC converter. . . . 49

5.1 Evolution of the stationary states of subsystem 1 as function of u_1^{st}. . . . 57

5.2 Stability indicator of $A(u_1^{st})$ for $u_1^{st} \in [0, 1]$. . . . 58

5.3 Open loop trajectories for the components of the vector $z(t)$ corresponding to $u_1^{st} = 0.2$, $u_1^{st} = 0.4$ and $u_1^{st} = 0.9$. . . . 58

5.4 Open loop trajectories in the phase plane (x_3,x_4) corresponding to $u_1^{st} = 0.2$, $u_1^{st} = 0.4$ and $u_1^{st} = 0.9$. . . . 59

5.5 Global control architecture for the complete system. . . . 60

5.6 Load power demand. . . . 61

5.7 regulated variables. . . . 62

5.8 rotor mechanical speed and currents injected in the DC bus by the bidirectional DC/DC converter and the Full bridge converter. . . . 63

5.9 control variables. 64

5.10 Schematic of the electrical motor testbed together with its Power electronics. . 66

5.11 Electrical motor testbed used for experimental validation and performance assessment of the proposed control strategy. 66

5.12 DC/DC Full Bridge converter. 67

5.13 Load power demand P_L at the input of the inverter for the electrical motor testbed. 68

5.14 Bus voltage V_{bus} and its reference value V_{bus}^{ref} for the electrical motor testbed. . 68

5.15 Supercapacitor voltage V_{sc} and its reference value V_{sc}^{ref} for the electrical motor testbed. 69

5.16 Output current of the DC/DC Full Bridge converter I_{Lfb} and its reference value I_{Lfb}^{ref} for the electrical motor testbed. 70

5.17 Rotational speed of the engine Ω, the rectified voltage V_{red} and the rectified current I_{red} with their respective reference values Ω^{ref}, V_{red}^{ref} and I_{red}^{ref} for the electrical motor testbed. 70

5.18 Duty ratios of the DC/DC Full Bridge converter (upper figure) and bidirectional DC/DC converter (lower figure) for the electrical motor testbed. 71

5.19 Electrical cabinets containing the energy conversion system 72

5.20 Overview of the first electrical cabinet 73

5.21 Overview of the second electrical cabinet 74

5.22 Load power demand P_L at the input of the inverter for the Stirling based power plant. 76

5.23 Bus voltage V_{bus} and its reference value V_{bus}^{ref} for the Stirling based power plant. 76

5.24 Supercapacitor voltage V_{sc} and its reference value V_{sc}^{ref} for the Stirling based power plant. 77

5.25 Output current of the DC/DC Full Bridge converter I_{Lfb} and its reference value I_{Lfb}^{ref} for the Stirling based power plant. 78

5.26 Rotational speed of the engine Ω, the rectified voltage V_{red} and the rectified current I_{red} with their respective reference values Ω^{ref}, V_{red}^{ref} and I_{red}^{ref} for the Stirling based power plant. 78

5.27 Duty ratios of the DC/DC Full Bridge converter (upper figure) and bidirectional DC/DC converter (lower figure) for the Stirling based power plant. 79

6.1 Typical disposition of the vectors field of the dynamic system (6.1c)-(6.1d) when $x_2 = x_2^{st}(x_3^*)$ and $x_5 = x_5^r$ are assumed to be constant. 87

6.2 Typical disposition of the vectors field of the dynamic system (6.1e)-(6.1f) for a given x_4 and for $x_7 > x_5^r$. 90

6.3 Control of the (x_5, x_6) system under constant x_4. Influence of the allowable values of x_6 on the settling time. Comparison between the cases $x_6^{max} = 10$ and $x_6^{max} = 20$. Note that the time axis is in milliseconds. The closed-loop system shows a minimum-time like behavior since it saturate the constraints on the current $x_6 = I_{Lbb}$ in order to accelerate the convergence. 95

6.4 Control of the (x_3, x_4) system under constant $x_5 = x_5^d$ after a step change of +20% on the desired value x_4^d. Note that the bounds on x_3 defined by (D.2)-(D.3) slow down the response in order to meet the constraints on x_2. The same scenario is depicted in Figure 6.8 using logarithmic scale in order to show the evolution of the variables during first milliseconds of the scenario. 96

6.5 Control of the (x_3, x_4) system under constant $x_5 = x_5^d$ after a step change of −20% on the desired value x_4^d. Note that the bounds on x_3 defined by (D.2)-(D.3) slow down the response in order to meet the constraints on x_2. The same scenario is depicted in Figure 6.9 using logarithmic scale in order to show the evolution of the variables during first milliseconds of the scenario. 97

6.6 Control of the (x_3, x_4) system under constant $x_5 = x_5^d$ after a step change of −20% on the desired value x_4^d. Influence of the constraints on x_2 on the response time of the system. 98

6.7 Control of the (x_3, x_4) system under constant $x_5 = x_5^d$ after a step change of +20% on the desired value x_4^d. Influence of the constraints on x_2 on the response time of the system. 99

6.8 Same scenario as the one depicted on Figure 6.4 using logarithmic scale on the time axis in order to show the beginning of the scenario. This scale enables the saturation on x_4 to be clearly shown. 99

6.9 Same scenario as the one depicted on Figure 6.5 using logarithmic scale on the time axis in order to show the beginning of the scenario. This scale enables the saturation on x_4 to be clearly shown. 100

6.10 Performance of the overall closed-loop system under varying power load demand. Case where $x_2^{max} = 5$. This scenario is worth comparing with the scenario depicted in Figure 6.11 where the upper bound $x_2^{max} = 4.8$ is used. . . 101

6.11 Performance of the overall closed-loop system under varying power load demand. Case where $x_2^{max} = 4.8$. This scenario is worth comparing with the scenario depicted in Figure 6.10 where the upper bound $x_2^{max} = 5$ is used. . . . 102

6.12 Performance of the overall closed-loop system under sinusoidal power load demand. 103

7.1 Picture of the ORC power plant prototype 110

7.2 Schematic of the Organic Rankine Cycle Power Plant. 111

7.3 Temperature-Entropy (T-S) diagram of the Organic Rankine Cycle Power Plant. 112

7.4 comparaison between the fitted polynomial for $T_{sat}(P_{vap})$ with the data provided by REFPROP®. 114

7.5 Moving Boundary paradigm applied to a condenser [Shah et al., 2003]. 116

7.6 Allure of the maps $B^j(.)$ for $\beta = 0.5$ and $n_m = 10$. 118

7.7 Control and exogenous variables profiles during Experiment 1. 121

7.8 Control and exogenous variables profiles during Experiment 2. 121

7.9 Identification results for T_{vap}. 123

7.10 Identification results for P_{vap}. 124

7.11 Identification results for P_{elec}. 125

7.12 Identification results for T_{fr}. 126

7.13 Identification results for $PeMot$. 126

7.14 Identification results for $TeMot$. 127

7.15 Identification results for ΔT_{vap}. 127

7.16 Linearization of the nonlinear maps $\Gamma^{-1}_{T_{vap}}(.)$, $\Gamma^{-1}_{P_{vap}}(.)$ and $\Gamma^{-1}_{P_{elec}}(.)$. 133

8.1 Principle diagram for extracting y_d from $carto^{ORC}(TaCH^{vect}, T^{vect}_{amb}, P^{vect}_{elec}, \Delta T^{vect}_{vap}, T^{vect}_{vap}, PeMot^{vect})$ based on the knowlege of P^{ref}_{elec}. 139

8.2 Diagram of the ORC control System. 142

8.3 Tracking results and disturbance rejection for the ORC turbine output electrical power P_{elec}. 143

8.4 ORC system actuators: f_{pump}, $\dot{V}_{hot}$, V^{aero}_{rot} and V^{circ}_{rot}. The red dashed lines indicate the minimum and maximum admissible values. 144

8.5 ORC system constrained variables. The red dashed lines indicate the minimum and maximum admissible values. 144

A.1 Schéma global d'une micro centrale solaire thermodynamique 150

A.2 Schéma global d'une micro centrale solaire thermodynamique à base d'un moteur Stirling 151

A.3 diagramme Pression-Volume (P-V) du cycle de Stirling et position des pistons pour un moteur Stirling de type alpha pendant un cycle complet. 152

A.4 Vue d'ensemble du système de production d'électricité à base de machine Stirling. 153

A.5 Procédure d'identification des paramètres inconnus du modèle de la machine Stirling. 154

A.6 Comparaison entre les valeurs mesurées et théoriques de: la puissance électrique produite, de la puissance thermiques absorbée et de la puissance thermique rejetée. 154

A.7 Comparaison entre les valeurs mesurées et théoriques des températures chaude et froide en sortie de la machine Stirling. 154

A.8 Architecture de la première loi de commande pour le système de conversion d'énergie associé à la machine Stirling. 157

A.9 Banc moteur électrique utilisé pour la validation expérimentale de la première loi de commande pour le système de conversion d'énergie associé au moteur Stirling. 158

A.10 Résultats expérimentaux validant la validation de la première loi de commande pour le système de conversion d'énergie associé au moteur Stirling. 159

A.11 Disposition typique des champs de vecteurs pour le système dynamique (A.2c)-(A.2d) quand $x_2 = x_2^{st}(x_3^*)$ et $x_5 = x_5^r$ sont supposés constants. 160

A.12 Contrôle du système (x_3, x_4) sous $x_5 = x_5^d$ après un changement de +20% pour la valeur désirée x_4^d. Il est à remarquer que les limitations sur x_3 ralentissent le temps de réponse du système afin de garantir le respect des contraintes sur x_2. 161

A.13 Schéma global d'une micro centrale solaire thermodynamique à base d'une machine ORC 162

A.14 Schéma du système de production d'électricité à base d'une machine à cycle de Rankine organique (ORC). 163

A.15 diagramme Température-Entropie (T-S) du système de production d'électricité à base d'une machine à cycle de Rankine organique (ORC). 163

A.16 Prototype du système de production d'électricité à base de machine ORC . . . 164

A.17 Résultats d'identification pour P_{elec}. 167

A.18 Architecture de contrôle du système ORC. 169

A.19 Résultats de la régulation et du rejet de perturbations pour la puissance électrique P_{elec} en sortie de la turbine du système ORC. 170

A.20 Actionneurs du système ORC: f_{pump}, $\dot{V}_{hot}$, V_{rot}^{aero} and V_{rot}^{circ}. Les lignes en pointillés rouge représentent les valeurs minimum et maximum admissibles. . . 171

A.21 Variables sous contrainte du système ORC. Les lignes en pointillés rouge représentent les valeurs minimum et maximum admissibles. 171

B.1 temporal diagram of the DC/DC Full Bridge. 174

B.2 Operational modes of the bidirectional DC/DC converter according to the current flow 176

B.3 Output current I_{Lbb} of the bidirectional DC/DC converter in the complementary control mode. 179

C.1 Overview of the Stirling based power plant and its associated power conversion system including the ATV32 variable speed drive 182

C.2 Starting procedure flowchart 183

D.1 Illustration of the proof of Lemma 6.1: Under the conditions of the Lemma, the position of the *pic* of $y = x_2$ is almost independent of x_3. 186

List of Tables

7.1 The identified parameters used to define the nonlinear maps for ΔT_{vap}, T_{vap}, P_{vap}, P_{elec}, T_{fr}, $PeMot$ and $TeMot$ 122

Notations and acronyms

Notations

$\leq, \geq, =$	element-wise operators
$\gg, \ll$	much greater than, much smaller than
$:=$	definition
$\approx$	approximately
$\oint$	cyclic integral
v^T	The transpose of a vector or matrix v
$\|v\|$	any norm of the vector v
$\|v\|_P$	weighted norm of the vector v by the matrix P
$\|v\|$	element wise absolute value of v
$A \otimes B$	Kronecker product of matrices A and B (see Definition 0.1)
$\mathbb{I}$	Identity matrix with appropriate dimension
$Sat(.)$	Saturation function
$ln(.)$	Natural logarithm
$\sum$	Sum Symbol
$\cup$	Union Symbol
∞	infinity value
$\lim_{x \to y} f(x)$	the limit of f of x, as x approaches y
$min(.)$	minimum value
$max(.)$	maximum value
$\arg\min_x f(x)$	argument x that minimizes the function $f(x)$
$\tanh(x)$	Hyperbolic Tangent of x
$\sin(.)$,$\cos(.)$	sine and cosine functions
$\arctan(.)$	arc tangent function
$\mathbb{I}_n$	Identity matrix of dimension n

1_n	Ones matrix of dimension n, $1_n \in \mathbb{R}^n$
$\mathbb{O}_{n_i \times n_j}$	Zeros matrix of dimension $n_i \times n_j$, $\mathbb{O}_{n_i \times n_j} \in \mathbb{R}^{n_i \times n_j}$
$\mathbb{O}_n$	Zeros matrix of dimension $n \times n$, $\mathbb{O}_{n \times n} \in \mathbb{R}^{n \times n}$

Acronyms

Control Theory

PID	Proportional Integral Derivative (controller)
MPC	Model Predictive Control
QP	Quadratic Programming (Optimization problem)
SQP	Sequential Quadratic Programming (Optimization problem)

Thermodynamics

ORC	Organic Rankine Cycle
NTU	Number of Transfer Units
P-V	Pressure-Volume (diagram)
T-S	Temperature-Entropy (diagram)
WHR	Waste Heat Recovery
FV	Finite Volume
MB	Moving Boundary

Electrical engineering

MPPT	Maximum Power Point Tracking
AC	Alternating Current
DC	Direct Current

PV	photovoltaic
UPS	Uninteruptible Power Source
SOC	State Of Charge
RPM	Rotation Per Minute
PMSG	Permanent Magnet Synchronous Generator
EMF	Electromotive Force
IGBT	Insulated Gate Bipolar Transistor
PWM	Pulse Width Modulation

Other

BipBop	Business, Innovation and People at the Base of the Pyramid
PLC	Programmable Logic Controller
NI	National Instrument®
DLL	Dynamic Link Library

Definition 0.1
Let $A \in \mathbb{R}^{n\times m}$ and $B \in \mathbb{R}^{p\times q}$. The Kronecker product $A \otimes B$ is defined by:

$$A \otimes B := \begin{pmatrix} A(1,1)\cdot B & A(1,2)\cdot B & \cdots & A(1,m)\cdot B \\ A(2,1)\cdot B & A(2,2)\cdot B & \cdots & A(2,m)\cdot B \\ \vdots & \vdots & \vdots & \vdots \\ A(n,1)\cdot B & A(n,2)\cdot B & \cdots & A(n,m)\cdot B \end{pmatrix}$$

Chapter 1

General Introduction

Contents

1.1 Context of the thesis 1
1.2 Aims of the thesis 4

1.1 Context of the thesis

Today, more than 1.4 billion people, that corresponds to 300 millions households, have no access to electrical energy. They earn less than 2 dollars per day and spend more than 15 dollars per month and per family for energy access [1]:

- 500 millions live in India.
- 100 millions live in Indonesia
- 100 millions live in Bangladesh
- 70 millions live in Nigeria.
- more than 220 millions live in Sub-Saharian Africa.

These populations generally live in areas where the electrical grid is not available, generally due to its high cost, or is unstable. However, the need for energy of these populations is increasingly growing since energy is the basis of a sustainable development[2]:

- Economical development via local entrepreneurship.
- Mechanization of agricultural production and rural depopulation limitation.
- Access to healthcare.

[1] BipBop program description: http://www.schneider-electric.fr/documents/sustainable-development-and-foundation/fr/bipbop-fr4.pdf

[2] BipBop program description: http://www2.schneider-electric.com/sites/corporate/en/group/sustainable-development-and-foundation/access-to-energy/presentation.page

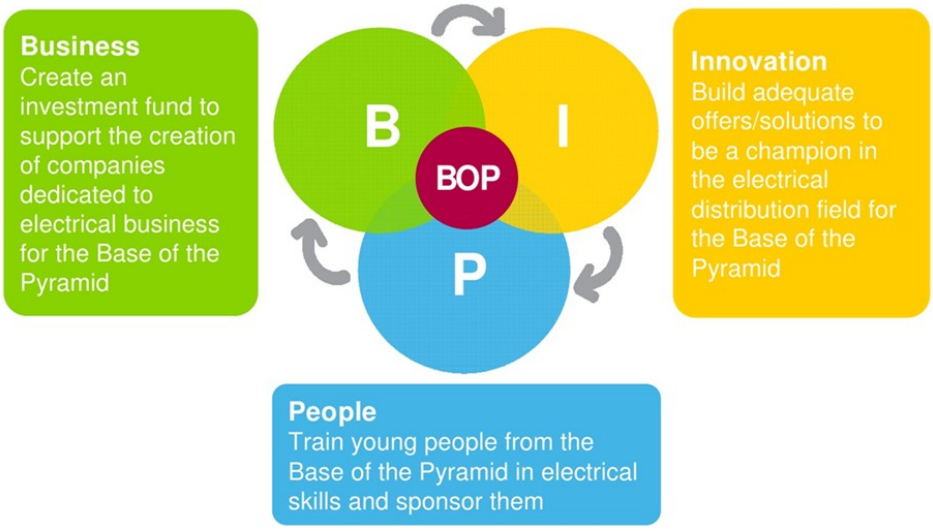

Figure 1.1: BipBop program axes

- Local living conditions improvement by the arrival of lighting, communication infrastructures and leisure activities (radio, television, mobile phones, Internet, street lighting and preservation means like refrigeration...etc).
- Reduction of health risks associated with kerosene and biomass use.

The fuel based generators (mainly Diesel engines) are typically used in this context but are not well adapted because of their low reactivity to changes in the power demand level, their high pollution, noise, and their low efficiency [Kalantar and Mousavi, 2010]. Moreover, the cost for fuel routing to the concerned areas is extremely expensive compared to the daily mean salary of the consumers.

In order to bring solutions to the energy access for those populations, Schneider Electric launched a program called BipBop[3] (Business, Innovation and People at the Base of the Pyramid) that aims at bringing safe, clean and affordable electricity to the "Base Of the Pyramid" (largest, but poorest socio-economic group) focusing on the following three axes[4] depicted in Figure 1.1:

- Development of a dedicated offer for new energy distribution solutions.
- Providing financial resources to promote the creation of innovative companies in the field of energy.
- Training young people from the "Base Of the Pyramid" in electrical fields.

[3]BipBop program description: `http://www.schneider-electric.fr/documents/sustainable-development-and-foundation/fr/bipbop-fr4.pdf`

[4]BipBop program description: `http://bopobs.com/2011/06/15/bip-bop-de-schneider-electric/`

Within the framework of the BipBop program, the "MICROSOL" project was launched within the "Advanced Mechatronics and Control" team (Innovation center) of Schneider Electric. This project aims at developing Off-grid solar thermodynamic micro power plants producing a minimum of $150kWh_{elec}$/day and functioning 24/24h thanks to an adequate environmentally friendly heat storage. The innovative solution proposed by MICROSOL is competitive and well adapted to the populations of the "Base Of the Pyramid" that do not have access to the electrical grid but located in areas with high sunlight potential.

Preliminary studies prior to MICROSOL have permitted to determine an adequate architecture for the solar thermodynamic micro power plant with a pressurized water tank, harmless for the environment, as a heat storage device. The choice of water as heat transfer and storage fluid is due to its low environmental impact in addition of being low cost. However, this choice limits the hot operational temperature and therefore the global efficiency of the plant. The innovations proposed by Schneider Electric and its partners are then crucial to overcome these limitations. In particular, efficient control strategies are essential to bring the plant at its maximum efficiency operating point regardless of the operating conditions (ambient temperature, weather conditions...).

In the beginning of the MICROSOL project, and taking into account the technological and industrial risks, two variants of the solar micro power plant were considered by Schneider Electric:

- A first variant uses solar collectors with fixed vacuum tubes, provided by SAED, heating water between $110°C$ and $150°C$ pressurized at a maximum pressure of 10 bars. A Stirling engine provided by STIRAL (`http://www.stiral.com`) is used in this configuration to transform heat into mechanical work driving an electrical generator while an energy conversion system provided by Schneider Electric adapts the produced power to the Off-grid loads.
- The second variant uses parabolic trough collectors with a system of sun tracking provided by EXOSUN (`http://www.exosun.fr/`). The collectors heat a pressurized water (at a maximum pressure of 15 bars) between $140°C$ and $180°C$. An Organic Rankine Cycle (ORC) system converts the water heat into mechanical work thanks to a Scroll turbine (see [Quoilin, 2011]) driving an electrical generator. An adequate power conversion system provided by Schneider Electric is interfaced between the turbine and the Off-grid loads.

Concerning the first variant, in the beginning of the project, the Stirling engine was in the design phase within STIRAL laboratories. It has been then decided to buy a Stirling engine prototype from the company "Cool Energy" (`http://coolenergy.com/`), that was not a project partner, in order to start the preliminary tests on the energy conversion system associated to this engine and developed by Schneider Electric, this to be ready when the Stirling engine prototype provided by STIRAL will be available. Because of some technical difficulties encountered by STIRAL and financial issues encountered by SAED, this first variant of the solar micro power plant was abandoned by Schneider Electric and the second variant was

selected as a candidate for the future solar micro power plants commercialized by Schneider Electric and its project partners. However, the tests on the Stirling engine prototype, provided by "Cool Energy", with its associated energy conversion system, developed by Schneider Electric, continued in collaboration with the CEA [5].

1.2 Aims of the thesis

This CIFRE [6] Ph.D. thesis was prepared within the Gipsa-lab laboratory in partnership with Schneider-Electric in the scope of the MICROSOL project. The general problem under consideration in this thesis is the development of advanced control strategies for the energy management of the two kinds of solar thermodynamic micro power plants considered in the MICROSOL project namely the Stirling based and the ORC based solar micro power systems. This thesis is then divided in two parts, each one focusing on a particular kind of solar micro power plant as follows:

Part I. This part is concerned with the control of an Off-grid Stirling based solar micro power plant focusing on the control of the energy conversion system associated to the Stirling engine hybridized to a supercapacitor that serves as an energy buffer during load power demand transients. For the considered system, the main issue to solve is the size reduction of the energy buffer consisting in the supercapacitor. This is done by controlling the Stirling engine through its electrical part such that to move from an operating point to another (during load power demand changes) as fast as possible while respecting the system constraints. In the literature, one can find many works that deal with the control of a similar power conversion system topology as the one used in the plant under consideration. However, the resulting controllers found in the literature do not induce optimal performances in term of settling time and do not handle explicitly the physical system constraints. Moreover, one of their major disadvantages is the fact that they are built upon cascaded controllers that necessitate a lot of parameters that could be tricky to tune especially when the system constraints (like actuator saturation) are not explicitly considered.

In this part, two different control architectures that tackle the aforementioned issues are proposed. After deriving the nonlinear model (validated experimentally) of the Stirling engine under consideration in Chapter 3 and the nonlinear dynamic model of its associated energy conversion system in Chapter 4, a first novel control strategy for the Stirling based power plant is proposed in Chapter 5. The closed loop system under the first proposed control strategy is endowed with near-to-optimal performances in term of settling time in addition of necessitating few design parameters. The control strategy was validated experimentally, first on a dedicated electrical motor testbed and finally on a real Stirling based power plant. A second control strategy, which is actually a control framework that holds for a family of power circuits, is proposed in Chapter 6. The novelty of the proposed solution is the explicit handling of the physical constraints of the energy conversion system while ensuring near-to-

[5] Commissariat à l'énergie atomique et aux énergies alternatives `http://www.cea.fr/`

[6] Convention Industrielle de Formation par la Recherche

optimal performances of this last one.

Part II. This part focuses on the control of an ORC based solar micro power plant hybridized with a battery bank as energy buffer to accommodate for the load power demand fast transients. Here again, the main issue to solve is the size reduction of the battery bank by optimally controlling the ORC system in order to move from an operating point to another as fast as possible while respecting the ORC system constraints. Contrary to the Stirling based power plant where the control is performed acting on its associated electrical part, in the ORC system under consideration, the control is performed through the thermo-hydraulic part acting on the pumps and fan associated to the ORC system in order to dynamically control the produced torque of the turbine to meet some desired electrical power. In this manuscript, we propose an innovative solution that responds to this need by first deriving in Chapter 7 nonlinear dynamic models of the ORC power plant using experimental data and then synthesizing in Chapter 7 the model based real time constrained optimal controller that regulates in an optimal manner the produced electrical power of the ORC system while respecting the physical constraints.

The works presented in this thesis have been the subject of the following publications:

- **Journals:**
  1. M. Alamir, M.A. Rahmani, and D. Gualino. *Constrained control framework for a stand-alone hybrid (stirling engine)/supercapacitor power generation system.* Applied Energy, Vol. 118, pp. 192-206, 2014.
  2. M. Alamir, M.A. Rahmani, and D. Gualino. *Generic model identification structure for thermodynamic engines for use in hybrid power stations control and simulation.* To appear in Journal of Process Control, 2014.
- Conferences:
  1. M. A. Rahmani, M. Alamir, D. Gualino and S. Lechat Sanjuan. *Experimental Validation of a Novel Control Strategy For An Off-Grid Hybrid Stirling Engine/Supercapacitor Power Generation System.* In Proc. of the IFAC World Congress, South Africa, 2014.
  2. M. A. Rahmani, M. Alamir and D. Gualino. *Control Strategy For An Off-Grid Hybrid Stirling Engine/Supercapacitor Power Generation System.* In Proc. of the American Control Conference, Washington DC, 2013.

Two **patents** have also been submitted within the framework of the this thesis:

1. M. A. Rahmani, D. Gualino and M. Alamir. *Method for producing electricity via an installation comprising a motor and an energy stocking device allowing the latency of motor load changes to be palliated*, FR1353642 (patent pending).
2. M. A. Rahmani, D. Gualino and M. Alamir. *Optimal Real time control of an off-grid Organic Rankine Cycle (ORC) power plant*, patent pending approval from Schneider Electric.

Chapter 2

Solar thermodynamic micro power plants

Contents

2.1 Introduction **7**

2.2 General description of a solar thermodynamic micro power plant . . **9**

2.2.1 The solar collector field and solar absorbers 9

2.2.2 The thermodynamic machines 12

2.2.3 The heat transfer fluid 12

2.3 Conclusion **13**

2.1 Introduction

Solar energy constitutes the greatest energetic potential available on earth and the idea of using this energy dates back to antiquity, however, the first experimental solar thermal power plant for practical use (pumping and irrigation) was built in Méadi (Egypt) only in 1913 by Franck Schumann [Mathieu, 2012]. Afterwards, the researches aiming at exploiting this energy experienced ups and downs especially because of the emergence of efficient and low cost fossil fuels. Indeed, the evolution of oil prices have often conditioned the evolution of the researches on solar thermal energy. Hence, because of the attractive cost of oil after the second world war, the researches on solar energy have almost stagnated until 1974 where a sharp rise on oil prices have revived the researches on renewable energies especially solar energy where many experimental solar facilities emerged in many industrialized countries. However, after the fall of oil's price in 1986 and its stabilization in the nineties, the researches on solar energy have also fallen.

Since the last fifteen years, global warming has aroused the attention and concern of the international community and public opinion. This, and because of the dramatic decrease of the accessible fossil energy stock, have revived the researches on alternative energies with a particular attention on solar energy since it is the greatest energy resource technically accessible on earth, especially in desert regions around equator, that can respond to the worldwide energetic demand in a sustainable manner. Indeed, it is estimated that if 1% of the surface in

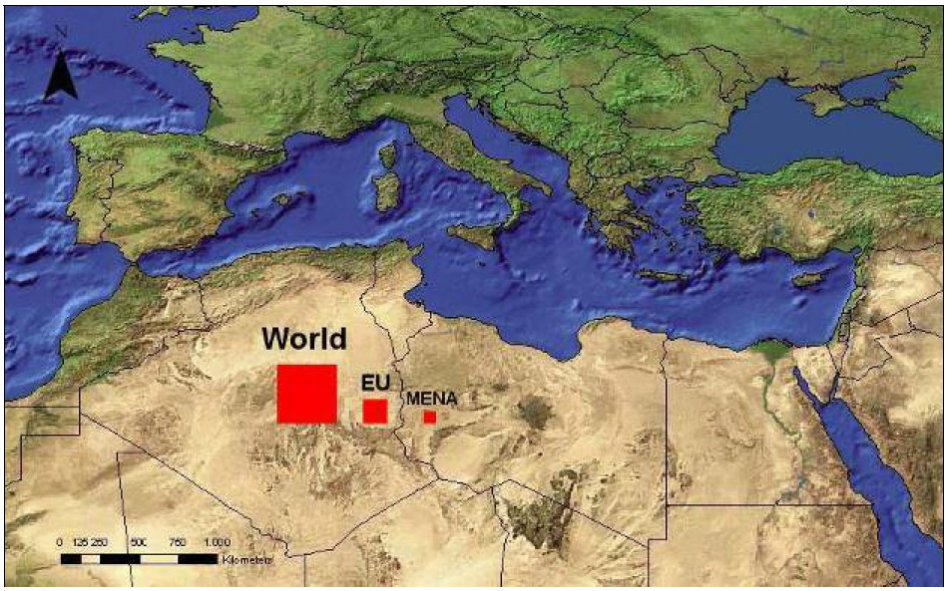

Figure 2.1: Representation of the needed Saharian surfaces to produce the currently consumed energy in MENA (Middle East and North Africa), EU (European Union) and the World. (provided by the German Aerospace Center (DLR), 2005.)

arid regions rich in sunlight (like in Sahara) is covered by solar power plants, the worldwide demand in electricity can be fulfilled [Mathieu, 2012] as it is illustrated in Figure 2.1.

The standard technological solution based on solar energy only consists in using photovoltaic panels associated to a battery bank as an energy storage. This solution leads to a price for a kWh_{elec} within 20 years lower than that of a solution consisting in using fuel based generators even if its initial investment cost is much higher. However, this solution suffers from many drawbacks:

- This solution needs a large amount of batteries to supply the loads in Off-grid areas during the night and the non sunny days.
- The price for such battery bank is high.
- The batteries lifetime is limited, especially in hot conditions, in addition of being significantly affected by the irregular charge/discharge due to the load power demand changes.
- The most commonly used batteries are lead-acid ones that are harmful for the environment and for the populations especially in isolated areas lacking of recycling networks.

Currently, the most commonly adopted solution that takes advantage of solar energy while necessitating less batteries consists in hybridizing fuel based generators with photovoltaic panels (associated to a smaller battery bank compared to the previous solution). This solution is currently adopted within the framework of the BipBop program since it is a good trade-off between the fuel saving and the number of electrochemical batteries.

The objective of the BipBop program with the MICROSOL project is to propose a "greener" solution for the electricity production exploiting the thermal energy of the sun through solar thermodynamic micro power plants with a thermal storage as a principal storage device instead of batteries that are used in small amounts during load power demand transients. The general architecture of a such typical solar thermodynamic micro power plants is described in the next section.

2.2 General description of a solar thermodynamic micro power plant

Figure 2.2 illustrates the general architecture of a typical solar thermodynamic micro power plant. It consists essentially of a solar collector field that collects the sunlight to heat some heat transfer fluid flowing inside solar absorbers, using a volumetric pump, between the solar collectors and a heat storage tank (containing the heat transfer fluid). The power plant contains also a cooling loop consisting of a circulation pump and a cooling fan that cools down an appropriate coolant (water-glycol mixture for the thermodynamic power plant under study). The heat transfer fluid and the coolant enter a thermodynamic machine that performs a thermodynamic cycle during which it absorbs heat from the heat transfer fluid through a heat exchanger and rejects heat to the coolant through another heat exchanger resulting in a positive motor torque that drives an electrical generator producing electricity. The electrical power at the output of the generator is then conditioned through an appropriate energy conversion system to supply the electrical loads (and the system auxiliaries). In Off-grid applications, the solar thermodynamic micro power plants are hybridized to an energy buffer (batteries and/or supercapacitor) linked to the energy conversion system associated to the thermodynamic engine. This energy buffer source responds in a fast manner to the load power demand transients while the thermodynamic machine adapts (through an appropriate control strategy) its produced power in a rather slower manner due to its mechanical and thermal inertia.

In the next sections some of the important components of a solar thermodynamic micro power plant, that greatly influence its price and efficiency, are briefly described.

2.2.1 The solar collector field and solar absorbers

There are many technological solutions for transforming sunlight into useful heat. One can find a good literature review of these techniques in [Mathieu, 2012]. In a general manner, the transfer fluid to be heated flows inside solar absorbers (receivers) whose casing has to be designed such that to maximize the absorption of radiation while minimizing the thermal losses. Many manufacturers provide such absorbers like the vacuum tube based SCHOTT PTR 70[1] solar absorber depicted in Figure 2.3. The absorbers used in the ORC based solar

[1]SCHOTT website: `http://www.schott.com/csp/french/download/schott_csp-datenblatt_ptr70-classic_fra.pdf`

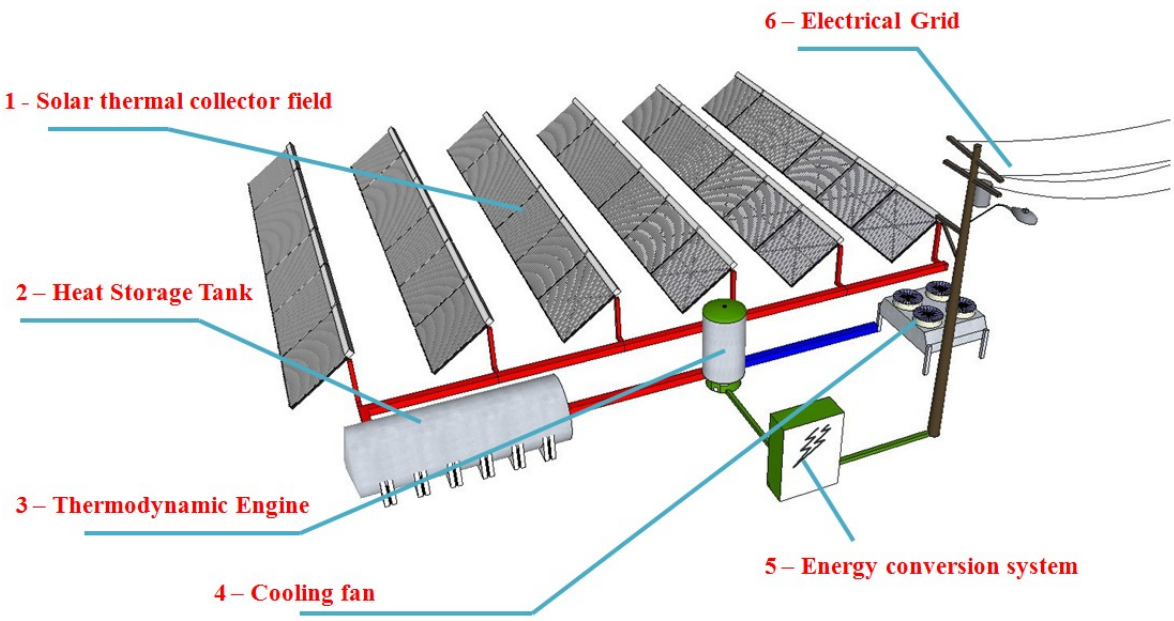

Figure 2.2: Schematic of a solar thermodynamic micro power plant

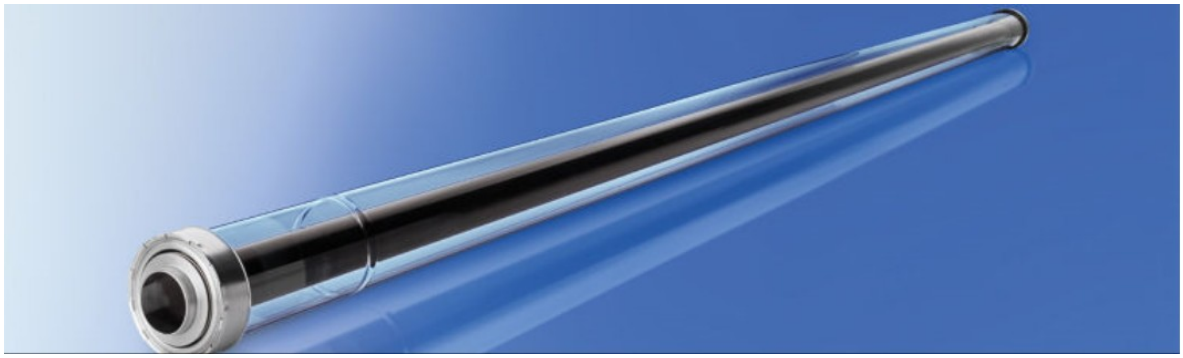

Figure 2.3: SCHOTT PTR 70 solar absorber

Figure 2.4: Parabolic trough mirrors constituting the solar collector field of the ORC based power generation system

thermodynamic micro power plant under consideration, presented in Chapter 7, consist of tubes coated with a selective layer (that absorbs a maximum of radiations while emitting a minimum of losses) and placed inside a glass enclosure.

The solar receivers can absorb the solar radiation using:

- a direct reception: when the absorbers are exposed directly to the solar radiation using simple colectors or advanced ones (see [Mathieu, 2012]).

- a reception by concentration: occurs when mirrors with paraboloid profiles are used to concentrate the sunlight into the mirror's focal.

For the ORC based power system under consideration, parabolic trough mirrors, endowed with one directional solar tracking system, are used to concentrate the solar radiations into the absorbers located in the focal of the mirrors as depicted in Figure 2.4.

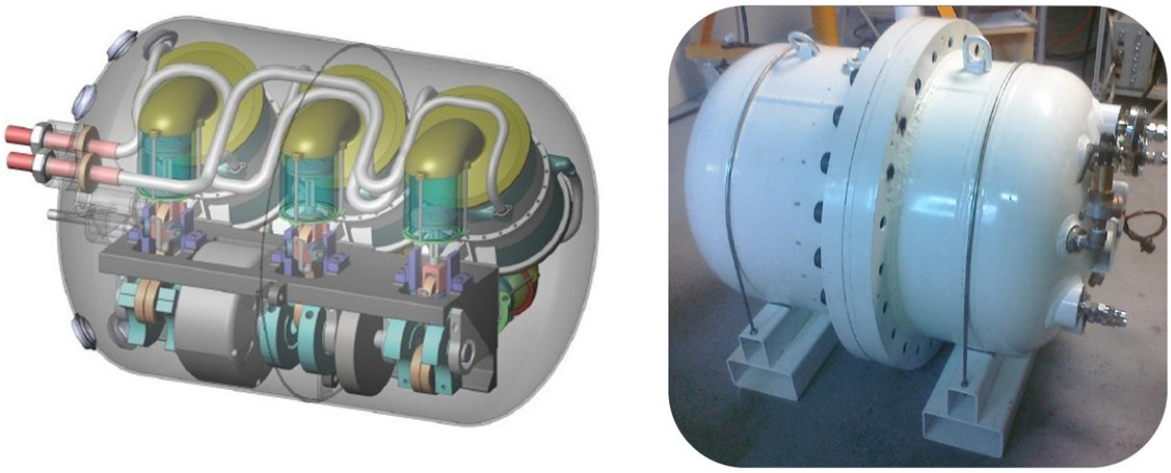

Figure 2.5: Stirling engine provided by "Cool Energy"

2.2.2 The thermodynamic machines

Many thermodynamic cycles can be used to convert the heat of the transfer fluid, stored in the heat storage tank, into mechanical work. In this thesis, two thermodynamic cycles have been considered:

- A Stirling cycle engine presented in Chapter 3. A prototype of this engine was provided by "Cool Energy" and depicted in Figure 2.5.
- Organic Rankine Cycle (ORC) presented in Chapter 7. A prototype of this engine was provided by EXOES and depicted in Figure 2.6.

2.2.3 The heat transfer fluid

The choice of an adequate heat transfer fluid greatly influences the thermal efficiency of the solar collector field and the thermodynamic engines.

Among the most used heat transfer fluids for solar thermal applications [Mathieu, 2012]: water, glycogen polymers, mineral oils, silicone based oils and synthetic oils. For the solar thermodynamic micro power system under study, the selected heat transfer fluid is water because it respects the following two conditions that are crucial when the rural electrification market is targeted:

- it has a low environmental impact and it is not dangerous (toxicity, inflammability...).
- it is low cost and easily transportable and can be safely manipulated by local staff.

Figure 2.6: ORC prototype provided by "EXOES"

Although liquid water is an excellent heat transfer fluid, its drawback is its low evaporating temperature at atmospheric conditions. In order to keep it in the liquid thermodynamic state, its pressure should be increased which increases also the price of the hydraulic components especially the pipes and the heat storage tank. For the considered application, the water pressure was limited to 10 bars at $180°C$.

This limitation of the hot water temperature induces technical challenges on the design of the thermodynamic engines (especially their heat exchangers) and on the control strategies used to dynamically optimize the thermoelectric efficiency of the power plants.

2.3 Conclusion

In this chapter a brief description of solar thermodynamic micro power plants has been presented focusing on their advantages. The main components of the solar thermodynamic micro power plants have also been discussed together with the technological choices of the MICROSOL project. In the following chapters, the two kinds of solar thermodynamic micro power plants considered within the framework of this project will be addressed in details focusing on the development of innovative and efficient control strategies for the electrical energy production in Off-grid mode.

Part I

Modeling, Simulation and control of an Off-Grid Stirling based Solar Thermodynamic Micro Power Plant.

Introduction

In this part, the control of the off-grid hybrid Stirling engine/Supercapacitor power plant under study is addressed and solved. The proposed controllers drive the system through its electrical part to satisfy the varying load power demand. Two novel controllers have been proposed to reach the control objectives. A first controller requiring a few tuning parameters is proposed in Chapter 5 based on a backstepping controller and a one step predictive controller. The closed loop system under this first proposed control is endowed with quasi optimal behavior. The control methodology was then experimentally validated first on a dedicated electrical motor testbed and then on the real Stirling based power system.

The second proposed control methodology presented in Chapter 6 tackles explicitly the physical constraints of the energy conversion system (associated to the Stirling engine) while ensuring quasi optimal behavior of this last one. This proposed methodology is more than a simple controller, it is a control framework that holds for a family of energy conversion systems.

A quick state of the art on controlling similar hybrid systems

Many hybrid power generation systems have been studied in the literature either for grid or off-grid applications. They combine different renewable energy sources essentially wind, solar photovoltaic, hydraulic and fuel cells. Different power electronics architectures associated to those hybrid power systems have been proposed and their corresponding control strategies developed. In [Haque et al., 2010], a variable speed wind turbine associated to a simple power electronics have been used to supply AC loads, an MPPT (Maximum Power Point Tracking) algorithm was used to extract maximum power from the wind using a DC/DC boost converter while an inverter was used to create the AC grid and to regulate the DC bus, however because of the random nature of the wind, the AC voltage was perturbed. In [Mendis et al., 2011], a similar system combined to a Diesel Engine and a battery bank was studied. The batteries act as a buffer source (through a buck-boost converter) to regulate the DC bus absorbing power in case of high wind and discharging in case of scarce wind. Linearized models were used to control the system at some operating points. However for many applications where the loads and power sources can vary significantly, such controllers are not suitable. In [Haruni et al., 2010], a similar system provided by dump loads and its associated switch was studied and PI based controllers were proposed. In [Ahmed et al., 2011] a hybrid wind/photovoltaic/fuel cell power system for grid-connected applications was proposed. An MPPT techniques were used to extract maximum power from the wind and PV panels while the fuel cells system suppress the grid power fluctuations. The objectives of such hybrid systems is to act as a battery-less uninteruptible power source (UPS). Valenciaga et al ([Valenciaga et al., 2000],[Valenciaga et al., 2004],[Valenciaga and Puleston, 2008]) proposed an interesting technique to control a hybrid wind/photovoltaic (and even extra power sources) with wind as a primary source and a battery bank on the DC bus as an energy storage device. The control design proposed by Valenciaga et al are based on passivity/sliding mode

techniques (and a second order sliding mode technique in [Valenciaga and Puleston, 2008]) for different wind regimes.

Supervisory controllers for such systems were proposed in [Valenciaga and Puleston, 2005], [Qi et al., 2011a] and [Qi et al., 2011b]. All the techniques previously cited don't handle explicitly the constraints of the system's state variables and controllers which can lead to some undesirable behaviors. Moreover, they do not necessarily induce optimal performance of the system in term of settling time which can lead to over-dimensioning of the energy buffer source especially when it consists of supercapacitors which is the case for our system because of their many advantages (see [Langlois, 2006] for more details).

Chapter 3

Nonlinear Static Model of the Stirling Engine

Contents

3.1 Generalities about Stirling engines 20
3.1.1 Stirling engines configurations 20
3.1.2 Stirling engine theoretical Pressure-Volume (P-V) diagram 22
3.2 Model with losses of an alpha type Stirling engine 24
3.2.1 Ideal Isothermal Analysis 24
3.2.2 Schmidt Analysis 26
3.2.3 Heat losses analysis 27
3.2.4 Heat transfer through the heat exchangers 30
3.2.5 Produced power and cycle efficiency 32
3.2.6 Summary of the Stirling engine equations 32
3.3 Stirling engine parameter identification 33
3.3.1 Description of the experimental testbed 33
3.3.2 Identification of the unknown parameters of the Stirling engine model . . 34
3.3.3 Stirling engine torque expression 37
3.4 Optimal Stirling engine motor torque controller 38
3.5 Conclusion 39

The aim of this chapter is to study the Stirling thermodynamic engine associated to the Stirling based off-grid power system under consideration. We first give some generalities about Stirling engines focusing on the alpha type motor since we have in our disposal a 3 kW alpha type low temperature Stirling motor (from "cool energy" company). Then, a static model of this device taking into account different heat losses will be developed and validated using real data gathered on the prototype. The static model will serve to simulate the behavior of the Stirling engine when connected to an adequate power electronics developed within Schneider Electric (a static model is sufficient since the dynamics of the thermodynamic part is much slower than that of the electrical part) and on which we designed a real time control strategy presented in Chapters 5 and 6. The static model of the Stirling engine will also serve to construct a cartography that, according to the operating conditions and load power demand, computes the hot and cold mass flow rates (of the external fluids flowing in the hot and cold heat exchangers) references that optimize the net thermoelectric efficiency of the plant.

3.1 Generalities about Stirling engines

The first prototype of Stirling engines was created by Robert Stirling who patented it in 1816 before his brother James industrialized it in 1843. This engine belongs to the family of external combustion engines in the sense that the needed heat is generated externally to the engine. The Stirling engine has many advantages, compared to other kinds of thermodynamic engines, among them [Bonnet, 2005]:

- The Stirling engine accepts any kind of heat sources particulary: the combustion of any kind of fuels (solid, liquid, gaseous, biomass...), solar energy, nuclear source and geothermal sources.
- Stirling engines have comparable performances to Diesel engines having the same nominal power.
- If a combustion of a fuel is used to generate heat, the process is continuous and external to the engine which implies:
  - the combustion is perfectly controlled and the rejected pollutants can be considerably reduced.
  - no explosion happens inside the engine.
  - the produced motor torque is regular and the engine mechanical parts are less solicited which enhance the engine lifetime.
  - extremely soundless engine operation.

One of the key elements of Stirling engines is the "regenerator" matrix (metal mesh or foam for example) which is an internal heat exchanger playing the role of temporary heat buffer placed between the hot and cold spaces of the engine such that the working fluid passes through it first in one direction, taking heat from the fluid, then the other, releasing heat to the fluid. The regenerator benefits from high surface area, high heat capacity, low conductivity and low flow friction. Its function is to retain within the system that heat which would otherwise be exchanged with the environment at temperatures intermediate to the maximum and minimum cycle temperatures, thus enabling the thermal efficiency of the cycle to approach the limiting Carnot efficiency (`http://en.wikipedia.org/wiki/Stirling_engine`) leading to higher power output for a given absorbed heat power.

3.1.1 Stirling engines configurations

There are three main kinds of Stirling engines, depending on their geometrical configurations, these are: the alpha, beta and gamma types.

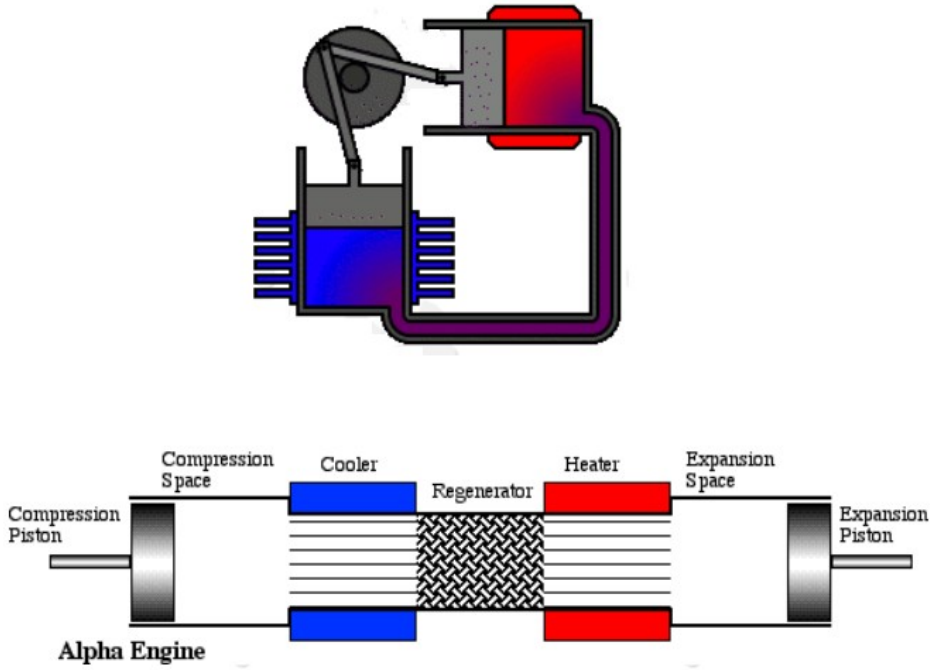

Figure 3.1: Diagram of an alpha type Stirling engine (`http://www.ohio.edu/mechanical/stirling/`)

3.1.1.1 Alpha type Stirling engine

The alpha type engines are bi-cylinder motors (see Figure 3.1) where each cylinder contains a piston linked mechanically to a rotating shaft and where the two pistons are out of phase by $\frac{\pi}{2}$ in such a way that their kinematic coupling enables the internal working fluid to circulate from one cylinder to another through a "regenerator" (which is one of the major element in the engine that greatly influences the engine efficiency) when the shaft is rotating. One cylinder is linked through an adequate heat exchanger to a heat source whereas the other is linked by another heat exchanger to a cold sink to evacuate heat.

3.1.1.2 Beta type Stirling engine

The beta type engine uses a displacer-piston arrangement (see Figure 3.2) where both the displacer and the piston are situated in an in-line cylinder system. The displacer enables the working fluid to be in contact with the hot source and the cold sink (through heat exchangers) when the piston, which is linked to the rotating shaft, is moving.

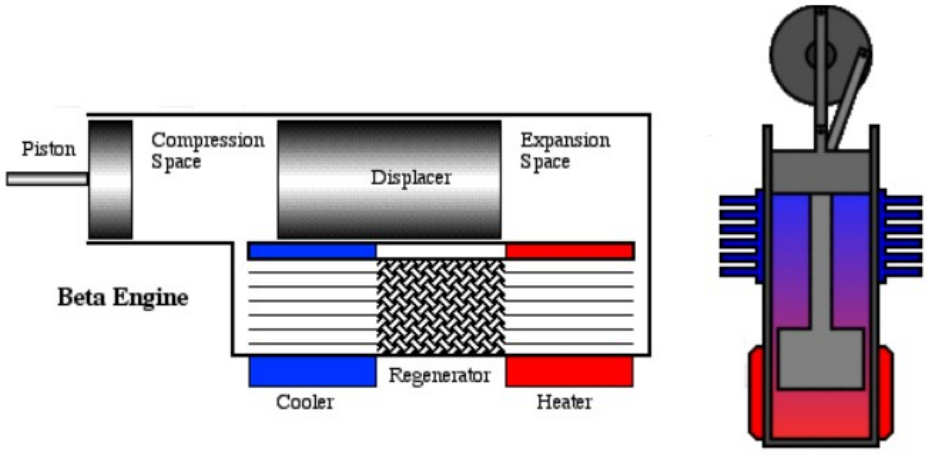

Figure 3.2: Diagram of a beta type Stirling engine (`http://www.ohio.edu/mechanical/stirling/`)

3.1.1.3 Gamma type Stirling engine

The gamma type engine uses also a displacer-piston arrangement but both the displacer and the piston are situated in separate cylinders (see Figure 3.3).

3.1.2 Stirling engine theoretical Pressure-Volume (P-V) diagram

Figure 3.4 depicts the theoretical (indicated) Pressure-Volume diagram of the Stirling cycle and the disposition of the cylinders during each step of the cycle(here we considered an alpha type configuration that corresponds to the prototype we have in our disposal).

Starting from point 1 (according to Figure 3.4), the working fluid undergoes an isothermal expansion at temperature T_h until point 2, the two pistons move down and the total volume increases. In order to ensure this isothermal behavior, the working fluid absorbs heat Q_{exp} from the external heat source. During this step, the engine produces a positive mechanical work W_{exp}.

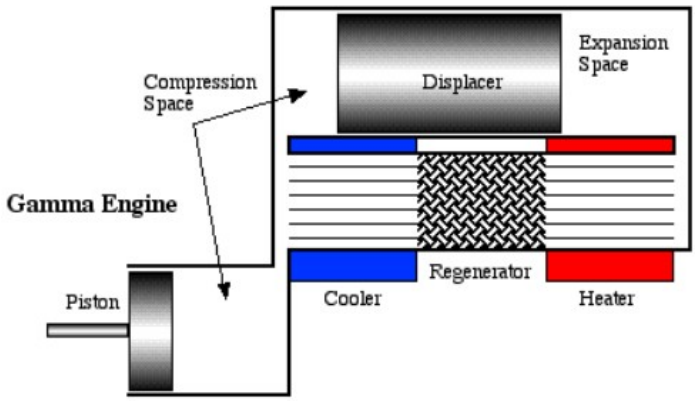

Figure 3.3: Diagram of a gamma type Stirling engine (`http://www.ohio.edu/mechanical/stirling/`)

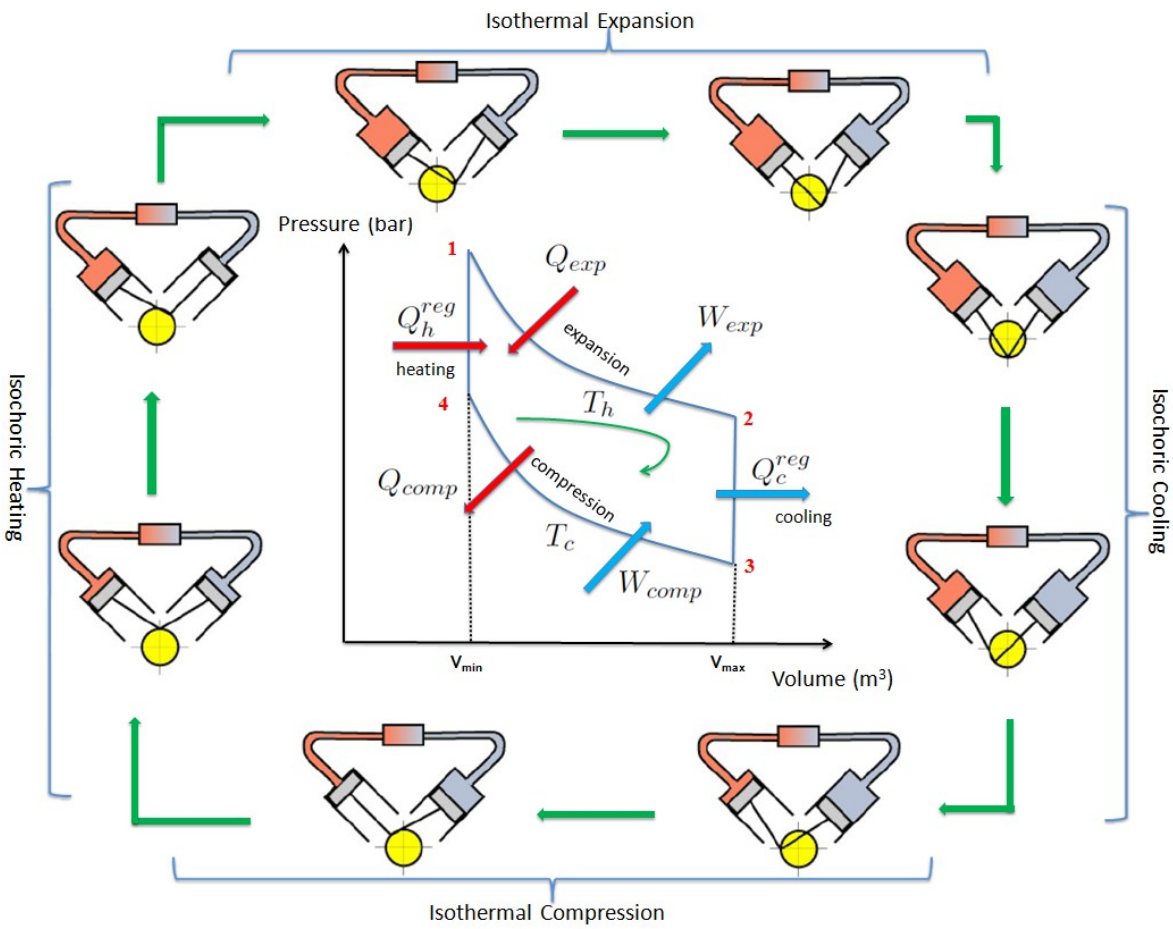

Figure 3.4: Pressure-Volume (P-V) diagram of the Stirling Cycle and pistons position for an alpha-type Stirling engine during a complete cycle

Between points 2 and 3, the working fluid undergoes an isochoric cooling where the fluid is discharged from the hot cylinder to the cold one at constant volume (isochoric behavior). During this step, the fluid releases a certain amount of heat Q_c^{reg} to the regenerator.

Between points 3 and 4, the working fluid undergoes an isothermal compression at temperature T_c where the two pistons move up simultaneously and the total volume decreases at constant temperature. During this step, the fluid consumes a mechanical work W_{comp} and releases heat Q_{comp} to the cold sink to ensure the isothermality of this stage.

The last step occurs between points 4 and 1, to close the cycle, where the working fluid undergoes an isochoric heating. During this last step, the fluid is discharged back to the hot cylinder at constant volume and absorbs a certain quantity of heat Q_h^{reg} from the regenerator which theoretically corresponds exactly to Q_c^{reg}.

The net produced mechanical work corresponds to the area delimited by the closed curve $1-2-3-4$.

3.2 Model with losses of an alpha type Stirling engine

To derive a basic model for the alpha type Stirling engine, we will base our study on the isothermal analysis presented in [Urieli and Berchowitz, 1984] which was perfectly summarized in `http://www.ohio.edu/mechanical/stirling/`. Based on this analysis, a modified static model for the Stirling engine that takes into account different losses will be derived.

3.2.1 Ideal Isothermal Analysis

Consider the simplified diagram of an alpha type Stirling engine depicted on the top of Figure 3.5. As it can be seen from this figure, the Stirling engine consists of a varying volume compression space followed by a fixed volume cold side heat exchanger, a regenerator and a hot side heat exchanger linked to a varying volume expansion space. In the ideal isothermal analysis, it is a assumed that the working gas in the compression space and the cold side heat exchanger space is maintained at the same lower bound temperature T_c while the gas in the expansion space and in the hot side heat exchanger space is at the same upper bound temperature T_h. The temperature in the regenerator is assumed to be varying linearly between T_c and T_h (see the bottom of Figure 3.5).

The total mass of gas M_g inside the whole working volume of the Stirling engine is the sum of gas masses inside each working space as follows:

$$M_g = m_{comp} + m_c + m_r + m_h + m_{exp} \tag{3.1}$$

where m_{comp}, m_c, m_r, m_h, m_{exp} denote respectively the mass in the compression space, the cooler space, the regenerator space, the heater space and the expansion space.

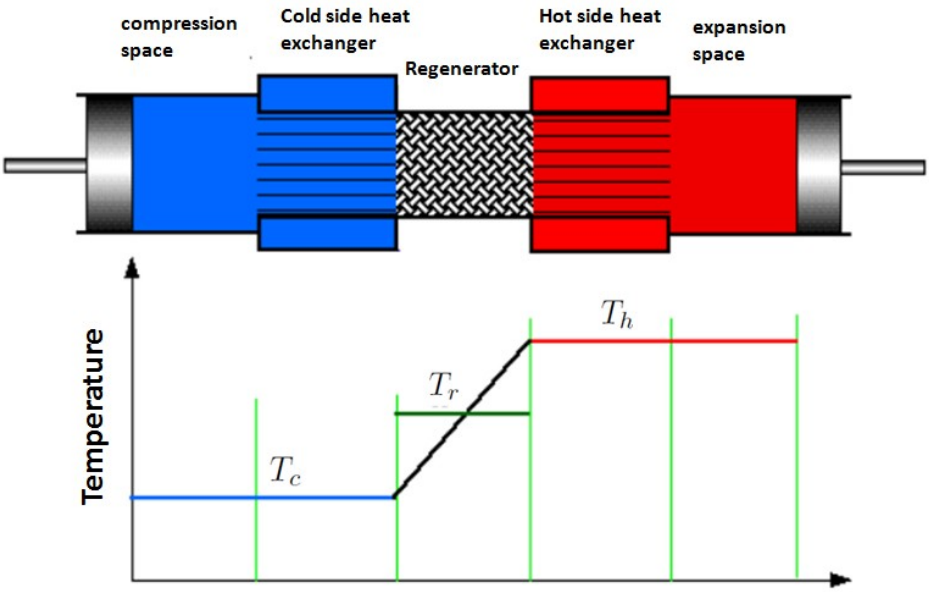

Figure 3.5: temperature distribution for an alpha type Stirling engine in the ideal isothermal model (`http://www.ohio.edu/mechanical/stirling/`).

Using the fundamental equation of perfect gases:

$$M = \frac{P.V}{R.T} \tag{3.2}$$

where M, P, V, R, T denote respectively the mass, pressure, volume, perfect gas constant and temperature, one obtains together with (3.1) the following equation for the total mass of the working gas M_g:

$$M_g = P.\frac{\frac{V_{comp}}{T_c} + \frac{V_c}{T_c} + \frac{V_r}{T_r} + \frac{V_h}{T_h} + \frac{V_{exp}}{T_h}}{R} \tag{3.3}$$

where V_{comp}, V_c, V_r, V_h, V_{exp} denote respectively the compression space, the cooler space, the regenerator space, the heater space and the expansion space volumes. In (`http://www.ohio.edu/mechanical/stirling/`), a mean effective regenerator temperature was defined by:

$$T_r = \frac{T_h - T_c}{ln(\frac{T_h}{T_c})} \tag{3.4}$$

This temperature T_r takes into account the fact that the the working gas mass distribution along the regenerator length is not uniform but depends on the temperature profile that is assumed to be linear as depicted in Figure 3.5.

Combining (3.3) and (3.4), one obtains:

$$P(\theta, T_h, T_c) = \frac{M_g.R}{\frac{V_{comp}}{T_c} + \frac{V_c}{T_c} + \frac{V_r.ln(\frac{T_h}{T_c})}{T_h - T_c} + \frac{V_h}{T_h} + \frac{V_{exp}}{T_h}} \tag{3.5}$$

where θ is the shaft angle. Note that the gas pressure given by (3.5) depends on θ since the volumes V_{comp} and V_{exp} depend also on this variable as it will be explained in Section 3.2.2.

The net work produced by the Stirling engine over a complete cycle is then given by the cyclic integration of the product $P.dV$ as follow:

$$\begin{aligned} W_{tot} &= W_{exp} + W_{comp} \\ &= \oint (P(\theta, T_h, T_c).dV_{exp}) + \oint (P(\theta, T_h, T_c).dV_{comp}) \\ &= \oint \Big(P(\theta, T_h, T_c).(\frac{dV_{exp}}{d\theta} + \frac{dV_{comp}}{d\theta}) \Big) d\theta \end{aligned} \tag{3.6}$$

By performing an energy analysis over a complete cycle for each cell of Figure 3.5 (see (`http://www.ohio.edu/mechanical/stirling/`) for more details) one obtains the following results:

$$Q_{exp} = W_{exp} \tag{3.7a}$$
$$Q_{comp} = W_{comp} \tag{3.7b}$$
$$Q_c = 0 \tag{3.7c}$$
$$Q_r = 0 \tag{3.7d}$$
$$Q_h = 0 \tag{3.7e}$$

Equations (3.7a)-(3.7b) give the relation between the absorbed (resp. the rejected) heat and the work produced (resp. consumed) which will serve further to compute the produced electrical power. According to (3.7c) and (3.7e), both the hot and cold heat exchangers seem to be redundant since the cyclic heat rejected from the cooler space Q_c and transferred to the heater space Q_h are set to zero. This is a direct result of the isothermal assumption for the compression and expansion spaces that implies maintaining these chambers at the respective cooler and heater temperatures.

The main issue in the presented model consists in computing the cyclic integral (3.6) which depends on the engine configuration. This is presented in the following section based on the Schmidt analysis.

3.2.2 Schmidt Analysis

In order to compute (3.6), Gustav Schmidt proposed in 1871 an analysis of the cycle assuming a sinusoidal volume variation for the compression and expansion chambers as illustrated in Figure 3.6. This leads to the following equations for the compression and expansion spaces volumes:

$$V_{comp} = V_{clc} + V_{swc}.(1 + \cos\theta)/2 \tag{3.8a}$$
$$V_{exp} = V_{cle} + V_{swe}.(1 + \cos(\theta + \alpha))/2 \tag{3.8b}$$

where V_{clc}, V_{swc} refer respectively to the clearance and swept volumes for the compression chambers (see Figure 3.6) while V_{cle}, V_{swe} refer respectively to the clearance and swept volumes for the expansion chambers.

The analysis proposed by Schmidt yields the closed form solution for the cycle given by (3.9) and (3.10) where the superscript *sch* refers to "Schmidt" (refer to (`http://www.ohio.edu/mechanical/stirling/`) for the detailed proof).

$$W_{comp}^{sch} = Q_{comp}^{sch} = \pi.V_{swc}.P_{mean}.\sin\beta.\frac{(\sqrt{1-b^2}-1)}{b} \tag{3.9a}$$

$$W_{exp}^{sch} = Q_{exp}^{sch} = \pi.V_{swh}.P_{mean}.\sin(\beta-\alpha).\frac{(\sqrt{1-b^2}-1)}{b} \tag{3.9b}$$

$$W_{tot}^{sch} = Q_{tot}^{sch} = W_{comp}^{sch} + W_{exp}^{sch} \tag{3.9c}$$

where

$$\beta = \arctan\left(\frac{\frac{V_{swh}.\sin\alpha}{T_h}}{\frac{V_{swh}.\cos\alpha}{T_h} + \frac{V_{swc}}{T_c}}\right) \tag{3.10a}$$

$$c = \frac{1}{2}.\sqrt{(\frac{V_{swh}}{T_h})^2 + 2.\frac{V_{swc}}{T_h}.\frac{V_{swc}}{T_c} + (\frac{V_{swc}}{T_c})^2} \tag{3.10b}$$

$$s = \frac{V_{swc}}{2.T_c} + \frac{V_{clc}}{T_c} + \frac{V_c}{T_c} + \frac{V_r.ln(\frac{T_h}{T_c})}{T_h - T_c} + \frac{V_h}{T_h} + \frac{V_{swh}}{2.T_h} + \frac{V_{clh}}{T_h} \tag{3.10c}$$

$$b = \frac{c}{s} \tag{3.10d}$$

$$P_{mean} = \frac{M_g.R}{s.\sqrt{1-b^2}} \tag{3.10e}$$

where P_{mean} is the mean working gas pressure inside the Stirling engine cycles.

To complete the previous ideal isothermal analysis, one needs to take into account the heat losses that occur inside the engine in order to be as close as possible from the reality. This is performed in the next section.

3.2.3 Heat losses analysis

The different heat losses that occur inside the engine are essentially due to the regenerator imperfection, the heat leaks, the friction losses and the joule effect inside the synchronous generator connected to the Stirling engine. In this section the mathematical model of each of the aforementioned heat losses is derived.

3.2.3.1 Regenerator losses

The regenerator is a cyclic device where during the first part of the cycle the hot gas flows from the heater to the cooler through the regenerator releasing some quantity of heat Q_c^{reg}

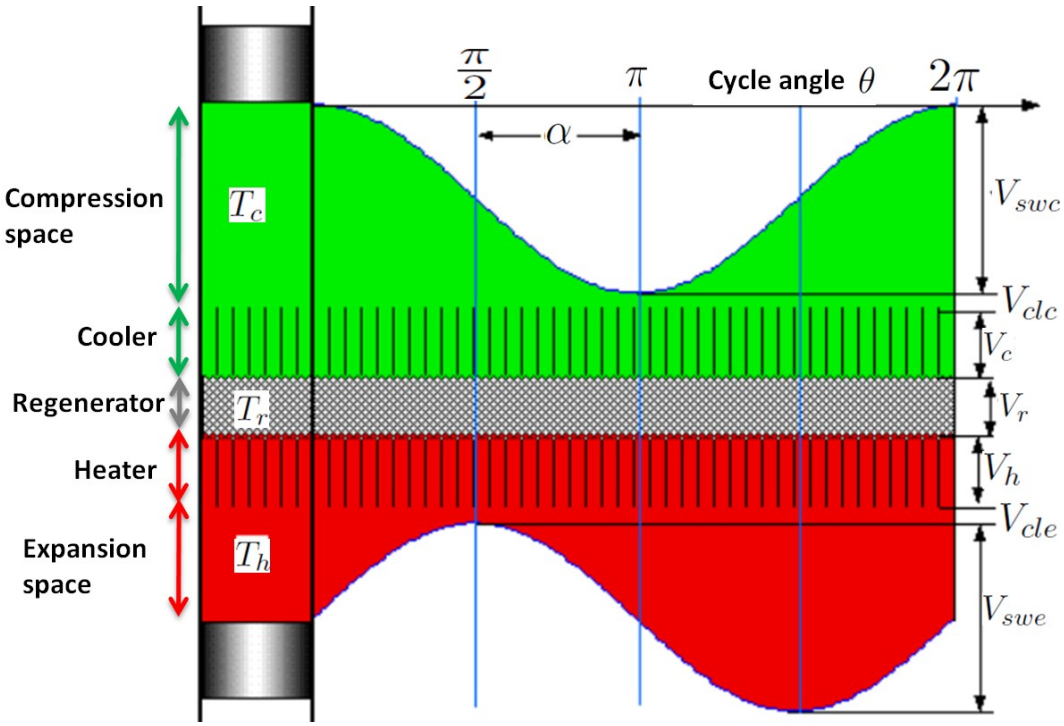

Figure 3.6: Sinusoidal volume variation (Schmidt analysis) for an alpha type Stirling engine (`http://www.ohio.edu/mechanical/stirling/`).

to the regenerator matrix. During the second part of the cycle, the cold gas comes back to the cooler through the regenerator and absorbs a quantity of heat Q_h^{reg} from the regenerator matrix. In an ideal regenerator $|Q_c^{reg}| = |Q_h^{reg}|$ that leads to a zero cyclic heat transferred externally to the regenerator: $Q_r = 0$. However, since the regeneration process is not perfect, when the working gas flows from the cooler to the heater (during the first part of the cycle) through the regenerator, it will have at the regenerator output a temperature lower than that of the heater. This induces an extra heat being externally supplied to increase the working gas temperature and bring it to the heater temperature T_h to comply with the isothermal analysis requirement. Analytically, this implies:

$$Q_{exp} = Q_{exp}^{sch} + Q_h^{reg}.(1 - \xi_{reg}) \tag{3.11}$$

where ξ_{reg} is the regenerator efficiency (that takes a value of 1 for ideal regenerator and 0 for a non regenerative process).

Similarly, during the second part of the cycle, when the working gas comes back from the heater to the cooler through the regenerator, an extra heat has to be rejected from the cooler to decrease the temperature at the output of the regenerator to set it at T_c. This implies:

$$Q_{comp} = Q_{comp}^{sch} - Q_c^{reg}.(1 - \xi_{reg}) \tag{3.12}$$

The ideal heat power transfered to the regenerator during each part of the cycle depends on the temperature difference between the heater and the cooler according to:

$$\dot{Q}_h^{reg} = \dot{Q}_c^{reg} = \frac{N_{rot}}{60}.M_g.c_p^{gas}.(T_h - T_c) \tag{3.13}$$

where N_{rot} is the shaft rotational speed in RPM (Rotation Per Minute) and c_p^{gas} is the working gas thermal capacity.

In (`http://www.ohio.edu/mechanical/stirling/`), it has been suggested that the regenerator efficiency can be expressed in term of the Number of Transfer Units (NTU) as follow:

$$\xi_{reg} = \frac{1}{1 + \frac{1}{NTU}} \tag{3.14}$$

This NTU variable, in addition of being dependent on the regenerator dimensions, depends on the working gas mass flow rate inside the regenerator which is proportional to N_{rot}. Thus, we suggested to set the following form for the regenerator efficiency:

$$\xi_{reg} = \frac{1}{1 + NTU_0.(\frac{N_{rot}}{N_0})^{\alpha_{reg}}} \tag{3.15}$$

where NTU_0, N_0 and α_{reg} are some parameters to be identified using experimental data.

3.2.3.2 Heat leaks

Since the Stirling engine enclosure is not totally adiabatic some heat leak exists from the hot source to the cold sink whose power $\dot{Q}_{leak}$ is set according to the following equation:

$$\dot{Q}_{leak} = K_{leak}.(T_h - T_c) \tag{3.16}$$

where K_{leak} is an unknown parameter to be identified. This leak power has to be added in the expression of the absorbed power $\dot{Q}_{exp}$ and substracted from the expression of the rejected power $\dot{Q}_{comp}$.

3.2.3.3 Friction losses

It is well known that the power of the mechanical friction losses are proportional to the rotational speed and its square value according to:

$$\dot{Q}_{mech} = (A + B.N_{rot}).N_{rot} \tag{3.17}$$

where A and B are some parameters to be identified. $\dot{Q}_{mech}$ has also to be respectively added and substracted from $\dot{Q}_{exp}$ and $\dot{Q}_{comp}$.

3.2.3.4 Heat loss by Joule effect

Since the Synchronous generator windings have a resistive effect (through the line winding resistance R_s), an extra heat has to be rejected from the cooler that is given by:

$$\dot{Q}_{res} = 3.R_s.I_{mot}^2 \tag{3.18}$$

where I_{mot} is the line current of the electrical generator connected to the Stirling engine.

3.2.4 Heat transfer through the heat exchangers

The Stirling engine is connected to the heat source and cold sink through heat exchangers to respectively absorb heat from the hot fluid (heated by mean of the solar collector field and stored inside the heat tank) and reject heat to the cooling loop. The hot fluid enters the Stirling engine at temperature Th_{in} with a mass flow rate $\dot{m}_h$ and exits the engine at temperature Th_{out} transferring a certain quantity of heat Q_{exp} to the working gas (inside the Stirling cycles) whose heat power $\dot{Q}_{exp}$ is given by:

$$\dot{Q}_{exp} = \dot{m}_h.c_p^h.(Th_{in} - Th_{out}) \tag{3.19}$$

where c_p^h is the hot fluid thermal capacity.

Suppose a mean temperature for the hot fluid inside the heat exchanger (hot fluid side):

$$TH = \frac{Th_{in} + Th_{out}}{2}$$

The heat transfer between the hot fluid and the working gas that occurs across the heat exchanger walls can be written in term of heat power as follows:

$$\dot{Q}_{exp} = K_h(N_{rot}, \dot{m}_h).(\frac{Th_{in} + Th_{out}}{2} - T_h) \tag{3.20}$$

where $K_h(N_{rot}, \dot{m}_h)$ is the thermal conductance of the heat exchanger which is due to the convective heat transfer between the hot fluid and the hot side heat exchanger wall (that depends on $\dot{m}_h$), the thermal conductance through the heat exchanger walls and the convective heat between the working gas inside the cycle and the other heat exchanger wall (that depends on N_{rot}). Neglecting the conductive heat transfer through the heat exchanger walls, $K_h(N_{rot}, \dot{m}_h)$ can be expressed as:

$$K_h(N_{rot}, \dot{m}_h) = \frac{1}{\frac{1}{K_h^{fluid}} + \frac{1}{K_g}} \tag{3.21}$$

where K_h^{fluid} is the heat conductance by convection between the hot fluid and the hot side heat exchanger wall which is proportional to the hot fluid mass flow rate and therfore can be set to:

$$K_h^{fluid} = K_h^{fluid,nom}.(\frac{\dot{m}_h}{\dot{m}_h^{nom}})^{\alpha_h} \tag{3.22}$$

where $K_h^{fluid,nom}$, $\dot{m}_h^{nom}$ and α_h are some parameters to be identified.

K_g is the heat conductance by convection between the working gas and the other heat exchanger wall that is inversely proportional to the rotational speed (when the rotational speed increases, the working fluid spends less time in contact with the heat exchanger wall which decreases the heat transfer) and can be set as:

$$K_g = K_g^{nom}.(\frac{N_{rot}^{nom}}{N_{rot}})^{\alpha_g} \tag{3.23}$$

where K_g^{nom}, N_{rot}^{nom} and α_g are some parameters to be identified.

A similar analysis can be performed for the heat transfer between the cold sink and the compression chamber. Thus, the coolant enters the Stirling engine at temperature Tc_{in} with a mass flow rate $\dot{m}_c$ and exits the engine at a higher temperature Tc_{out} absorbing a certain quantity of heat Q_{comp} whose power $\dot{Q}_{comp}$ is given by:

$$\dot{Q}_{comp} = \dot{m}_c.c_p^c.(Tc_{in} - Tc_{out}) \tag{3.24}$$

where c_p^c is the thermal capacity of the cooling fluid.

Also, supposing a mean temperature of the cooling fluid inside the cold fluid side heat exchanger:

$$TC = \frac{Tc_{in} + Tc_{out}}{2}$$

The heat power rejected to the cold sink can be expressed as follows:

$$\dot{Q}_{comp} = K_c(N_{rot}, \dot{m}_c).(\frac{Tc_{in} + Tc_{out}}{2} - T_c) \tag{3.25}$$

where $K_c(N_{rot}, \dot{m}_c)$ is the heat conductance for the cold side heat exchanger given by:

$$K_c(N_{rot}, \dot{m}_h) = \frac{1}{\frac{1}{K_c^{fluid}} + \frac{1}{K_g}} \tag{3.26}$$

where K_c^{fluid} is the heat conductance by convection between the cold fluid and the cold side heat exchanger wall which is proportional the cold fluid mass flow rate $\dot{m}_c$ and therefore can be set to:

$$K_c^{fluid} = K_c^{fluid,nom}.(\frac{\dot{m}_c}{\dot{m}_c^{nom}})^{\alpha_c} \tag{3.27}$$

where $K_c^{fluid,nom}$, $\dot{m}_c^{nom}$ and α_c are some parameters to be identified.

3.2.5 Produced power and cycle efficiency

The Stirling engine cyclic produced power P_{elec}^{cyclic} denoted for convenience P_{elec} is given by the sum of the cyclic absorbed power $\dot{W}_{comp}$ and the cyclic produced power $\dot{W}_{exp}$ which corresponds to the area of the closed curve $1-2-3-4$ of the Stirling engine P-V diagram (see Figure 3.4) multiplied by the engine frequency $\frac{N_{rot}}{60}$ as follow:

$$P_{elec} = \frac{N_{rot}}{60}.(W_{comp} + W_{exp}) = \dot{W}_{comp} + \dot{W}_{exp} \tag{3.28}$$

The cycle efficiency is by definition given by the ratio of the produced power P_{elec} and the absorbed power $\dot{Q}_{exp}$:

$$\eta_{cycle} = \frac{P_{elec}}{\dot{Q}_{exp}} \tag{3.29}$$

3.2.6 Summary of the Stirling engine equations

According to the analysis performed in previous sections, the Stirling engine equations that take into account the heat losses are summarized below:

$$\begin{aligned}
\dot{Q}_{exp} &= n_{cyl}.\frac{N_{rot}}{60}.Q_{exp}^{sch} + n_{cyl}.M_g.c_p^g.(1-\xi_{reg}).(T_h - T_c) + K_{leak}.(T_h - T_c) && (3.30a)\\
\dot{Q}_{comp} &= n_{cyl}.\frac{N_{rot}}{60}.Q_{comp}^{sch} - n_{cyl}.M_g.c_p^g.(1-\xi_{reg}).(T_h - T_c) - K_{leak}.(T_h - T_c) && (3.30b)\\
& -(A + B.N_{rot}).N_{rot} && (3.30c)\\
\dot{Q}_{exp} &= \dot{m}_h.c_p^h.(Th_{in} - Th_{out}) && (3.30d)\\
\dot{Q}_{exp} &= K_h(N_{rot}, \dot{m}_h).(\frac{Th_{in} + Th_{out}}{2} - T_h) && (3.30e)\\
\dot{Q}_{comp} &= \dot{m}_c.c_p^c.(Tc_{in} - Tc_{out}) && (3.30f)\\
\dot{Q}_{comp} &= K_c(N_{rot}, \dot{m}_c).(\frac{Tc_{in} + Tc_{out}}{2} - T_c) && (3.30g)\\
P_{elec} &= \dot{Q}_{exp} + \dot{Q}_{comp} && (3.30h)\\
\eta_{cycle} &= \frac{P_{elec}}{\dot{Q}_{exp}} && (3.30i)
\end{aligned}$$

where:

$$\xi_{reg} = \frac{1}{1 + NTU_0.(\frac{N_{rot}}{N_0})^{\alpha_{reg}}} \tag{3.31a}$$

$$K_h(N_{rot}, \dot{m}_h) = \frac{1}{\frac{1}{K_h^{fluid}} + \frac{1}{K_g}} \tag{3.31b}$$

$$K_c(N_{rot}, \dot{m}_c) = \frac{1}{\frac{1}{K_c^{fluid}} + \frac{1}{K_g}} \tag{3.31c}$$

and:

$$K_g = K_g^{nom}.(\frac{N_{rot}^{nom}}{N_{rot}})^{\alpha_g} \tag{3.32a}$$

$$K_h^{fluid} = K_h^{fluid,nom}.(\frac{\dot{m}_h}{\dot{m}_h^{nom}})^{\alpha_h} \tag{3.32b}$$

$$K_c^{fluid} = K_c^{fluid,nom}.(\frac{\dot{m}_c}{\dot{m}_c^{nom}})^{\alpha_c} \tag{3.32c}$$

Q_{exp}^{sch} and Q_{comp}^{sch} are the indicated exchanged heat coming from the Schmidt analysis and given by (3.9a)-(3.9b) and (3.10).

Note from (3.30a)-(3.30c) that a multiplicative term n_{cyl} has been introduced to account for the number of cylinder pairs that behave identically and linked to the rotating shaft.

In the previous equations the following set of parameters have to be identified experimentally (as described in section 3.3): K_{leak}, A, B, NTU_0, N_0, α_{reg}, K_g^{nom}, N_{rot}^{nom}, α_g, $K_h^{fluid,nom}$, $\dot{m}_h^{nom}$, α_h, $K_c^{fluid,nom}$, $\dot{m}_c^{nom}$ and α_c.

3.3 Stirling engine parameter identification

This section validates experimentally the nonlinear static model of the Stirling engine developed in Section 3.2 using experimental data gathered on a real testbed that is described below.

3.3.1 Description of the experimental testbed

Figure 3.7 gives an overview of the experimental Stirling based power system under consideration. The cooling loop depicted in Figure 3.8 that consists essentially of a circulating pump and a cooling fan serves as a cold sink to evacuate heat from the Stirling engine. The electrical heater (see Figure 3.7) serves to heat the oil (therminol 66) that enters the hot side Stirling engine heat exchanger. The power conversion system depicted in Figure 3.7 that is used to drive dynamically the Stirling engine acting on the electrical part will be presented in Chapter 4. To generate the data used to identify the unknown parameters of the Stirling engine

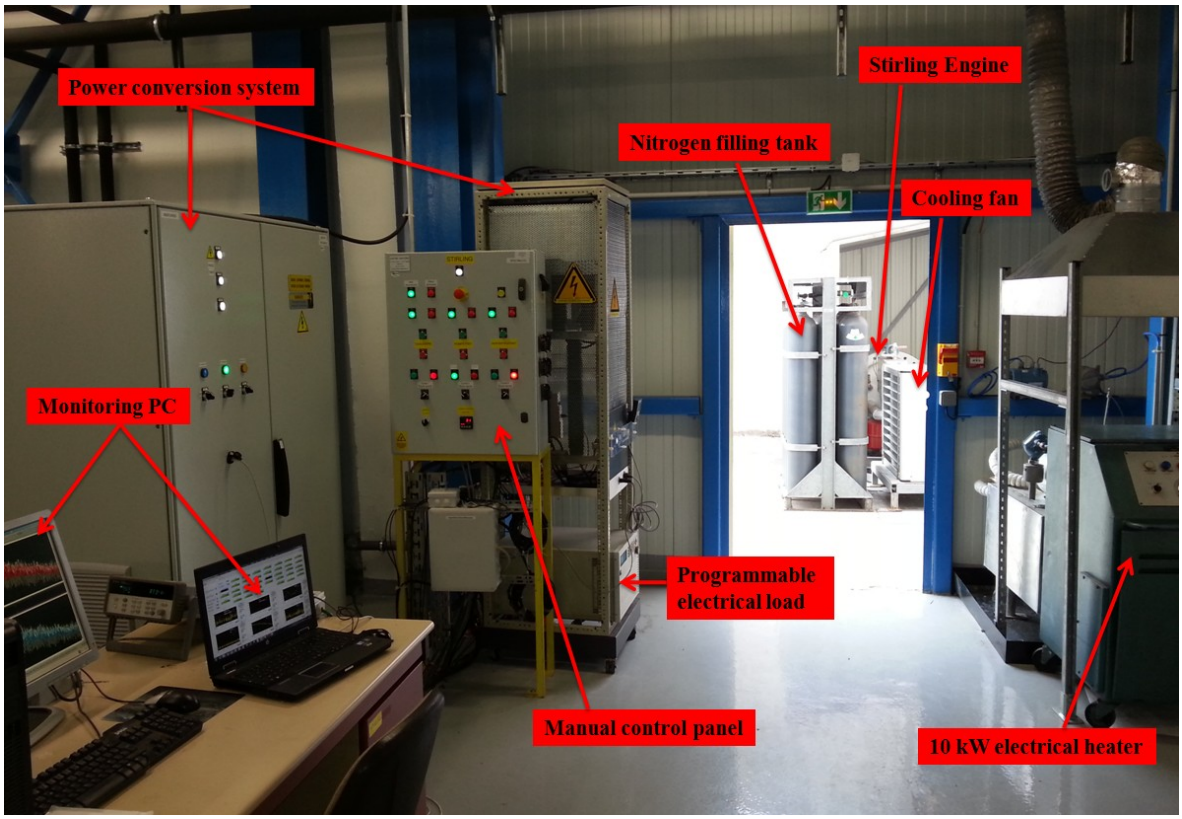

Figure 3.7: Overview of the Stirling based power system

model, the Permanent Magnet Synchronous Generator (PMSG) associated to the Stirling is connected directly to the programmable electrical load through a rectifier. By this way, for a given value of the electrical load resistance R_{load} corresponds some rotational speed of the engine N_{rot} (in steady state).

3.3.2 Identification of the unknown parameters of the Stirling engine model

Each static operating point of the $3kW_{elec}$ (maximum electrical output at $300°C$ for the hot fluid temperature) alpha type Stirling engine is determined by fixing a value for: Th_{in}, Tc_{in}, $\dot{m}_h$, $\dot{m}_c$, P_{mean} and N_{rot}. To identify the unknown parameters of the Stirling engine model, we have collected measurements on the Stirling testbed corresponding to different operating conditions (covering all the operating range of the machine) by varying Th_{in}, Tc_{in}, $\dot{m}_h$, $\dot{m}_c$, P_{mean} and N_{rot} over their admissible range with some discretization such that to have a good trade-off between the number of obtained operating points and the time spent to obtain these points. After eliminating the outlier points, it resulted 187 operating points used during the identification process.

Initially, we set the problem of finding the unknown parameters in the form of a nonlinear

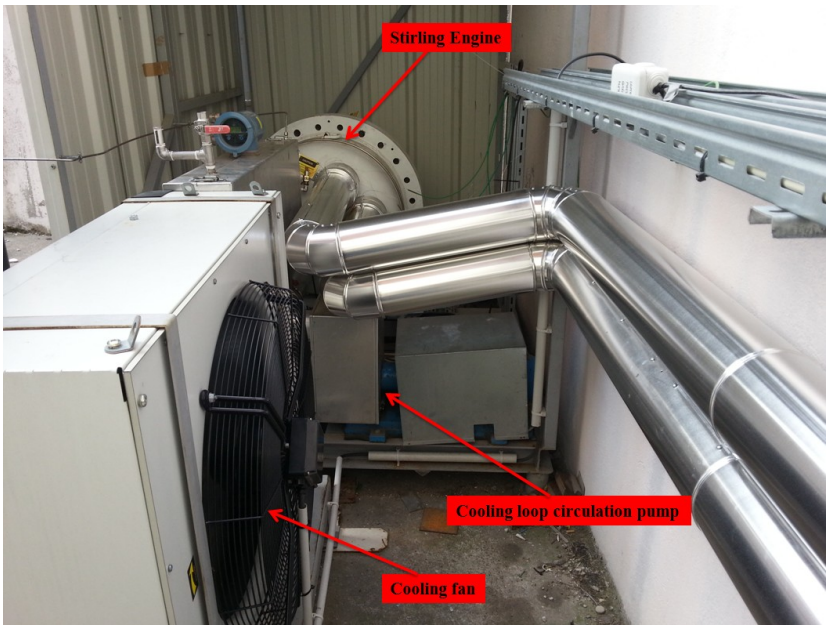

Figure 3.8: Zoom on the Stirling engine and the cooling loop

curve-fitting (data-fitting) problem in least-squares sense. We tried to use the nonlinear curve fitting routines of MATLAB® like "lsqcurvefit" but we could not find the optimal parameters because of the presence of multiple local minima for the objective function to be minimized. Afterwards, we used the functions of the "Global Optimization toolbox" of MATLAB® especially the "MultiStart" functions that enable to find a global minimum among multiple local minima leading to the determination of the optimal parameters and hence solving the identification problem. The unknown Stirling engine model parameters given below:

K_{leak}=2.6×10^{-14} W/K	α_{reg}=-0.653	$\dot{m}_h^{nom}$=0.176 Kg/s
A=2.22 × 10^{-14} J	K_g^{nom}=563.5 W/K	α_h=0.78
B= 2.22 × 10^{-5}J.s	N_{rot}^{nom}=545.2 RPM	$K_c^{fluid,nom}$=611.45 W/K
NTU_0=0.1	α_g=-1.699	$\dot{m}_c^{nom}$=0.971 Kg/s
N_0=200 RPM	$K_h^{fluid,nom}$=69.9 W/K	α_c=0.493

These parameters make the Stirling engine model fits in a least squares sense the experimental measurements as illustrated in Figure 3.9.

To assess the parameter identification procedure quality and the model validity, a comparison between some of the Stirling engine model outputs and their corresponding measured signals is performed. Hence Figure 3.10 compares the experimental output electrical power, the absorbed and rejected heat powers with their corresponding model outputs for all the operating points while Figure 3.11 compares the measured and theoretical output hot and cold temperatures. From Figure 3.10 and Figure 3.11 one can appreciate the good model quality since most of the points in the plane (measured variables-output model variables) lie near the identity line.

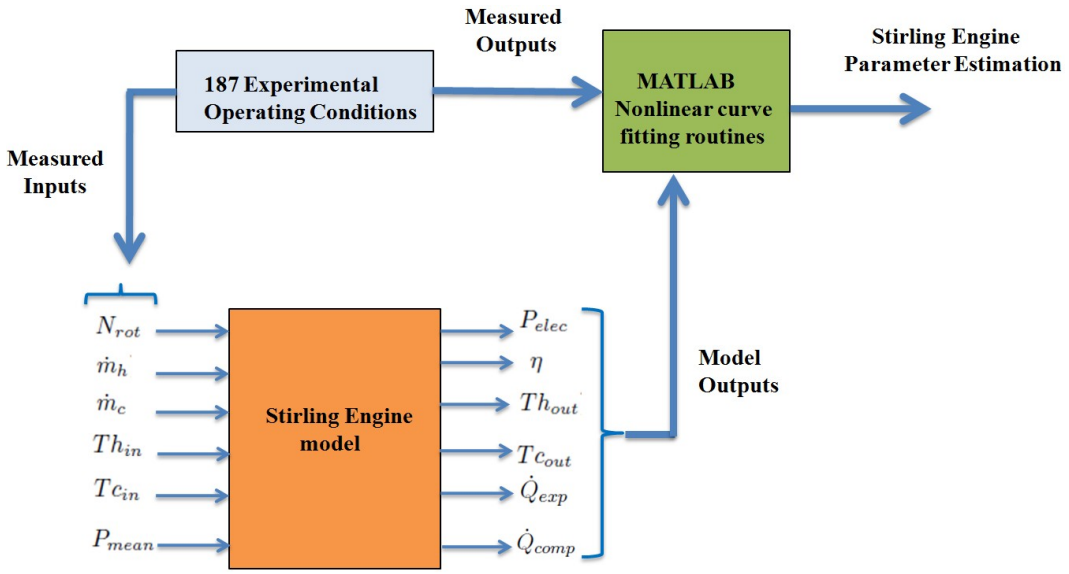

Figure 3.9: Identification procedure for the Stirling engine unknown parameters

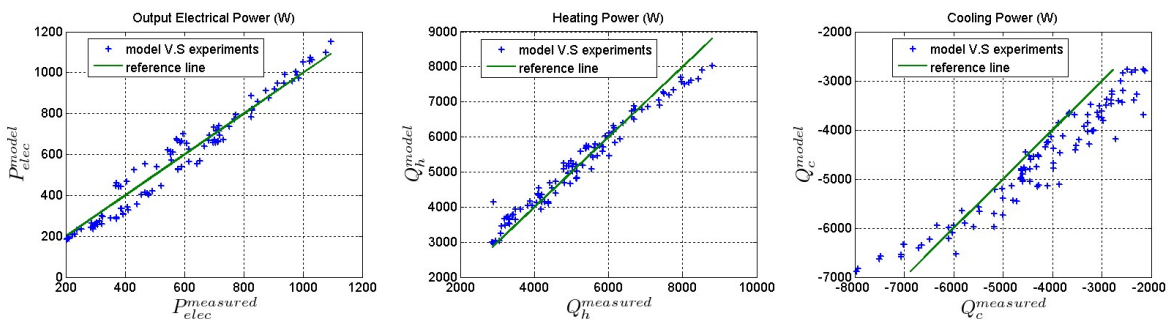

Figure 3.10: Comparaison between the measured and the theoretical output electrical power, absorbed and rejected heat powers

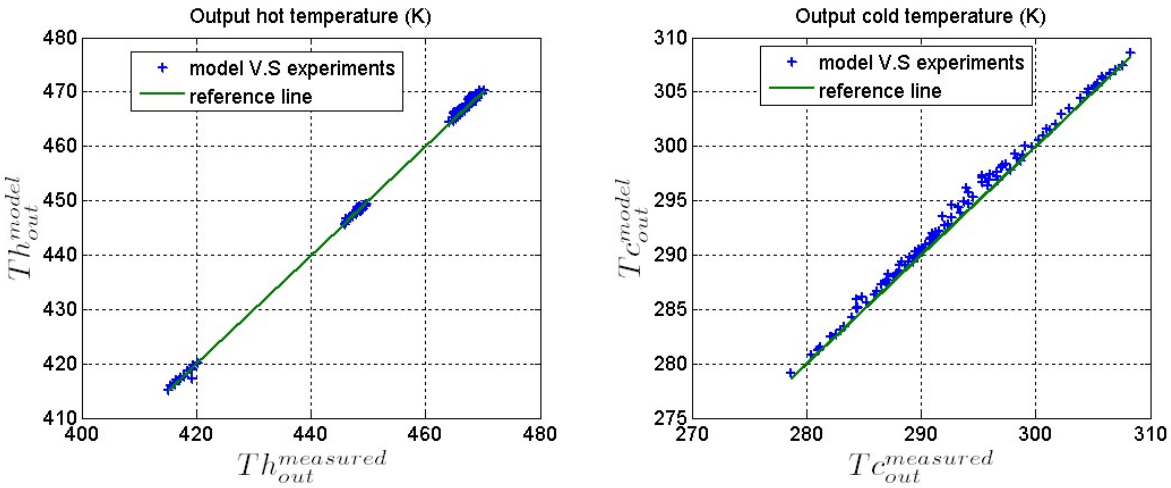

Figure 3.11: Comparaison between the measured and theoretical output hot and cold temperatures

3.3.3 Stirling engine torque expression

In order to derive a simpler expression of the Stirling engine motor torque T_{mot} that will be used during the control design of the energy conversion system (that will be discussed in Chapters 5 and 6), the following expression for T_{mot} (that has been initially suggested in [Meyer, 2011]) has been fitted to the experimental data:

$$T_{mot} = \alpha(\dot{m}_h, \dot{m}_c, Th_{in}, Tc_{in}).\Omega(t) + \beta(\dot{m}_h, \dot{m}_c, Th_{in}, Tc_{in}) \tag{3.33}$$

where $\alpha(.)$ and $\beta(.)$ are the functions identified from the experimental measurements, using the Eureqa-Formulize® equation fitter software[1] ([Schmidt and Lipson, 2009]), and given by:

$$\begin{aligned}
\alpha(\dot{m}_h, Th_{in}, Tc_{in}) &= 0.2498 + 0.004109.Th_{in} + 3.13 \times 10^{-5}.Th_{in}.Tc_{in}.\dot{m}_h \\
&\quad -1.812.\dot{m}_h - 1.655 \times 10^{-5}.Th_{in}.Tc_{in} - 0.007562.Tc_{in}\dot{m}_h \\
\beta(Th_{in}) &= 0.1.Th_{in} - 30.03
\end{aligned}$$

Figure 3.12 compares the fitted motor torque (3.33) with the experimental measurements. One can see from this figure that the derived motor torque expression nicely fits to experimental measurements even if for some operating conditions the model errors can reach 20%. These identifications errors will be dynamically estimated using a Luenberger observer as it will be explained in Chapter 5 (see Section 5.3.2)

[1] `http://www.eureqa.com/`

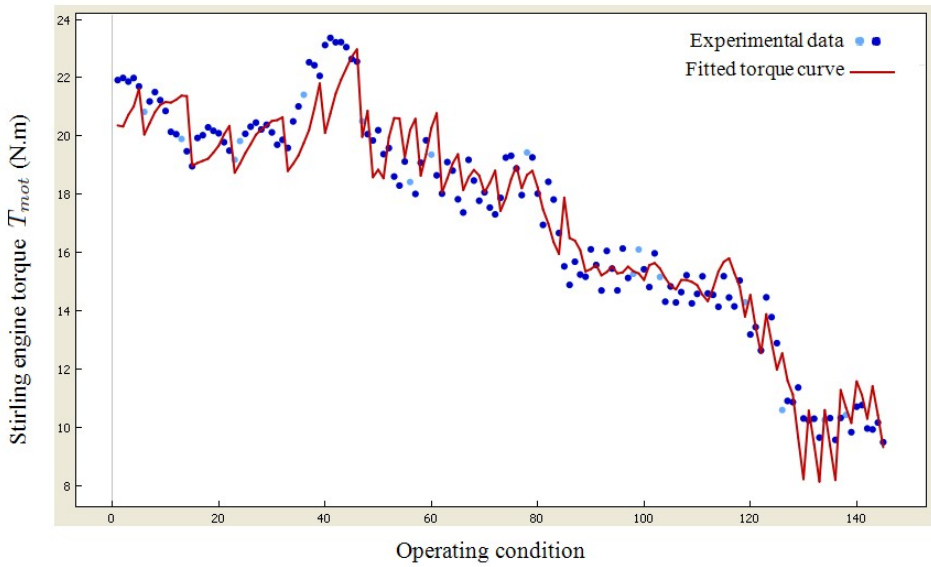

Figure 3.12: Comparison between the fitted Stirling engine torque equation and the torque derived from the experimental data. each point in the figure corresponds to an operating condition defined by N_{rot}, $\dot{m}_h$, $\dot{m}_c$, Th_{in} and Tc_{in}

3.4 Optimal Stirling engine motor torque controller

The main control objective of the Stirling based power plant is to track some desired electrical power reference value. Since the power produced by the Stirling engine is the product of its motor torque T_{mot} by its rotational speed $\Omega(t)$, one can control these two quantities to achieve the control objectives. Since these two quantities evolve in two separate time scales, it is possible to design the two controllers in a separate manner. The control of the Stirling engine rotational speed will be discussed in Chapters 5 and 6 when designing the control strategy for the energy conversion system. Concerning the control of the motor torque, this is done by acting on the hot and cold mass flow rates namely $\dot{m}_h$ and $\dot{m}_c$ (since the cooling fan speed is set to a constant value in our application and considering Th_{in} and Tc_{in} as exogenous signals) through controlling the hot side and the cold side circulation pumps. By changing the setpoints of the hot and cold mass flow rates, the pumps will consume more or less electrical power. Since our main control objective is to supply the net electrical power requested by the loads (excluding the pumps), the mass flow rates setpoints are chosen such that to maximize the net thermoelectric efficiency of the Stirling based power plant leading to the following formula:

$$(\dot{m}_h^{opt}, \dot{m}_c^{opt}) = \arg\max_{\dot{m}_h, \dot{m}_c} \eta_{thermoelectric}^{net} = \frac{P_{elec}^{load} - P_{elec}^{pumps}}{\dot{Q}_{exp}} \tag{3.34}$$

Since (3.34) is rather complex to solve online (due to the Stirling engine model complexity),

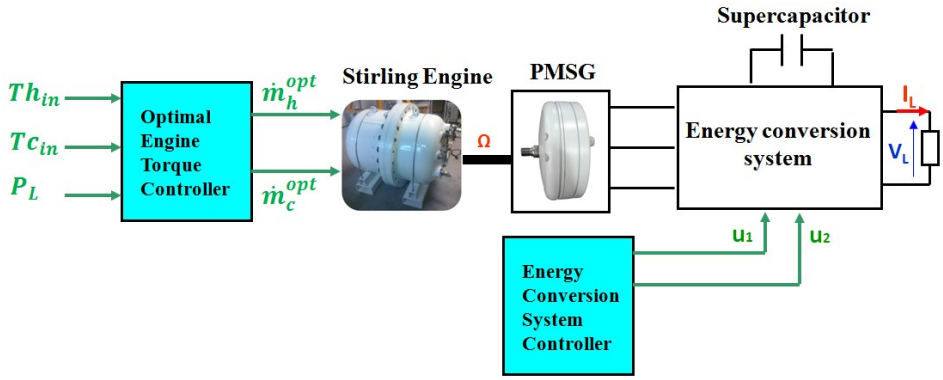

Figure 3.13: Stirling engine optimal torque controller

the optimization is performed off-line to construct two cartographies that give, according to the operating conditions (Th_{in} and Tc_{in}) and the load power demand P_L, the optimal references for the hot and cold mass flow rates namely $\dot{m}_h^{opt}$ and $\dot{m}_c^{opt}$ as illustrated in Figure 3.13. The inputs of the cartographies, namely Th_{in}, Tc_{in} and P_L, are discretized such that to minimize the number of points in these cartographies (to minimize the time needed to construct these cartographies and the time needed during the interpolations) while having a good enough resolution. We have chosen for Th_{in} and Tc_{in} a step size of $10°C$ and for P_L a step size of $100W$.

Figures 3.14 and 3.15 give the picture of the off-line computed cartographies by depicting the isolines of $\dot{m}_h^{ref}$ and $\dot{m}_c^{ref}$ for a fixed value of P_{elec}^{ref}. Figure 3.16 gives an example of the resulting optimal mass flow rates for $Th_{in} = 170°C$ and $Tc_{in} = 20°C$.

3.5 Conclusion

In this chapter, the Stirling engine based power system under study was presented. Then, a static model of the engine taking into account the different losses was derived, identified and validated using experimental data gathered on the prototype. Finally, a cartography based controller was developed to optimally control the Stirling engine motor torque.

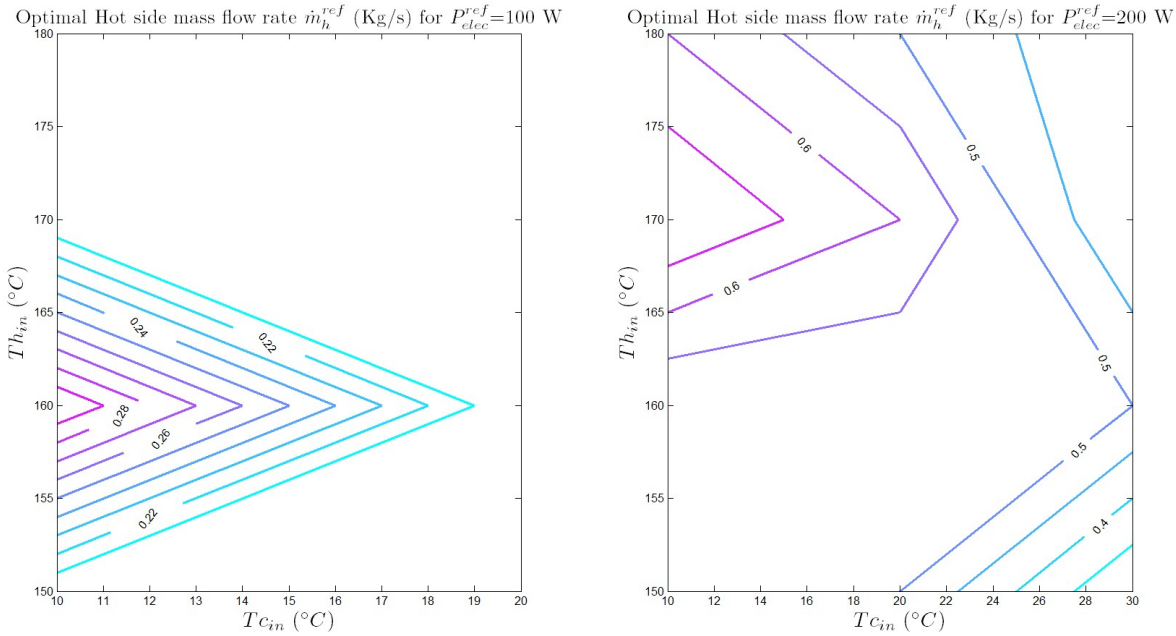

Figure 3.14: Isolines of the optimal hot side mass flow rate $\dot{m}_h^{ref}$ for P_{elec}^{ref}=100 W and P_{elec}^{ref}=200.

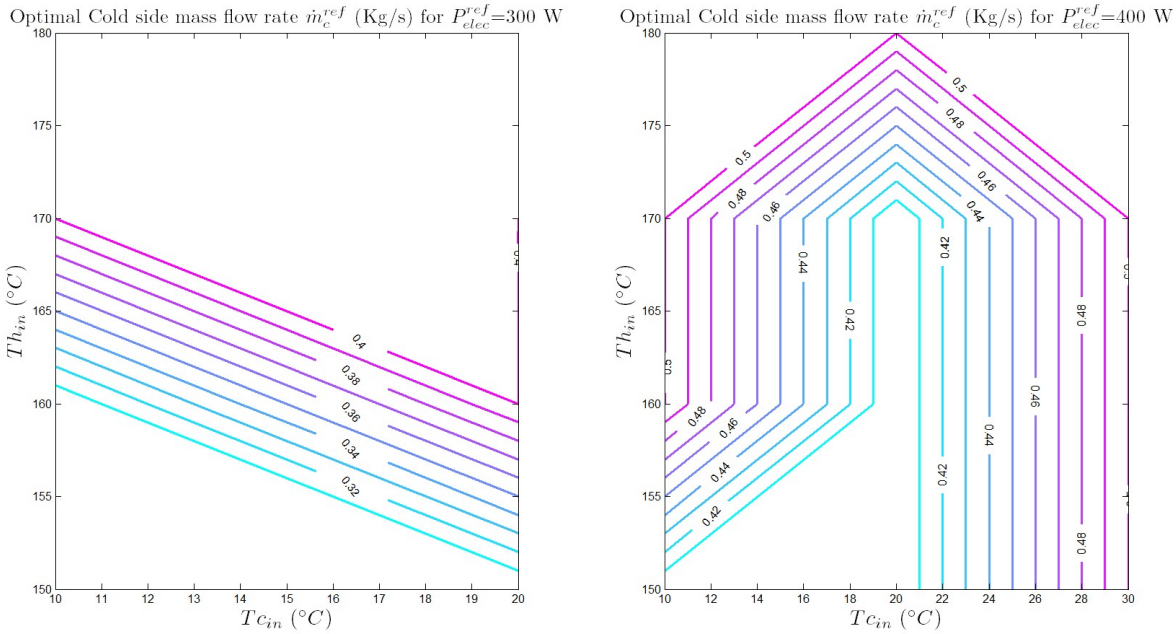

Figure 3.15: Isolines of the optimal cold side mass flow rate $\dot{m}_c^{ref}$ for P_{elec}^{ref}=300 W and P_{elec}^{ref}=400.

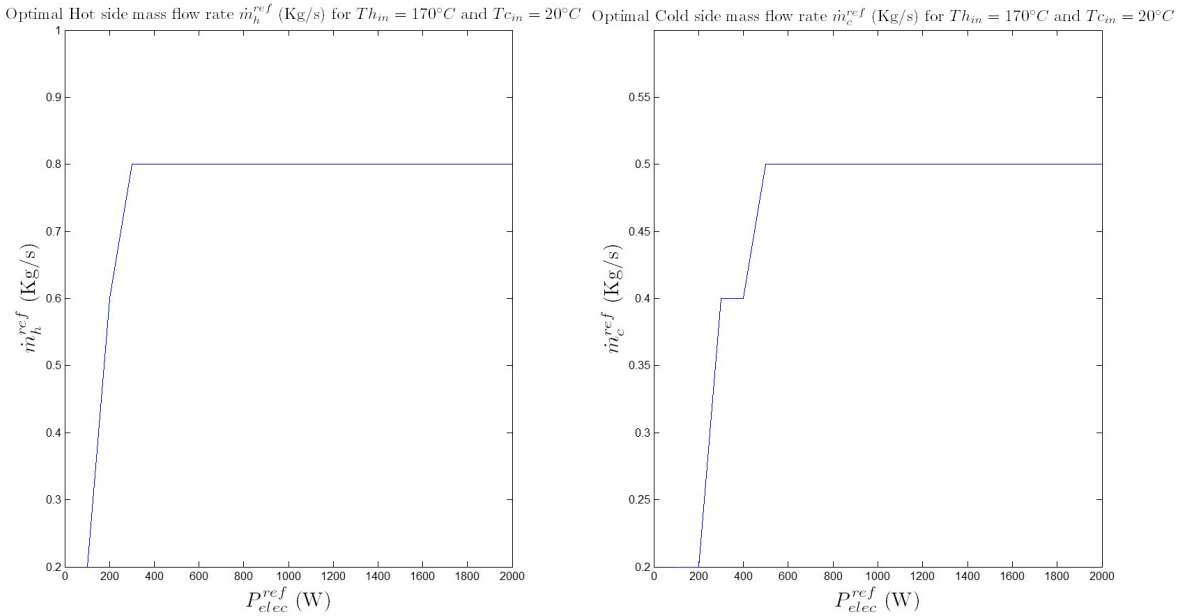

Figure 3.16: Optimal hot and cold mass flow rates references for the following operating conditions : $Th_{in} = 170°C$ and $Tc_{in} = 20°C$.

Chapter 4

Dynamic Model of the Energy Conversion System associated with the Stirling Engine

Contents

4.1 Energy conversion system architecture 43
4.2 Dynamic modeling of the energy conversion system 44
4.2.1 Dynamic model of the Permanent Magnet Synchronous Generator (PMSG) 44
4.2.2 Model of the full wave diode bridge 46
4.2.3 Modeling the association of the PMSG and the diode bridge 46
4.2.4 Rotor dynamics 47
4.2.5 Modeling the DC/DC full bridge converter 48
4.2.6 Modeling the bidirectional DC/DC converter 48
4.2.7 DC bus equation 49
4.2.8 Modeling of the single phase inverter 50
4.2.9 Summary of the energy conversion system equations 50
4.3 State Space representation of the energy conversion system and control objectives 51
4.3.1 State Space representation of the energy conversion system 51
4.3.2 Control objectives and constraints 51
4.4 Conclusion 52

In this chapter, the energy conversion system associated to the Stirling engine (see Figure 3.13) is presented and its dynamic model derived leading to a state space representation of this system that will be used in Chapters 5 and 6 to design advanced control strategies that optimally drive the power plant.

4.1 Energy conversion system architecture

Figure 4.1 shows an overview of the solar thermodynamic micro power plant that consists of an alpha type Stirling engine linked mechanically to a Permanent Magnet Synchronous

Generator (PMSG) connected to the off-grid load to be supplied through an appropriate power conversion system (voltage conditioning stage). The Stirling engine is hybridized with a supercapacitor which serves as fast energy buffer to dynamically supply the energy requested by the off-grid loads during fast transients while the Stirling engine adapts its produced power (by an appropriate control Strategy developed in Chapters 5 and 6) in a rather slower manner due to its mechanical and thermal inertia.

The general principle of functioning of such system is as follows: the Stirling engine transforms the absorbed heat from the heat source into mechanical work (refer to Chapter 3) by performing a Stirling thermodynamic cycle at each shaft rotation. The produced Stirling torque is used to drive the PMSG that reacts electrically by producing an electromagnetic torque which together with the motor torque (and the friction torque) impose the rotational speed of the shaft. Because of the variable engine speed, the voltage at the output of the PMSG is of variable amplitude and frequency which is not directly usable by the loads. Hence, this voltage is first rectified through a diode bridge before being conditioned through a DC/DC full bridge converter whose output voltage is maintained (through an appropriate control strategy) to a constant bus voltage $V_{bus} = 50V$ which is compatible with a good functionning of the inverter (linked to the DC bus) that supplies the off-grid load with 230V and 50Hz AC voltage.

The supercapacitor is connected to the DC bus through a bidirectional DC/DC converter that is controlled though its duty ratio $u_2 = \alpha_{bb}$ to tightly regulate the DC bus voltage V_{bus}. The control $u_1 = \alpha_{fb}$ (duty ratio of the DC/DC full bridge converter) has then to be used to control the output current of the DC/DC full bridge converter namely I_{Lfb} at some desired reference value computed so as to meet the load power demand and to enable the charge/discharge of the supercapacitor in order to recover its desired voltage V_{sc}^{ref}.

4.2 Dynamic modeling of the energy conversion system

In this section the dynamic equations for each component of the energy conversion system depicted in Figure 4.1 are presented and when needed proved in the appendices.

4.2.1 Dynamic model of the Permanent Magnet Synchronous Generator (PMSG)

In the literature, one can find many papers and books that treat the modeling and simulation of different kinds of synchronous machines (see for instance [Chatelain, 1983], [Mouni et al., 2008] and [Barakat et al., 2010]). These models range from the most complex ones (detailed behavioral models) to simpler models. To simulate the dynamic behavior of the synchronous machine under consideration, the simplified Behn-Eshenbourg (see [Bracikowski, 2012]) model is considered whose per-phase schematic is depicted in Figure 4.2.

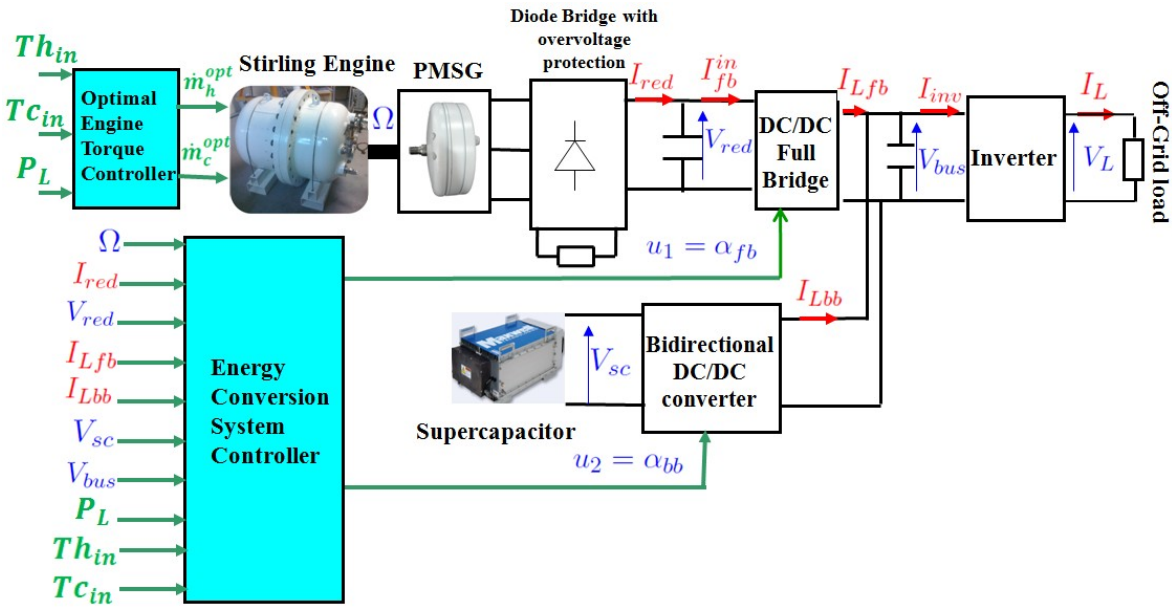

Figure 4.1: Overview of the Stirling based thermodynamic power plant and its associated power conversion system

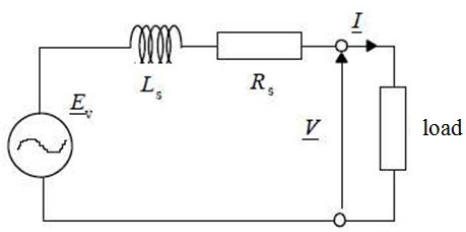

Figure 4.2: Behn-Eshenbourg simplified model for the PMSG

According to this model, the 3-phase output voltage in the (abc) frame is given by:

$$[V]_3 = [E_v]_3 - [R_s]_3.[I]_3 - [L_s]_3.\frac{d[I]_3}{dt} \tag{4.1}$$

where: $[V]_3 = \begin{bmatrix} V_a & V_b & V_c \end{bmatrix}^T$ is the 3-phase output voltage of the PMSG and $[I]_3 = \begin{bmatrix} I_a & I_b & I_c \end{bmatrix}^T$ is the 3-phase line current.

The 3-phase electromotive force (EMF) of the PSMG denoted by $[E_v]_3$ is proportional to the shaft rotational speed according to the following equation:

$$[E_v]_3 = \begin{pmatrix} E_{va} \\ E_{vb} \\ E_{vc} \end{pmatrix} = p.\phi_f.\Omega. \begin{bmatrix} \sin(p.\Omega.t) \\ \sin(p.\Omega.t - \frac{2.\pi}{3}) \\ sin(p.\Omega.t - \frac{4.\pi}{3}) \end{bmatrix} \tag{4.2}$$

where p is the number of pair poles of the PMSG, ϕ_f is the EMF constant of the motor and $\Omega(t)$ is the shaft rotational speed in rad/s. The inductance and resistance matrices respectively $[L_s]_3$ and $[R_s]_3$ are given by:

$$[L_s]_3 = \begin{bmatrix} L_s & M_s & M_s \\ M_s & L_s & M_s \\ M_s & M_s & L_s \end{bmatrix} \text{ and } [R_s]_3 = \begin{bmatrix} R_s & 0 & 0 \\ 0 & R_s & 0 \\ 0 & 0 & R_s \end{bmatrix}$$

where L_s and R_s are respectively the line inductance and line resistance of the PMSG and M_s is the mutual inductance.

Since the electromagnetic torque of the PMSG corresponds to the ratio of its produced electrical power by its rotational speed, its equation is given by:

$$T_{em} = \frac{E_{va}.I_a + E_{vb}.I_b + E_{vc}.I_c}{\Omega(t)}$$

4.2.2 Model of the full wave diode bridge

The diode bridge depicted in Figure 4.3 is an uncontrolled DC rectifier whose mean average output voltage V_{red} depends on the input voltage amplitude $V^{max} = V_a^{max} = V_b^{max} = V_c^{max}$ according to the following equation ([Skvarenina, 2002]):

$$V_{red} = \frac{3.\sqrt{3}}{\pi}.V^{max}$$

4.2.3 Modeling the association of the PMSG and the diode bridge

The models of the Synchronous generator and the diode bridge presented respectively in Sections 4.2.1 and 4.2.2 are used for the simulation of these components. In order to simplify further the model of the system consisting in the synchronous generator connected to the

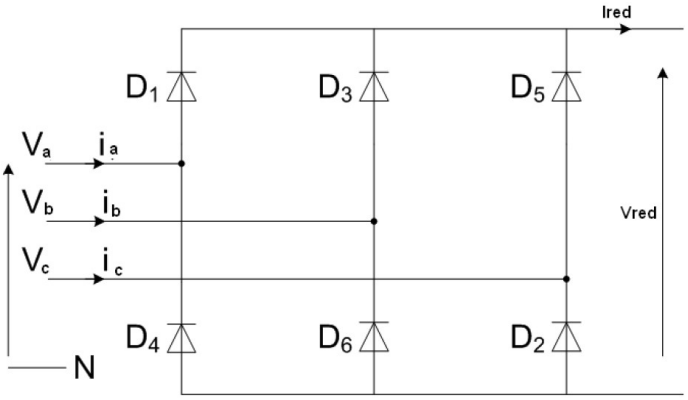

Figure 4.3: Full wave diode bridge.

diode bridge, its equivalent DC machine model, which is a control oriented model, is considered which supposes an equivalent serially connected inductance (neglecting the mutual inductance effect), resistance and EMF voltage source of the association PMSG-diode bridge forming an equivalent DC machine electrical circuit whose equations are given by (see [Abdelli, 2007] for more details):

$$\frac{dI_{red}}{dt} = -\frac{R_s}{L_s}.I_{red} - \frac{3.p}{2.\pi}.\Omega(t).I_{red} + \frac{3.\sqrt{3}}{2.\pi.L_s}.E_m(t) - \frac{1}{2.L_s}.V_{red} \tag{4.3a}$$

$$E_m(t) = p \cdot \Omega(t) \cdot \phi_f \tag{4.3b}$$

$$T_{em}(t) = p.\frac{3.\sqrt{3}}{\pi}.\phi_f.I_{red}(t) \tag{4.3c}$$

where V_{red} is the rectified voltage, I_{red} is the output current of the diode bridge, T_{em} designates the electromagnetic torque of the PMSG, $E_m(t)$ its EMF (electromotive force) and ϕ_f is the EMF constant of the motor.

4.2.4 Rotor dynamics

The dynamic equation of the shaft rotational speed results from the motor torque applied by the Stirling engine T_{mot} whose equation is given by (3.33), the electromagnetic torque of the PMSG given by (4.3c) and the friction torque proportional to the speed according to $T_{fr} = D_{fr}.\Omega(t)$ where D_{fr} is the friction coefficient. This leads to the following well known equation for the speed dynamics:

$$J_{rot}.\frac{d\Omega(t)}{dt} = T_{mot}(t) - T_{em}(t) - D_{fr}.\Omega(t) \tag{4.4}$$

where J_{rot} is the total inertia of the rotating parts.

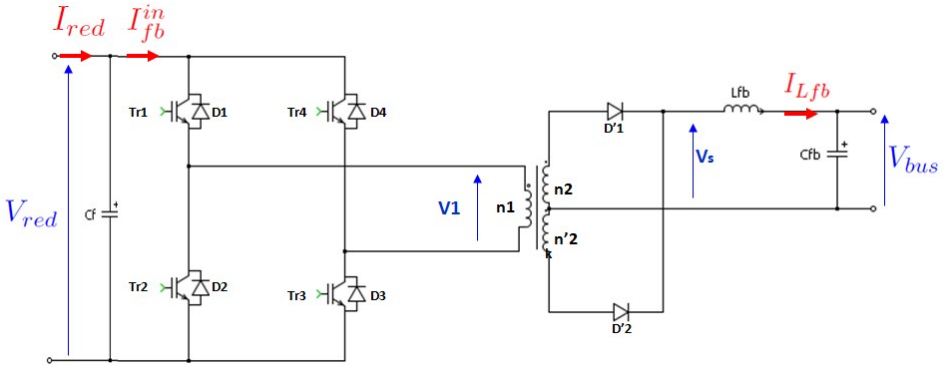

Figure 4.4: DC/DC Full Bridge converter.

4.2.5 Modeling the DC/DC full bridge converter

The DC/DC full bridge converter illustrated in Figure 4.4 is an isolated (due to the isolation transformer) buck transformer consisting in two IGBT (Insulated Gate Bipolar Transistors) legs at the primary of the transformer and a diode full-wave rectifier at the secondary of the transformer (see [Foch et al., 1992] for more details). In order to model such switching device the mean model formalism is used [Skvarenina, 2002]. In this modeling approach, the averaged model (averaging of the signals and control variable) of the converter over a switching period T_{sw} is considered in which the control variable becomes the duty ratio of the converter which is the ratio of the period on which some appropriate IGBT are enabled over the switching period. By applying this methodology on the considered DC/DC full bridge converter, its mean average model is derived (as explained in detail in Appendix B) and given by the following equations:

$$L_{fb}.\frac{\mathrm{d}I_{Lfb}}{\mathrm{d}t} = k.V_{red}.\alpha_{fb} - V_{bus} \tag{4.5a}$$

$$C_f.\frac{\mathrm{d}V_{red}}{\mathrm{d}t} = I_{red} - I_{fb}^{in} \tag{4.5b}$$

$$I_{fb}^{in} = k.I_{Lfb}.\alpha_{fb} \tag{4.5c}$$

where α_{fb} is the duty ratio of the Full bridge converter, L_{fb} is the output inductance of the DC/DC full bridge, C_f is the value of the input capacitor, k is the transformer winding ratio, I_{Lfb} is the output current of the DC/DC full bridge and I_{fb}^{in} is the current at the input of the converter.

4.2.6 Modeling the bidirectional DC/DC converter

The bidirectional DC/DC converter illustrated in Figure 4.5 is a current reversible DC/DC converter that interfaces the supercapacitor to the DC bus in order to adequately control the supercapacitor delivered power. This converter behaves as a buck converter when its output

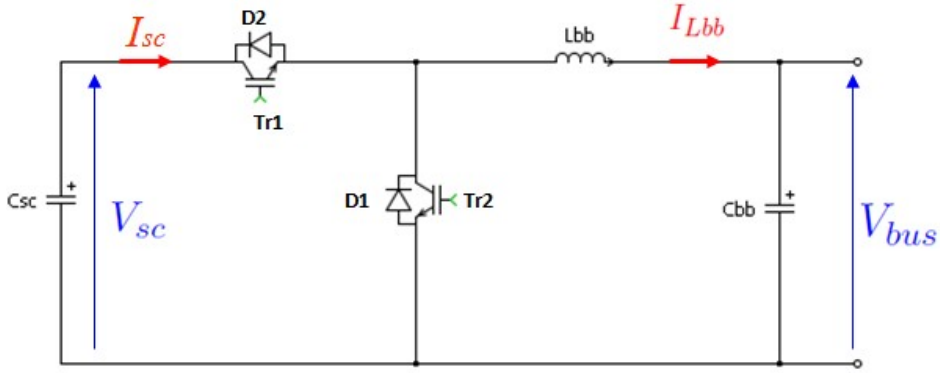

Figure 4.5: bidirectional DC/DC converter.

current (current of the output inductance L_{bb}) denoted by I_{Lbb} flows from the supercapacitor to the DC bus (positive current value) and behaves as a boost converter when the output current flows on the opposite direction (negative current value). Here also, we consider the average modeling approach of this device with a preference for the complementary control (see [Skvarenina, 2002]) that avoids the discontinuous conduction mode of the converter by activating both IGBT (but not simultanously) during a switching period T_{sw}. Assuming that such precaution is taken in the hardware, the mean model used in the control design can be given by (see Appendix B for the detailed proof):

$$L_{bb}.\frac{\mathrm{d}I_{Lbb}}{\mathrm{d}t} = V_{sc}.\alpha_{bb} - V_{bus} \tag{4.6a}$$

$$C_{sc}.\frac{\mathrm{d}V_{sc}}{\mathrm{d}t} = -I_{Lbb}.\alpha_{bb} \tag{4.6b}$$

where α_{bb} is the duty ratio of the bidirectional DC/DC converter, C_{sc} is the supercapacitor capacitance, V_{bus} is the DC bus voltage and V_{sc} is the supercapacitor voltage.

4.2.7 DC bus equation

The equation of the DC bus is given by (see Figure 4.1):

$$C_{tot}.\frac{dV_{bus}}{dt} = I_{Lfb} + I_{Lbb} - I_{inv} \tag{4.7a}$$

$$C_{tot} = C_{bb} + C_{fb} + C_{inv} \tag{4.7b}$$

where C_{bb} and C_{fb} are the values of the output capacitors of the bidirectional DC/DC converter and DC/DC full bridge converter respectively. C_{inv} is the value of the input capacitor of the inverter and C_{tot} is the equivalent capacitance of the three capacitors in parallel. I_{inv} denotes the input current of the inverter.

4.2.8 Modeling of the single phase inverter

The single phase inverter depicted in Figure 4.1 used in the testbed under consideration (as explained in Chapter 5) is a commercial product with its own integrated controller. Since we do not have any degree of freedom on this device, we will simply model it by an equation reflecting the power conversion between its input and its output as follows:

$$P_L = \eta_{inv}.V_{bus}.I_{inv} \tag{4.8}$$

where η_{inv} is the electrical efficiency of the inverter and P_L is the load power demand.

4.2.9 Summary of the energy conversion system equations

The dynamic equations governing the behavior of the energy conversion system are summarized as follows:

$$J_{rot}.\frac{\mathrm{d}\Omega}{\mathrm{d}t} = \alpha(\dot{m}_h, Th_{in}, Tc_{in}).\Omega + \beta(Th_{in}) - p.\frac{3.\sqrt{3}}{\pi}.\phi_f.I_{red} - D_{fr}.\Omega \tag{4.9a}$$

$$\frac{\mathrm{d}I_{red}}{\mathrm{d}t} = -\frac{Rs}{Ls}.I_{red} - \frac{3.p}{2.\pi}.\Omega.I_{red} + \frac{3.\sqrt{3}.p.\phi_f}{2.\pi.L_s}.\Omega - \frac{1}{2.Ls}.V_{red} \tag{4.9b}$$

$$C_f.\frac{\mathrm{d}V_{red}}{\mathrm{d}t} = I_{red} - k.I_{Lfb}.\alpha_{fb} \tag{4.9c}$$

$$L_{fb}.\frac{\mathrm{d}I_{Lfb}}{\mathrm{d}t} = k.V_{red}.\alpha_{fb} - V_{bus} \tag{4.9d}$$

$$C_{tot}.\frac{dV_{bus}}{dt} = I_{Lfb} + I_{Lbb} - \frac{P_L}{\eta_{inv}.V_{bus}} \tag{4.9e}$$

$$L_{bb}.\frac{\mathrm{d}I_{Lbb}}{\mathrm{d}t} = V_{sc}.\alpha_{bb} - V_{bus} \tag{4.9f}$$

$$C_{sc}.\frac{\mathrm{d}V_{sc}}{\mathrm{d}t} = -I_{Lbb}.\alpha_{bb} \tag{4.9g}$$

4.3 State Space representation of the energy conversion system and control objectives

4.3.1 State Space representation of the energy conversion system

The set of physical equations (4.9) for the energy conversion system can be rewritten in a simpler state space form, to facilitate the control design, as follows:

$$\dot{x}_1 = a_1.x_1 - a_3.x_2 + a_2 \tag{4.10a}$$
$$\dot{x}_2 = -a_4.x_2 - a_5.x_1.x_2 + a_6.x_1 - a_7.x_3 \tag{4.10b}$$
$$\dot{x}_3 = a_8.x_2 - a_8.k.x_4.u_1 \tag{4.10c}$$
$$\dot{x}_4 = -a_9.x_5 + k.a_9.x_3.u_1 \tag{4.10d}$$
$$\dot{x}_5 = a_{10}.(x_4 + x_6) - \frac{a_{10}}{\eta_{inv}}.\frac{P_L}{x_5} \tag{4.10e}$$
$$\dot{x}_6 = -a_{11}.x_5 + a_{11}.x_7.u_2 \tag{4.10f}$$
$$\dot{x}_7 = -a_{12}.x_6.u_2 \tag{4.10g}$$

where $x_1 = \Omega$ (rd/s), $x_2 = I_{red}$ (A), $x_3 = V_{red}$ (V), $x_4 = I_{Lfb}$ (A), $x_5 = V_{bus}$ (V), $x_6 = I_{Lbb}$ (A), $x_7 = V_{sc}$ (V). The control variables are: $u_1 = \alpha_{fb}$ and $u_2 = \alpha_{bb}$ corresponding to both duty ratios of the DC/DC Full Bridge and bidirectional DC/DC converters respectively.

The coefficients a_i used in the state equations are given by:

$a_1 = \frac{\alpha(\dot{m}_h, Th_{in}, Tc_{in}) - D_{fr}}{J_{rot}}$, $a_2 = \frac{\beta(Th_{in})}{J_{rot}}$, $a_3 = \frac{p.3.\sqrt{3}.\Phi_f}{\pi.J_{rot}}$, $a_4 = \frac{Rs}{Ls}$, $a_5 = \frac{3.p}{2.\pi}$, $a_6 = \frac{p.3.\sqrt{3}.\Phi_f}{2.\pi.Ls}$, $a_7 = \frac{1}{2.Ls}$, $a_8 = \frac{1}{Cf}$, $a_9 = \frac{1}{L_{fb}}$, $a_{10} = \frac{1}{C_{tot}}$, $a_{11} = \frac{1}{Lbb}$, $a_{12} = \frac{1}{C_{sc}}$.

4.3.2 Control objectives and constraints

Based on the system description explained in Section 4.1 for the energy conversion system, we can translate the control objectives in terms of the notation given in Section 4.3.1 as follows:

- regulate in a stiff manner x_5=V_{bus} around x_5^{st}=V_{bus}^{ref}=50V which is compatible with the good functioning of the commercial inverter.
- maintain x_7=V_{sc} around x_7^{st}=V_{sc}^{ref}, in a rather slower manner, to always have an adequate amount of energy in the supercapacitor.

The energy conversion system is subject to the following system constraints:

✓ **positivity constraints**: $x_i \geq 0$ except for x_6: Indeed, the bidirectional DC/DC converter is a current reversible converter, therefore the current $x_6 = I_{Lbb}$ can be either positive or negative to enable the charge/discharge of the supercapacitor. However, since the DC/DC

Full Bridge converter is not current-reversible, its output current I_{Lfb} is always positive. Moreover, its average current value must be greater than half of the ripple current in order to avoid discontinuous conduction mode, in which case the differential equations for this converter become more complicated (see for example [Sun et al., 2006]) in addition of having to switch between the equations for the continuous and the discontinuous conduction mode according to the value of the current.

✓ **strong saturation on the control variables** since:

- $u_1 \in [0, 1]$: duty ratio of the DC/DC Full Bridge.
- $u_2 \in [0, 1]$: duty ratio of the bidirectional DC/DC converter.

Moreover, the energy conversion system is also subject to the following input disturbances:

- P_L: load power demand that can vary in a fast manner.
- Th_{in} and Tc_{in}: the input temperatures respectively at the hot side and cold side of the Stirling engine. These temperatures, that enter in the definition of the parameters a_1 and a_2 in (4.10a), have a slow variations compared to the dynamics of the electric stage.

4.4 Conclusion

In this chapter, the energy conversion system associated to the Stirling engine has been presented and its dynamic equations derived leading to a state space representation of the system that will be used in Chapters 5 and 6 to design efficient control strategies that will be validated in a real Stirling engine based power system prototype.

Chapter 5

Development of a first control strategy for the Energy Conversion System associated to the Off-Grid Stirling based power Plant.

Contents

5.1 Analysis and control of the energy conversion system 54
5.1.1 Global analysis of the system 54
5.1.2 Analysis and control of subsystem 2 55
5.1.3 Analysis and control of subsystem 1 56
5.1.4 Global control of the system 60
5.1.5 Closed loop simulations 61
5.2 Experimental Validation on a dedicated electrical motor testbed . . . 65
5.2.1 Description of the electrical motor testbed 65
5.2.2 Experimental results on the electrical motor testbed 67
5.3 Experimental Validation on the Stirling engine based power system . 69
5.3.1 Energy conversion system prototype description 69
5.3.2 Corrective term observer for the Stirling engine torque 71
5.3.3 Experimental results on the Stirling based power system prototype 75
5.4 Conclusion 79

Now that we have set in Section 4.3.1 the state space equations for the energy conversion system associated to the Stirling based power plant (see Figure 4.1), we present in this chapter a first model based control strategy that enables the system to reach its control objectives as stated in Section 4.3.2 by controlling the electrical part of the power plant. Among the advantages of the proposed control strategy, the limited number of controller parameters to be tuned and the interesting way to generate the references for the key state variables that will be regulated in near to optimal manner. We present also in this chapter the experimental results that validate the performances of the developed method first on a dedicated electrical motor testbed (Section 5.2) that reproduces the functioning of the Stirling engine thanks to a torque-controlled DC motor and then on the real Stirling based power system (Section 5.3).

5.1 Analysis and control of the energy conversion system

In this section the state space equations (4.10) of the energy conversion system will be analyzed and used to synthesize the control strategy that drives the Stirling based power system through its electrical part to track some desired reference load power demand P_L of the Off-grid load. These equations are recalled below for convenience:

$$\dot{x}_1 = a_1.x_1 - a_3.x_2 + a_2 \tag{5.1a}$$
$$\dot{x}_2 = -a_4.x_2 - a_5.x_1.x_2 + a_6.x_1 - a_7.x_3 \tag{5.1b}$$
$$\dot{x}_3 = a_8.x_2 - a_8.k.x_4.u_1 \tag{5.1c}$$
$$\dot{x}_4 = -a_9.x_5 + k.a_9.x_3.u_1 \tag{5.1d}$$
$$\dot{x}_5 = a_{10}.(x_4 + x_6) - \frac{a_{10}}{\eta_{inv}}.\frac{P_L}{x_5} \tag{5.1e}$$
$$\dot{x}_6 = -a_{11}.x_5 + a_{11}.x_7.u_2 \tag{5.1f}$$
$$\dot{x}_7 = -a_{12}.x_6.u_2 \tag{5.1g}$$

where $x_1 = \Omega$, $x_2 = I_{red}$, $x_3 = V_{red}$, $x_4 = I_{Lfb}$, $x_5 = V_{bus}$, $x_6 = I_{Lbb}$, $x_7 = V_{sc}$, $u_1 = \alpha_{fb}$ and $u_2 = \alpha_{bb}$.

The coefficients a_i used in the state equations are given by:

$a_1 = \frac{\alpha(\dot{m}_h, Th_{in}, Tc_{in}) - D_{fr}}{J_{rot}}$, $a_2 = \frac{\beta(Th_{in})}{J_{rot}}$, $a_3 = \frac{p.3.\sqrt{3}.\Phi_f}{\pi.J_{rot}}$, $a_4 = \frac{Rs}{Ls}$, $a_5 = \frac{3.p}{2.\pi}$, $a_6 = \frac{p.3.\sqrt{3}.\Phi_f}{2.\pi.Ls}$, $a_7 = \frac{1}{2.Ls}$, $a_8 = \frac{1}{Cf}$, $a_9 = \frac{1}{L_{fb}}$, $a_{10} = \frac{1}{C_{tot}}$, $a_{11} = \frac{1}{Lbb}$, $a_{12} = \frac{1}{C_{sc}}$.

First, a global system analysis will be performed leading to some system decomposition and then a controller will be designed for each subsystem while ensuring the stability of the global closed loop system.

Note that the parameters a_1 and a_2 are time varying with a very slow dynamics compared to the dynamics of the electrical part. Moreover these parameters are known since they depend on measured thermodynamic variables.

5.1.1 Global analysis of the system

The first step in the system global analysis consists in performing some parametric study by replacing the system parameters by the values of the real testbed under consideration. By doing so, one can show that the term corresponding to the diode bridge voltage drop "$a_5.x_1.x_2$" can be neglected in (5.1b) compared to the other terms of the equation.

By observing the structure of the state space equations (5.1), one can also see that it is possible to split the global system into two subsystems as follow:

1) **The first subsystem (subsystem 1)** given by (5.1a)-(5.1d) involves only u_1 as a control variable and is driven by the exogenous signal a_2 (corresponding to the Stirling engine

torque). This subsystem depends also on x_5, but assuming that this variable is perfectly regulated around its reference (this will be proved later), x_5 can be replaced by its stationary (desired) value x_5^{st}. Therefore, the equations of subsystem 1 (5.1a)-(5.1d) can be rewritten in the following condensed form:

$$\dot{z} = A(u_1).z + B.\begin{pmatrix} a_2 \\ x_5^{st} \end{pmatrix} \tag{5.2}$$

where $z = \begin{pmatrix} x_1 & x_2 & x_3 & x_4 \end{pmatrix}^T$ is a reduced state vector.

2) **The second subsystem (subsystem 2)** corresponding to equations (5.1e)-(5.1g) where u_2 is the only control variable being involved.

Note that the two subsystems evolve in a separate time scales. Indeed the equations of subsystem 1 involve the mechanical dynamics associated with the Stirling engine and the motor shaft which makes the evolution of subsystem 1 slower than that of subsystem 2 which involves only the electrical dynamics. Then, in the next subsections, equations of subsystem 2 will be used to tightly regulate x_5=V_{bus} at x_5^{st}=V_{bus}^{ref}=50V in a fast manner using the control variable u_2. These equations will also serve to define an appropriate reference value for $x_4 = i_{Lfb}$ namely x_4^{st} that will adapt the state of charge of the supercapacitor by maintaining x_7=V_{sc} around its setpoint value x_7^{st}=V_{sc}^{ref}. Finally, the equations of subsystem 1 will be used to derive an appropriate stationary reference value for u_1 and z namely u_1^{st} and $z^{st}(u_1^{st})$ respectively that will be tracked acting on the control variable u_1 and using the equations of subsystem 1.

5.1.2 Analysis and control of subsystem 2

As mentioned in Section 5.1.1 equations of subsystem 2 (5.1e)-(5.1g) are used to reach one of the control objectives consisting in maintaining tightly x_5 around its setpoint value x_5^{st}=V_{bus}^{ref}=50V. Since (5.1e)-(5.1f) are in the strict-feedback form, a simple backstepping controller (see [Khalil, 1996]) will be designed for this purpose as follows:

Step 1: In (5.1e), we use the variable x_6 as a virtual control to regulate x_5=V_{bus} around x_5^{st}.

The regulation error being $\epsilon_5 = x_5 - x_5^{st}$, we use the following positive definite function: $V_5 = \frac{1}{2}.\epsilon_5^2$ as a Lyapunov function where its time derivative is given by:

$$\dot{V_5} = \epsilon_5.\dot{\epsilon_5} = \epsilon_5.(a_{10}.(x_4 + x_6) - \frac{a_{10}}{\eta_{inv}}.\frac{P_L}{x_5})$$

By setting $\dot{V_5} = -\rho_5.\epsilon_5^2 < 0$, with $\rho_5 > 0$ is a design parameter, we get :

$$x_6^{ref} = \frac{P_L}{\eta_{inv}.x_5} - x_4 + \frac{\rho_5}{a_{10}}.(x_5^{st} - x_5) \tag{5.3}$$

Step 2: In (5.1f), to regulate x_6 around x_6^{ref}, the control variable u_2 is used.

The regulation error being $\epsilon_6 = x_6 - x_6^{ref}$, we use the following positive definite function: $V_6 = V_5 + \frac{1}{2}.\epsilon_6^2$ as a Lyapunov function for subsystem 2 where its time derivative is given by:

$$\begin{aligned}
\dot{V_6} &= \epsilon_5.\dot{\epsilon}_5 + \epsilon_6.\dot{\epsilon}_6 \\
&= \epsilon_5.(a_{10}.x_4 + a_{10}.(x_6^{ref} + \epsilon_6) - \frac{a_{10}}{\eta_{inv}}.\frac{P_L}{x_5}) \\
&\quad +\epsilon_6.(-a_{11}.x_5 + a_{11}.x_7.u_2 - \dot{x_6}^{ref}) \\
&= -\rho_5.\epsilon_5^2 + +\epsilon_6.(-a_{11}.x_5 + a_{11}.x_7.u_2 - \dot{x_6}^{ref} + a_{10}.\epsilon_5)
\end{aligned}$$

By setting $\dot{V_6} = -\rho_5.\epsilon_5^2 - \rho_6.\epsilon_6^2 < 0$, with ρ_6 another design parameter, we get:

$$u_2(x) := \frac{1}{a_{11}.x_7}.(a_{11}.x_5 - a_{10}.(x_5 - x_5^{st}) + \dot{x}_6^{ref} - \rho_6.(x_6 - x_6^{ref})) \tag{5.4}$$

Hence, (5.3) and (5.4) locally stabilizes x_5 around its setpoint x_5^{st}=V_{bus}^{ref} in a fast manner leading rapidly to the following stationary equation ($\dot{x}_5 \approx 0$):

$$x_6 = -x_4 + \frac{P_L}{\eta_{inv}.x_5^{st}} \tag{5.5}$$

In order to meet the second control objective consisting in maintaining the supercapacitor voltage x_7 around its reference value x_7^{st} in a rather slower manner, one can choose the following stationary value for x_6 which together with equation (5.1g) obviously stabilizes x_7 around x_7^{st}:

$$x_6^{st} = k_6.\tanh(\beta.(x_7 - x_7^{st})) \tag{5.6}$$

where k_6 and β are some design parameters.

Replacing (5.6) in (5.5), the following stationary desired value for x_4 namely x_4^{st} is derived:

$$x_4^{st} = -k_6.\tanh(\beta.(x_7 - x_7^{st})) + \frac{P_L}{\eta_{inv}.x_5^{st}} \tag{5.7}$$

In the next subsection, an appropriate control strategy for subsystem 1 will be designed to track x_4^{st} which enables to regulate the supercapacitor voltage and to respond to the load power demand.

5.1.3 Analysis and control of subsystem 1

Now that we have defined according to (5.7) the desired stationary value for x_4 namely x_4^{st}, one can determine online the remaining components of the desired stationary state vector z^{st} and the stationary value for u_1 namely u_1^{st} by solving analytically the following equation corresponding to $\dot{z} = 0$ (see (5.2)):

$$z^{st}(u_1^{st}) := -[A(u_1^{st})]^{-1}B.\begin{pmatrix} a_2 \\ x_5^{st} \end{pmatrix} \tag{5.8}$$

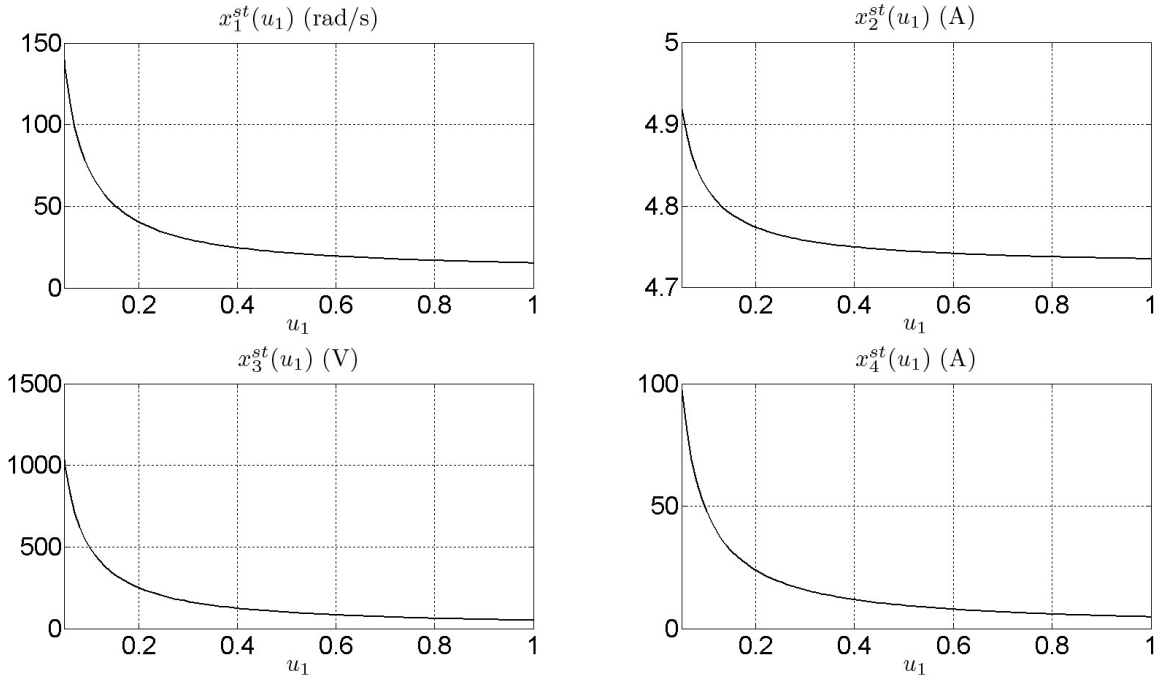

Figure 5.1: Evolution of the stationary states of subsystem 1 as function of u_1^{st}.

This leads to the following equations:

$x_2^{st} = \frac{-B+\sqrt{\Delta}}{2.A}$, $x_1^{st} = \frac{a_3.x_2^{st}}{a_1}$, $x_3^{st} = \frac{x_4^{st}.x_5^{st}}{x_2^{st}}$, $u_1^{st} = \frac{x_2^{st}}{k.x_4^{st}}$

where: $A = \frac{a_3.a_6}{a_1} - a_4$, $B = \frac{-a_2.a_6}{a_1}$, $C = -a_7.x_4^{st}.x_5^{st}$ and $\Delta = B^2 - 4.A.C$.

Figure 5.1 shows the components of the stationary vector z^{st} with respect to u_1^{st}.

By computing the eigenvalues of the dynamic matrix $A(u_1^{st})$ for some values of $u_1^{st} \in [0, 1]$, it appears that subsystem 1 is open-loop stable (see Figure 5.2 where the stability indicator of $A(u_1^{st})$, that corresponds to its maximum eigenvalues real part for different $u_1^{st} \in [0, 1]$, is plotted) but contains highly oscillatory modes as it can be observed from Figure 5.3 where some open-loop trajectories for the components of the vector z are plotted for three different values of u_1^{st}. Figure 5.4 illustrates the same behavior in the phase plane (x_3, x_4). One can conclude from Figures 5.3 and 5.4 that starting from some initial state, in order to reach some desired state vector z^{st} compatible with some desired x_4^{st}, applying directly its corresponding u_1^{st} would almost systematically lead to positiveness constraints violation of the state variables (see Section 4.3.2) that are additionally oscillatory with uncontrolled transients.

Then, it is necessary to design an appropriate control strategy other than $u_1 = u_1^{st}$ to reach some desired stationary vector z^{st} compatible with some desired x_4^{st}. For this purpose, we opted for a one step (because of the limitation on the controller computation time that is fixed to 100 μs) predictive control [Mayne et al., 2000] that leads to near to optimal behavior of the

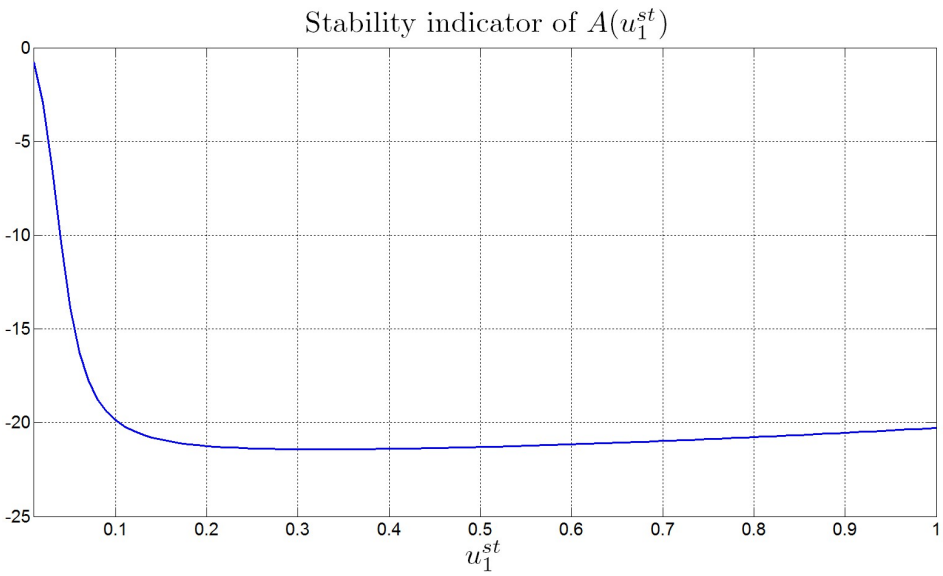

Figure 5.2: Stability indicator of $A(u_1^{st})$ for $u_1^{st} \in [0, 1]$.

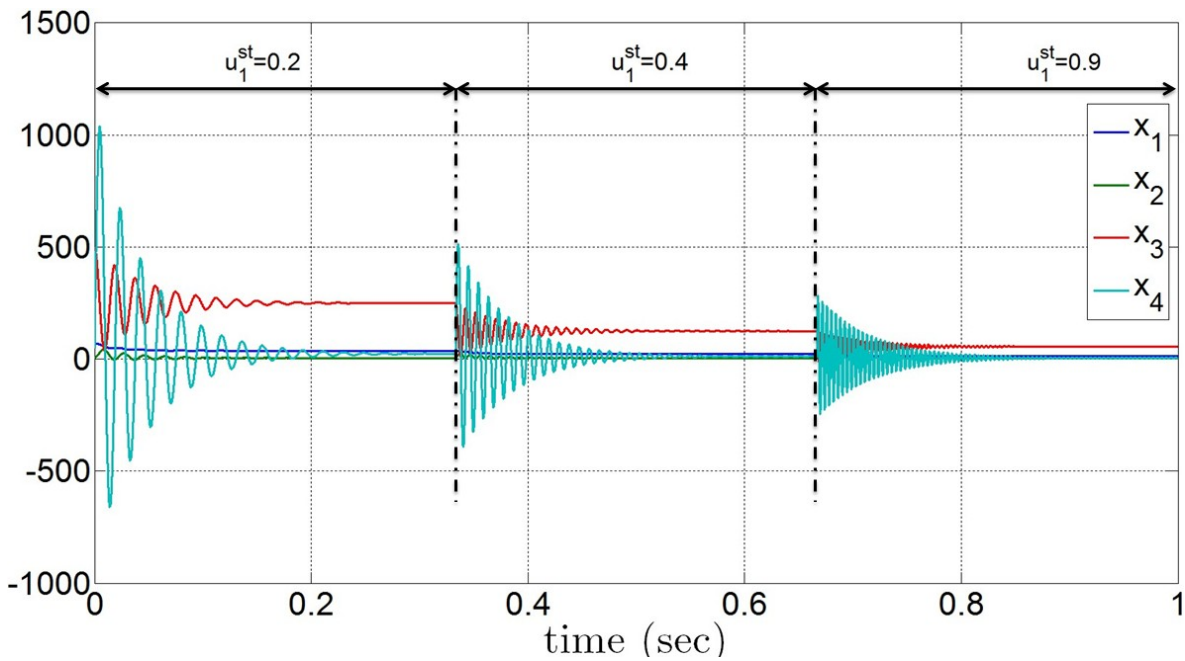

Figure 5.3: Open loop trajectories for the components of the vector $z(t)$ corresponding to $u_1^{st} = 0.2$, $u_1^{st} = 0.4$ and $u_1^{st} = 0.9$.

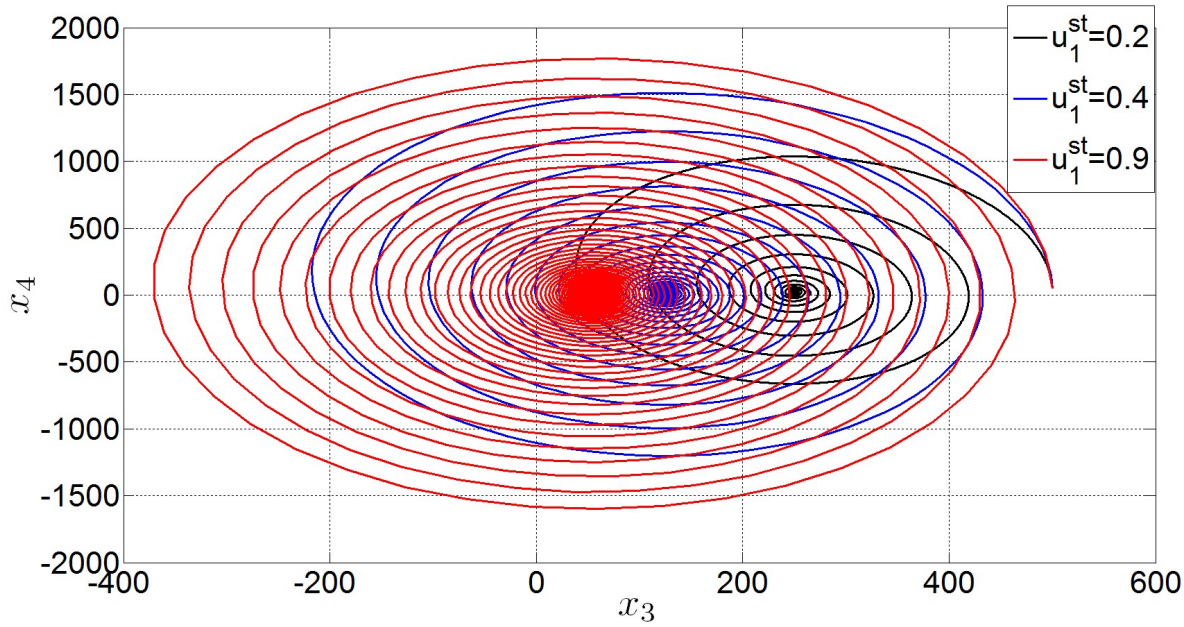

Figure 5.4: Open loop trajectories in the phase plane (x_3,x_4) corresponding to $u_1^{st} = 0.2$, $u_1^{st} = 0.4$ and $u_1^{st} = 0.9$.

closed-loop system in addition of being real time implementable with few tuning parameters and solved by standard SQP (Sequential Quadratic Programming) iterations.

First, the subsystem 1 equations given by (5.2) are discretized based on the second order approximation of the exponential term leading to the following discrete version of subsystem 1 equations:

$$z^+(u_1) = A_d(u_1)z + B_d(u_1).\begin{pmatrix} a_2 \\ x_5^{st} \end{pmatrix} \tag{5.9}$$

Then, to track some desired stationary reference value z^{st} compatible with the desired x_4^{st} and its corresponding u_1^{st}, the following one step predictive controller is used:

$$u_1^{opt} = \arg \min_{u_1 \in [0,1]} J(u_1) := \left[\left\| z^+(u_1) - z^{st} \right\|^2_{P_d(u_1^{st})} \right] \tag{5.10}$$

where $P_d(u_1^{st})$ is the Lyapunov stability matrix of subsystem 1 (depending on u_1^{st}) used as a weighting matrix in the previous cost function.

From preliminary simulations of the closed-loop subsystem 1 under the control u_1 given by (5.10), it appears that x_4 undergoes an undershoot (or an overshoot) during positive (or negative) step changes in x_4^{st}, which can lead to positiveness constraints violation. To tackle this problem, the reference value x_4^{st} given by (5.7) is filtered (using an ad hoc first order filter) to smooth the convergence of x_4. In addition to this, a corrective term (slow integrator) is added to x_4^{st} (before the filtering) to correct the static error on x_4 (which is a crucial state variable that adapts the state of charge of the supercapacitor) due to some model uncertainties.

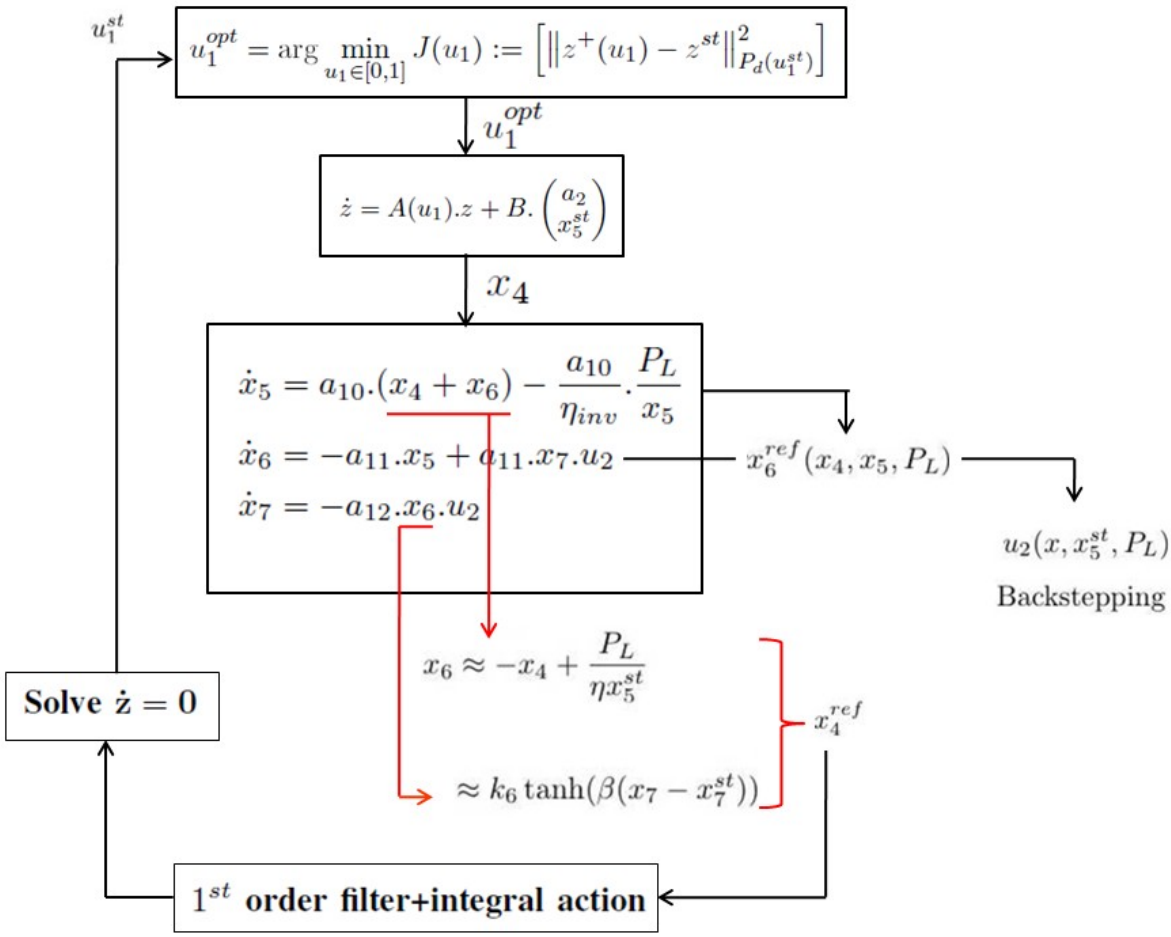

Figure 5.5: Global control architecture for the complete system.

This leads to the following modified reference value for x_4 namely $\bar{x_4}^{st}$ in the discrete form:

$$\bar{x_4}^{st}(k+1) = \alpha_f.(x_4^{st}(k) + \epsilon(k)) + (1 - \alpha_f).\bar{x_4}^{st}(k) \tag{5.11a}$$

$$\epsilon(k+1) = k_{aw}.\epsilon(k) + \eta_{corr}.(x_4^{st}(k) - x_4(k)) \tag{5.11b}$$

where α_f is a filtering parameter, η_{corr} is the integrator gain and k_{aw} is an anti windup gain.

5.1.4 Global control of the system

Figure 5.5 summarizes the global control architecture of the energy conversion system derived from the combination of the subsystem 1 controller (Section 5.1.3) and subsystem 2 controller (Section 5.1.2). The resulting closed loop system is stable and its performances assessed in the next sections.

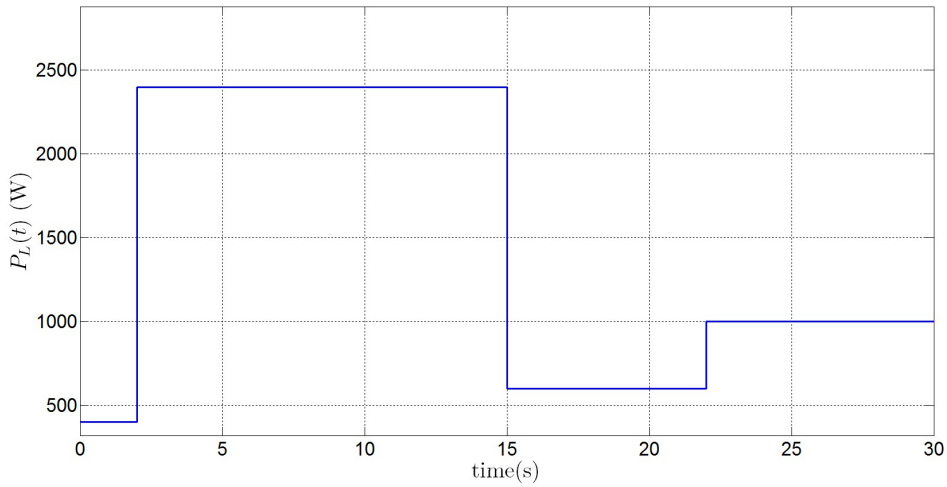

Figure 5.6: Load power demand.

5.1.5 Closed loop simulations

In order to assess by simulation the performances of the proposed control strategy for the energy conversion system, a load power demand profile is applied to the system as depicted in Figure 5.6. One can observe from Figures 5.7a and 5.7b that the controller tightly regulates the DC bus voltage to its setpoint enabling the good functioning of the inverter that supplies the AC load with a 230V 50Hz AC voltage. According to Figure 5.7c, the proposed controller also maintains the supercapacitor voltage to its reference value enabling having sufficient amount of energy to palliate to the load power demand transients. Figure 5.8b gives the online computed desired stationary value of the DC/DC full bridge converter output current namely $x_4^{st} = I_{Lfb}^{ref}$ and its instantaneous value $I_{Lfb}(t)$. One can see from this figure that this current is always positive enabling a continuous conduction mode of the device. Figure 5.8a plots the shaft rotational speed $\Omega(t)$ that is always stabilized to its setpoint derived from x_4^{st}.

In Figure 5.8c, one can see the output current of the bidirectional DC/DC converter I_{Lbb}. At $t = 2s$, this current becomes positive to compensate for an increase in the load power demand (Figure 5.6) that appears between time $t = 2s$ and $t = 15s$ resulting in a discharge of the supercapacitor (see Figure 5.7c). Between $t = 2s$ and $t = 15s$, I_{Lbb} takes negative and positive values to respectively charge and discharge the supercapacitor in order to maintain its voltage at the desired value. The same remarks hold for the time interval $[15s, 30s]$ where we first have a decrease and then an increase in the load power demand.

Figures 5.9a and 5.9b give the time profiles of the control variables u_1 and u_2. One can observe from Figure 5.9b that some peaks appear on u_2, however by zooming on these peaks one observe the same behavior as in Figure 5.7b which is admissible for the system.

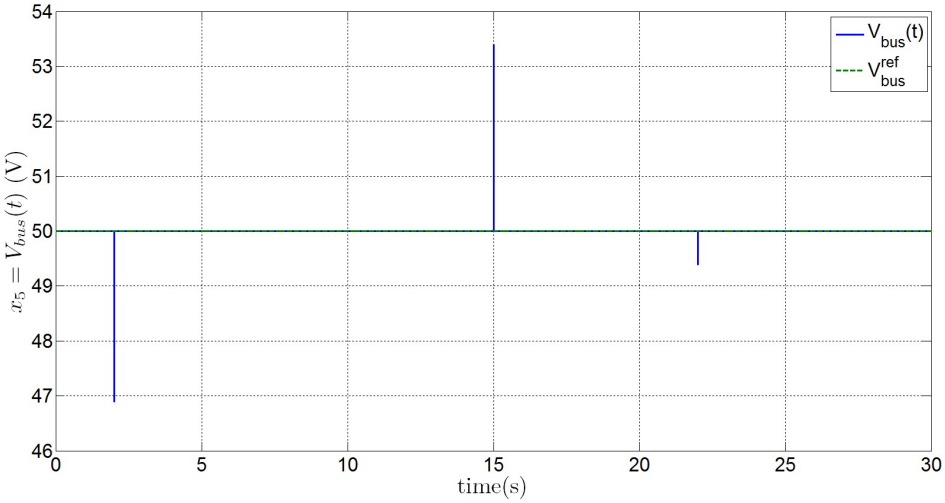

(a) DC bus voltage V_{bus} and its reference V_{bus}^{ref}.

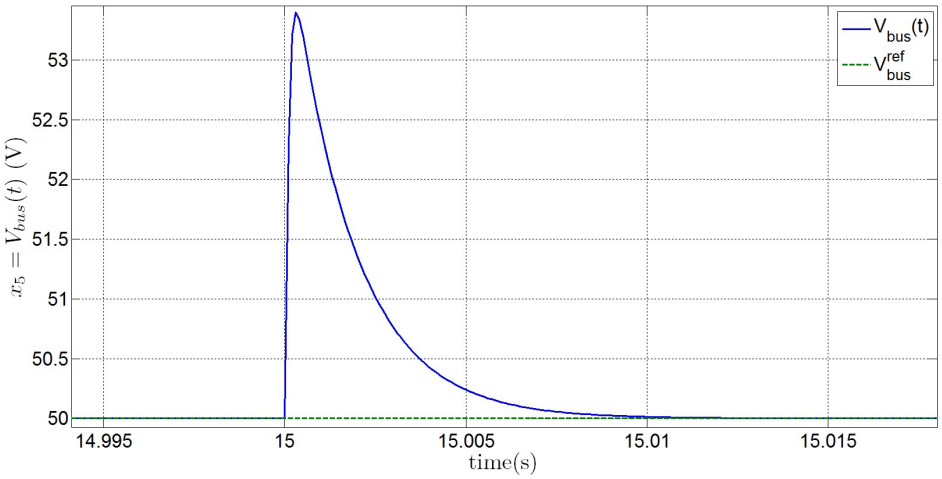

(b) Zoom on Figure 5.7a at $t = 15$s.

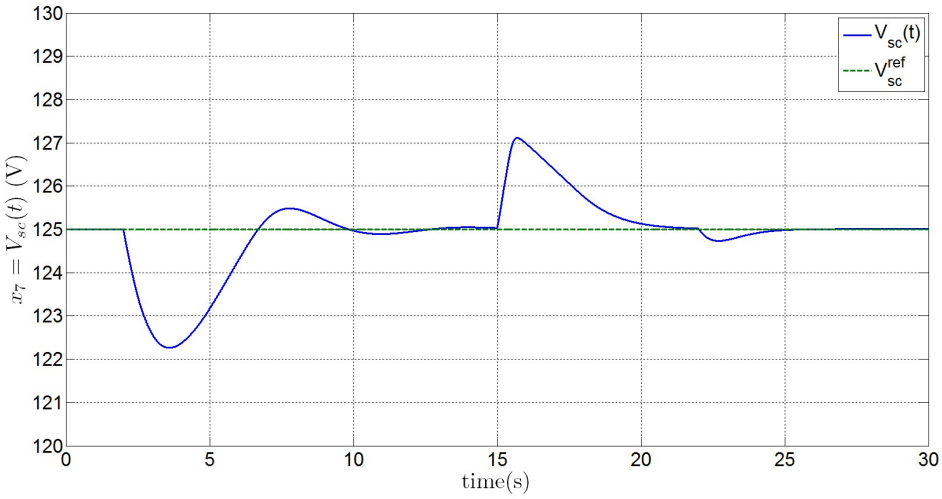

(c) supercapacitor voltage V_{sc} and its reference V_{sc}^{ref}.

Figure 5.7: regulated variables.

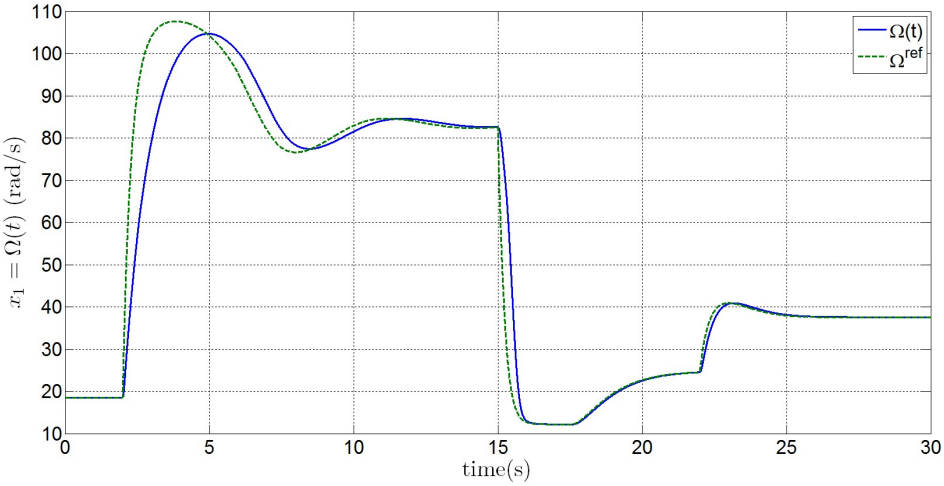

(a) rotor mechanical speed $\Omega(t)$ and its setpoint $\Omega^{ref}(t)$.

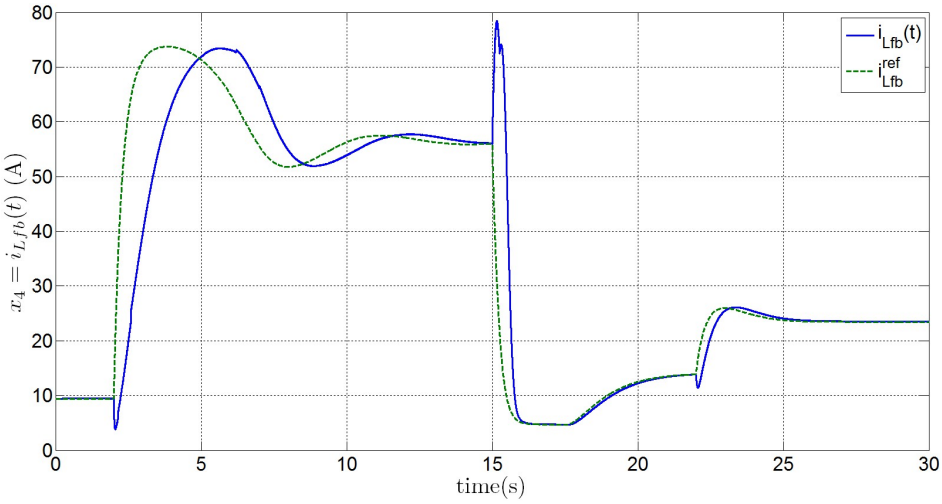

(b) output current of the DC/DC full bridge converter $I_{Lfb}(t)$ and its setpoint $I^{ref}_{Lfb}(t)$.

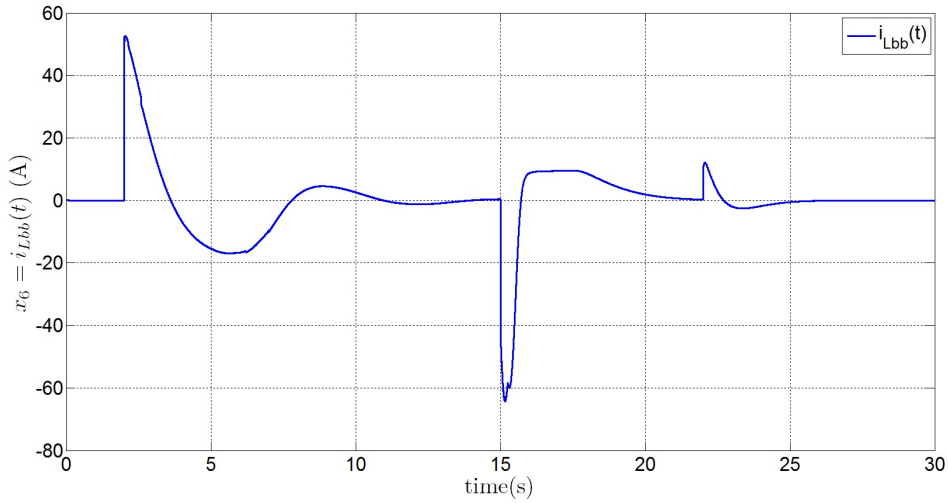

(c) output current of the bidirectional DC/DC converter $I_{Lbb}(t)$ and its setpoint $I^{ref}_{Lbb}(t)$.

Figure 5.8: rotor mechanical speed and currents injected in the DC bus by the bidirectional DC/DC converter and the Full bridge converter.

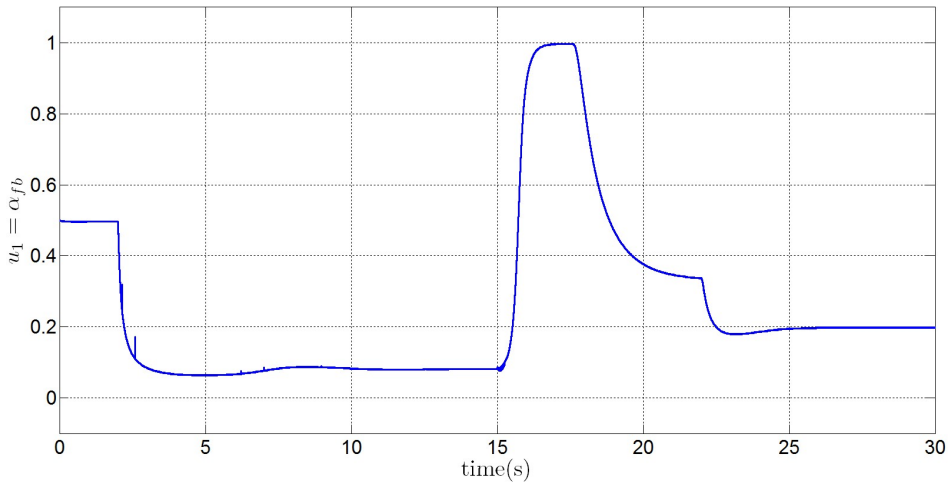

(a) Duty ratio of the DC/DC Full bridge converter α_{fb}

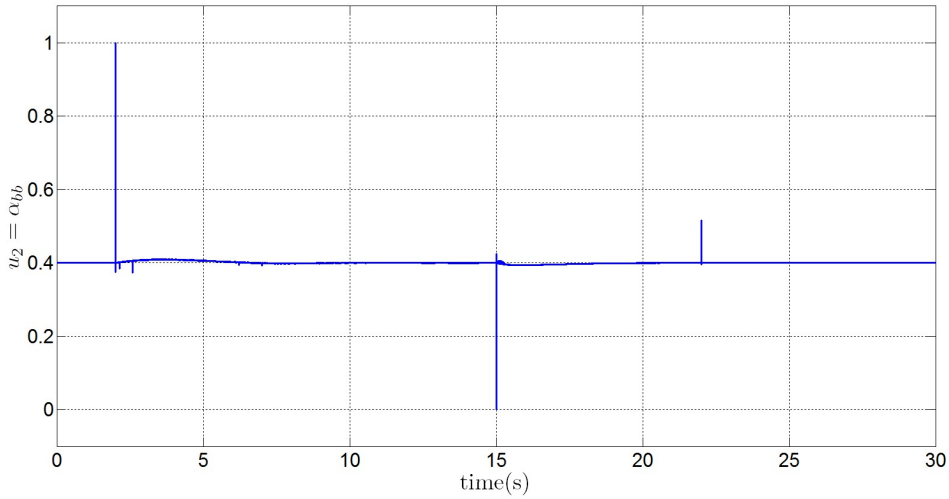

(b) Duty ratio of the bidirectional DC/DC converter α_{bb}

Figure 5.9: control variables.

5.2 Experimental Validation on a dedicated electrical motor testbed

Before testing the proposed control strategy on the real Stirling based power system, an experimental electrical motor testbed was built to serve as a first experimental validation platform in which the behavior of the Stirling engine is reproduced by a DC machine torque-controlled by mean of a commercial drive and linked mechanically to the synchronous generator which is connected electrically to the energy conversion system we want to control.

The need for this intermediate platform is due to two main reasons. The first one being that we did not have in our disposal the real Stirling engine at the time we developed the control strategy but we wanted to experimentally validate it in another manner. The second reason is that we wanted to first validate the control strategy on a more flexible testbed especially for motor torque variations and the electrical motor testbed seemed to be the best choice in order to ensure this flexibility.

5.2.1 Description of the electrical motor testbed

Figure 5.10 gives the schematic of the electrical motor testbed under consideration. The energy conversion system which is the same as in Figure 4.1 is connected electrically to a synchronous generator linked to a DC machine (reproducing the functioning of the Stirling engine) torque-controlled by mean of a commercial drive. A programmable AC load connected at the output of the inverter is used to generate a variable load profile. Figure 5.11 gives an overview of the experimental testbed for which the following system parameters hold:

PMSG nominal power: 1.8kW, J_{rot}=0.0672$Kg.m^2$, $\alpha(\dot{m}_h, \dot{m}_c)$=-0.0111, $\beta(TH_{in}, TC_{in})$=45, ϕ_f=0.6014, R_s=5, L_s=0.28 mH, p=8, C_f=2400 μF, L_{fb}=150μH, L_{bb}=223μH, C_{fb}=50μF, C_{bb}=136mF, C_{sc}=63 F.

This leads to the following numerical values for a_i parameters: $a_1 = -0.183$, $a_2 = 558.11$, $a_3 = 118.4453$, $a_4 = 9615.4$, $a_5 = 1.3712$,$a_6 = 5101.1$, $a_7 = 641.02$, $a_8 = 425.53$, $a_9 = 6666.7$, $a_{10} = 7.34$, $a_{11} = 4484.3$, $a_{12} = 0.0159$, $\eta_{inv} = 0.95$ and $k = 0.5$.

Because of some physical limitations on the DC/DC full bridge converter used in the testbed, the duty ratio of this device belongs to the interval $\alpha_{fb} \in [0, 0.9]$. This duty ratio is first conditioned before it is applied to drive the DC/DC Full Bridge converter as it is illustrated in Figure 5.12. In this figure, α_{fb} is first divided by two before generating its corresponding electrical signal α_{fb}^{elec} in order to drive the two pairs of Insulated Gate Bipolar Transistors (IGBT) (Tr_1,Tr_3) and (Tr_2,Tr_4), during a cutting frequency $T_{sw} = 20$ kHz, with the same period but 180° out of phase (see Section B.1 for more details).

Note also that the bidirectional DC/DC converter used in the testbed does not work in a complementary mode but during a switching period only one IGBT is activated at a time. However, the mean model (5.1f)-(5.1g) is still valid for control design with a slight

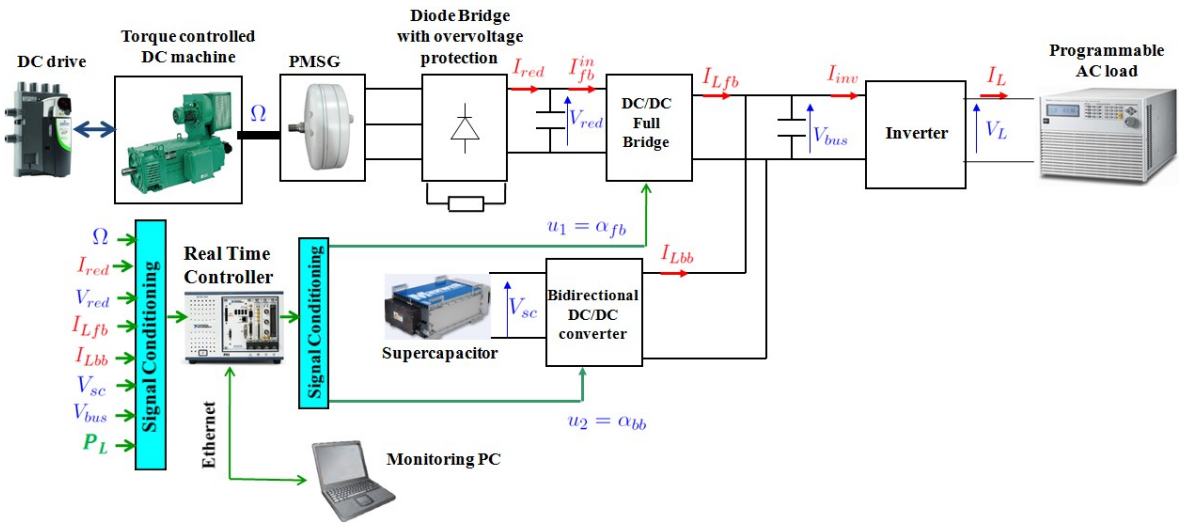

Figure 5.10: Schematic of the electrical motor testbed together with its Power electronics.

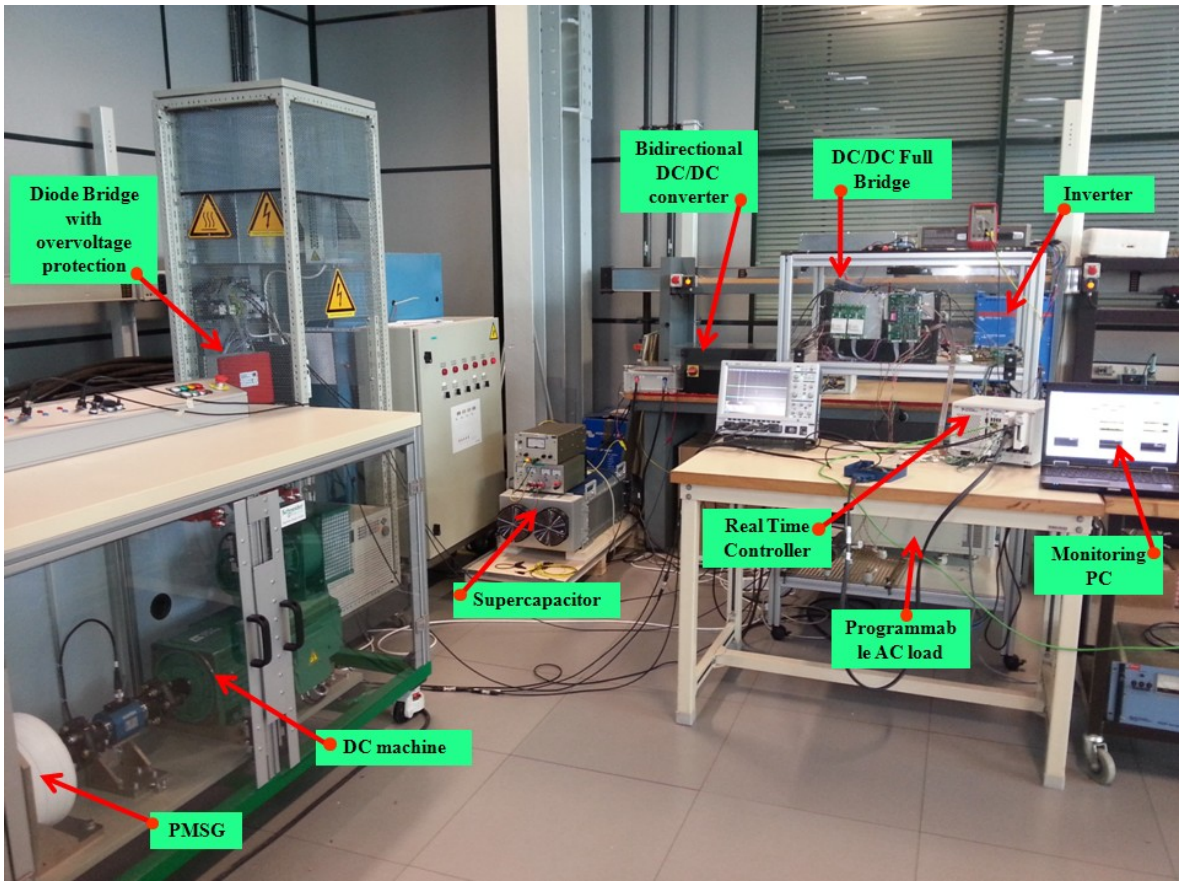

Figure 5.11: Electrical motor testbed used for experimental validation and performance assessment of the proposed control strategy.

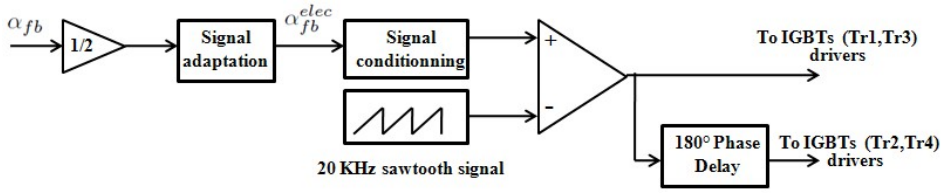

Figure 5.12: DC/DC Full Bridge converter.

modification before driving the converter. Indeed, the real duty ratio applied to the converter $\alpha_{bb}^{real} \in [-0.95, 0.95]$ is derived from α_{bb} as follow:

$$\alpha_{bb}^{real} = \alpha_{bb} - \frac{V_{bus}}{V_{sc}} \tag{5.12}$$

Finally, the duty ratio is transformed to a PWM signal using standard PWM techniques similar to the one of Figure 5.12 where Tr_1 (see Figure 4.5) is activated during a fraction of the switching period corresponding to $\mid \alpha_{bb}^{real} \mid .T_{sw}$ if α_{bb}^{real} is positive otherwise Tr_2 will be activated during the same fraction of the switching period. Concerning the real time controller on which the developed control strategy is implemented, we opted for a National Instrument controller based on NI PXI-8109 (`http://www.ni.com/pdf/manuals/373172a.pdf`) real time target (2.66 GHz Dual-Core embedded controller). The control strategies are transcribed in MATLAB/Simulink® environment and ".dll" file embedding a C code is generated thanks to Simulink coder®. The generated file is then deployed on the National Instrument real time target using the National Instrument Veristand® platform (installed on a host PC) that is also used to monitor the system and make data acquisitions.

5.2.2 Experimental results on the electrical motor testbed

In order to assess the performances of the developed control strategy on the experimental electrical motor testbed, a load power demand profile is generated acting on the electronic programmable load (see Figure 5.10), the resulting power profile measured at the input of the inverter is shown in Figure 5.13. Figure 5.14 shows that despite the sharp changes in the load power demand, the DC bus voltage is well regulated around its reference value of 50V, acting on $u_2 = \alpha_{bb}$ (depicted in the bottom of Figure 5.18), which guarantees the good functioning of the inverter that supplies the AC load with uninterruptible 230V 50Hz voltage.

The supercapacitor voltage is also maintained to its setpoint according to Figure 5.15. This enables the system to always have enough energy (and free energy stock) to supply (or absorb) during future increase (or decrease) in the load power demand.

The reference stationary value for the output current of the DC/DC full bridge converter namely x_4^{st} needed to adapt the SOC (State Of Charge) of the supercapacitor (see Section 5.1.2) is also tracked with a good settling time according to Figure 5.16. As discussed in Section 5.1.3, x_4^{st} is used to generate the reference values $x_1^{ref} = \Omega^{ref}$,$x_2^{ref} = I_{red}^{ref}$ and $x_3^{ref} = V_{red}^{ref}$

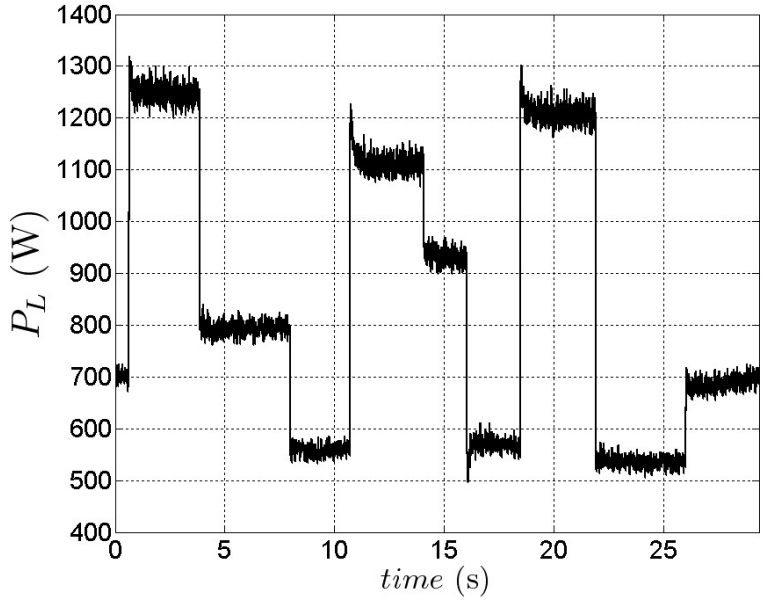

Figure 5.13: Load power demand P_L at the input of the inverter for the electrical motor testbed.

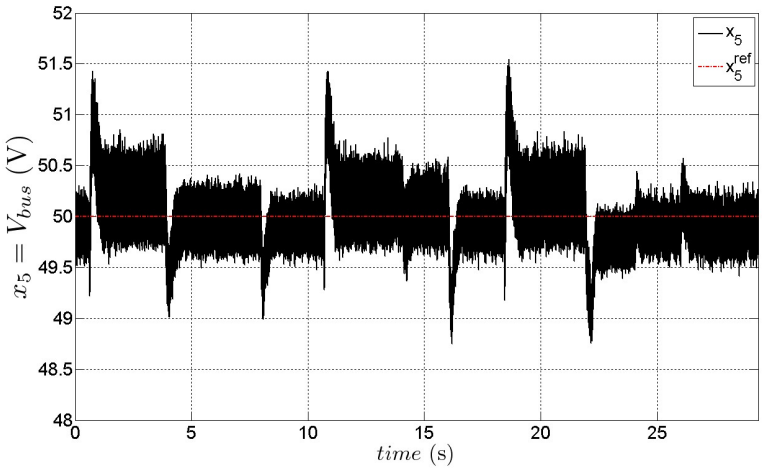

Figure 5.14: Bus voltage V_{bus} and its reference value V_{bus}^{ref} for the electrical motor testbed.

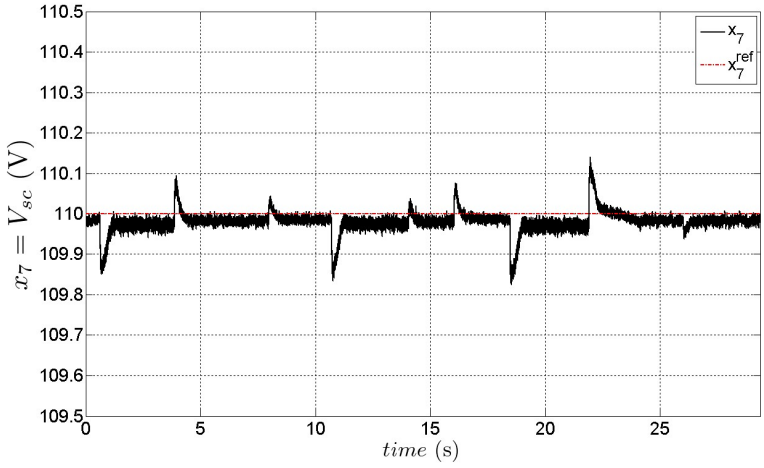

Figure 5.15: Supercapacitor voltage V_{sc} and its reference value V_{sc}^{ref} for the electrical motor testbed.

that are tracked as illustrated in Figure 5.17 acting the duty ratio of the DC/DC full bridge converter $u_1 = \alpha_{fb}$ depicted in the top of Figure 5.18. From Figure 5.17, one can observe some small static errors in the tracking of $x_1^{ref} = \Omega^{ref}$,$x_2^{ref} = I_{red}^{ref}$ and $x_3^{ref} = V_{red}^{ref}$ which is due to the modification of the reference signal for x_4 according to (5.11). However this static error will not affect the global performances of the system since the crucial objective being the regulation of $x_4 = I_{Lfb}$.

5.3 Experimental Validation on the Stirling engine based power system

Now that we have validated on the dedicated electrical motor testbed (see Section 5.2) the proposed control strategy for the energy conversion system, we will discuss in this section the experimental results obtained on the real Stirling engine based power plant prototype. First, a brief description of this prototype will be given focussing on the energy conversion system, then a slight modification of the developed control strategy will be addressed taking into account a corrective term for the Stirling engine torque obtained through an additional state observer. Finally, the experimental results on the Stirling engine power plant will be given and analyzed.

5.3.1 Energy conversion system prototype description

The Stirling based power system prototype under consideration is the one depicted in Figure 3.7 whose thermodynamic part was described in Section 3.3.1. The power conversion system whose schematic is depicted in Figure 4.1 and that was used in the experimental electrical

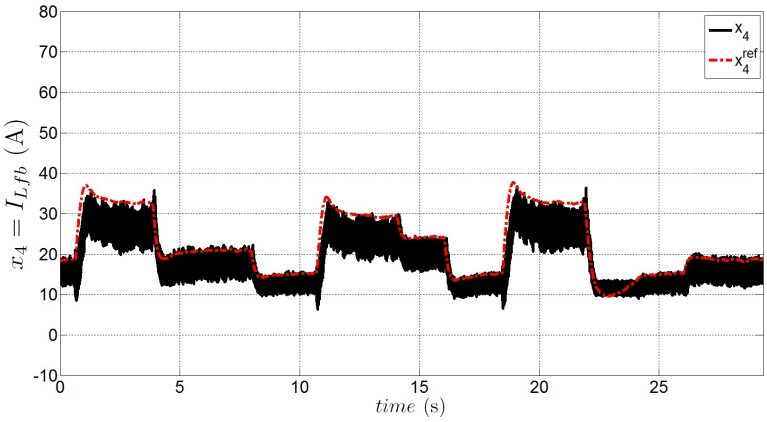

Figure 5.16: Output current of the DC/DC Full Bridge converter I_{Lfb} and its reference value I_{Lfb}^{ref} for the electrical motor testbed.

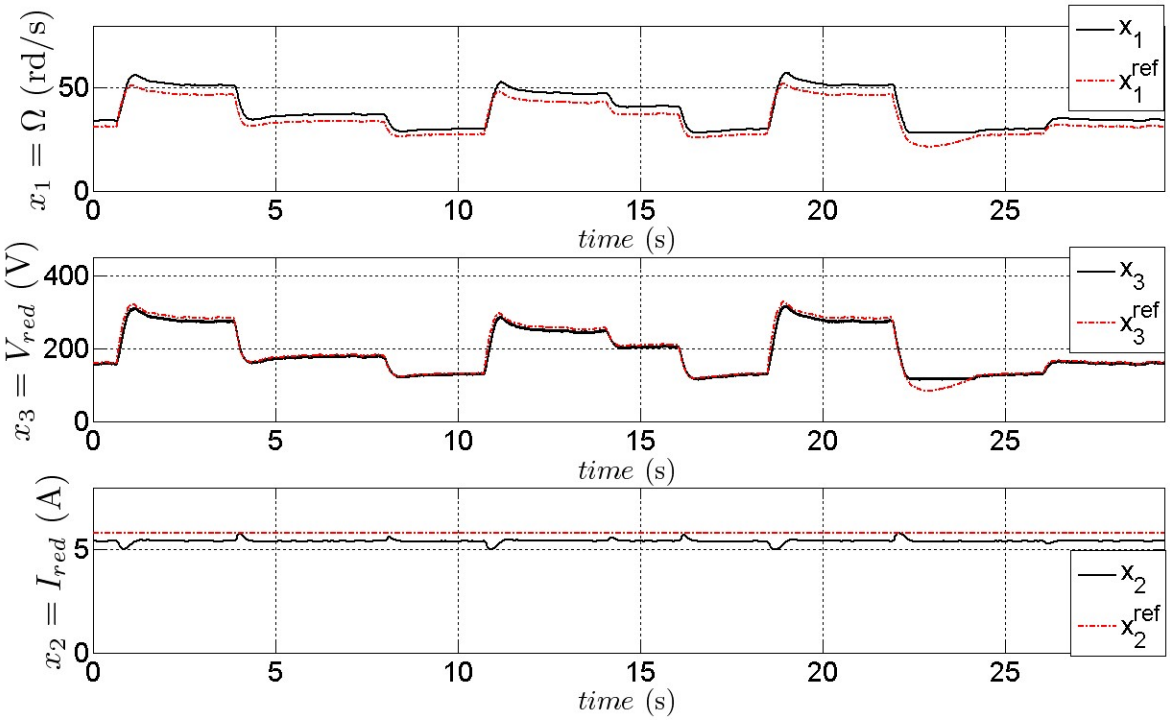

Figure 5.17: Rotational speed of the engine Ω, the rectified voltage V_{red} and the rectified current I_{red} with their respective reference values Ω^{ref}, V_{red}^{ref} and I_{red}^{ref} for the electrical motor testbed.

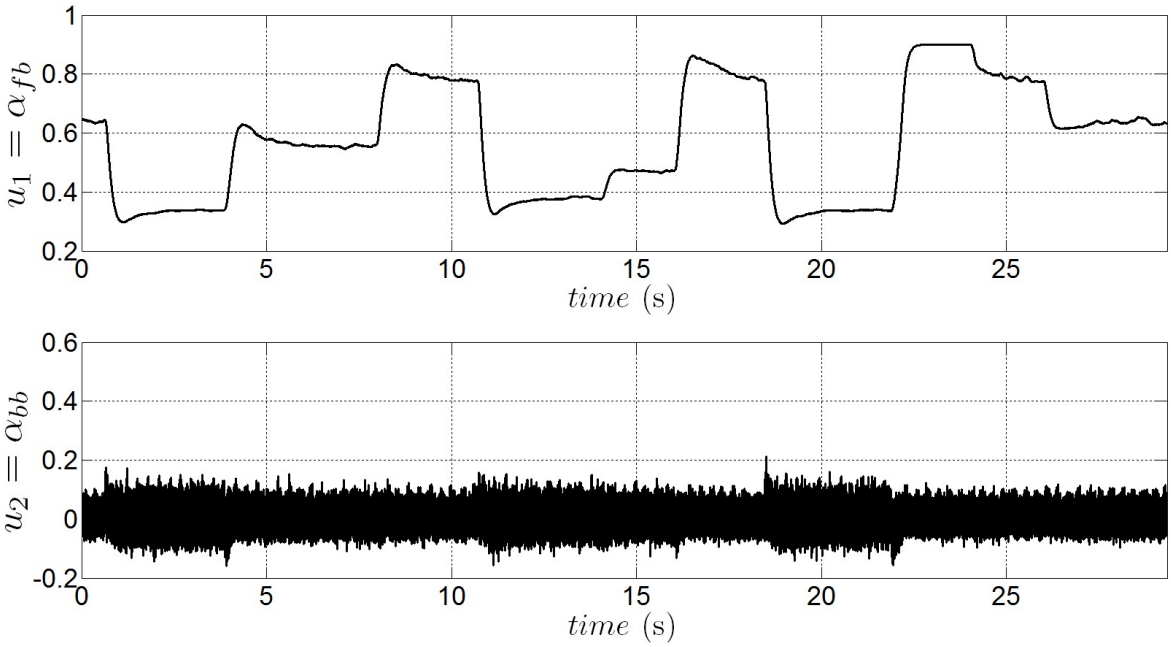

Figure 5.18: Duty ratios of the DC/DC Full Bridge converter (upper figure) and bidirectional DC/DC converter (lower figure) for the electrical motor testbed.

motor testbed of Figure 5.11 has been set in two electrical cabinets as depicted in Figure 3.7 and 5.19. The first electrical cabinet depicted in Figure 5.20 contains among others the DC/DC full bridge converter, the bidirectional DC/DC converter, the commercial inverter, the NI PXI-8109 real time target (and its associated signal conditioning stage) and the supercapacitor. The second electrical cabinet depicted in Figure 5.21 contains among others the diode bridge and its associated over-voltage protection system (windy boy protection box [1]). This cabinet contains also a commercial variable speed drive (ATV32[2] variable speed drive) used during the starting procedure (see Appendix C) to initially bring the Stirling engine to some desired speed in order to enable motor torque production.

5.3.2 Corrective term observer for the Stirling engine torque

In Section 3.3.3 an expression of the Stirling engine torque T_{mot} was identified using experimental data resulting in equation (3.33) for the motor torque that was then used in equation (4.9a) leading to the state equation (5.1a) in which a_1 and a_2 contain the terms of the motor torque. Because of some model errors in the torque identification process, it has been added a simple Luenberger observer [Besançon, 2007] that estimates the model error in the Stirling torque identification ΔT_{mot} that has to be added to the calculated torque T_{mot}^{calc} given by (3.33). Preliminary results without adding this observer showed that the closed loop system under the

[1] http://ust.su/upload/iblock/892/WBP-Box-IEN103320.pdf

[2] http://www.schneider-electric.com/download/hk/en/details/2619521-Altivar-32-variable-speed-drives-catalog?showAsIframe=false&reference=DIA2ED2100401EN

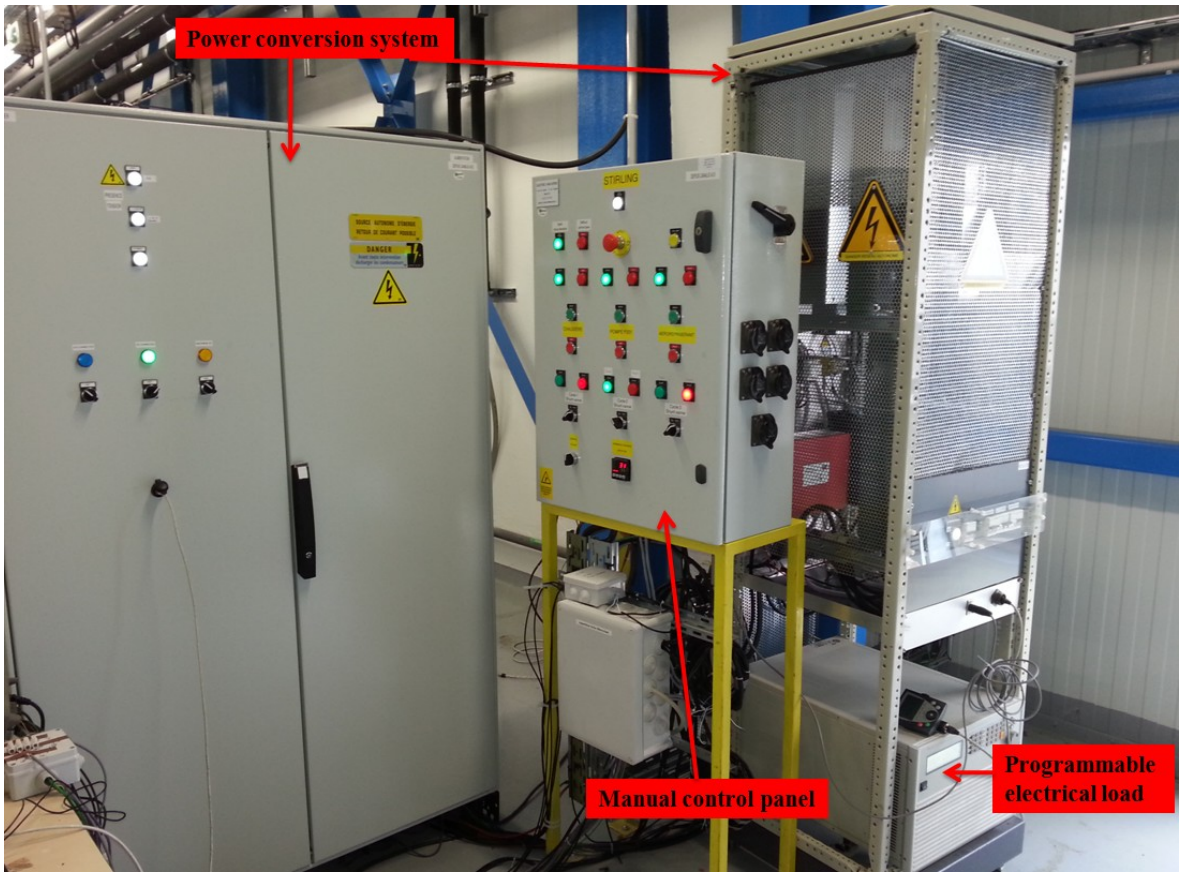

Figure 5.19: Electrical cabinets containing the energy conversion system

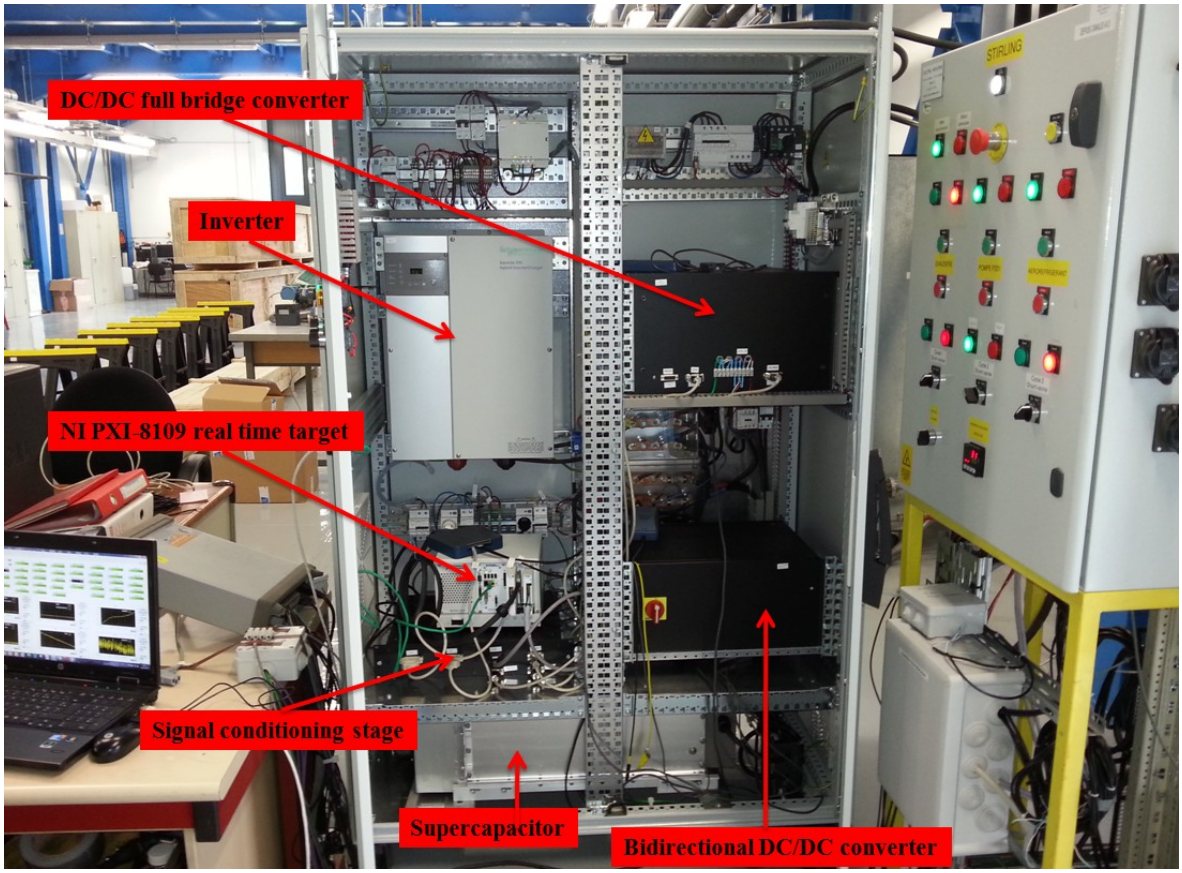

Figure 5.20: Overview of the first electrical cabinet

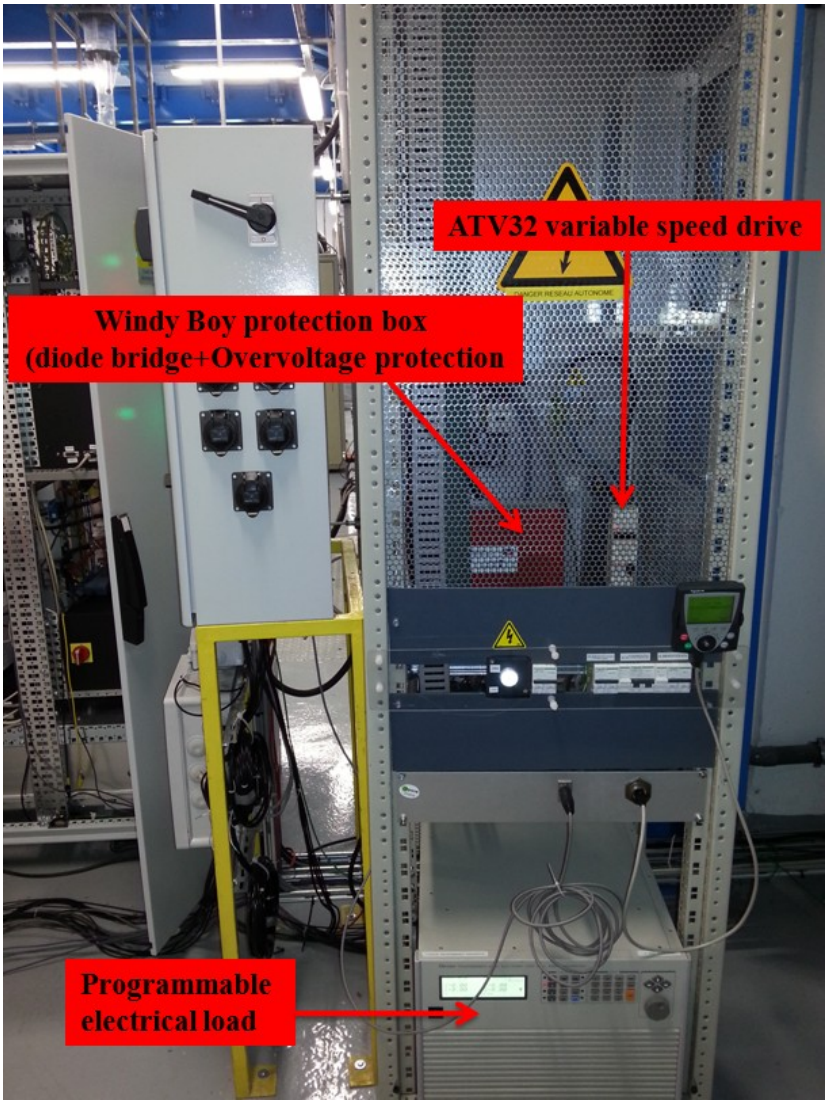

Figure 5.21: Overview of the second electrical cabinet

proposed controller was subjected to some tracking errors on the state variables (x_1,x_2,x_3,x_4). This justifies the design of the proposed observer that starts from rewriting (5.1a) which is recalled below:

$$\dot{x}_1 = a_1.x_1 - a_3.x_2 + a_2$$

where: $a_1 = \frac{\alpha(\dot{m}_h,\dot{m}_c)-D_{fr}}{J_{rot}}$, $a_2 = \frac{\beta(TH_{in},TC_{in})}{J_{rot}}$, $a_3 = \frac{p.3.\sqrt{3}.\Phi_f}{\pi * J_{rot}}$, in the following form:

$$\dot{x}_1 = a_1'.x_1 + a_2^{calc} + \gamma \tag{5.13}$$

where: $a_1' = \frac{-D_{fr}}{J_{rot}}$, $a_2^{calc} = \frac{T_{mot}^{calc}}{J_{rot}}$, $\gamma = -a_3.x_2 + \Delta a_2$ and $\Delta a_2 = \frac{\Delta T_{mot}}{J_{rot}}$

Considering the slow dynamics on x_2 (and hence on γ), the following augmented system is considered:

$$\dot{x}_1 = a_1'.x_1 + a_2^{calc} + \gamma \tag{5.14a}$$
$$\dot{\gamma} = 0 \tag{5.14b}$$
$$y_{obs} = x_1 \tag{5.14c}$$

that can be rewritten in the following condensed form considering $X_{obs} = \begin{pmatrix} x_1 & \gamma \end{pmatrix}^T$:

$$X_{obs} = A_{obs}.X_{obs} + B_{obs}.a_2^{calc} \tag{5.15a}$$
$$y_{obs} = C_{obs}.X_{obs} \tag{5.15b}$$

where $A_{obs} = \begin{pmatrix} a_1' & 1 \\ 0 & 0 \end{pmatrix}$, $B_{obs} = \begin{pmatrix} 1 \\ 0 \end{pmatrix}$ and $C_{obs} = \begin{pmatrix} 1 & 0 \end{pmatrix}$

Then the following Luenberger observer is applied on the discrete version of (5.15) to estimate X_{obs}:

$$\hat{X}_{obs}(k+1) = A_{obs}^d.\hat{X}_{obs} + B_{obs}^d.a_2^{calc} + L_{obs}.(y_{obs} - \hat{y}_{obs}) \tag{5.16a}$$
$$\hat{y}_{obs} = C_{obs}.\hat{X}_{obs} \tag{5.16b}$$

where A_{obs}^d and B_{obs}^d are obtained from (5.15) considering a zero-order hold on the inputs discretization. L_{obs} is the observer gain such that $A_{obs}^d - L_{obs}.C_{obs}$ is stable.

Finally, the corrective term on the motor torque is obtained as follow:

$$\hat{\Delta a_2} = \hat{\gamma} + a_3.x_2^f \tag{5.17}$$

where x_2^f is obtained by filtering x_2 using a first order filter in order to get just the slow dynamics of this variable which is compatible with the dynamics of the Stirling engine torque.

5.3.3 Experimental results on the Stirling based power system prototype

In this section, we present the experimental results on the real Stirling engine prototype depicted in Figure 3.7. Similarly to Section 5.2.2 that validates the developed control strategy

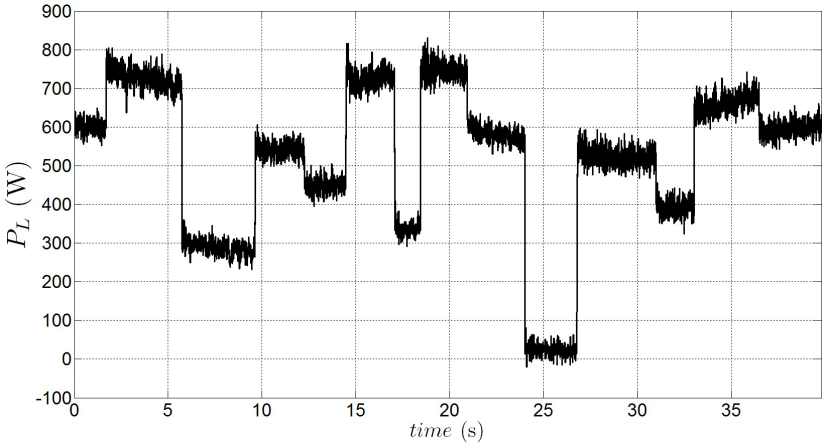

Figure 5.22: Load power demand P_L at the input of the inverter for the Stirling based power plant.

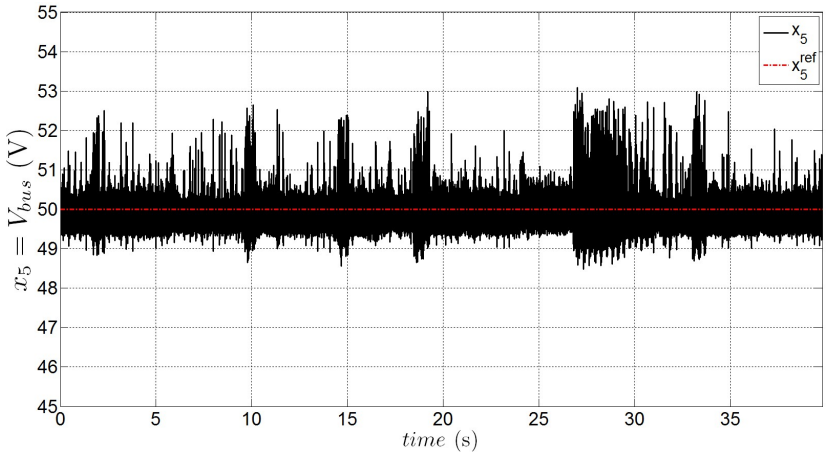

Figure 5.23: Bus voltage V_{bus} and its reference value V_{bus}^{ref} for the Stirling based power plant.

on the dedicated electrical motor testbed, a load power profile depicted in Figure 5.22 is generated acting on the electronic load. One can appreciate from Figure 5.23 that the bus voltage is tightly regulated to its reference value despite the step changes in the load power demand. According to Figure 5.24 the supercapacitor voltage is also maintained around its reference value in a fast manner. The measurements disturbances on the DC bus voltage (Figure 5.23) are due to electromagnetic compatibility problems that occurred after setting the DC/DC converters in the electrical cabinets. A low pass filter (with high cutting frequency) has been introduced to limit these measurement disturbances even if these ones have not been totally attenuated. However, the DC bus voltage remains within its admissible range (44V to 56V).

Figure 5.25 shows good results concerning the tracking of the output current of the DC/DC full bridge converter I_{Lfb} to its reference value $x_4^{ref} = I_{Lfb}^{ref}$ calculated according to (5.11) from

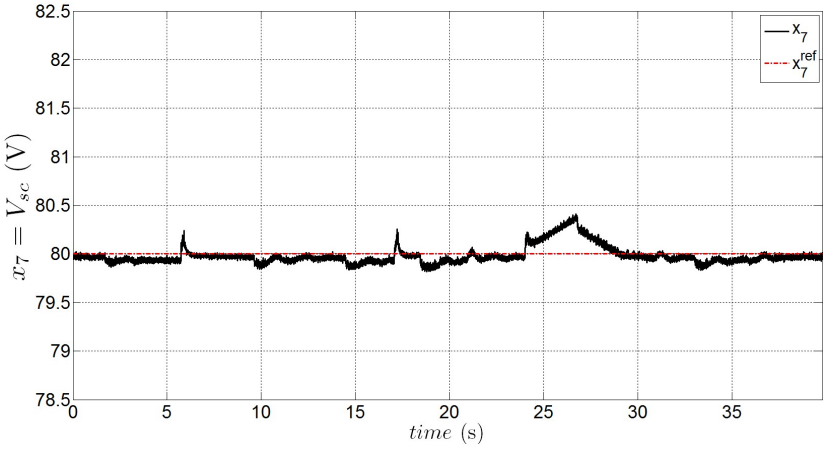

Figure 5.24: Supercapacitor voltage V_{sc} and its reference value V_{sc}^{ref} for the Stirling based power plant.

which the reference signals $x_1^{ref} = \Omega^{ref}$,$x_2^{ref} = I_{red}^{ref}$ and $x_3^{ref} = V_{red}^{ref}$ are extracted (see Section 5.1.3) and depicted in Figure 5.26 that gives the tracking results for these variables. Figure 5.27 plots the control signals $u_1 = \alpha_{fb}$, used to track $x_1^{ref} = \Omega^{ref}$,$x_2^{ref} = I_{red}^{ref}$, $x_3^{ref} = V_{red}^{ref}$ and $x_4^{ref} = I_{Lfb}^{ref}$, and $u_2 = \alpha_{bb}$ used to regulate $x_5 = V_{bus}$ to its setpoint $x_5^{st} = V_{bus}^{ref}$.

Note from Figure 5.22 that between $t = 24$s and $t = 27$s the load has been disconnected which explains that during this time interval the supercapacitor voltage keeps increasing (see Figure 5.24). During this time interval and according to Figures 5.25 and 5.26 the state variables $x_1 = \Omega$, $x_2 = I_{red}$, $x_3 = V_{red}$ and $x_4 = I_{Lfb}$ do not track anymore their respective references but are limited to some lower bound due to the duty ratio α_{fb} saturation as it can be seen from the top of Figure 5.27. If the load is kept disconnected, the supercapacitor voltage will keep increasing until it reaches its maximum value leading to the system shut down (or activating dump loads). One can also see from Figure 5.26 that the measurement of the rotational speed $x_1 = \Omega$ is also disturbed in high speed (high frequency) due to electromagnetic compatibility problems. These disturbances have been greatly attenuated using a low pass filter.

The obtained time responses of the closed loop system are very satisfying for the considered application. The reason is that the developed control strategy is based upon an optimal criterion (even if the prediction horizon is one step) and the time constant of the first order filter given by (5.11a), that limits the undershoots and overshoots effects, has been chosen as low as possible.

Concerning the oscillations observed in Figures 5.25 and 5.26, they are due to the rapid changes in the load power demand (Figure 5.22) which is an extreme behavior for the system. Indeed, at some time instants, before the system reaches its steady state it sees another step change in the load power demand. Despite this extreme behavior, the closed loop system remains stable with a very satisfying time constants.

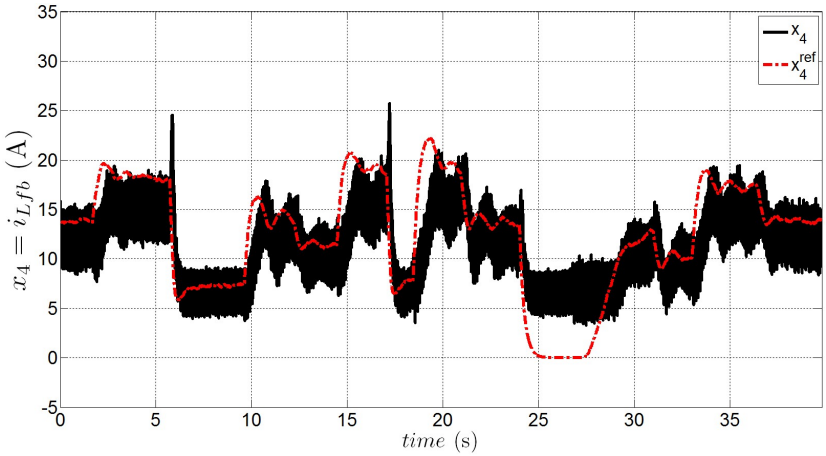

Figure 5.25: Output current of the DC/DC Full Bridge converter I_{Lfb} and its reference value I_{Lfb}^{ref} for the Stirling based power plant.

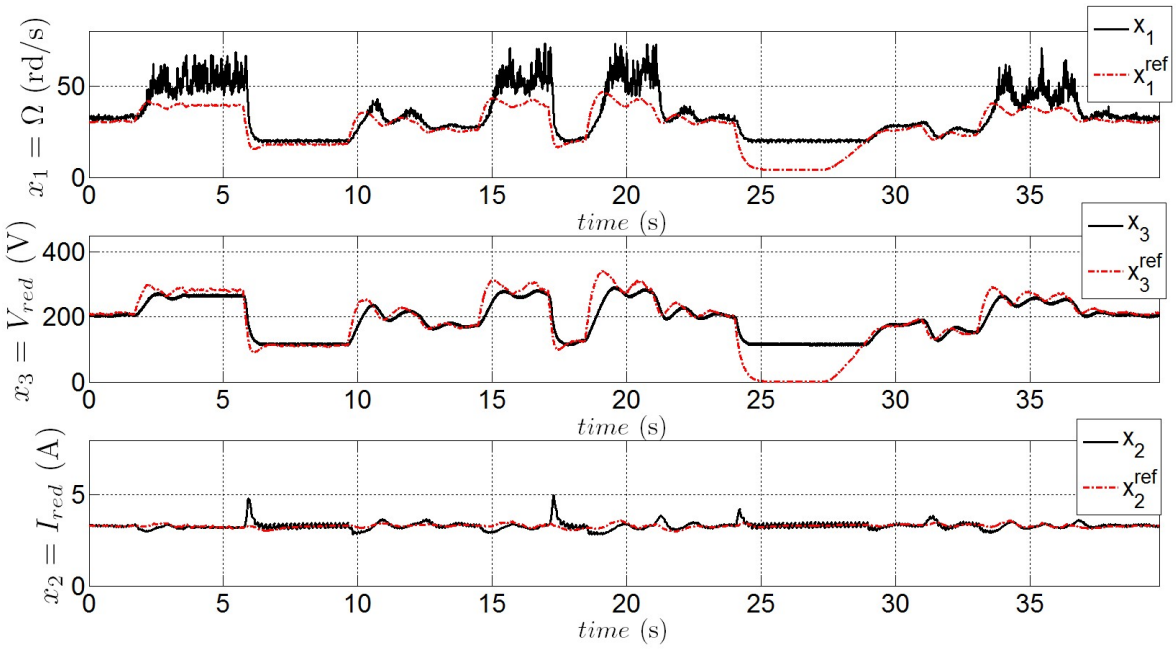

Figure 5.26: Rotational speed of the engine Ω, the rectified voltage V_{red} and the rectified current I_{red} with their respective reference values Ω^{ref}, V_{red}^{ref} and I_{red}^{ref} for the Stirling based power plant.

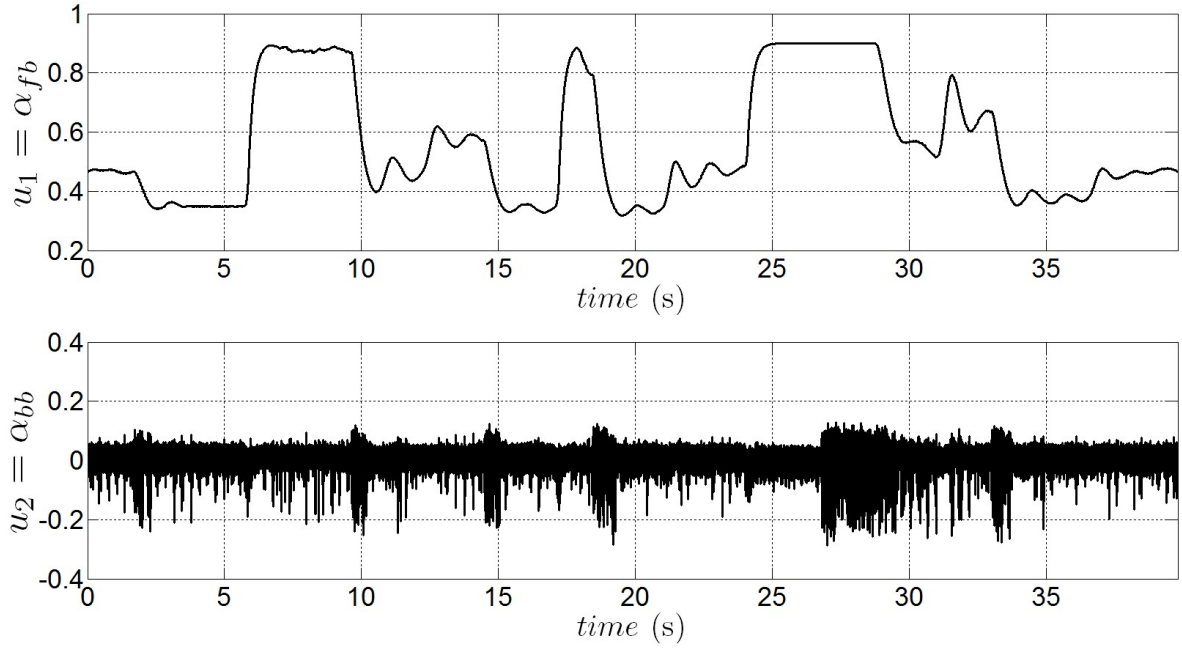

Figure 5.27: Duty ratios of the DC/DC Full Bridge converter (upper figure) and bidirectional DC/DC converter (lower figure) for the Stirling based power plant.

Note also that the same remark as in Section 5.2.2 holds concerning the origin of the static errors in the tracking of $x_1^{ref} = \Omega^{ref}$,$x_2^{ref} = I_{red}^{ref}$ and $x_3^{ref} = V_{red}^{ref}$ (see Figure 5.26) which are due to the modification of the reference signal for x_4 according to (5.11). Here also, this will not affect the global performances of the system since the crucial variable for the control is $x_4 = I_{Lfb}$.

5.4 Conclusion

In this chapter, a novel control strategy for an Off-Grid hybrid Stirling engine/supercapacitor power plant was developed relying on a specific way to generate the references for the key state variables that were tracked combining a backstepping controller and a one step predictive controller. The performances of the closed loop system were assessed first by simulations before their implementation on a dedicated electrical motor testbed. Once the control methodology was validated on this testbed, the final step consisting in implementing the control strategy on the real Stirling based power system was successfully achieved.

Chapter 6

Real time constrained control framework for the Energy Conversion System associated to the Off-Grid Stirling based thermodynamic power Plant.

Contents

6.1 Deeper in the system analysis 82
6.2 Constrained Sliding Mode control of the energy conversion system . 85
6.2.1 Analysis and constrained sliding mode control for "subsystem 1" 85
6.2.2 Analysis and constrained sliding mode control for "subsystem 2" 90
6.3 The State Feedback law 92
6.4 Simulation-based validation 94
6.4.1 Decoupled Simulations 94
6.4.2 Global Simulation 98
6.5 Conclusion 100

In Chapter 5, a novel control strategy that drives the Stirling based power system through its electrical part was presented and experimentally validated. Although the proposed methodology endows the closed-loop system with near to optimal performances in term of settling time, it does not handle explicitly the system constraints. Instead, saturations and ad hoc filters has been added to palliate these constraints and enlarge the domain of applicability of the proposed solution.

In this chapter, a constrained control methodology for the energy conversion system is presented. The resulting feedback laws are real time compatible and they handle explicitly the constraints on the state variables. Moreover, a nice feature in the proposed solution is that it suggests a general control design methodology for a family of power circuits despite the fact that its success may depend on the quantitative design of the circuit components. The proposed design underlines the conditions under which the framework is successful and can therefore be also used to guide the design step.

6.1 Deeper in the system analysis

This section provides additional results to complement the ones provided in Section 5.1. These results will serve in further sections to construct the constrained feedback laws for the energy conversion system whose state space equations given by (4.10a-4.10g) are recalled thereafter for convenience:

$$\dot{x}_1 = a_1.x_1 - a_3.x_2 + a_2 \tag{6.1a}$$
$$\dot{x}_2 = -a_4.x_2 - a_5.x_1.x_2 + a_6.x_1 - a_7.x_3 \tag{6.1b}$$
$$\dot{x}_3 = a_8.x_2 - a_8.k.x_4.u_1 \tag{6.1c}$$
$$\dot{x}_4 = -a_9.x_5 + k.a_9.x_3.u_1 \tag{6.1d}$$
$$\dot{x}_5 = a_{10}.(x_4 + x_6) - \frac{a_{10}}{\eta_{inv}}.\frac{P_L}{x_5} \tag{6.1e}$$
$$\dot{x}_6 = -a_{11}.x_5 + a_{11}.x_7.u_2 \tag{6.1f}$$
$$\dot{x}_7 = -a_{12}.x_6.u_2 \tag{6.1g}$$

where $x_1 = \Omega$, $x_2 = I_{red}$, $x_3 = V_{red}$, $x_4 = I_{Lfb}$, $x_5 = V_{bus}$, $x_6 = I_{Lbb}$, $x_7 = V_{sc}$, $u_1 = \alpha_{fb}$ and $u_2 = \alpha_{bb}$.

The coefficients a_i used in the state equations are given by:

$a_1 = \frac{\alpha(\dot{m}_h, Th_{in}, Tc_{in}) - D_{fr}}{J_{rot}}$, $a_2 = \frac{\beta(Th_{in})}{J_{rot}}$, $a_3 = \frac{p.3.\sqrt{3}.\Phi_f}{\pi.J_{rot}}$, $a_4 = \frac{Rs}{Ls}$, $a_5 = \frac{3.p}{2.\pi}$, $a_6 = \frac{p.3.\sqrt{3}.\Phi_f}{2.\pi.Ls}$, $a_7 = \frac{1}{2.Ls}$, $a_8 = \frac{1}{Cf}$, $a_9 = \frac{1}{L_{fb}}$, $a_{10} = \frac{1}{C_{tot}}$, $a_{11} = \frac{1}{Lbb}$, $a_{12} = \frac{1}{C_{sc}}$.

First of all, note that since the Stirling torque variations are assumed to be very slow compared to the electric stage characteristic times and since we are interested in controlling optimally the energy conversion system, the Stirling engine torque T_{mot} is supposed hereafter to be constant resulting in a constant parameters a_1 and a_2 in (6.1a).

Note also that since the supercapacitor used in the experimental testbed presented in Section 5.3 was oversized, we consider here for the simulations a value of $5F$ for the supercapacitor in order to assess more the performances of the proposed methodology especially for the supercapacitor voltage recovery.

For recall, the control objectives consist in regulating x_5=V_{bus} and x_7=V_{sc} around their respective values $x_5^r = x_5^{st}$=V_{bus}^{ref} and x_7^{st}=V_{sc}^{ref} during load power demand P_L transients while respecting the following set of constraints:

$$x_i \in [x_i^{min}, x_i^{max}] \quad ; \quad i \in \{2, 3, 4, 6\} \tag{6.2}$$

The constraints on the regulated variables x_5 and x_7 will be naturally respected by the success of the control loop while the controlled excursion on x_1 is implicitly imposed through the constraints on both x_2 and x_3 as it can be inferred from equations (6.1a)-(6.1b).

The same system decomposition presented in Section 5.1.1, for the energy conversion system, holds for this chapter: "subsystem 1" which is given by (6.1a)-(6.1d) where u_1 is the

control variable and x_5 is assumed to be regulated around its setpoint (by mean of the control u_2 using "subsystem 2" equations) is rewritten in the condensed form (5.2) recalled thereafter:

$$\dot{z} = A(u_1).z + B.\begin{pmatrix} a_2 \\ x_5^{st} \end{pmatrix} \tag{6.3}$$

where $z = \begin{pmatrix} x_1 & x_2 & x_3 & x_4 \end{pmatrix}^T$ being the reduced state vector for this subsystem and the "subsystem 2" equations are given by (6.1e)-(6.1g). As mentioned before, the "subsystem 2" equations will serve to regulate x_5 to its setpoint using u_2 and to define an appropriate reference value for x_4 namely x_4^{st} that will be tracked using "subsystem 1" equations acting on u_1.

The following assumptions are formulated following [Alamir et al., 2014b] and apply throughout this chapter.

Assumption 6.1
The linear system in the state (x_1, x_2) defined by (6.1a)-(6.1b) (steered by the exogenous signal x_3) shows two separated negative real eigenvalues λ_f and λ_s such that $|\lambda_f| \gg |\lambda_s|$.

For the studied system, this assumption is satisfied with $|\lambda_f| \approx 9552$ Hz $\gg |\lambda_s| \approx 63.4$ Hz. This feature is likely to be satisfied on any motor testbed as it reflects the co-existence of mechanical (x_1) and electrical (x_2) variables which generally evolve among separated time scales.

Assumption 6.2
The lower bound for x_3 has to satisfy $x_3^{min} > \frac{x_5^{st}}{k}$

Indeed, this condition has to be satisfied to ensure the controllablity of x_4 using $u_1 \in [0, 1]$ as it can be inferred from (6.1d).

Assumption 6.3
The bounds x_3^{min} and x_3^{max} invoked in (6.2) are compatible with the constraints on x_2, namely the steady values of x_2 belong to $[x_2^{min}, x_2^{max}]$ for all constant value of $x_3 \in [x_3^{min}, x_3^{max}]$.

This assumption can be easily checked through Figure 5.1 where the steady states of (6.1a)-(6.1d) (in which $x_5 = x_5^{st}$) namely $x_i^{st}(u_1)$, $i \in \{1, \ldots, 4\}$ are plotted. Moreover, one can observe from this figure that a wide variation range of x_1, x_3 and x_4 corresponds to a small variation range of x_2 denoted hereafter by ϵ_2 defined as follow:

$$\varepsilon_2 := \max_{u_1 \in [0,1]} x_2^{st}(u_1) - \min_{u_1 \in [0,1]} x_2^{st}(u_1) \tag{6.4}$$

The central value of $x_2^{st}(\cdot)$ is denoted hereafter by $x_2^{st,c}$. Consequently, $x_2^{st}(u_1) \in \mathcal{I}_2 := x_2^{st,c} + [-\frac{\varepsilon_2}{2}, +\frac{\varepsilon_2}{2}]$.

Note that the parameters ε_2 and $x_2^{st,c}$ are determined by the dimensioning of the system

and does not depend on any control design. For the system under consideration, $x_2^{st,c} \approx 4.82$ while $\varepsilon_2 \approx 0.12$ which corresponds to a relative variation of less than 2.5% (see Figure 5.1).

Another feature that can be observed in Figure 5.1 is that all the maps are monotonic so that the following notations can be used:

$$x_i^{st}(x_j^{st}), u_1^{st}(x_j^{st}) \quad (i,j) \in \{1,\dots,4\}$$

to denote the stationary values of x_i and u_1 that correspond to a given stationary value x_j of the j-th component of the state vector z. This is extensively used in the sequel.

According to Assumption 6.3, it is possible to ensure the fulfillment of the constraints on $x_2 = I_{red}$ by monitoring the excursion of the exogenous signal x_3 (exogenous with respect to the subsystem defined by (6.1a)-(6.1b)). This is enunciated in the following lemma:

Lemma 6.1
There are easily computable maps $\underline{x}_3(x_1, x_2)$ and $\bar{x}_3(x_1, x_2)$ such that all trajectories of (6.1a)-(6.1b) starting from an admissible initial conditions (regarding the constraints on x_2) and steered by a profile $x_3(\cdot)$ meeting the following condition:

$$x_3(t) \in \Big[\underline{x}_3\big(x_1(t), x_2(t)\big), \bar{x}_3\big(x_1(t), x_2(t)\big)\Big] \tag{6.5}$$

satisfy the saturation constraints on x_2.

Proof: See Appendix D.1 where explicit expressions (D.2)-(D.3) are given for $\underline{x}_3(x_1, x_2)$ and $\bar{x}_3(x_1, x_2)$. □

The next two lemmas constitute a formalization of the results obtained in Section 5.1.2.

Lemma 6.2
Any appropriate control that asymptotically steers x_5 to its reference value x_5^r leads to the following property:

$$\lim_{t\to\infty} [x_6(t) - x_6^r(t)] = 0 \tag{6.6}$$

where $x_6^r(t)$ is given by:

$$x_6^r(t) = \frac{P_L}{\eta_{inv} \cdot x_5^r} - x_4(t) \tag{6.7}$$

where P_L is the load power demand.

Proof: This directly follows from equation (6.1e) in which x_5 is replaced by x_5^r while $\dot{x}_5 = 0$ is used. □

It comes from Lemma 6.2 together with equation (6.1g) that it is possible to regulate the supercapacitor voltage x_7 by choosing the following reference value for x_4:

$$x_4^{st} = -k_6 \cdot \tanh(\beta \cdot (x_7 - x_7^{st})) + \frac{P_L}{\eta_{inv} \cdot x_5^{st}} \quad ; \quad k_6 > 0 \tag{6.8}$$

since according to (6.6)-(6.7) this asymptotically infers the following dynamics to x_7:

$$\dot{x}_7 = a_{12} \cdot u_2 \cdot k_6 \cdot \tanh(\beta \cdot (x_7 - x_7^{st})) \tag{6.9}$$

which obviously stabilizes x_7 around x_7^{st}.

Note however that for (6.9) to be compatible with the constraints on x_4, the following conditions are needed:

$$x_4^{min} + k_6 \leq \frac{P_L}{\eta_{inv} \cdot x_5^r} \leq x_4^{max} - k_6 \tag{6.10}$$

This obviously introduces constraints on the possible load power levels that are compatible with a sustainable operation. This is rigorously stated in the following assumption:

Assumption 6.4
There is a positive real k_6 such that all possible values P_L of the load power demand satisfy the inequalities (6.10).

Lemma 6.3
The state feedback law given by:

$$u_2^*(x) := \frac{1}{a_{11}.x_7}.(a_{11}.x_5 - a_{10}.(x_5 - x_5^r) + \dot{x}_6^{ref} - \rho_6.(x_6 - x_6^{ref})) \tag{6.11}$$

where:

$$x_6^{ref} = \frac{P_L}{\eta_{inv} \cdot x_5} - x_4 + \frac{\rho_5}{a_{10}}(x_5^r - x_5) \tag{6.12}$$

in which ρ_5 and ρ_6 are positive design parameters, locally asymptotically steers the pair $(x_5(t), x_6(t))$ to the reference $(x_5^r, x_6^r(t))$, namely:

$$\lim_{t\to\infty} \| \begin{pmatrix} x_5(t) \\ x_6(t) \end{pmatrix} - \begin{pmatrix} x_5^r \\ x_6^r(t) \end{pmatrix} \| = 0 \tag{6.13}$$

Proof: This result was proved in Section 5.1.2.

In the following sections the previous results will serve to design constrained sliding mode controllers based on vector fields analysis for each subsystem.

6.2 Constrained Sliding Mode control of the energy conversion system

6.2.1 Analysis and constrained sliding mode control for "subsystem 1"

Now that we have defined the reference value for the output current of the DC/DC full bridge converter namely $x_4^{st} = I_{red}^{ref}$ given by (6.8) leading to the asymptotic stabilization of the

supercapacitor voltage $x_7 = V_{sc}$ to its reference value, in this section a feedback law for the control variable u_1 that tacks x_4^{st} in near-to-optimal manner while respecting the system constraints is derived using "subsystem 1" equations given by (6.3) in which $x_5 = x_5^r = x_5^{st}$.

Because of the limitations on x_3 given by (6.5) regarding the fulfillment of the saturation constraints on x_2 (refer to Lemma 6.1), a new reference value for x_4 namely $x_4^* = x_4^{st}(x_3^*)$ has to be derived and tracked acting on u_1, where x_3^* is defined to be the closest value to $x_3^{st}(x_4^{st})$ [see (6.8)] that is compatible with the requirement on the excursion of x_2. More precisely:

$$x_3^*(x, P_L) := \arg \min_{z_3 \in [\underline{x}_3(x), \bar{x}_3(x)]} |z_3 - x_3^{st}(x_4^{st}(x, P_L))| \tag{6.14}$$

where $x_4^{st}(x, P_L)$ is given by (6.8) depending on the current value of the supercapacitor voltage x_7 and the present load demand P_L. Note that by doing so, the rate with which the supercapacitor voltage is regulated around its reference value is moderated by the dynamic of the mechanical part of the system which is directly linked to the Stirling engine performance. This is done through the definition of the admissible interval $\Big[\underline{x}_3\big(x_1(t), x_2(t)\big), \bar{x}_3\big(x_1(t), x_2(t)\big)\Big]$.

Remark 6.1
Note that in Chapter 5 (especially in Section 5.1.3) where a first control strategy for the energy conversion system has been developed, it has been observed that in order to avoid negative excursions on some of the system's variables, the variation of the set-point x_4^{st} needs to be filtered or slowed down. However, contrary to Chapter 5 where this feature has been observed, *the discussion above gives a deeper interpretation and a more systematic, efficient and dynamic way to address this limitation. Indeed, while the filter introduced in Chapter 5 operates continuously slowing down the system unconditionally, the values that result from (6.14) slow down the system only when necessary. This is a general fact making explicit handling of the constraint preferable to worst-case-based unconstrained design.*

Based on the observation made in Section 6.1 regarding the excursion of the stationary values of x_2, it can be argued that if the conclusion of Lemma 6.1 is used to define bounds on the variations of x_3 such that x_2 remains in a tight interval around $x_2^{st,c}$, then it becomes relevant to analyze the behavior of the dynamic system (6.1c)-(6.1d) in which the state is (x_3, x_4) while x_2 and x_5 are considered to be constant. Such an analysis can then be performed by visualizing the vector fields in the plan (x_3, x_4). When doing this analysis using the numerical values of the system under consideration, it comes that the following assumption is satisfied:

Assumption 6.5
For any admissible desired pair $(x_3^*, x_4^{st}(x_3^*))$, the picture of the vector fields of the dynamic system (6.1c)-(6.1d) in which $x_2 = x_2^{st}(x_3^*) \in \mathcal{I}_2$ and $x_5 = x_5^r$ is the one depicted in Figure 6.1, more precisely:

1. *The horizontal lines AB and DE correspond to the lines $x_4 = x_4^{min}$ and $x_4 = x_4^{max}$ respectively.*
2. *C is the desired steady point $(x_3^*, x_4^{st}(x_3^*))$ while $u_1^* = u_1^{st}(x_3^*)$ is the corresponding steady control.*

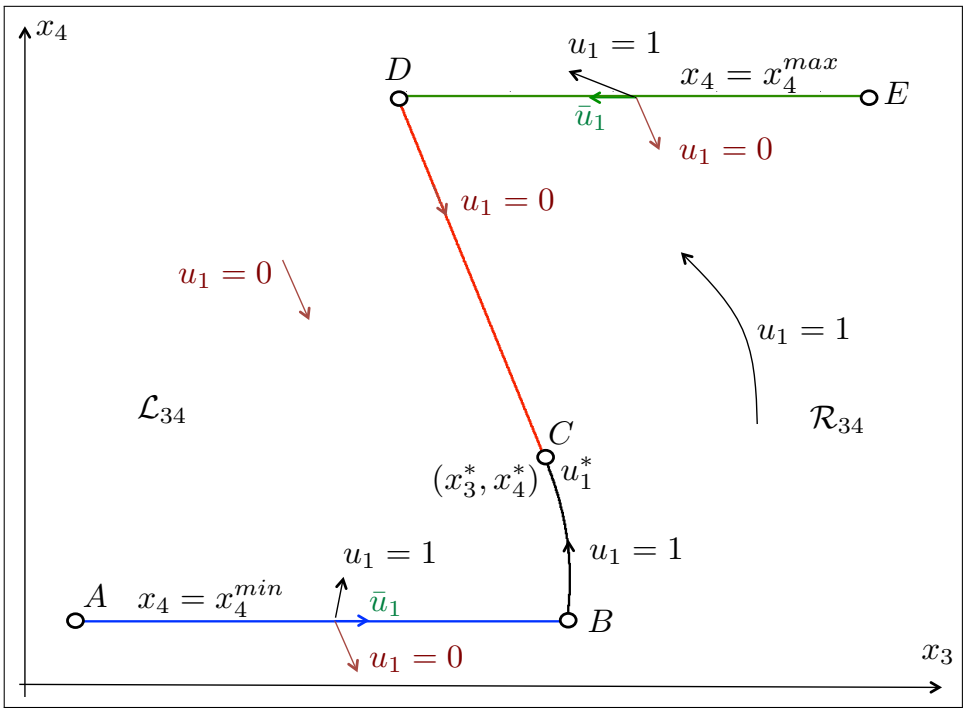

Figure 6.1: Typical disposition of the vectors field of the dynamic system (6.1c)-(6.1d) when $x_2 = x_2^{st}(x_3^*)$ and $x_5 = x_5^r$ are assumed to be constant.

3. *DC is the trajectory under the control $u_1 = 0$ that starts at D and ends at C (this defines D).*

4. *BC is the trajectory under the control $u_1 = 1$ that starts at B and ends at C (this defines B).*

5. *The disposition of the vector fields on the line AB and DE are such that the control $\bar{u}_1(x)$ given by:*

$$\bar{u}_1(x) := \begin{cases} \dfrac{1}{kx_3}\Big[x_5 + \rho_4(x_4^{max} - x_4)\Big] & \text{on DE} \\[2ex] \dfrac{1}{kx_3}\Big[x_5 + \rho_4(x_4^{min} - x_4)\Big] & \text{on AB} \end{cases} \tag{6.15}$$

steers the state towards D (resp. B) when $x_4 = x_4^{max}$ (resp. x_4^{min}) while keeping x_4 constant.

6. *The line ABCDE is attractive under the control $u_1 = 1$ for any starting point that lies to the right of the curve BCD (this region is denoted by $\mathcal{R}_{34}$ on Figure 6.1).*

7. *The line ABCDE is attractive under the control $u_1 = 0$ for any starting point that lies to the left of the curve BCD (this region is denoted by $\mathcal{L}_{34}$ on Figure 6.1)*

Note that the first 4 items of Assumption 6.5 are only definitions. The item 5) can be easily checked by investigating the disposition of the vector fields on the horizontal lines AB and DE. It is also possible to formulate algebraic conditions [see (D.4)-(D.7)] to check items 5), 6) and 7) above as it is shown in Appendix D.2.

Although the conditions (D.4)-(D.7) might seem tricky to check, it is likely that the topology of the vector fields depicted in Figure 6.1 holds for a wide class of such voltage conditioning systems. The above conditions are only given for completeness.

Note also that the disposition of the vector fields obviously suggests that a sliding modes controller can be defined in which the curves ABCDE is the sliding surface while the equivalent control on the sliding surface steers the system towards the desired point C. Here we prefer to use continuous control because the equations (6.1a)-(6.1d) represent the mean dynamic and in order to derive an easy to use closed-loop systems avoiding the numerical difficulties associated to the sliding modes controllers simulation when long tuning and assessing scenarios are required as it is the case here (see later).

Rather than using the sliding modes formulation, a 2D interpolation techniques is used in the (x_3, x_4) plan. Namely, an interpolated expression of the feedback is derived in which, the expressions $u_1 = 1$ or $u_1 = 0$ are obtained when the current state (x_3, x_4) is far from the curve ABCDE while u_1 takes the appropriate values when (x_3, x_4) lies on the curve ABCDE. The appropriate value is itself obtained by appropriate interpolation between the values depicted on Figure 6.1 according to the position of the current point (x_3, x_4) on the curve ABCDE.

In order to properly define the 2D interpolated expression, the following auxiliary function is needed:

$$\varphi(r, v_1, v_2) := v_1 + Sat(1 - e^{-\lambda r}) \cdot (v_2 - v_1) \tag{6.16}$$

which simply takes the value v_1 for $r = 0$ and v_2 when $r \gg 0$ with a transition rate defined by the positive constant λ.

Based on the above discussion, the following explicit feedback can be defined for a given target point $(x_3^*, x_4^{st}(x_3^*))$:

Definition 6.1
Let a desired point $(x_3^*, x_4^{st}(x_3^*))$ be defined. Given a current position $p := (x_3, x_4)$ such that $x_4 \in [x_4^{min}, x_4^{max}]$, compute the following quantities:

- *Compute $u_1^{DE}(x)$ and $u_1^{AB}(x)$ according to:*

$$u_1^{DE}(x) := \varphi\Big(\frac{x_3 - x_3(D)}{x_3(D)}, 0, \bar{u}_1(x)\Big) \tag{6.17}$$

$$u_1^{AB}(x) := \varphi\Big(\frac{x_3(B) - x_3}{x_3(B)}, 1, \bar{u}_1(x)\Big) \tag{6.18}$$

where $\bar{u}_1(x)$ is given by (6.15).

- *Compute* $u_1^{BCD}(x)$ *according to:*

$$u_1^{BCD}(x) := \begin{cases} \varphi\Big(\dfrac{x_4^{max} - x_4}{x_4^{max}}, 0, u_1^*\Big) & \text{if } x_4 > x_4^* \\ \varphi\Big(\dfrac{x_4 - x_4^{min}}{x_4^{min}}, 1, u_1^*\Big) & \text{if } x_4 \leq x_4^* \end{cases}$$

  where $u_1^* := u_1^{st}(x_3^*)$.

- *Compute the abscissa* $\hat{x}_3$ *of the horizontal projection of* p *on BCD.*

- *Compute the vertical interpolation* $u_1^v(x)$ *according to:*

$$u_1^v(x) := \begin{cases} \varphi\Big(\dfrac{x_4^{max} - x_4}{x_4^{max}}, u_1^{DE}(x), 1\Big) & \text{if } x_3 > \hat{x}_3 \\ \varphi\Big(\dfrac{x_4 - x_4^{min}}{x_4^{min}}, u_1^{AB}(x), 0\Big) & \text{if } x_3 \leq \hat{x}_3 \end{cases}$$

- *Compute* $u_1(x|x_3^*)$ *by horizontal interpolation between* $u_1^v(x)$ *and* $u_1^{BCD}(x)$ *according to:*

$$u_1(x|x_3^*) = K_1(x|P_L) := \varphi\Big(\frac{|x_3 - \hat{x}_3|}{|\hat{x}_3|}, u_1^{BCD}(x), u_1^v(x)\Big) \tag{6.19}$$

Note that the resulting feedback control $u_1(x|x_3^*) = K_1(x|P_L)$ defined by (6.19) is continuous with respect to x for a given target $(x_3^*, x_4^*) = (x_3^*, x_4^{st}(x_3^*))$. Indeed, for a given value of x_4, continuity w.r.t x_3 is guaranteed by the continuity w.r.t x_3 of the expressions (6.17), (6.18) and (6.19) while the continuity w.r.t x_4 for a given x_3 is guaranteed by the continuity w.r.t x_4 of the expressions of $u_1^{BCD}(x)$ and $u_1^v(x)$.

Note that the success of the state feedback $u_1(x|x_3^*)$ in steering the state (x_3, x_4) to the desired (x_3^*, x_4^*) is conditioned by the fact that the excursion of x_2 is small. Indeed, under this assumption, the picture depicted in Figure 6.1 remains relevant while x_2 is slightly moving. Note however that for this excursion to be small, the following two requirements are needed:

- The range of variation ε_2 given by (6.4) of the steady values of x_2 is small.
- The variations of x_3 remains inside the moving interval $[\underline{x}_3(x_1, x_2), \bar{x}_3(x_1, x_2)]$ which is computed online based on the admissible range $[x_2^{min}, x_2^{max}]$ [see (D.2)-(D.3) in the appendix].

The first requirement mentioned above depends on the choice of the system's components and has to be satisfied by construction. The second requirement can be satisfied by an appropriate management of the desired value x_3^* according to (6.14).

The preceding discussion completely defines the feedback law

$$u_1 = K_1(x, P_L) := u_1(x|x_3^*(x, P_L))$$

The next section is dedicated to the definition of the feedback law $u_2 = K_2(x, P_L)$ through the analysis of "subsystem 2" equations.

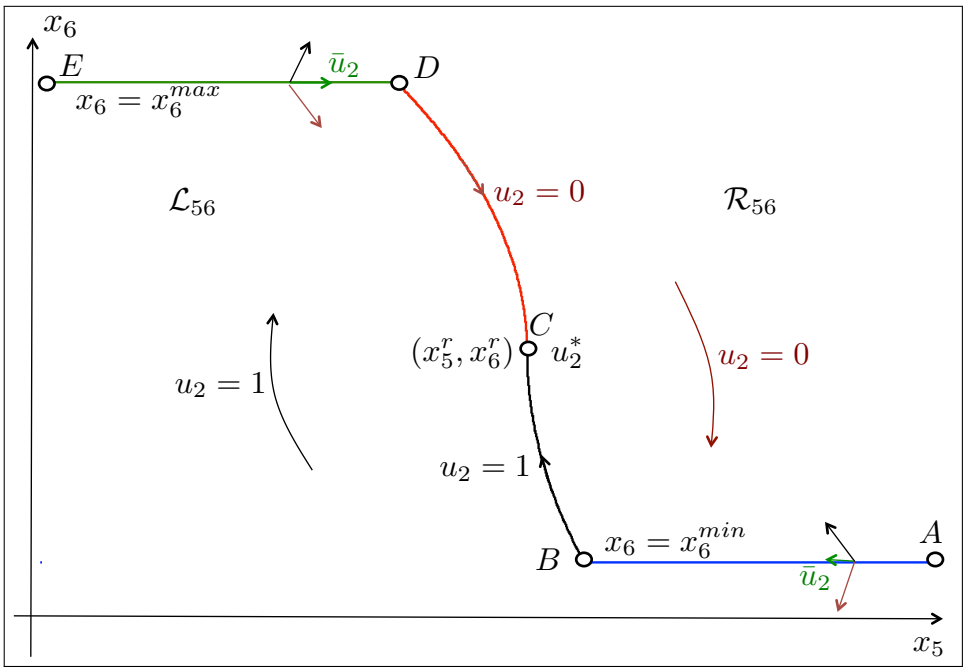

Figure 6.2: Typical disposition of the vectors field of the dynamic system (6.1e)-(6.1f) for a given x_4 and for $x_7 > x_5^r$.

6.2.2 Analysis and constrained sliding mode control for "subsystem 2"

By observing the structure of (6.1e)-(6.1f) it appears that the same graphical analysis as in Section 6.2.1 can be done in the 2D plan (x_5, x_6) for a given value of x_4. This analysis is relevant under (6.14) since as it is explained earlier, equation (6.14) leads to rather slow variations of (x_3, x_4) inducing hence two separated time scales, a slow one for x_i, $i \in \{1, 2, 3, 4, 7\}$ on one hand and a fast one for x_5 and x_6 on the other hand.

When considering the vector fields of (6.1e)-(6.1f) for a given value of x_4, it can be shown that the following assumption holds for the studied system:

Assumption 6.6
For a given admissible x_4 and a supercapacitor voltage $x_7 > x_5^r$, the disposition of the vector fields around the desired pair (x_5^r, x_6^r) where x_6^r is defined by (6.7) is the one given in Figure 6.2, more precisely:

1. *The horizontal lines AB and DE correspond to the lines $x_6 = x_6^{min}$ and $x_6 = x_6^{max}$ respectively.*

2. *C is the desired steady point (x_5^r, x_6^r) while u_2^* is the locally stabilizing feedback invoked in Lemma 6.3:*

3. *DC is the trajectory under the control $u_2 = 0$ that starts at D and ends at C (this defines*

D).

4. *BC is the trajectory under the control $u_2 = 1$ that starts at B and ends at C (this defines B).*

5. *The disposition of the vector fields on the line AB and DE are such that the controls $\bar{u}_2$ given by:*

$$\bar{u}_2(x) := \begin{cases} \dfrac{1}{x_7}\Big[x_5 + \dfrac{\rho_6}{a_{11}}(x_6^{max} - x_6)\Big] & \text{on DE} \\ \\ \dfrac{1}{x_7}\Big[x_5 + \dfrac{\rho_6}{a_{11}}(x_6^{min} - x_6)\Big] & \text{on AB} \end{cases} \tag{6.20}$$

steers the state towards D (resp. B) when $x_6 = x_6^{max}$ (resp. when $x_6 = x_6^{min}$) while keeping x_6 constant.

6. *The line ABCDE is attractive under the control $u_2 = 1$ for any starting point that lies to the left of the curve BCD (this region is denoted by $\mathcal{L}_{56}$ on Figure 6.2).*

7. *The line ABCDE is attractive under the control $u_2 = 0$ for any starting point that lies to the right of the curve BCD (this region is denoted by $\mathcal{R}_{56}$ on Figure 6.2).*

Note that the same comments that followed assumption 6.5 can be reproduced here regarding the items invoked in Assumption 6.6. In particular, there is here also the possibility to check them through explicit conditions similar to (D.4)-(D.7).

Based on the observation of Figure 5, an interpolation-based state feedback $K_2(x|P_L)$ can be defined in a similar way to the one already used in Definition 6.1 to define $K_1(x|P_L)$.

Definition 6.2
Let be given a load power demand P_L. Consider the corresponding desired pair (x_5^r, x_6^r) using x_6^r defined by (6.7). Compute the following quantities based on the current point $p = (x_5, x_6)^T$:

- *Compute $u_2^{DE}(x)$ and $u_1^{AB}(x)$ according to:*

$$u_2^{DE}(x) := \varphi(\frac{x_5(D) - x_5}{x_5(D)}, 0, \bar{u}_2(x)) \tag{6.21}$$

$$u_2^{AB}(x) := \varphi(\frac{x_5 - x_5(B)}{x_5(B)}, 1, \bar{u}_2(x)) \tag{6.22}$$

where $\bar{u}_2(x)$ is given by (6.20).

- *Compute $u_2^{BCD}(x)$ according to:*

$$u_2^{BCD}(x) := \begin{cases} \varphi(\dfrac{x_6^{max} - x_6}{x_6^{max}}, 0, u_2^*(x)) & \text{if } x_6 > x_6^r \\ \varphi(\dfrac{x_6 - x_6^{min}}{|x_6^{min}|}, 1, u_2^*(x)) & \text{if } x_6 \leq x_6^r \end{cases}$$

where $u_2^*(x)$ is given by (6.11).

- *Compute the abscissa $\hat{x}_5$ of the horizontal projection of p on BCD*

- *Compute the vertical interpolation $u_2^v(x)$ according to*

$$u_2^v(x) := \begin{cases} \varphi(\dfrac{x_6^{max} - x_6}{x_6^{max}}, u_2^{DE}(x), 1) & \text{if } x_5 < \hat{x}_5 \\ \varphi(\dfrac{x_6 - x_6^{min}}{|x_6^{min}|}, u_2^{AB}(x), 0) & \text{if } x_5 \geq \hat{x}_5 \end{cases}$$

- *The feedback $u_2 = K_2(x|P_L)$ is obtained by horizontal interpolation between $u_2^v(x)$ and $u_2^{BCD}(x)$ according to:*

$$u_2(x|P_L) = K_2(x|P_L) := \varphi(\frac{|x_5 - \hat{x}_5|}{|\hat{x}_5|}, u_2^{BCD}(x), u_2^v(x)) \tag{6.23}$$

6.3 The State Feedback law

Note that by definition of the interpolated feedback laws $K_1(x, P_L)$ and $K_2(x, P_L)$, the resulting closed-loop trajectories passes through neighborhoods $\mathcal{V}_{34}(x_3^*, x_4^*)$ and $\mathcal{V}_{56}(x_5^r, x_6^r)$ of the targeted pairs (x_3^*, x_4^*) and (x_5^r, x_6^r) of size $O(1/\lambda)$ after a finite time. In other words by choosing $\lambda > 0$ (used in the interpolation map (6.16)) sufficiently high, the trajectories cross neighborhoods that are as small as required. In particular, $\lambda > 0$ can be taken sufficiently high so as to make these neighborhoods entirely contained in the basins of attraction of the locally asymptotically stable dynamics under the local control laws $u_1^{st}(x_3^*)$ and $u_2^*(x)$. If then, the feedbacks $u_1^{st}(x_3^*)$ and $u_2^*(x)$ are maintained, then asymptotic stability follows.

The preceding discussion suggests a dual-mode controller. Namely, when the state (x_3, x_4) [resp. (x_5, x_6)] is far from the desired pair, the interpolated law K_1 [resp. K_2] is used to steer the state to small neighborhood of the desired pair. When the state is inside this neighborhood, a switch to the locally asymptotically stabilizing law $u_1^{st}(x_3^*)$ [resp. $u_2^*(x)$] is operated.

It is worth underlying also that if the neighborhoods are taken sufficiently small (that is λ is taken sufficiently high), then the transient excursions still meet all the saturation constraints on the states. The overall control law is therefore admissible.

Note however that such a dual-mode control design has to be done with care in order to avoid undesirable chattering-like behavior (the state enters and leaves the small neighborhood with a high frequency). This is generally avoided by defining the size of the final neighborhoods using the Lyapunov functions level of the local feedback. This is more rigorously defined as follows:

Definition 6.3
For each admissible x_3^*, the Lyapunov matrix reflecting the stability of $A(u_1^{st}(x_3^*))$ is denoted

by $S_{34}(x_3^*)$. Moreover, for any given pair (x_3, x_4), the following function is defined:

$$d_{34}(x, P_L) := \left\| \begin{pmatrix} 0 \\ 0 \\ x_3 - x_3^* \\ x_4 - x_4^{st}(x_3^*) \end{pmatrix} \right\|_{S_{34}(x_3^*)} \tag{6.24}$$

where x_3^* is given by (6.14).

Definition 6.4
Define $S_{56} \in \mathbb{R}^2$ to be the Lyapunov matrix corresponding to the following Hurwitz matrix:

$$\begin{pmatrix} -\dfrac{a_{10} P_L}{\eta_{inv}(x_5^r)^2} & a_{10} \\ 0 & -\rho_6 \end{pmatrix} \tag{6.25}$$

Moreover, for any pair (x_5, x_6), the following function can be defined:

$$d_{56}(x, P_L) := \left\| \begin{pmatrix} x_5 - x_5^r \\ x_6 - x_6^r(x, P_L) \end{pmatrix} \right\|_{S_{56}} \tag{6.26}$$

where x_6^r is defined by (6.7).

By now, we have everything we need to define the complete state feedback:

Definition 6.5
Let $\lambda > 0$ be the positive scalar invoked in the definition of the interpolation map (6.16). Let $\gamma_{34} > 0$ and $\gamma_{56} > 0$ be some positive reals. Let P_L be a load power demand. The state feedback law is defined as follows:

$$u_1 := \begin{cases} K_1(x, P_L) & \text{if } d_{34}(x, P_L) > \gamma_{34} \\ u_1^{st}(x_3^*(x, P_L)) & \text{otherwise} \end{cases} \tag{6.27}$$

$$u_2 := \begin{cases} K_2(x, P_L) & \text{if } d_{56}(x, P_L) > \gamma_{56} \\ u_2^*(x, P_L) & \text{otherwise} \end{cases} \tag{6.28}$$

Based on the discussions above, the following result can be proved:

Proposition 6.1
If Assumptions 6.1-6.6 are satisfied, then there exist sufficiently small $\gamma_{34} > 0$, $\gamma_{56} > 0$ and sufficiently high $\lambda \times max(\gamma_{34}, \gamma_{56}) > 0$ such that the closed-system obtained by applying the state feedback laws (6.27)-(6.28) to the dynamic system (6.1a)-(6.1g) asymptotically stabilizes the system's state at a steady value that is compatible with the desired values x_5^r and x_7^r of x_5 and x_7 respectively while meeting the problem's constraints (6.2) and using admissible control $u \in [0, 1]^2$.

Proof: See Appendix D.3.

6.4 Simulation-based validation

In this section some simulations are proposed to illustrate several facts regarding the proposed state feedback design. More precisely, the validation is split into two stages:

1. In the first stage, referred hereafter as the *decoupled simulations*, each feedback law is validated separately by decoupling the two subsystems. This is done by simulating:

   ✓ the system with state $(x_1, x_2, x_3, x_4)^T$ in which $x_5 = x_5^d$ is used.

   ✓ the system with state (x_5, x_6, x_7) with a given and constant value of x_4.

   These decoupled simulations enable us to show the impact of the saturation on the different state variables on the settling time of the corresponding controlled system to be shown. This stage obviously shows that there are two separate time scales which explains the success of the whole scheme.

2. In the second stage, the whole closed-loop system is precisely simulated under varying power demand in order to assess the ability of the control law to tightly regulate the bus voltage x_5 under varying power demand P_L while regulating in a slower time scale the super-capacitor voltage x_7.

6.4.1 Decoupled Simulations

Figure 6.3 shows how the voltage x_5 is regulated around the desired value $x_5^d = 50$ V while the desired value $x_4^d = 14.7$ is considered. Two scenarios are plotted in this Figure for two different values of the maximum current $x_6^{max} \in \{50, 60\}$.These scenarios clearly shows that closed-loop behavior shows a sort of minimum-time behavior since it saturates the current in order to accelerate the convergence towards the desired value.

Figure 6.4 shows how the state x_4 (and therefore x_3) are steered to the desired steady pair (x_3^d, x_4^d) which corresponds to +20% increase in the value of x_4^d while meeting the constraints on all the state variables. In particular, a minimum value of $x_2^{min} = 4$ A is considered. This figures clearly shows how the bounding values defined by (D.2)-(D.3) which guarantee the fulfillment of the constraints on x_2 slow down the possible evolution of the pair (x_3, x_4). Figure 6.5 shows the same kind of results when a decrease of the desired value x_4^d of -20% is considered. Note that in this case, the upper bound $x_2^{max} = 5$ A is saturated in order to accelerate the convergence.

It is worth noting that during the scenarios of Figures 6.4 and 6.5, the state variable x_4 itself does hit the constraints during the first milliseconds. This is difficult to see because of the time scale. This is the reason why the same evolutions are plotted in Figures 6.8 and 6.9 using a logarithmic time scale.

Figures 6.6 and 6.7 shows the impact of the saturation level x_2^{min} and x_2^{max} on the state variable x_2 on the response time of the closed-loop system when $\pm 20\%$ change in the desired

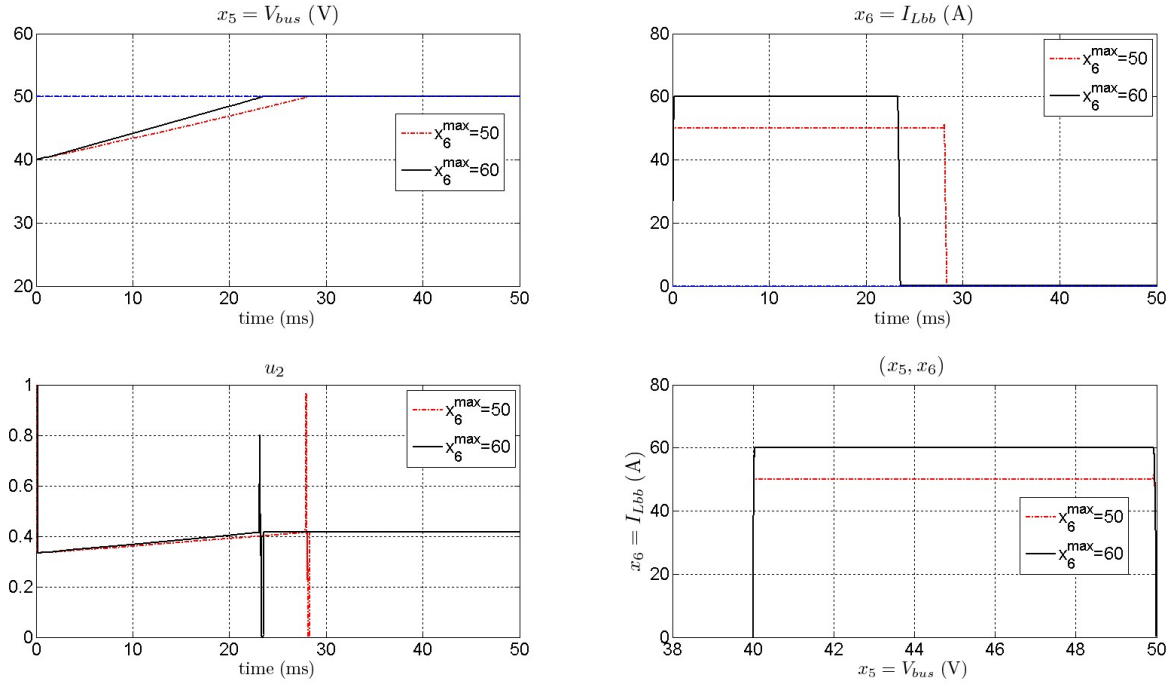

Figure 6.3: Control of the (x_5, x_6) system under constant x_4. Influence of the allowable values of x_6 on the settling time. Comparison between the cases $x_6^{max} = 10$ and $x_6^{max} = 20$. Note that the time axis is in milliseconds. The closed-loop system shows a minimum-time like behavior since it saturate the constraints on the current $x_6 = I_{Lbb}$ in order to accelerate the convergence.

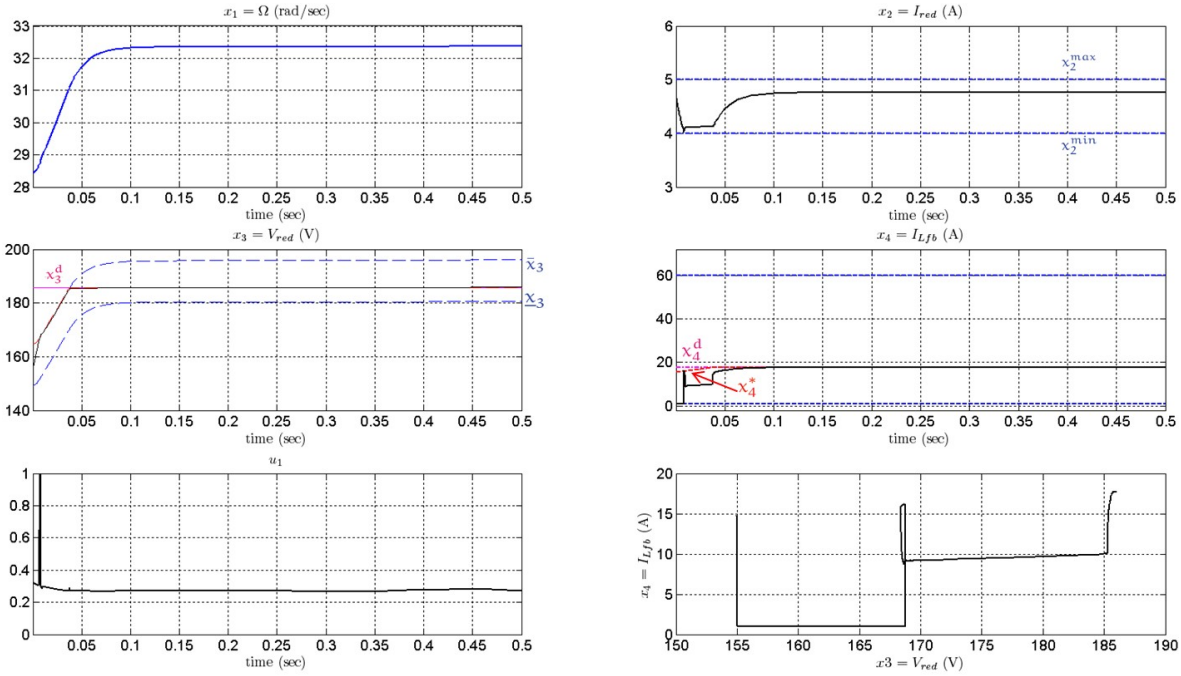

Figure 6.4: Control of the (x_3, x_4) system under constant $x_5 = x_5^d$ after a step change of +20% on the desired value x_4^d. Note that the bounds on x_3 defined by (D.2)-(D.3) slow down the response in order to meet the constraints on x_2. The same scenario is depicted in Figure 6.8 using logarithmic scale in order to show the evolution of the variables during first milliseconds of the scenario.

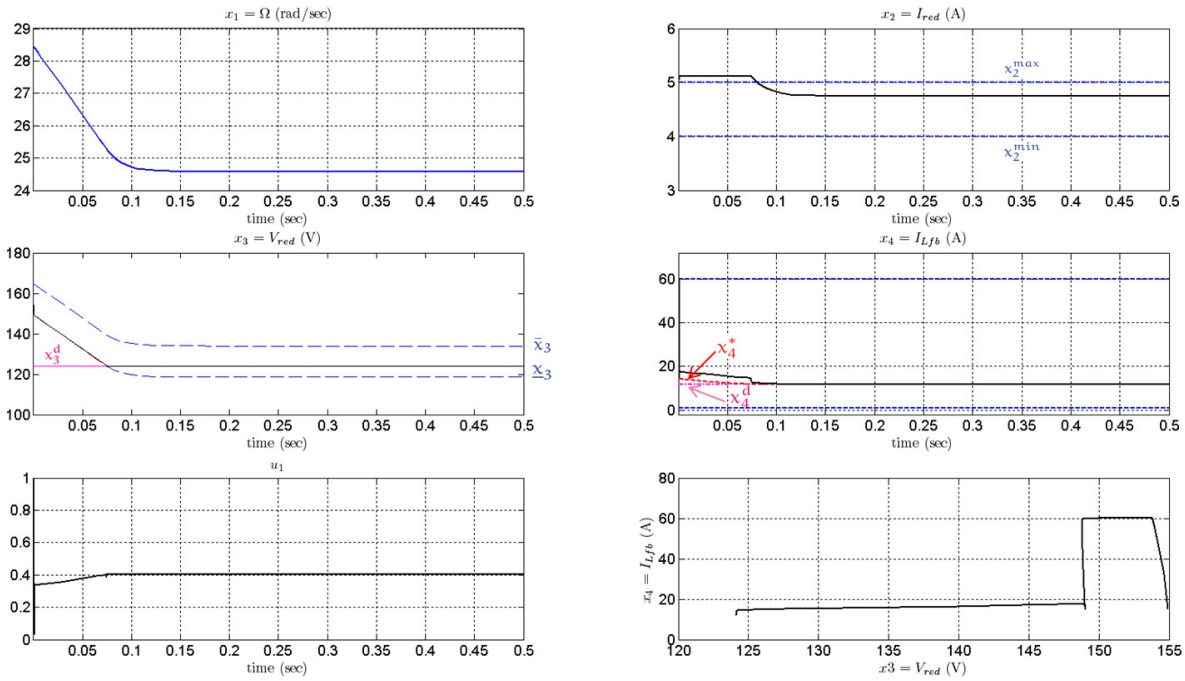

Figure 6.5: Control of the (x_3, x_4) system under constant $x_5 = x_5^d$ after a step change of -20% on the desired value x_4^d. Note that the bounds on x_3 defined by (D.2)-(D.3) slow down the response in order to meet the constraints on x_2. The same scenario is depicted in Figure 6.9 using logarithmic scale in order to show the evolution of the variables during first milliseconds of the scenario.

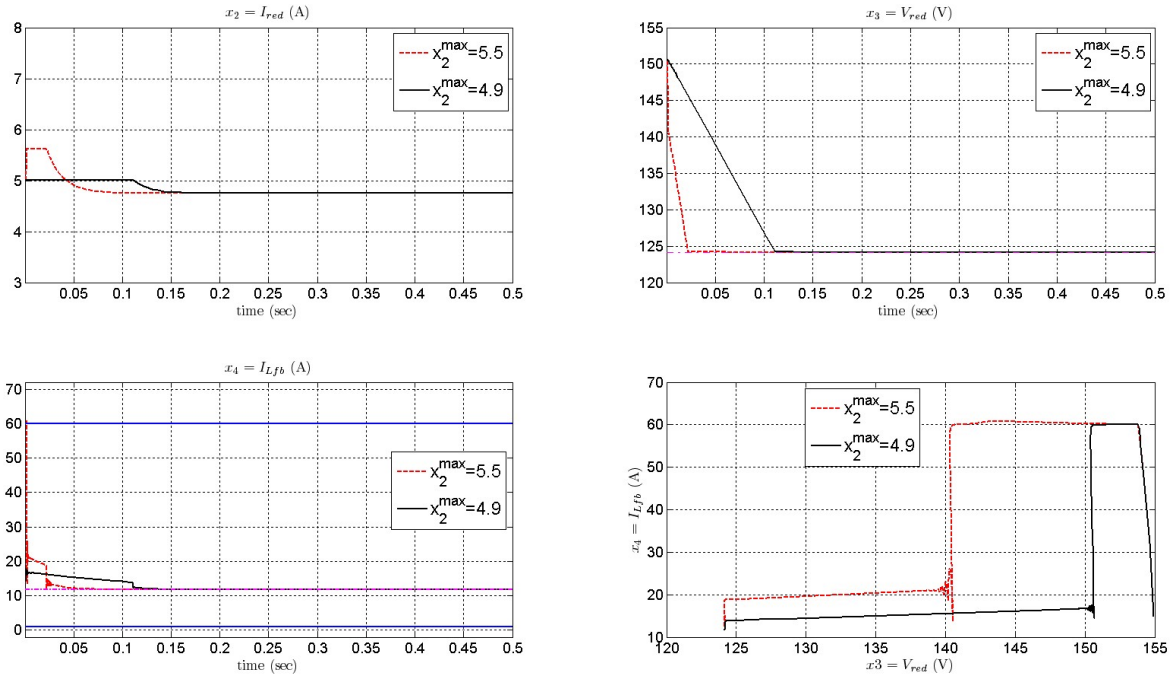

Figure 6.6: Control of the (x_3, x_4) system under constant $x_5 = x_5^d$ after a step change of -20% on the desired value x_4^d. Influence of the constraints on x_2 on the response time of the system.

value x_4^d is applied. Here again, the closed-loop shows a sort of minimum time behavior since it systematically saturates the constraints in order to accelerate the convergence.

6.4.2 Global Simulation

The decoupled set of simulations proposed in section 6.4.1 clearly shows that the time scale of the two subsystems are quite separated. Indeed, the response time of the bus voltage related subsystem is in the range of milliseconds while the response time of the current $x_4 = I_{Lfb}$ that is used to charge the supercapacitor voltage is in the range of seconds. This justifies the decoupled design. Nevertheless, the global control design is validated in the present section through closed-loop simulation of the whole system under varying power demand scenario.

Figures 6.10, 6.11 and 6.12 show three different scenarios that investigate the overall closed-loop performance under time varying power load demand profiles. In particular, Figures 6.10 and 6.11 show two scenarios that differ only by the maximal allowed value x_2^{max} on the current $x_2 = I_{red}$ which is set to $x_2^{max} = 5$ A and $x_2^{max} = 4.8$ A respectively. Note how this slight difference has a great impact on the amplitude of the excursion of the supercapacitor voltage $x_7 = V_{sc}$. This suggests that the maximum allowable current x_2 which heavily depends on the choice of the component has to be jointly designed with the choice of the supercapacitor.

All the simulations clearly show that the control objectives are met in the sense that the

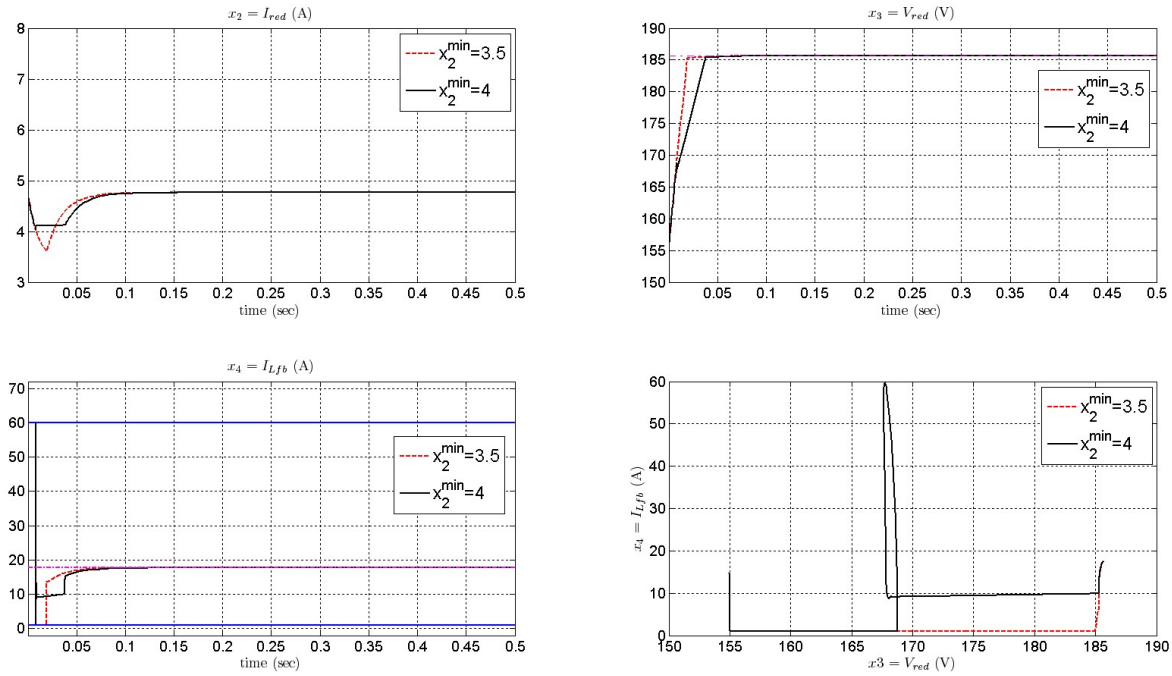

Figure 6.7: Control of the (x_3, x_4) system under constant $x_5 = x_5^d$ after a step change of +20% on the desired value x_4^d. Influence of the constraints on x_2 on the response time of the system.

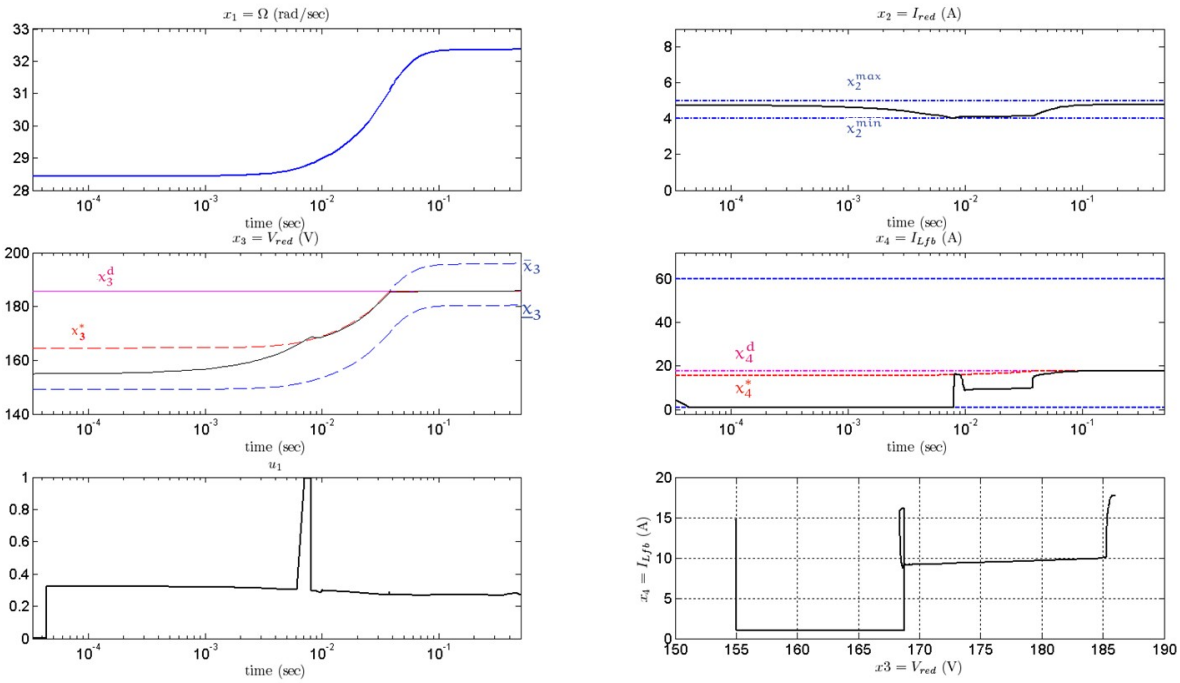

Figure 6.8: Same scenario as the one depicted on Figure 6.4 using logarithmic scale on the time axis in order to show the beginning of the scenario. This scale enables the saturation on x_4 to be clearly shown.

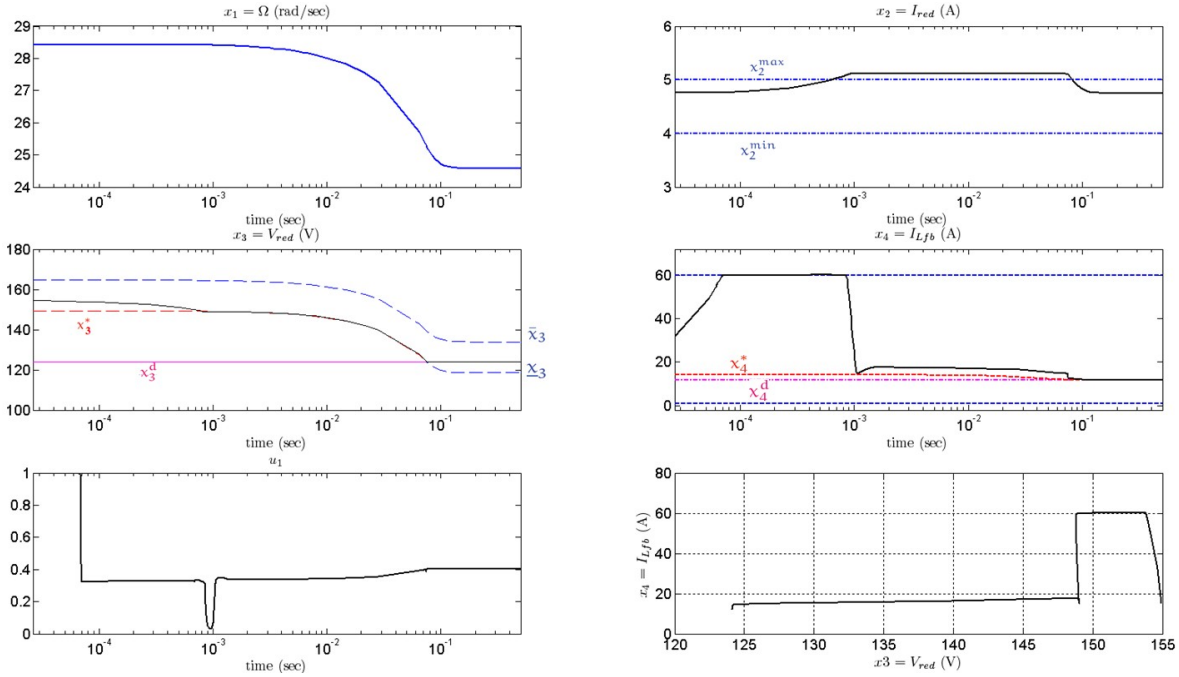

Figure 6.9: Same scenario as the one depicted on Figure 6.5 using logarithmic scale on the time axis in order to show the beginning of the scenario. This scale enables the saturation on x_4 to be clearly shown.

bus voltage is tightly regulated while the supercapacitor voltage is restored as soon as the constraints on the different control and state variables enable it.

6.5 Conclusion

In this chapter, a global constrained control framework is proposed for the stand-alone hybrid (stirling engine)/supercapacitor power generation system. The control architecture explicitly handles saturations on the control variables as well as on the components of the state vector. The resulting closed-loop behavior can be used in the design step where the choice of the components and the class of power demand profiles have to be investigated. This is because such choices highly impact the size of the supercapacitor that can afford the different power demand profiles.

Beyond the specific system that has been considered in the present paper, it is our claim that the control design methodology can be extended to a wide variety of power conditioning stages that can be encountered even when other thermodynamic cycles and/or different storing devices are used.

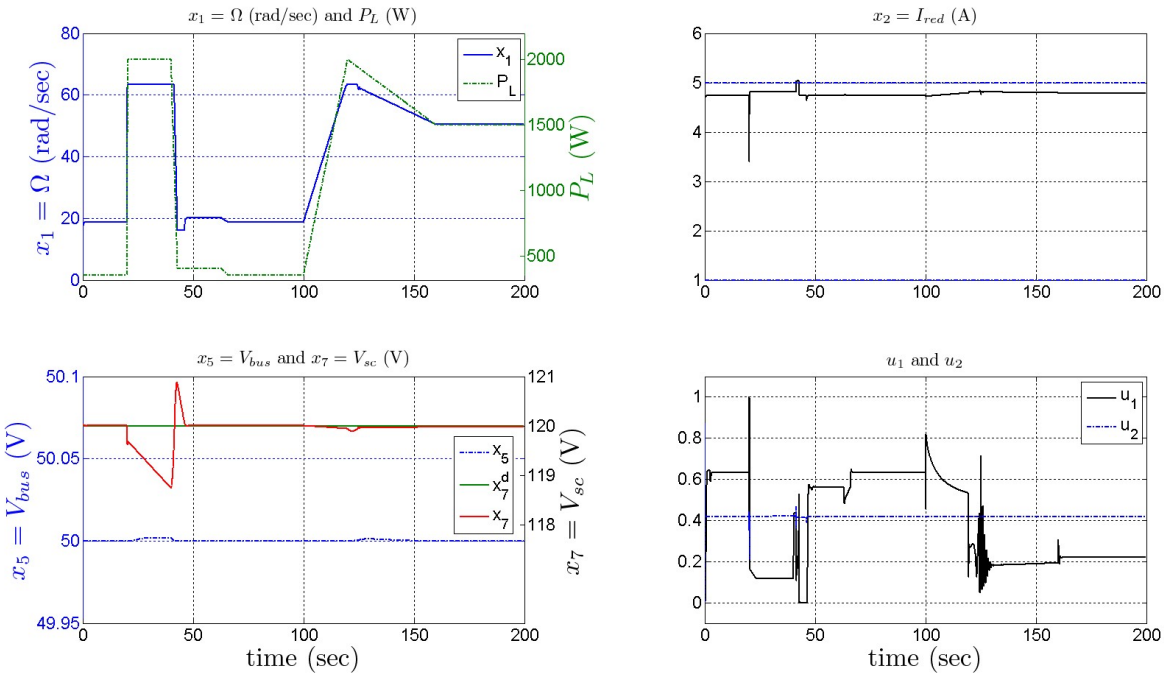

Figure 6.10: Performance of the overall closed-loop system under varying power load demand. Case where $x_2^{max} = 5$. This scenario is worth comparing with the scenario depicted in Figure 6.11 where the upper bound $x_2^{max} = 4.8$ is used.

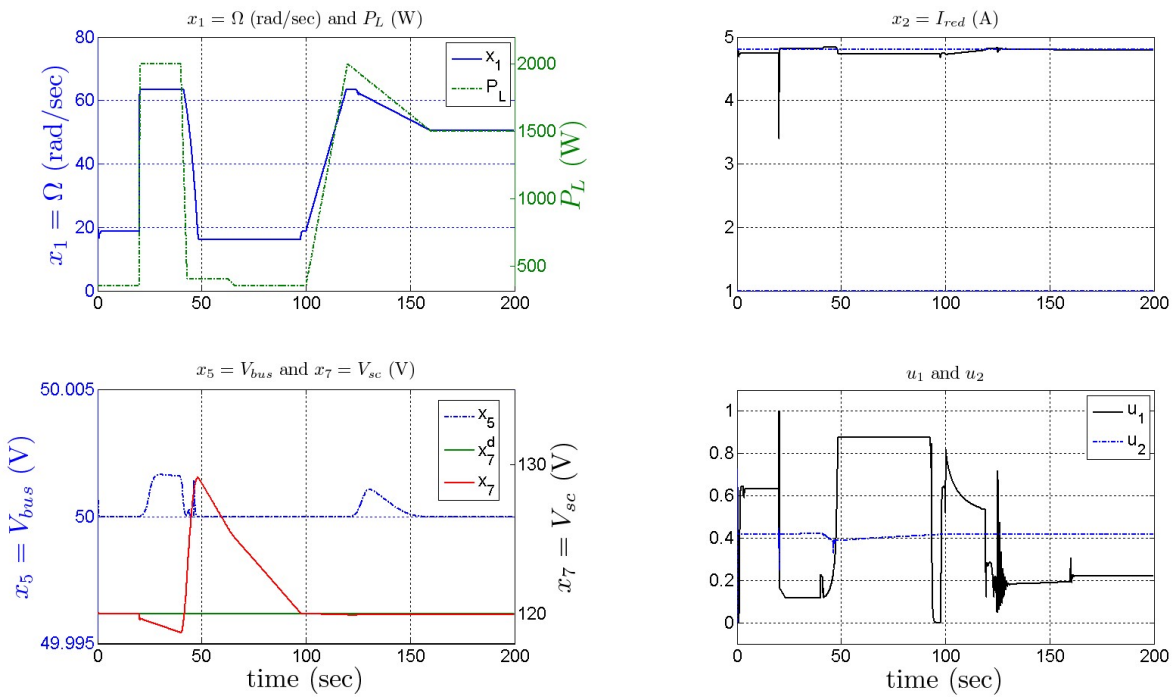

Figure 6.11: Performance of the overall closed-loop system under varying power load demand. Case where $x_2^{max} = 4.8$. This scenario is worth comparing with the scenario depicted in Figure 6.10 where the upper bound $x_2^{max} = 5$ is used.

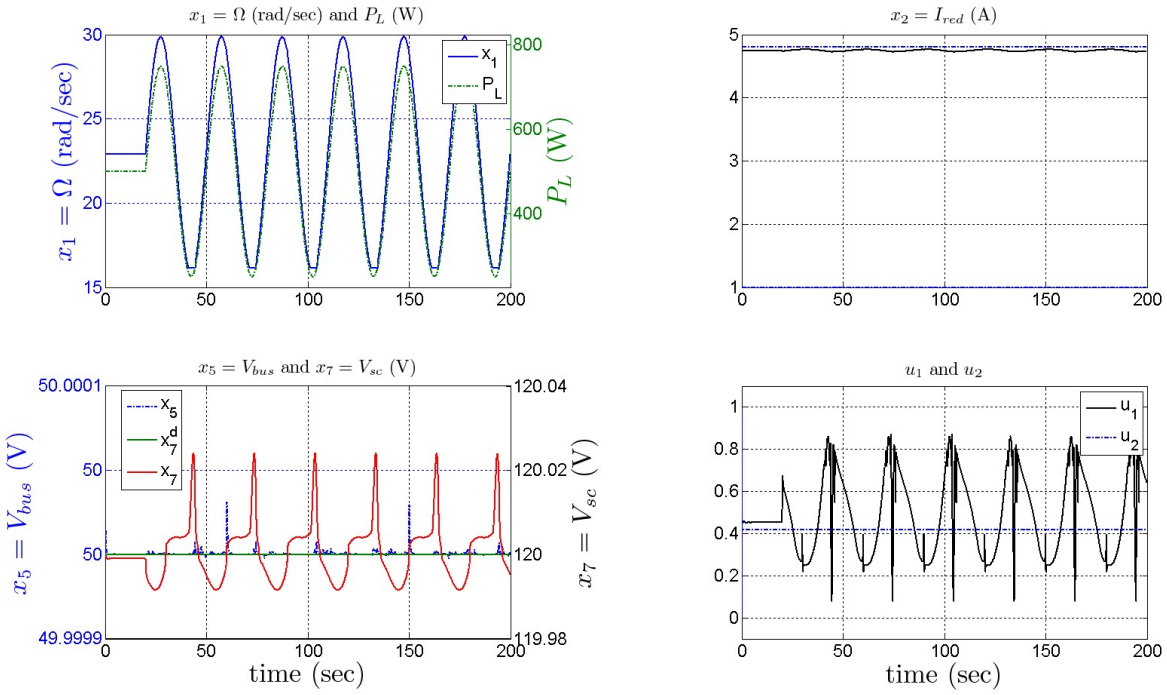

Figure 6.12: Performance of the overall closed-loop system under sinusoidal power load demand.

Part II

Modeling, Simulation and control of an Off-Grid Organic Rankine Cycle (ORC) based Solar Thermodynamic Micro Power Plant.

Introduction

As discussed in Section 1.1, the final prototype of the solar thermodynamic micro power plant selected by Schneider Electric consists in having an Organic Rankine Cycle (ORC) power plant as thermodynamic machine transforming the water heat into electricity. This ORC turbine was regulated by EXOES (which is one of the MICROSOL project partners) using PI based controllers associated to static maps (for feedforward terms) determined experimentally off-line. Two main drawbacks were identified on the control methodology used by EXOES. The first drawback is the slow response time of the turbine while moving from an operating point to another during load power demand changes. Indeed, this impacts significantly the sizing of the energy buffer consisting in the battery banks that adapts the power consumed by the loads during transients. The other drawback is the way the maps that determine the feed-forward terms are computed. Indeed, the methodology consists in browsing experimentally all the possible static operating points (obviously by mean of an adequate step values) and selecting the optimal ones in term of turbine efficiency and minimum auxiliaries consumption. although this methodology is the most commonly used by the thermal engineers since it is experience-based, it is very time consuming and it has to be repeated each time a serious modification is performed on the ORC cycle.

In the next chapters, we present a control methodology that tackles the aforementioned drawbacks. The methodology consists in first identifying a control oriented nonlinear dynamic model of the ORC power plant using real data gathered on the prototype, then an optimal controller in terms of settling time and minimum consumption respecting the system constraints will be designed based on the identified models. Among the advantages of the proposed methodology, the response time of the system is significantly decreased which has a very good impact on the battery sizing. Indeed, the time response obtained by EXOES using their PI-based control methodology was about 30 s (to respond to a 1kW electrical power demand) while this response time was reduced by half according to simulation results obtained using the proposed constrained optimal control strategy. The proposed methodology can also be viewed as a quasi systematic method for regulating this kind of thermodynamic engines while reducing the necessary time for developing the control laws compared to the traditional methods.

Chapter 7

Nonlinear Dynamic Model Identification of an ORC power plant

Contents

7.1 Presentation of the ORC power plant prototype 110

7.2 Control objectives and system constraints 113

7.3 Brief state of the art on physical and semi physical ORC power plants dynamic models 115

7.4 Wiener Models based Identification Structure 117

7.4.1 Presentation of the methodology 117

7.4.2 Application of the identification framework to the ORC power system . . 119

7.4.3 Identification Results 120

7.5 State Space representation of the ORC power plant identified dynamic models 122

7.5.1 Nonlinear State Space Model of the ORC power plant 122

7.5.2 ORC Model Linearization 131

7.5.3 Filtering control variables 132

7.6 Conclusion 133

In this chapter, an identification framework recently developed in [Alamir et al., 2014c], that was used to derive a nonlinear black-box model of a beta-type Stirling engine with rhomic-drive mechanism, is presented. The simulation results presented in [Alamir et al., 2014c] have shown good agreement between the knowledge-based model (used as a data generator) and the identified model all the more that this last one was very fast to simulate which is a very interesting feature for the identified nonlinear models. This identification framework will be applied in this chapter to derive nonlinear maps for each variable of interest for the ORC power plant under study. Then, a state space representation is derived from these nonlinear maps and a linearized model that approximates the nonlinear one is obtained and used in the controller design presented in Chapter 8.

In the literature, one can find many identification frameworks that deal with nonlinear models like Wiener-Hammerstein, Volterra Serries based formulations (see [Doyle et al., 2001]) and many others. However, the adopted identification framework stands out from the others by its simplicity in term of model complexity and by the fact that it results in solving a

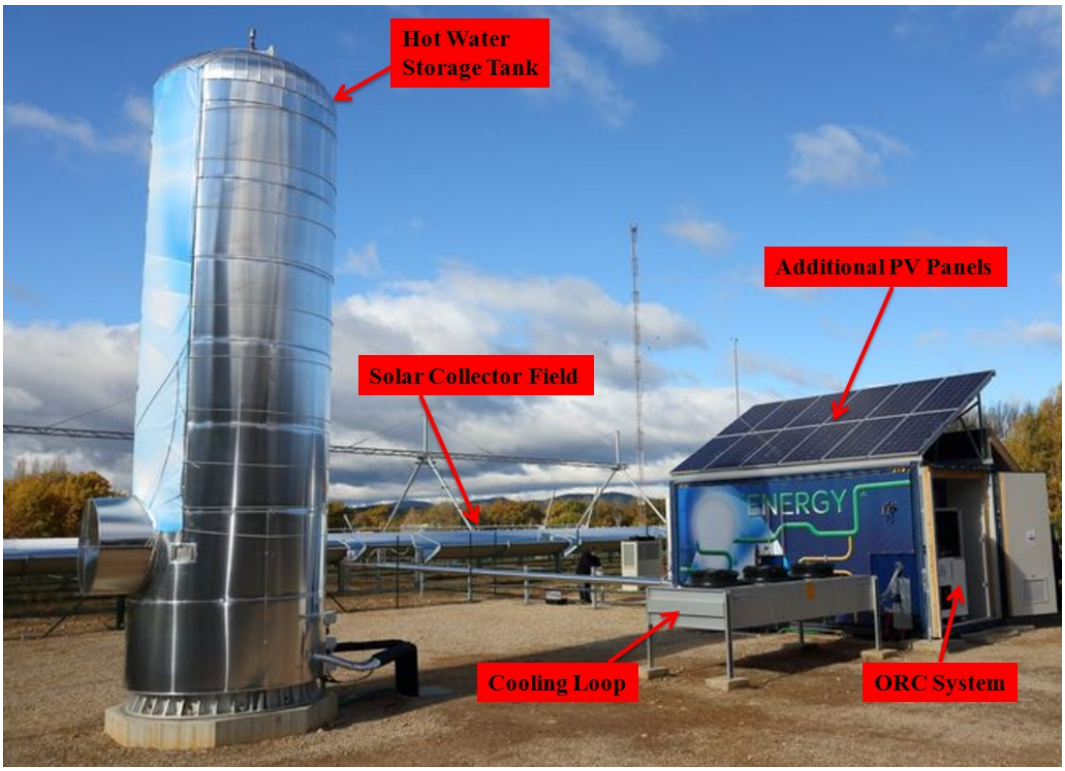

Figure 7.1: Picture of the ORC power plant prototype

Quadratic Programming (QP) problem which is quite easy to solve online, then enabling the models to be updated during the system lifetime which is an interesting feature while performing online system diagnosis for example.

This chapter is organized as follows: first, the ORC system under consideration, its principle of functioning, the control objectives and system constraints are presented, then a brief review on modeling such systems is given. Thereafter, the adopted Wiener-based identification framework is discussed and the identification results on the ORC power plant prototype are given and analyzed to assess the performance of the identification framework. Finally, a state space model of the ORC system under consideration is derived.

7.1 Presentation of the ORC power plant prototype

The solar thermodynamic micro power plant under consideration that is depicted in Figure 7.1 is a prototype that aims at producing both electricity (thanks to an ORC system) and drinking water (thanks to an appropriate water desalination system provided by a project partners). A set of photovoltaic (PV) panels are also present as a second energy source (which is crucial during the starting procedure). In this work, we focus on the study of the electrical energy production thanks to the ORC process depicted in Figure 2.6 and whose schematic

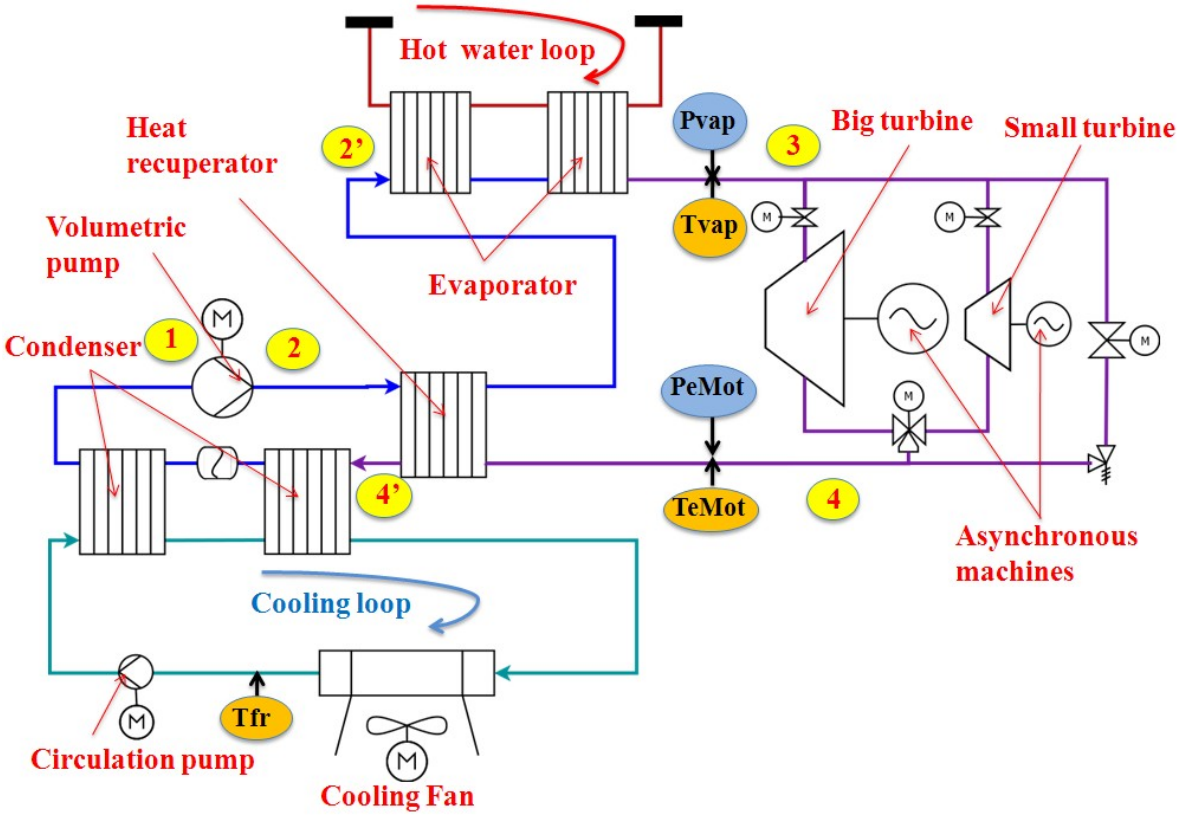

Figure 7.2: Schematic of the Organic Rankine Cycle Power Plant.

is depicted in Figure 7.2 while its corresponding Rankine cycle in the Temperature-Entropy (T-S) diagram is depicted in Figure 7.3.

As for the Stirling engine based power plant, the ORC system consists in a hot water loop (hot source) and a cooling loop (cold sink) interfaced through heat exchangers to an internal loop wherein flows the working fluid (R245Fa organic fluid).

The hot water loop (top of Figure 7.2) whose elements are not represented in Figure 7.2 consists of a pump that makes the hot water circulating between the evaporator and a storage tank. Another loop (which is out of the scope of this work) enables hot water to circulate between the storage tank and the solar collector field. The cooling loop, on the other hand, enables a water-glycogen mixture to circulate in order to absorb heat from the internal loop (cold sink). The main elements of this loop are the circulation pump and the cooling fan.

The principle of operation of this ORC power plant can be described using both the T-S diagram of Figure 7.3 and the schematic of Figure 7.2. Staring at the volumetric pump inlet (point 1 of Figure 7.2 and Figure 7.3), the working fluid is in subcooled liquid state. This fluid undergoes an isentropic (meaning some pump efficiency) increase in pressure through the volumetric pump to end up at point 2. The fluid then absorbs through the heat recuperator (that enhances the cycle efficiency) between points 2 and $2^{'}$ a certain quantity of heat released

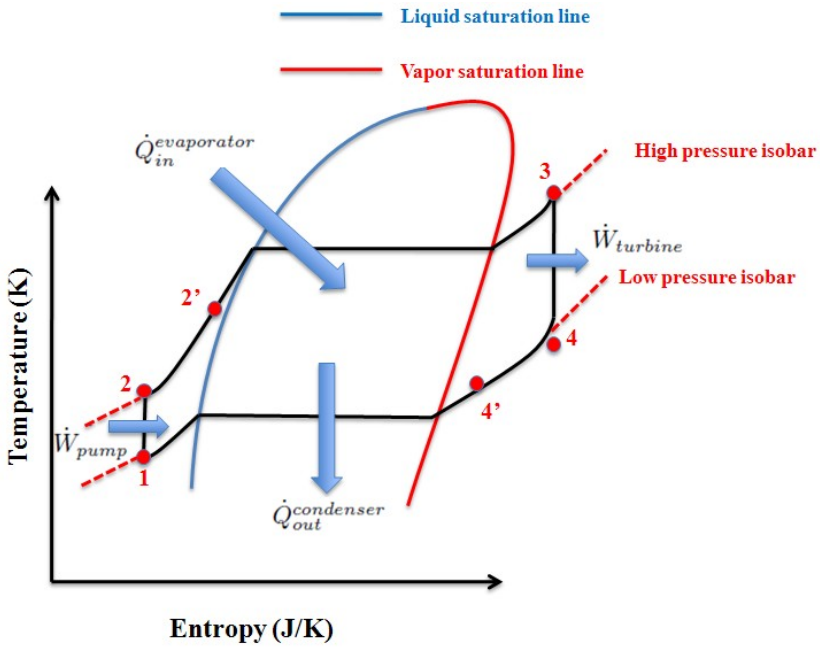

Figure 7.3: Temperature-Entropy (T-S) diagram of the Organic Rankine Cycle Power Plant.

by the same fluid at the output of the turbine and then enters the evaporator where it absorbs heat from the hot water (Hot water loop) between points $2^{'}$ and 3. During this step, the working fluid is heated and brought to its liquid saturation line where it continues absorbing heat in two-phase thermodynamic state (mixture of liquid and vapor in thermodynamic equilibrium). In the last stage of this step, the fluid is superheated to avoid the presence of droplets in the turbine (which can be damageable). At point 3 the working fluid is at the inlet of the "scroll" turbine (see [Quoilin, 2011] for more details) and undergoes an isentropic expansion between points 3 and 4 resulting in an output mechanical work $W_{turbine}$ used to drive an asynchronous generator producing an electrical power P_{elec} that is conditioned through an appropriate power electronics (not represented in Figure 7.2). Finally the working fluid begins its condensation by first releasing a quantity of heat between points 4 and $4^{'}$ through the heat recuperator (the same quantity of heat absorbed between points 2 an $2^{'}$) and enters the condenser where it releases heat to the external cooling loop to end up with a subcooled liquid at the input of the volumetric pump.

As it can be seen in Figure 7.2, the ORC system prototype consists in two scroll turbines: a big turbine (15 kW nominal power) and a small turbine (4 kW nominal power and 5kW maximum power). The two turbines can work either alone or in parallel. In the next sections, we focus our study (model identification and control) on the small turbine (the big turbine being disconnected from the hydraulic circuit). Since the two turbines are from a similar nature, the same analysis can be performed with the big turbine.

7.2 Control objectives and system constraints

The ORC power plant is designed to operate either in grid-connected mode or in off-grid mode. A supervisor (which is out of the scope of this study) that manages the load consumption and the transition between the two modes of operation generates an electrical power reference P_{elec}^{ref}, based on the batteries SOC (State Of Charge), that the ORC power plant has to track acting on the pumps (volumetric pump, hot water pump and circulation pump) and the cooling fan. The response time of the ORC system in tracking this power setpoint is crucial for the battery sizing especially when the system performs in off-grid mode since the battery banks dynamically meet the load power demand while the ORC turbine adapts its produced power P_{elec} in a rather medium time scale.

The ORC system is subject to a set of constraints in term of minimum and maximum temperatures, pressures and actuator limitations. These constraints are as follows:

- The fluid at the inlet of the turbine has to be in superheated vapor state with a superheating $3°C < \Delta T_{vap} < 15°C$ such that:

$$\Delta T_{vap} = T_{vap} - T_{sat}(P_{vap}) \tag{7.1}$$

  where $T_{vap} \in [85°C, 135°C]$ and $P_{vap} \in [8bar, 25bar]$ are respectively the temperature and the pressure of the working fluid at the outlet of the evaporator (inlet of the turbine) and $T_{sat}(P_{vap})$ is the saturation temperature of the working fluid (which is a function of the evaporation pressure) whose values will be given by thermodynamic tables for the R245Fa fluid provided by the REFPROP® software (`http://www.nist.gov/srd/nist23.cfm`). This constraint is crucial since it avoids droplets to be present at the input of the turbine.

  Note that $T_{sat}(P_{vap})$ can be calculated online using the following fourth order polynomial fitted by REFPROP® data (see Figure 7.4):

$$T_{sat}(P_{vap}) = -0.0003.P_{vap}^4 + 0.023.P_{vap}^3 - 0.79.P_{vap}^2 + 14.32.P_{vap} + 279.49 \tag{7.2}$$

- The temperature and pressure at the outlet of the turbine respectively $TeMot$ and $PeMot$ has to be such that $TeMot < 110°C$ and $1.7bar < PeMot < 7bar$. The upper bound on $PeMot$ is due to the mechanical restrictions on the volumetric pump while the lower bound insures that the the working fluid at the outlet of the condenser is in subcooled state to avoid pump cavitation.

- The temperature of the cooling fluid (water glycol) at the output of the cooling fan T_{fr} must be such that $30°C < T_{fr} < 80°C$.

Moreover, the ORC power plant is subject to the following input measured disturbances (exogenous signals):

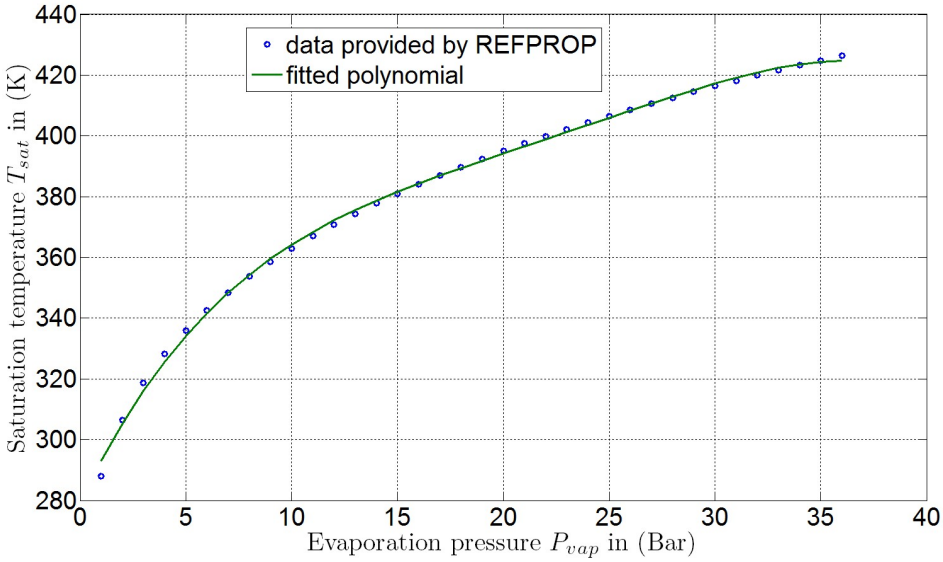

Figure 7.4: comparaison between the fitted polynomial for $T_{sat}(P_{vap})$ with the data provided by REFPROP®.

- $TaCh$: temperature in Kelvin of the hot water at the inlet of the evaporator (hot water side).
- T_{amb}: ambient temperature in Kelvin.

The control variables (manipulated variables) used to achieve the control objectives while respecting the previous constraints are defined below together with their domain of variation:

- $f_{pump} \in [1, 50]$ (Hz): rotational frequency of the motor pump (volumetric pump).
- $\dot{V}_{hot} \in [0, 6000]$ (L/h): volume flow rate setpoint for the hot water side pump.
- $V_{rot}^{aero} \in [10, 100]$: rotational speed of the ventilator in (%) relative to its maximal value.
- $V_{rot}^{circ} \in [5, 100]$: rotational speed of the circulation pump (cold side) in (%) relative to its maximal value.

These control variables have also to be penalized in the expression of the cost function in order to minimize the electrical consumption of the auxiliaries.

To summarize, the control objective for the ORC power plant is to track some defined electrical reference power P_{elec}^{ref} while minimizing the consumed power in the auxiliaries (pumps

and fans) and respecting the following set of constraints:

$$3°C \leq \Delta T_{vap} \leq 15°C \tag{7.3a}$$
$$85°C \leq T_{vap} \leq 135°C \tag{7.3b}$$
$$8bar \leq P_{vap} \leq 25bar \tag{7.3c}$$
$$TeMot \leq 110°C \tag{7.3d}$$
$$1.7bar \leq PeMot \leq 7bar \tag{7.3e}$$
$$30°C \leq T_{fr} \leq 80°C \tag{7.3f}$$
$$1 \leq f_{pump} \leq 50Hz \tag{7.3g}$$
$$0 \leq \dot{V}_{hot} \leq 6000l/h \tag{7.3h}$$
$$10\% \leq V_{rot}^{aero} \leq 100\% \tag{7.3i}$$
$$10\% \leq V_{rot}^{circ} \leq 100\% \tag{7.3j}$$

Before designing a controller that achieves the previous control objectives while respecting the constraints, a model for the ORC power plant under consideration has to be derived. In the literature, one can find many papers that deal with such problem as it is discussed in Section 7.3.

7.3 Brief state of the art on physical and semi physical ORC power plants dynamic models

Because of their simplicity and the availability of their components, ORC systems have been widely used in many applications essentially in solar thermal and waste heat recovery (WHR) applications. One can find in the literature many papers that deal with the optimal sizing of such systems (see [Quoilin, 2011, Quoilin et al., 2011b] for example) but few documents exist that deal with dynamic modeling and control of ORC power plants. In [Quoilin et al., 2011a], a physical modeling of a small scale ORC power plant for waste heat recovery was proposed focusing on the dynamic modeling of a simple evaporator which is one of the main element (and most difficult to model) in the ORC system. Since the model developed in [Quoilin et al., 2011a] is too computationally heavy, it was not dedicated to real time control but was implemented in Modelica® to serve as a simulator. A static model was also derived to compute feedforward terms that optimize the static ORC efficiency while simple tunable PID based controllers were used to reach the control objectives. Since the heat exchangers, especially the evaporator, is the most challenging part to model in the ORC power plant, many papers can be found that deal with this problem. Two main paradigms exist to model the evaporator: the finite volume (FV) paradigm and the Moving Boundary (MB) paradigm. In [Quoilin et al., 2011a] the finite volume paradigm was used to model a simple evaporator consisting of a hot fluid and a cold fluid (working fluid) channels separated by a wall. The evaporator was decomposed in a set of finite volumes where the mass, energy and heat balances were applied to each finite volume resulting in a large number of nonlinear ordinary differential equations. In [Feru et al., 2013], the same paradigm was applied to model a simple evaporator

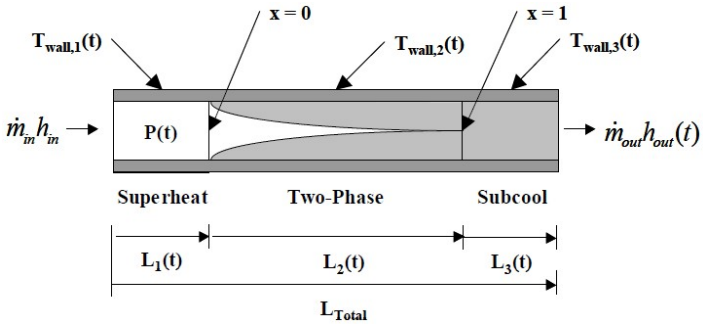

Figure 7.5: Moving Boundary paradigm applied to a condenser [Shah et al., 2003].

(for diesel engines WHR applications), but instead of using external thermodynamic tables (as in [Quoilin et al., 2011a]) data fitted polynomials were used.

Concerning the Moving Boundary (MB) paradigm depicted in Figure 7.5, it consists in decomposing the evaporator (or the condenser) into three regions (liquid, two phase and superheated) whose length is made time dependent and for each region a mass and energy balance is applied to end up with the following nonlinear state space representation (see [Shah et al., 2003, Rasmussen and Alleyne, 2006, Peralez et al., 2012] for more details):

$$Z(x,u).\dot{x} = f(x,u) \tag{7.4}$$

In [Shah et al., 2003, Rasmussen and Alleyne, 2006] for example, the authors decided to take for the condenser model a state vector $x(t)$ that depends on the pressure, the regions lengths, the output enthalpy and the wall temperatures for each region. In [McKinley and Alleyne, 2008], the author proposed a switching model methodology that tackles the problem of model instability that occurs when one of the thermodynamic state for the working fluid becomes much smaller compared to the other thermodynamic phases (which makes $Z(x,u)$ of 7.4 non invertible).

Concerning the models of the other components, [Quoilin, 2011, Twomey et al., 2013] proposed a static models for the scroll expander and the pump that resulted in a large number of parameters to be identified offline using experimental data.

In our approach, we do not consider such physical or semi physical modeling approaches that typically lead to complex and parameter sensitive models. We prefer using a model identification approach that leads to a parsimonious model which means a model that incorporates only the necessary elements needed to design the feedback law. These models can also serve to build fast simulators for the ORC power plants.

Hence, Section 7.4 presents the proposed nonlinear identification framework used to derive nonlinear relationships that link each of the variables of interest: regulated variable P_{elec} and constrained variables (ΔT_{vap}, T_{vap}, P_{vap}, $TeMot$, $PeMot$ and T_{fr}) to some or all of the system control variables (f_{pump}, $\dot{V}_{hot}$, V_{rot}^{aero} and V_{rot}^{circ}) and the exogenous signals (uncontrolled measured input disturbances) $TaCh$ and T_{amb}.

7.4 Wiener Models based Identification Structure

In this section the identification framework introduced in ([Alamir, 2013], [Alamir et al., 2014a] and [Alamir et al., 2014c]) will be used to derive nonlinear dynamic models for the ORC power system under study. One of the major advantages of this identification methodology is that it results in solving a QP problem and ending up with an easy to use nonlinear model as it can be seen in later sections.

7.4.1 Presentation of the methodology

Consider the identification problem consisting in finding a nonlinear map $E(.)$ that links some desired identified variable $q(i)$ to some: state vector $x(i)$, control vector $u(i)$ and a vector of measured uncontrolled signals $w(i)$. Then, one has to find $E(.)$, such that:

$$q(i.\tau_s) = q(i) \approx E(x(i), u(i), w(i)) \tag{7.5}$$

where τ_s is the sampling period of the signals.

As for many identification methods, one has to define some regressor $Z(i)$ that contains the following extended vector: $U(i) = \begin{pmatrix} x(i) & u(i) & w(i) \end{pmatrix} \in \mathbb{R}^{n_U}$ and its $(N-1)$ past values (N being the regressor buffer length) as follows:

$$Z(i) = \begin{pmatrix} U(i) \\ U(i-m) \\ \vdots \\ U(i-(N-1).m) \end{pmatrix} \in \mathbb{R}^{n_z} \; ; n_z = N.n_U$$

then (7.5) can be rewritten in term of a new nonlinear map $F(.)$, that has to be found, as follows:

$$q(i) \approx F(Z(i)) \tag{7.6}$$

where n_U is the length of the vector $U(i)$ and m is some under sampling integer.
Suppose now, that one has N_{data} learning data samples used during the identification process. The identification problem can be defined as follows:

Definition 7.1
Given the learning data:

$$\Big\{(q(i), Z(i))\Big\}_{i=1}^{i=N_{data}} \qquad ; \qquad \mathbb{K} = \{1, \ldots, N_{data}\}$$

the identification problem consists in finding a map $F : \mathbb{R}^{n_z} \to \mathbb{R}$ that approximately maps Z to q in a least squares sense, namely

$$\min_F \sum_{i \in \mathbb{K}} \|q(i) - F(Z(i))\|^2 \tag{7.7}$$

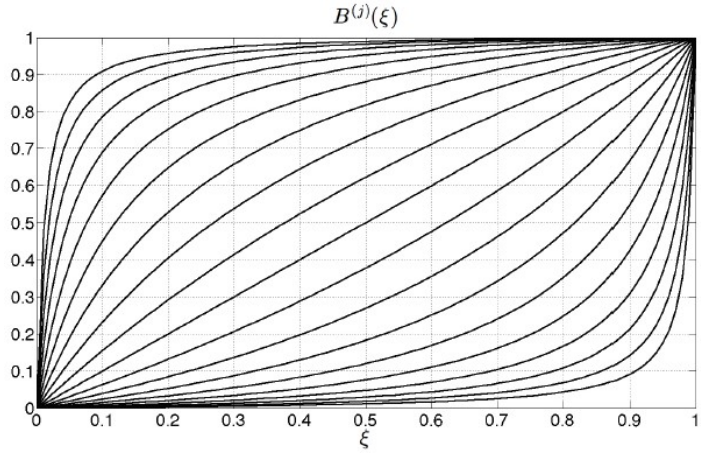

Figure 7.6: Allure of the maps $B^j(.)$ for $\beta = 0.5$ and $n_m = 10$.

In the literature, one can find many nonlinear structures for the map $F(.)$. In the present work, we constrain $F(.)$ to take the following form:

$$F(Z) = \Gamma^{-1}(Z^T.L); \quad \Gamma(.) \ \textit{streactly increasing} \tag{7.8}$$

Where $L \in \mathbb{R}^{n_z}$ is a parameter vector to be identified together with the nonlinear function $\Gamma(.)$. The restriction regarding the monotonicity of $\Gamma(.)$ comes from the need for this function to be invertible. Thus, applying the function, $\Gamma(.)$ to each side of (7.8) results in:

$$\Gamma(q) \approx Z^T.L \tag{7.9}$$

In [Alamir et al., 2014a], it has been chosen to parametrize $\Gamma(.)$ using the following structure:

$$\Gamma(q) = \sum_{j=1}^{n_b} \Big[B^j(\xi(q))\Big].\mu_j; \quad \xi(q) := \frac{q - q_{min}}{q_{max} - q_{min}} \quad \in [0,1] \tag{7.10}$$

where q_{min} and q_{max} are the minimum and maximum values of q over the learning data and μ_j the set of parameters to be identified .The set of function basis $B^j(.)$ defined on $[0,1]$ are given by:

$$\{B^j\}_{j=1}^{j=n_b} = \{1\} \cup \{B_1^l\}_{l=1}^{n_m-1} \cup \{B_2^l\}_{l=1}^{n_m} \tag{7.11}$$

in which $n_b = 2n_m$ is the number of functions in the basis and:

$$B_1^l(\eta) = (1+\alpha_l).\frac{\eta}{1+\alpha_l.\eta} \ ; \ B_2^l(\eta) = \frac{\eta}{1+\alpha_l.(1-\eta)} \tag{7.12}$$

where the coefficients α_l are given by: $\alpha_l = \exp^{\beta.(l-1)} - 1$ for some constant $\beta > 0$. Figure 7.6 shows the allure of these maps for $\beta = 0.5$.

By putting (7.10) in the following matrix form:

$$\Gamma(q) = \Big[B(\xi(q))\Big].\mu \tag{7.13}$$

Where $B(\xi(q)) \in \mathbb{R}^{1\times n_b}$ is the vector whose elements are all the $\{B^j(\xi(q))\}_{j=1}^{j=n_b}$ and $\mu \in \mathbb{R}^{n_b}$ is the vector of parameters to be identified, (7.9) can be transformed into:

$$\Big[B(\xi(q)), -Z^T\Big].\begin{pmatrix}\mu\\ L\end{pmatrix} \approx 0 \tag{7.14}$$

which has to be solved in a least squares sense under the following constraints on μ:

- Constraints ensuring that $\Gamma(.)$ is strictly increasing:

$$\forall\xi \in [0,1], \quad \Big[\frac{\mathrm{d}B(\xi)}{\mathrm{d}\xi}\Big].\mu \geq \epsilon \tag{7.15}$$

  for some $\epsilon > 0$

- Normalization constraint to avoid the trivial solution: $\mu = 0$ and $L = 0$:

$$\Big[\int_0^1 B(\xi)\mathrm{d}\xi\Big].\mu = \frac{q_{min} + q_{max}}{2} \tag{7.16}$$

By defining a sufficiently dense grid of ξ values on $[0,1]$, (7.15)-(7.16) can be transformed into a finite set of linear constraints which together with (7.14) define the QP problem that has to be solved to derive the optimal parameters namely: $\hat{L} \in \mathbb{R}^{n_z}$ and $\hat{\mu} \in \mathbb{R}^{n_b}$

Note that the total number of model parameters for each nonlinear map is:

$$n_p = n_b + n_z = 2n_m + n_z \tag{7.17}$$

Note also that a good indicator for the degree of compactness of the learning data into the identified nonlinear map is given by the compression factor which is equal to:

$$compressionfactor = \frac{N_{data}}{n_p} \tag{7.18}$$

7.4.2 Application of the identification framework to the ORC power system

Now that we have defined in Section 7.4.1 the identification framework, we will apply this methodology to the case of the ORC power plant described in Section 7.1. But before going further into details, it is important to emphasize an interesting feature regarding our ORC system that holds also for any thermodynamic machine in general. This feature concerns the inherent open-loop stability of such systems. Indeed, for a given value of the control vector,

the ORC system will always converge to some steady state, not necessarily the desired one, but a stable state anyway. Then, one can exploit an interesting feature of open-loop stable systems which is the asymptotic disappearance of the initial state effect as time progresses which implies that the ORC system state vector $x(i)$ can be approximated as a function of the input profiles (controlled and uncontrolled signals) during the last N samples, provided that N is chosen sufficiently high and the sampling period sufficiently small, as follows:

$$x(i) = G\Big(u(i), u(i-1)...u(i-N+1)\Big) \tag{7.19}$$

This implies that for each variable of interest y to be identified which could be the regulated variable P_{elec} or one of the constrained variables (ΔT_{vap}, T_{vap}, P_{vap}, $TeMot$, $PeMot$ and T_{fr}), one can identify a nonlinear relationship that links $y(i)$ to some regressor $Z^y(i)$ that depends only on the vector $u^y(i)$ (n_u^y dimentional vector containing some controlled and uncontrolled measured signals) and its $(N^y - 1)$ past values such that:

$$Z_y(i) = \begin{pmatrix} u^y(i) \\ u^y(i-m) \\ \vdots \\ u^y(i-(N^y-1).m) \end{pmatrix} \in \mathbb{R}^{n_z^y} \quad ; \quad n_z^y = N^y.n_u^y \tag{7.20}$$

To perform the identification task, we have in our disposal experimental data sampled at $\tau_s = 1s$ coming from two experiments namely "Experiment 1" and "Experiment 2" performed on the ORC prototype. For each variable y to be identified, we combine a data subset of "Experiment 1" and a data subset of "Experiment 2" to generate the set of learning data $\Big\{(y(i), Z_y(i))\Big\}_{i=1}^{i=N_{data}}$ while the whole data set will serve as validation data. These learning data have to contain the maximum and minimum values of the whole data set in order to make the identified models valid on this range. Figure 7.7 and Figure 7.8 show the input variables for Experiment 1 and Experiment 2 respectively. These variables will be used in the definition of the regressor for each identified variable.

7.4.3 Identification Results

For each variable of interest to be identified, namely P_{elec}, T_{vap}, P_{vap}, T_{fr}, $PeMot$, $TeMot$ and ΔT_{vap}, one has to build a regressor as defined in (A.8) used in the identification process. The following input vectors were chosen to construct the regressors for the identified variables:

$$u^{T_{vap}}(i) = \begin{pmatrix} f_{pump} & \dot{V}_{hot} & TaCh & T_{amb} \end{pmatrix}^T \tag{7.21a}$$

$$u^{P_{vap}}(i) = u^{T_{vap}}(i) \tag{7.21b}$$

$$u^{P_{elec}}(i) = \begin{pmatrix} f_{pump} & \dot{V}_{hot} & V_{rot}^{aero} & V_{rot}^{circ} & TaCh & T_{amb} \end{pmatrix}^T \tag{7.21c}$$

$$u^{T_{fr}}(i) = u^{PeMot}(i) = u^{TeMot}(i) = u^{P_{elec}}(i) \tag{7.21d}$$

By performing several identification tests, the parameters of Table 7.1 gave the best iden-

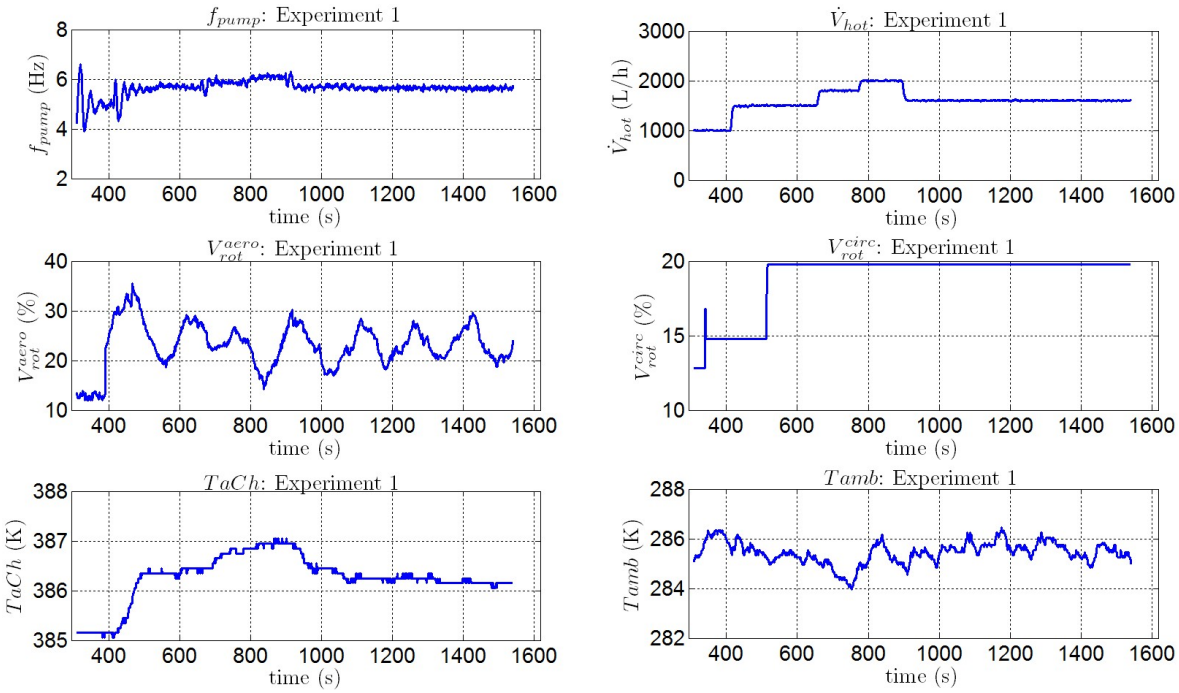

Figure 7.7: Control and exogenous variables profiles during Experiment 1.

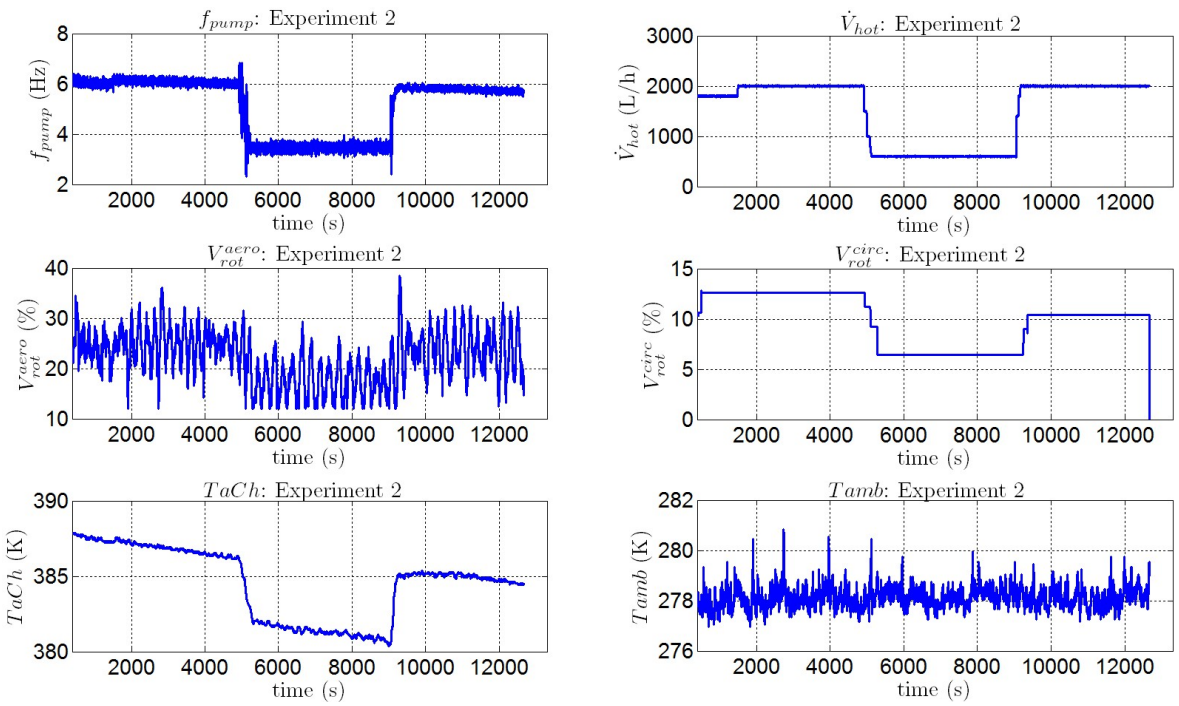

Figure 7.8: Control and exogenous variables profiles during Experiment 2.

Table 7.1: The identified parameters used to define the nonlinear maps for ΔT_{vap}, T_{vap}, P_{vap}, P_{elec}, T_{fr}, $PeMot$ and $TeMot$

	n_m	β	N	m	n_u	n_z	n_p	$CompressionFactor = \frac{N_{data}}{n_p}$
ΔT_{vap}	3	0.5	10	1	4	40	46	54
T_{vap}	4	0.5	10	1	4	40	48	44
P_{vap}	4	0.5	4	1	4	16	24	96
P_{elec}	4	0.5	6	1	6	36	44	52
T_{fr}	2	0.5	5	1	6	30	34	78
$PeMot$	2	1	4	1	6	24	26	92
$TeMot$	3	1	10	1	6	70	76	55

tification results (refer to Section 7.4.1 for the parameters definition) as it can be seen from Figures 7.9a-7.11a and 7.12-7.15 that compare the time profiles of the experimental and identified variables of interest (namely: T_{vap}, P_{vap}, P_{elec}, T_{fr}, $PeMot$, $TeMot$ and ΔT_{vap}) on the whole data set for both experiments. One can observe from Figures 7.9a-7.11a and 7.12-7.15 that a good matching is obtained between the experimental data and the identified nonlinear models for the variables of interest. Note that the learning data used to derive the nonlinear maps during the identification process are plotted in red color.

The models resulting from the identification of the maps for T_{fr}, $PeMot$, $TeMot$ and ΔT_{vap} were linear. However, concerning the variables T_{vap}, P_{vap} and P_{elec}, nonlinear models were needed to capture the nonlinear character of the relationship for these variables as illustrated in Figures 7.9b-7.11b where the shapes of the nonlinear maps and their corresponding gradients (to assess the degree of nonlinearity) for the nonlinear models of T_{vap},P_{vap} and P_{elec} respectively were plotted.

In the next section, the identified nonlinear maps for each variable of interest will serve to derive a nonlinear state space model for the ORC power plant under consideration. Then a linearized model of the system will be obtained to be used in the design of the constrained optimal controller as explained in Chapter 8.

7.5 State Space representation of the ORC power plant identified dynamic models

7.5.1 Nonlinear State Space Model of the ORC power plant

Consider the generic variable $y(i)$ that could be one of the following variables of interest: regulated variable P_{elec} or constrained variables (ΔT_{vap}, T_{vap}, P_{vap}, $TeMot$, $PeMot$ and T_{fr}) that have been previously identified by the following nonlinear map:

$$y(i.\tau_s) = y(i) = F_y(Z_y(i)) = \Gamma_y^{-1}(Z_y^T(i).L_y) \tag{7.22}$$

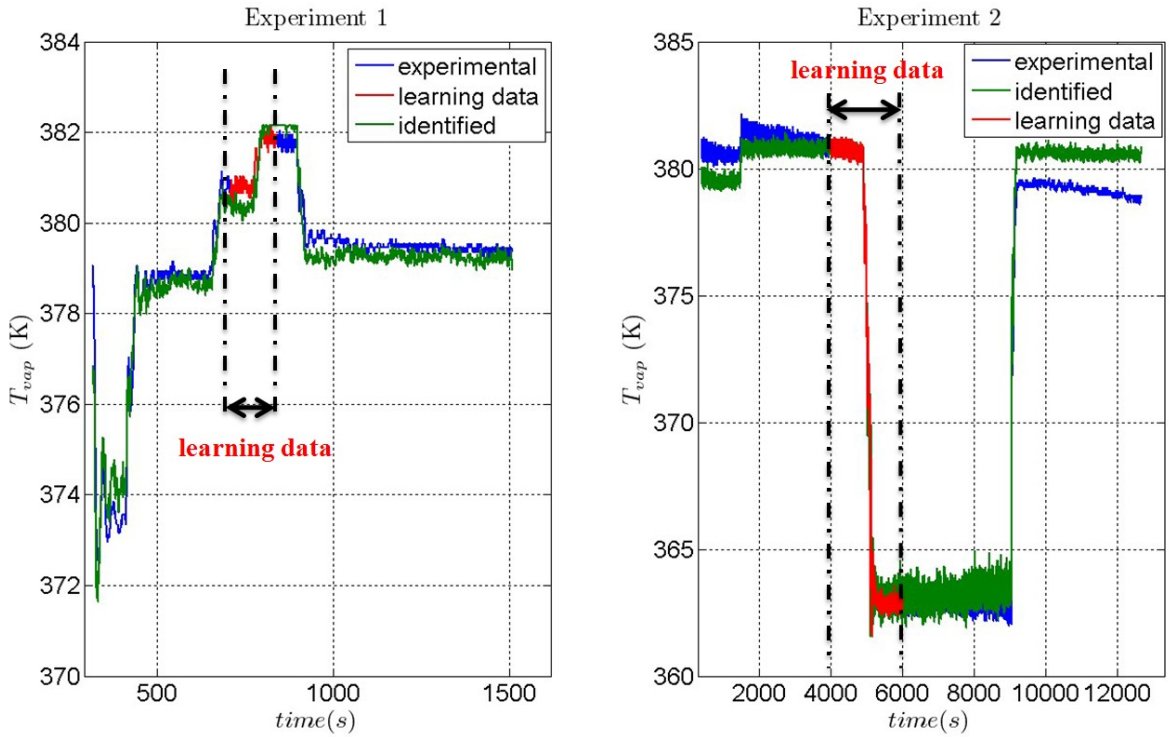

(a) Time profiles of the identified and the experimental T_{vap} on the learning and validation data.

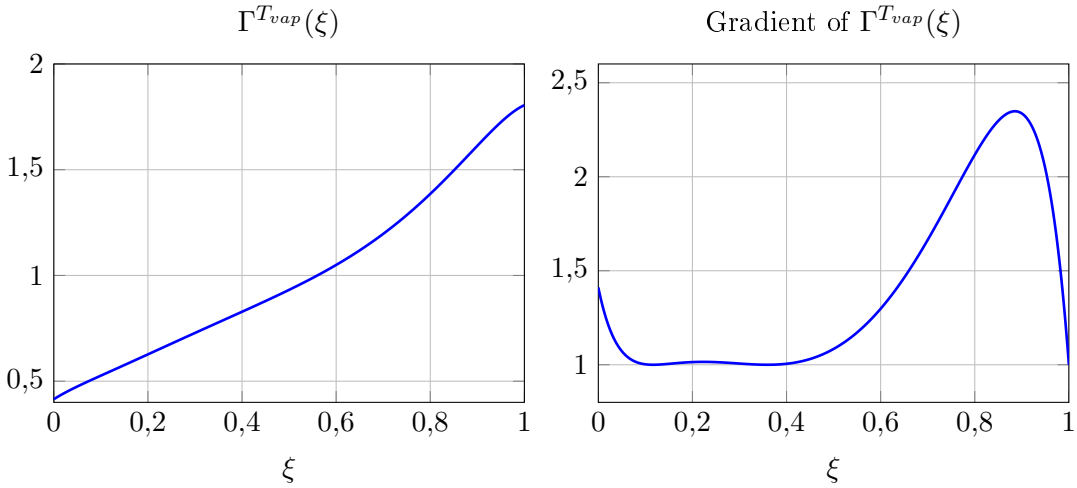

(b) The nonlinear map (given by (7.10)) and its gradient for the T_{vap}-related identification.

Figure 7.9: Identification results for T_{vap}.

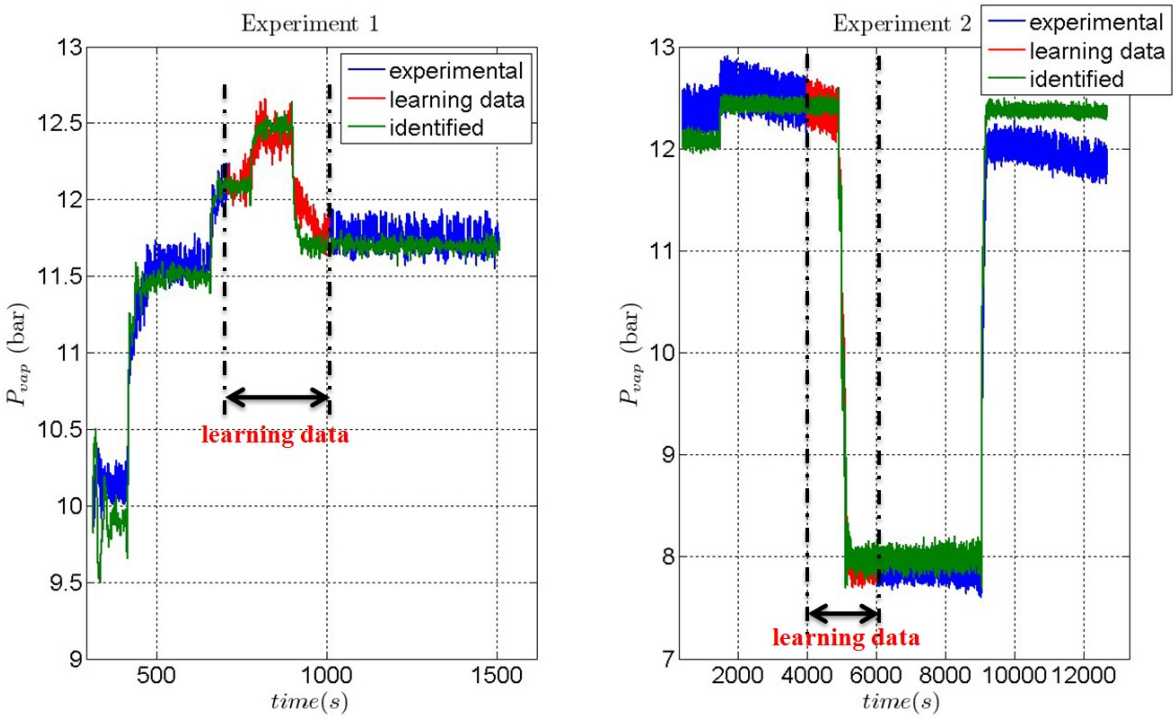

(a) Time profiles of the identified and the experimental P_{vap} on the learning and validation data.

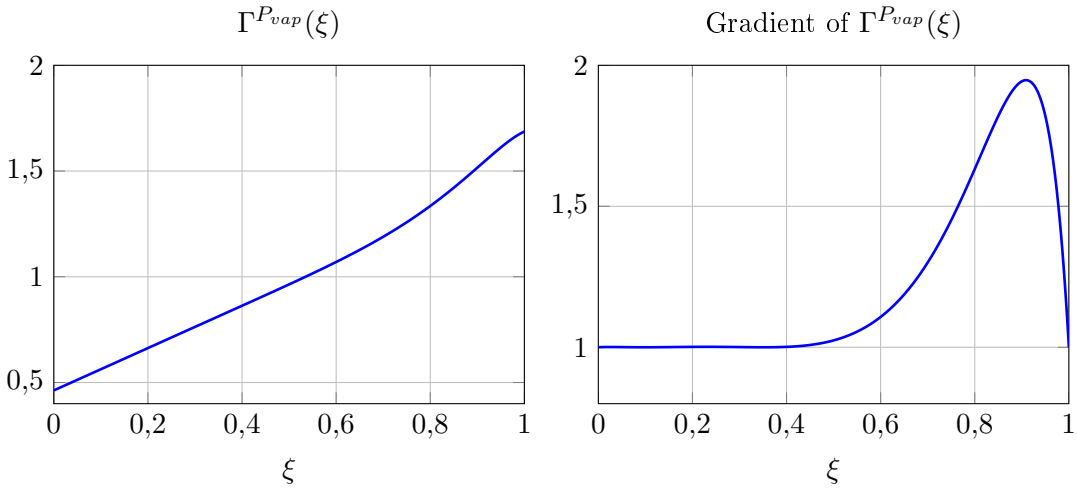

(b) The nonlinear map (given by (7.10)) and its gradient for the P_{vap}-related identification.

Figure 7.10: Identification results for P_{vap}.

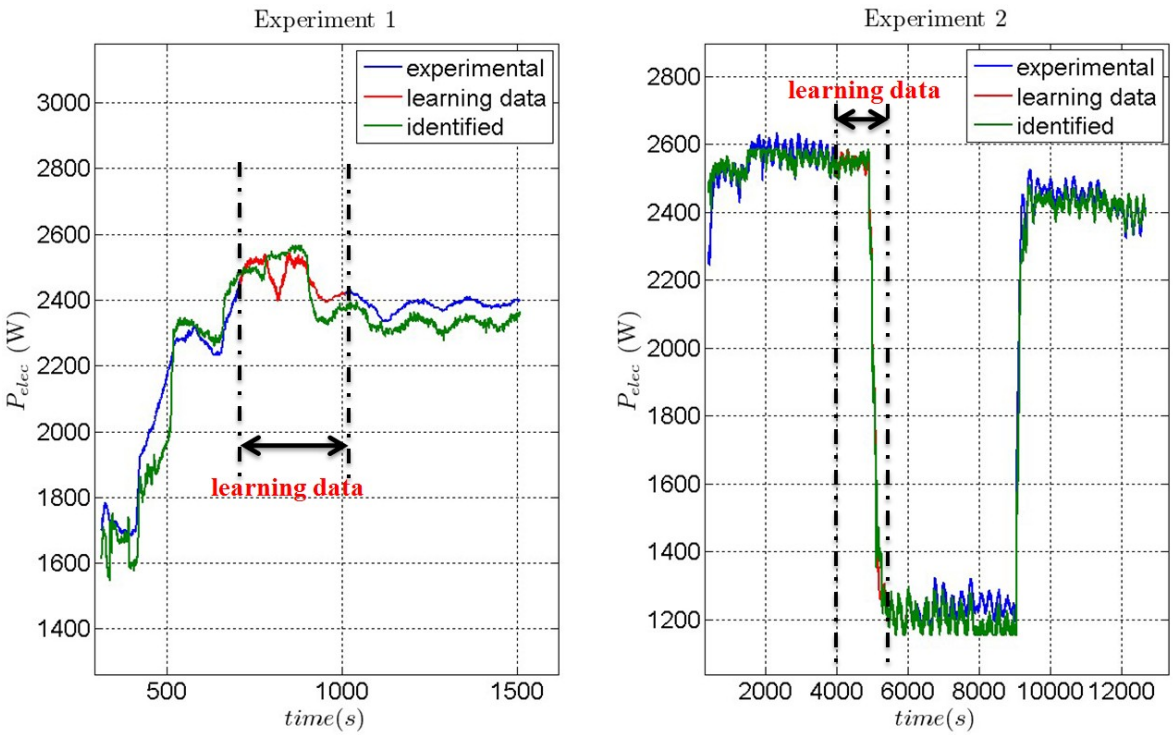

(a) Time profiles of the identified and the experimental P_{elec} on the learning and validation data.

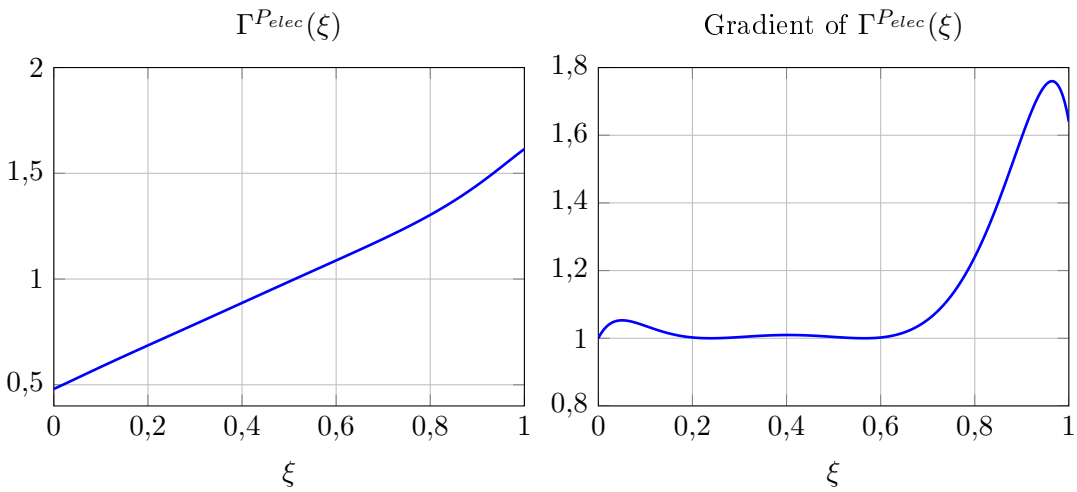

(b) The nonlinear map (given by (7.10)) and its gradient for the P_{elec}-related identification.

Figure 7.11: Identification results for P_{elec}.

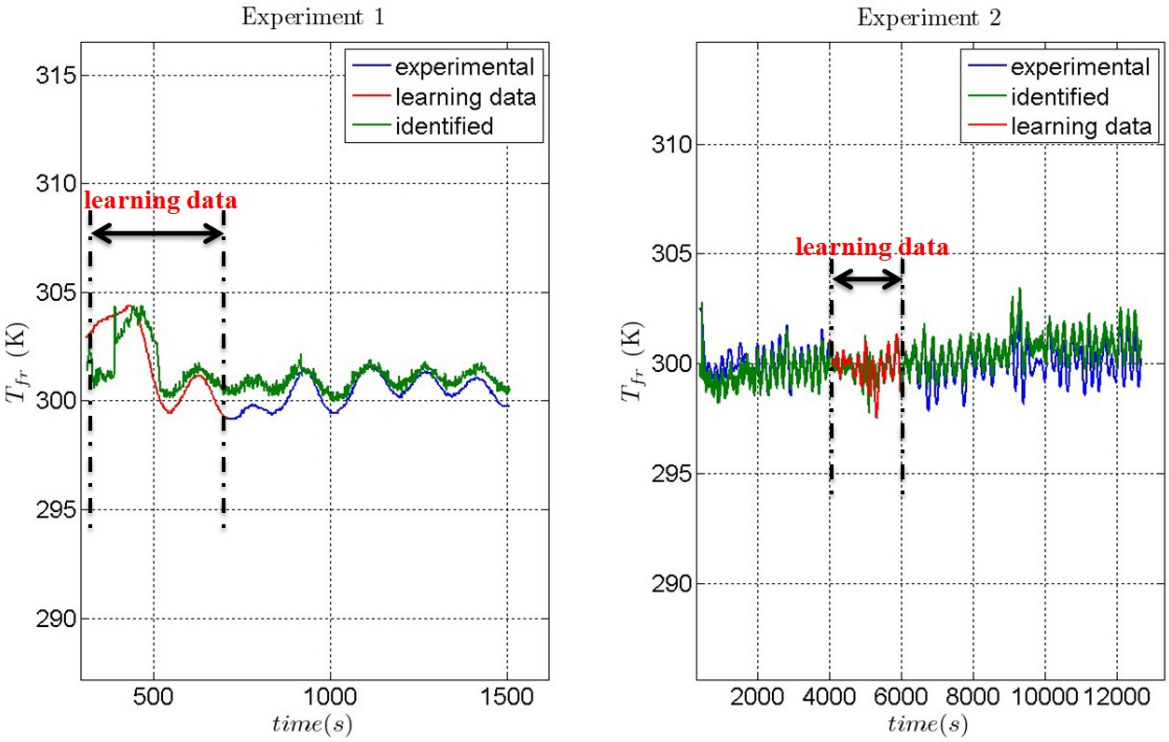

Figure 7.12: Identification results for T_{fr}.

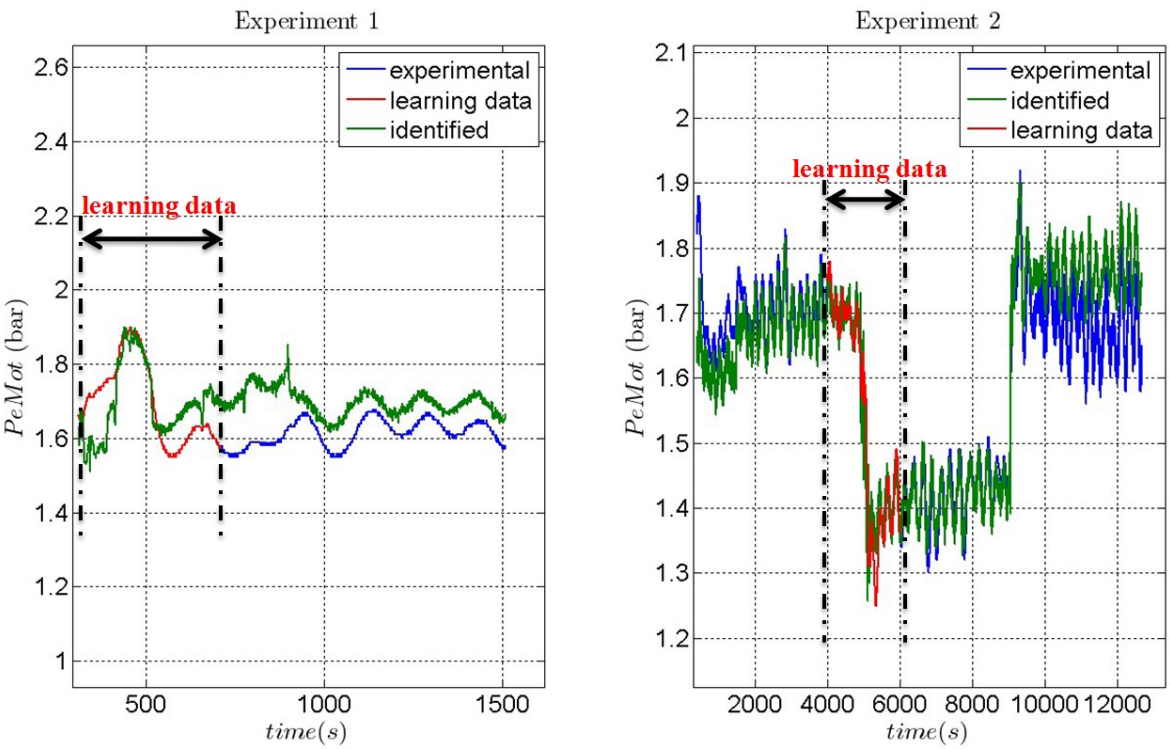

Figure 7.13: Identification results for $PeMot$.

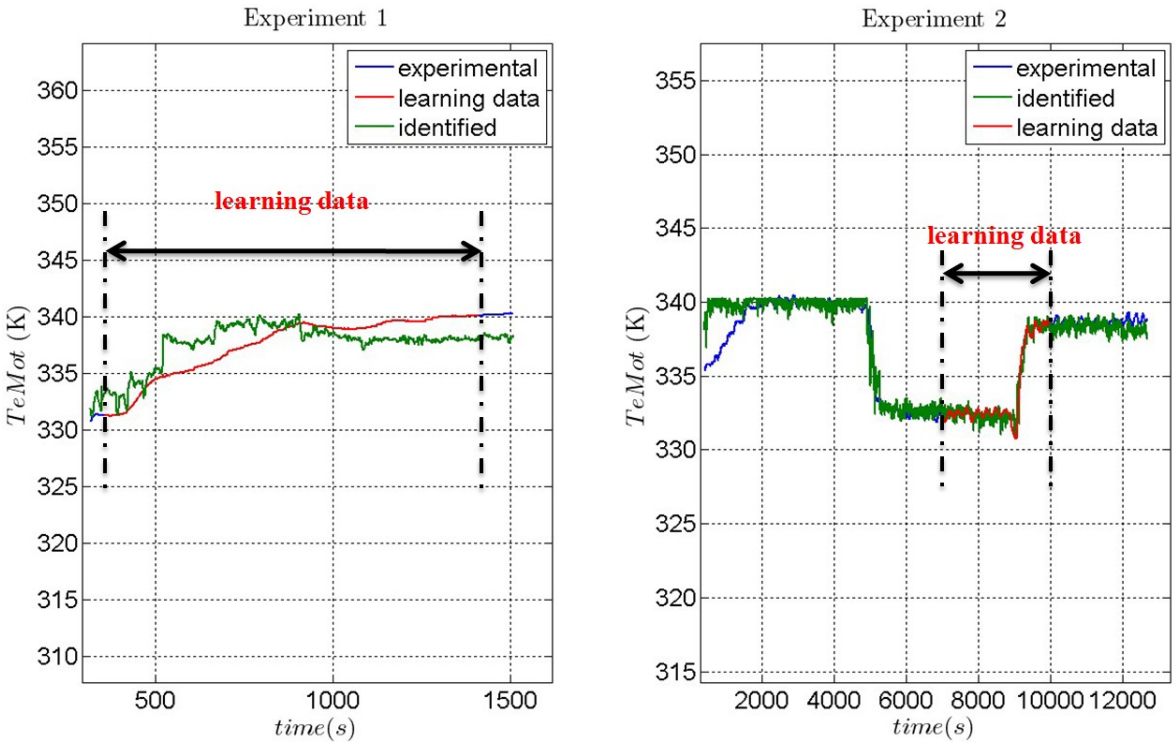

Figure 7.14: Identification results for $TeMot$.

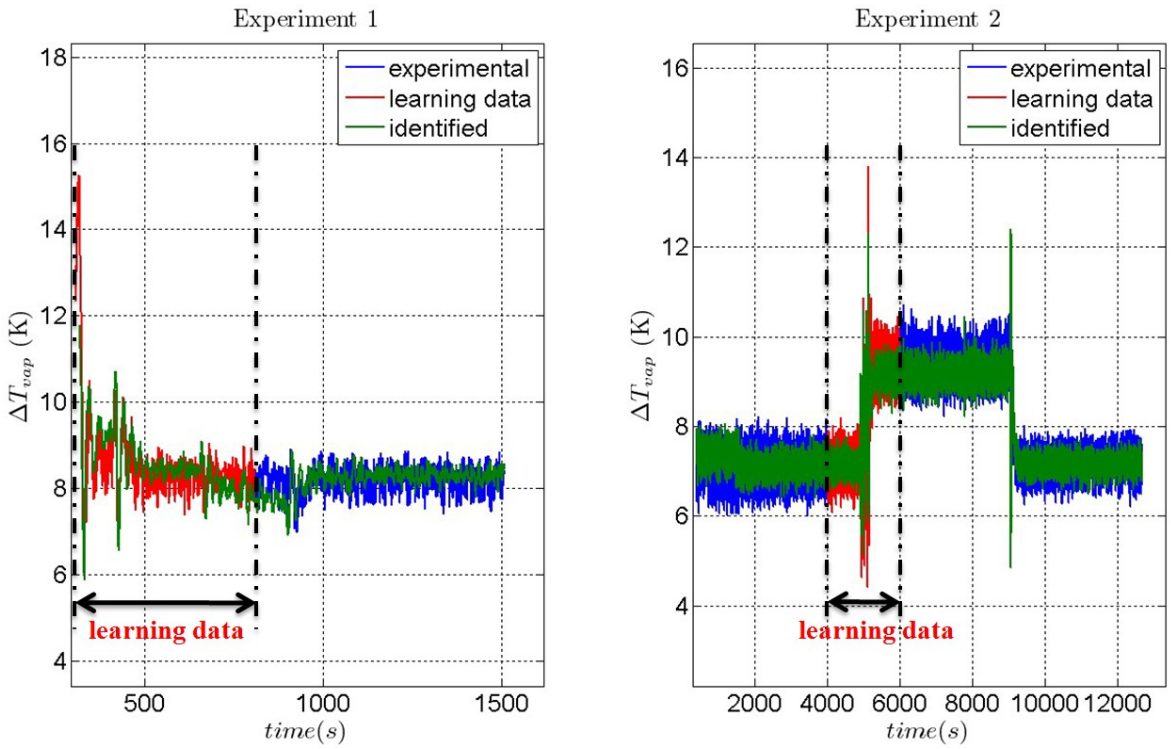

Figure 7.15: Identification results for ΔT_{vap}.

where:

$$Z_y(i) = \begin{pmatrix} u^y(i) \\ u^y(i-m) \\ \vdots \\ u^y(i-(N^y-1).m) \end{pmatrix} \in \mathbb{R}^{n_u^y.N^y}$$

The vector $u^y(i)$ used in the definition of the previous regressor can be one of the vectors defined in (7.21).

Since all the identified variables are based upon regressors of different buffer lengths and different control vectors, one needs to define a common regressor for all the variables of interest in order to construct a common state vector and state space equation (as shown in next paragraphs). Then, using the identified nonlinear maps, the relation with the common state vector will be established for each of the identified variables.

To construct the common regressor, consider the following regressor length:

$$N = max\{N^{\Delta T_{vap}}, N^{T_{vap}}, N^{P_{vap}}, N^{P_{elec}}, N^{T_{fr}}, N^{TeMot}, N^{PeMot}\} \tag{7.23}$$

and the following input vector that contains all actuation and exogenous variables:

$$u(i) = \begin{pmatrix} f_{pump}(i) & \dot{V}_{hot}(i) & V_{rot}^{aero}(i) & V_{rot}^{circ}(i) & TaCh(i) & T_{amb}(i) \end{pmatrix}^T \in \mathbb{R}^{n_u} \tag{7.24}$$

Now, one can define a common regressor for all the variables of interest as follow:

$$Z(i) = \begin{pmatrix} u(i) \\ u(i-m) \\ \vdots \\ u(i-(N-1).m) \end{pmatrix} \in \mathbb{R}^{n_u.N} \tag{7.25}$$

If we consider the following common state vector (a part of the common regressor $Z(i)$) :

$$x(i) = \begin{pmatrix} u(i-m) \\ u(i-2.m) \\ \vdots \\ u(i-(N-1).m) \end{pmatrix} \in \mathbb{R}^{(N-1).n_u} \tag{7.26}$$

then the state space equation, updated at a period $\tau_m = m\tau_s$, that is common for all the variables of interest will be given by:

$$x(i+m) = \begin{pmatrix} u(i) \\ u(i-m) \\ \vdots \\ u(i-(N-2).m) \end{pmatrix} = A.x(i) + B.u(i) \tag{7.27}$$

where:

$$A = \begin{pmatrix} \mathbb{O}_{n_u} & \mathbb{O}_{n_u} & \cdots & \cdots & \mathbb{O}_{n_u} \\ \mathbb{I}_{n_u} & \mathbb{O}_{n_u} & \cdots & \cdots & \mathbb{O}_{n_u} \\ \mathbb{O}_{n_u} & \mathbb{I}_{n_u} & \mathbb{O}_{n_u} & \cdots & \mathbb{O}_{n_u} \\ \vdots & \ddots & \ddots & \ddots & \vdots \\ \mathbb{O}_{n_u} & \cdots & \mathbb{O}_{n_u} & \mathbb{I}_{n_u} & \mathbb{O}_{n_u} \end{pmatrix} \in \mathbb{R}^{(N-1).n_u \times (N-1).n_u} \text{ and}$$

$$B = \begin{pmatrix} \mathbb{I}_{n_u} \\ \mathbb{O}_{n_u} \\ \vdots \\ \mathbb{O}_{n_u} \end{pmatrix} \in \mathbb{R}^{(N-1).n_u \times n_u}$$

$\mathbb{O}_{n_u} \in \mathbb{R}^{n_u \times n_u}$ and $\mathbb{I}_{n_u} \in \mathbb{R}^{n_u \times n_u}$ denote respectively the zero and identity matrices.

By making the index change $i = km$, the new state space equation becomes:

$$x((k+1)\tau_m) = x(k+1) = A.x(k) + B.u(k) \tag{7.28}$$

where the state vector $x(k)$ is given by:

$$x(k) = \begin{pmatrix} u(k-1) \\ u(k-2) \\ \vdots \\ u(k-(N-1)) \end{pmatrix} \in \mathbb{R}^{(N-1).n_u} \tag{7.29}$$

Similarly, one can rewrite the expressions of the common regressor $Z(k)$ and the generic variable of interest $y(k)$ in term of the new index k as follows:

$$Z(k) = \begin{pmatrix} u(k) \\ u(k-1) \\ \vdots \\ u(k-(N-1)) \end{pmatrix} \in \mathbb{R}^{n_u.N} \tag{7.30}$$

$$y(k.\tau_m) = y(k) = F_y(Z_y(k)) = \Gamma_y^{-1}(Z_y^T(k).L_y) \tag{7.31}$$

Note that since $u(k)$ can be split into:

$$u(k) = \begin{pmatrix} u_{con}^T(k) & u_{unc}^T(k) \end{pmatrix} \tag{7.32}$$

where

$$u_{con}(k) = \begin{pmatrix} f_{pump}(k) & \dot{V}_{hot}(k) & V_{rot}^{aero} & V_{rot}^{circ} \end{pmatrix}^T \in \mathbb{R}^{n_u^{con}} \tag{7.33}$$

is the vector of controllable actuators and

$$u_{unc}(k) = \begin{pmatrix} TaCh(k) & T_{amb}(k) \end{pmatrix}^T \in \mathbb{R}^{n_u^{unc}} \tag{7.34}$$

is the vector of measured uncontrolled (operational) variables, the common state space equation (7.28) can be rewritten as follows:

$$x(k+1) \quad = \quad A.x(k) + B_{con}.u_{con}(k) + B_{unc}.u_{unc}(k) \tag{7.35}$$

where $B = \begin{pmatrix} B_{con} & B_{unc} \end{pmatrix}$ such that $B_{con} \in \mathbb{R}^{(N-1).n_u \times n_u^{con}}$ and $B_{unc} \in \mathbb{R}^{(N-1).n_u \times n_u^{unc}}$.

Now since for each variable of interest $y(k)$ (that could be either $T_{vap}(k)$, $P_{vap}(k)$, $T_{fr}(k)$, $P_{elec}(k)$, $PeMot(k)$, $TeMot(k)$ or ΔT_{vap}) the corresponding input vector $u^y(k)$ (used in the regressor definition) can be related to the common control input using the following relation:

$$u^y(k) = R^y_{ed}.u(k) \tag{7.36}$$

where $R^y_{ed} \in \mathbb{R}^{n_u^y \times n_u}$ (the notation R_{ed} comes from the fact that $u^y(k)$ is a "reduced" vector deduced from $u(k)$) is given for each variable of interest by the following set of matrices:

$$R^{P_{vap}}_{ed} = R^{T_{vap}}_{ed} = R^{\Delta T_{vap}}_{ed} = \begin{pmatrix} 1 & 0 & 0 & 0 & 0 & 0 \\ 0 & 1 & 0 & 0 & 0 & 0 \\ 0 & 0 & 0 & 0 & 1 & 0 \\ 0 & 0 & 0 & 0 & 0 & 1 \end{pmatrix},$$

$$R^{P_{elec}}_{ed} = R^{T_{fr}}_{ed} = R^{TeMot}_{ed} = R^{PeMot}_{ed} = \mathbb{I}_6$$

Then it is possible to relate each regressor $Z^y(k)$ for each variable of interest $y(k)$ to the common regressor $Z(k)$ by first expressing $Z^y(k)$ in terms of the common input vector $u(k)$ as follows:

$$Z_y(k) = \begin{pmatrix} u^y(k) \\ u^y(k-1) \\ \vdots \\ u^y(k-(N^y-1)) \end{pmatrix} = \begin{pmatrix} R^y_{ed}.u(k) \\ R^y_{ed}.u(k-1) \\ \vdots \\ R^y_{ed}.u(k-(N^y-1)) \end{pmatrix} = RED^y_Z. \begin{pmatrix} u(k) \\ u(k-1) \\ \vdots \\ u(k-(N^y-1)) \end{pmatrix} \tag{7.37}$$

where $RED^y_Z = \mathbb{I}_{N^y} \otimes R^y_{ed} \in \mathbb{R}^{N^y.n_u^y \times N^y.n_u}$ and the symbol $\otimes$ denotes the Kronecker product (see Definition 0.1)
Then making $Z(k)$ appear as follow:

$$\begin{aligned} \begin{pmatrix} u(k) \\ u(k-1) \\ \vdots \\ u(k-(N^y-1)) \end{pmatrix} &= \Pi^{(n_u,N)}_{1\to N^y}. \begin{pmatrix} u(k) \\ u(k-1) \\ \vdots \\ u(k-(N^y-1)) \\ u(k-N^y) \\ \vdots \\ u(k-(N-1)) \end{pmatrix} \\ &= \Pi^{(n_u,N)}_{1\to N^y}.Z(k) \end{aligned} \tag{7.38}$$

where $\Pi_{1\to N^y}^{(n_u,N)} = \begin{pmatrix}\mathbb{I}_{N^y} & \mathbb{O}_{N^y\times(N-N^y)}\end{pmatrix} \otimes \mathbb{I}_{n_u} \in \mathbb{R}^{N^y.n_u\times N.n_u}$

By combining (7.37) and (7.38), the relation between $Z^y(k)$ and $Z(k)$ becomes:

$$Z_y(k) \quad = \quad RED_Z^y.\Pi_{1\to N^y}^{(n_u,N)}.Z(k) \tag{7.39}$$

Knowing that: (see (7.30), (7.29) and (7.32))

$$Z(k) = \begin{pmatrix} u_{con}(k) \\ u_{unc}(k) \\ x(x) \end{pmatrix}$$

and making the following matrix decomposition:

$$RED_Z^y.\Pi_{1\to N^y}^{(n_u,N)} = \begin{pmatrix} M_{u_{con}}^y & M_{u_{unc}}^y & M_x^y \end{pmatrix} \tag{7.40}$$

where : $M_{u_{con}}^y \in \mathbb{R}^{N^y.n_u^y\times n_u^{con}}$, $M_{u_{unc}}^y \in \mathbb{R}^{N^y.n_u^y\times n_u^{unc}}$ and $M_x^y \in \mathbb{R}^{N^y.n_u^y\times(N-1).n_u}$, one obtains the relation between each variable related regressor $Z^y(k)$ and the common state vector $x(k)$, the common control vector $u_{con}(k)$ and the vector of measured uncontrolled signals $u_{unc}(k)$:

$$Z_y(k) = M_x^y.x(k) + M_{u_{con}}^y.u_{con}(k) + +M_{u_{unc}}^y.u_{unc}(k) \tag{7.41}$$

Now by combining (7.31) and (7.41), one obtains the output equation of each variable of interest $y(k)$ in terms of $x(k)$, $u_{con}(k)$ and $u_{unc}(k)$:

$$y(k) = \Gamma_y^{-1}\Big[(L_y^T.M_x^y).x(k) + (L_y^T.M_{u_{con}}^y).u_{con}(k) + (L_y^T.M_{u_{unc}}^y).u_{unc}(k)\Big] \tag{7.42}$$

Then, the state space model for each variable of interest is given by:

$$\begin{aligned} x(k+1) &= A.x(k) + B_{con}.u_{con}(k) + B_{unc}.u_{unc}(k) \\ y(k) &= \Gamma_y^{-1}\Big[(L_y^T.M_x^y).x(k) + (L_y^T.M_{u_{con}}^y).u_{con}(k) + (L_y^T.M_{u_{unc}}^y).u_{unc}(k)\Big] \end{aligned}$$

This model is obviously observable since the state vector is based upon the past values of the input vector according to (7.29).

7.5.2 ORC Model Linearization

According to Section 7.4.3, the identification of the maps for T_{fr}, $PeMot$, $TeMot$ and ΔT_{vap} resulted in linear models unlike the identification of the maps for T_{vap}, P_{vap} and P_{elec} where nonlinear models were needed to capture the nonlinear character of the relationship for these variables. However, according to the shape of the nonlinear maps for T_{vap}, P_{vap} and P_{elec} (illustrated in Figures 7.9b-7.11b), it is possible to find a straight line that approximates in

a least squares sense these nonlinear map resulting in the end in a linear model for the ORC system that optimally approximates the nonlinear model. The linear model will then be used in the controller design and the model errors will be corrected through slow integrators.

Let σ be defined as follows (according to (7.42)):

$$\sigma = (L_y^T.M_x^y).x(k) + (L_y^T.M_{u_{con}}^y).u_{con}(k) + (L_y^T.M_{u_{unc}}^y).u_{unc}(k) \tag{7.44}$$

Hence, by approximating in a least squares sense the nonlinear map $\Gamma_y^{-1}(\sigma)$, given by (7.42) for each variable of interest $y(k)$, as follows:

$$y(k) = \Gamma_y^{-1}(\sigma) = a_y.\sigma + b_y \tag{7.45}$$

and using (7.44), one obtains the final output equation for each variable of interest $y(k)$:

$$y(k) = C^y.x(k) + D_{con}^y.u_{con}(k) + D_{unc}^y.u_{unc}(k) + E^y \tag{7.46}$$

Where: $C^y = a_y.L_y^T.M_x^y$, $D_{con}^y = a^y.L_y^T.M_{u_{con}}^y$, $D_{unc}^y = a^y.L_y^T.M_{u_{unc}}^y$ and $E^y = b_y$.

Figure 7.16 gives the linearization results (equation (7.45)) for the nonlinear maps $\Gamma_{T_{vap}}^{-1}(.)$, $\Gamma_{P_{vap}}^{-1}(.)$ and $\Gamma_{P_{elec}}^{-1}(.)$ to assess how close the linear model approximates the nonlinear one for these variables. However, according to the discussion of Section 7.4.3, $\Gamma_{T_{fr}}^{-1}(.)$, $\Gamma_{PeMot}^{-1}(.)$, $\Gamma_{TeMot}^{-1}(.)$ and $\Gamma_{\Delta T_{vap}}^{-1}(.)$ were found to be linear, so it is not worthwhile to show their corresponding linearization results since there is an exact matching between $\Gamma^{-1}(.)$ for these variables and their corresponding linear approximations.

7.5.3 Filtering control variables

Considering the approximated linear state space model for each variable of interest $y(k)$ that was defined by equations (7.35) and (7.46), it is interesting to add a first order filter on the vector of controlled actuator namely $u_{con}(k)$. Indeed adding this filter will induce the following benefits:

- Eliminates the direct feedthrough matrix D_{con}^y in the output equation for each variable of interest $y(k)$.
- Avoids the need for introducing rate constraints on control signals (since the rate of variation for the control signals will be defined by the time constants of the filter). This reduces the complexity of the controller.

Hence, the state space model after filtering the control vector becomes as follow:

$$x(k+1) = A.x(k) + B_{con}.u_{con}(k) + B_{unc}.u_{unc}(k) \tag{7.47a}$$

$$u_{con}(k+1) = A_f.u_{con}(k) + B_f.u_f(k) \tag{7.47b}$$

$$y(k) = C^y.x(k) + D_{con}^y.u_{con}(k) + D_{unc}^y.u_{unc}(k) + E^y \tag{7.47c}$$

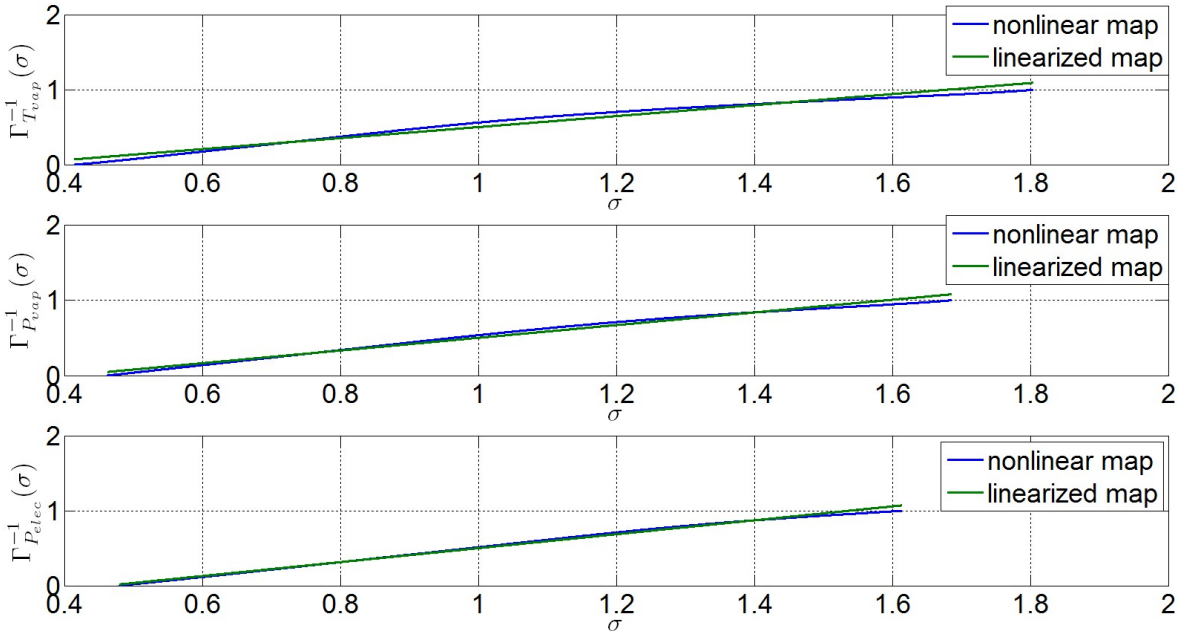

Figure 7.16: Linearization of the nonlinear maps $\Gamma^{-1}_{T_{vap}}(.)$, $\Gamma^{-1}_{P_{vap}}(.)$ and $\Gamma^{-1}_{P_{elec}}(.)$.

With: $B_f = I_{n_u^{con}} - A_f$, where A_f is a diagonal filtering matrix whose diagonal elements are set according to the desired filter time constants corresponding to each element of the control vector $u_{con}(k)$. The new control vector becomes $u_f(k)$ which has the same dimension as the filtered control vector $u_{con}(k)$.

By extending the state vector with the vector of controlled variables $u_{con}(k)$ as follow:

$$\bar{X}(k) = \begin{pmatrix} x(k) \\ u_{con}(k) \end{pmatrix} \quad \in \mathbb{R}^{n_{\bar{x}}} \quad where \quad n_{\bar{x}} = n_x + n_u^{con} \tag{7.48}$$

the new state space equations for each variable of interest become:

$$\bar{X}(k+1) = \bar{A}.\bar{X}(k) + \bar{B}_{con}.u_f(k) + \bar{B}_{unc}.u_{unc}(k) \tag{7.49a}$$
$$y(k) = \bar{C}^y.\bar{X}(k) + D^y_{unc}.u_{unc}(k) + E^y \tag{7.49b}$$

Where: $\bar{A} = \begin{pmatrix} A & B_{con} \\ \mathbb{O} & A_f \end{pmatrix}$, $\bar{B}_{con} = \begin{pmatrix} \mathbb{O} \\ B_f \end{pmatrix}$ and $\bar{C}^y = \begin{pmatrix} C^y & D^y_{con} \end{pmatrix}$

7.6 Conclusion

In this chapter a recently developed identification framework was applied to derive nonlinear models for the ORC power plant. The nonlinear models so obtained were validated using experimental data gathered on a real prototype. Then a global state space model of the ORC

power plant was derived from the identified models and will be used in the next chapter to derive an optimal control strategy to reach the system objectives while respecting the physical constraints.

Chapter 8

Constrained Optimal Control of the ORC based power plant

Contents

8.1 Study of the admissible steady states 135

8.2 Constrained Model Predictive Control of the ORC power plant . . . 140

8.2.1 Measured uncontrolled signals handling 140

8.2.2 MPC controller design 141

8.2.3 Simulation Results 142

8.3 Conclusion 145

This chapter addresses the problem of designing a constrained optimal control strategy for the ORC power plant based on the state space model (7.49) given for each variable of interest. The presented controller optimally makes the ORC system track some reference electrical power namely P_{elec}^{ref} while respecting the system constraints in term of temperatures and pressures for some key thermodynamic variables. Prior to the control design step, an analysis of the admissible desired steady states is performed to derive feedforward terms that enhance the controller performances.

8.1 Study of the admissible steady states

Now that we have defined the state space equations (7.49) and before developing the constrained optimal control strategy for the ORC power plant, it is necessary to study the admissible desired steady states i.e. the steady states that are compatible with some desired reference electrical power P_{elec}^{ref} leading to the respect of the system constraints set in Section 7.2 while penalizing the control vector in the expression of the cost function.

At equilibrium, (7.49a) becomes:

$$\bar{X}_d(k+1) = \bar{A}.\bar{X}_d(k) + \bar{B}_{con}.u_{fd}(k) + \bar{B}_{unc}.u_{unc}(k) = \bar{X}_d(k) \tag{8.1}$$

where the superscript "d" stands for "desired".

Now, consider some vector of regulated variables $y_r(k)$ (that obviously contains at least $P_{elec}(k)$ as one of its components) that will be defined later in this section. At equilibrium and according to (7.49b), the resulting desired vector of regulated variables will be given by:

$$y_d(k) = \bar{C}^{y_r}.\bar{X}_d(k) + D^{y_r}_{unc}.u_{unc}(k) + E^{y_r} \tag{8.2}$$

where $\bar{C}^{y_r}$, $D^{y_r}_{unc}$ and E^{y_r} will be formed by concatenating line by line the matrices $\bar{C}^y$, D^y_{unc} and E^y respectively corresponding to each output variable $y(k)$ which is part of the vector $y_r(k)$.

Combining (8.1) and (8.2) in matrix form results in:

$$\begin{pmatrix} (\bar{A} - I_{n_{\bar{x}}}) & \bar{B}_{con} \\ \bar{C}^{y_r} & \mathbb{O} \end{pmatrix} . \begin{pmatrix} \bar{X}_d(k) \\ u_{fd}(k) \end{pmatrix} + \begin{pmatrix} \bar{B}_{unc} \\ D_{unc} \end{pmatrix} .u_{unc}(k) + \begin{pmatrix} \mathbb{O} \\ E^{y_r} \end{pmatrix} = \begin{pmatrix} \mathbb{O} \\ \mathbb{I} \end{pmatrix} .y_d \tag{8.3}$$

Note from (8.3) that the steady state equation is time dependent since the vector of the measured uncontrolled signals $u_{unc}(k)$, which is time dependent with a slow dynamics compared to the other variables of interest (because it depends on $TaCh$ and T_{amb} that vary slowly), is involved in this equation.

By denoting:

$$A_c = \begin{pmatrix} (\bar{A} - I_{n_{\bar{x}}}) & \bar{B}_{con} \\ \bar{C}^{y_r} & \mathbb{O} \end{pmatrix}, B^{unc}_c = \begin{pmatrix} \bar{B}_{unc} \\ D_{unc} \end{pmatrix}, E_c = \begin{pmatrix} \mathbb{O} \\ E^{y_r} \end{pmatrix}, B_c = \begin{pmatrix} \mathbb{O} \\ \mathbb{I} \end{pmatrix} \text{ and } Z_d = \begin{pmatrix} \bar{X}_d(k) \\ u_{fd}(k) \end{pmatrix}$$

the steady state equation (8.3) becomes:

$$A_c.Z_d + B^{unc}_c.u_{unc}(k) + E_c = B_c.y_d \tag{8.4}$$

Furthermore, as mentioned in the beginning of this section, the desired steady states must lead to the respect of the ORC system constraints. It is then necessary to express the vector of constrained variables at equilibrium in term of Z_d. This begins by expressing the output equation of each variable of interest $y(k)$ as follow:

$$\begin{aligned} y(k) &= \bar{C}^y.\bar{X}(k) + D^y_{unc}.u_{unc}(k) + E^y \\ &= C^y_c.\begin{pmatrix} \bar{X}(k) \\ u_f(k) \end{pmatrix} + D^y_{unc}.u_{unc}(k) + E^y \end{aligned} \tag{8.5}$$

where $C^y_c = \begin{pmatrix} \bar{C}^y & \mathbb{O}_{n^{con}_u} \end{pmatrix}$

Now, consider the following vector of constrained variables:
$y_c = \begin{pmatrix} P_{vap} & T_{vap} & \Delta T_{vap} & T_{fr} & TeMot & PeMot \end{pmatrix}^T \in \mathbb{R}^6$ that has to satisfy according to Section 7.2:

$$y^{min}_c \leq y_c \leq y^{max}_c \tag{8.6}$$

Moreover, since the steady vector Z_d is based upon the vector of controlled variables and its past values, it has to satisfy the following inequality constraints:

$$Z^{min}_d \leq Z_d \leq Z^{max}_d \tag{8.7}$$

Thus combining (8.6) and (8.7) and taking into account (8.5), the steady values have to satisfy the following inequality constraints:

$$Y_{c,Z_d}^{min} - E_{Z_d} - D_{Z_d}.u_{unc}(k) \leq C_c^{Z_d}.Z_d \leq Y_{c,Z_d}^{max} - E_{Z_d} - D_{Z_d}.u_{unc}(k) \tag{8.8}$$

where

$$Y_{c,Z_d}^{min} = \begin{pmatrix} y_c^{min} \\ Z_d^{min} \end{pmatrix} \quad ; \quad Y_{c,Z_d}^{max} = \begin{pmatrix} y_c^{max} \\ Z_d^{max} \end{pmatrix}$$

and

$$E_{Z_d} = \begin{pmatrix} E^{P_{vap}} \\ E^{T_{vap}} \\ E^{\Delta T_{vap}} \\ E^{T_{fr}} \\ E^{TeMot} \\ E^{PeMot} \\ \mathbb{O}_{(n_{\bar{x}}+n_u^{con})\times 1} \end{pmatrix} \quad D_{Z_d} = \begin{pmatrix} D_{unc}^{P_{vap}} \\ D_{unc}^{T_{vap}} \\ D_{unc}^{\Delta T_{vap}} \\ D_{unc}^{T_{fr}} \\ D_{unc}^{TeMot} \\ D_{unc}^{PeMot} \\ \mathbb{O}_{(n_{\bar{x}}+n_u^{con})\times n_u^{unc}} \end{pmatrix} \quad C_c^{Z_d} = \begin{pmatrix} C_c^{P_{vap}} \\ C_c^{T_{vap}} \\ C_c^{\Delta T_{vap}} \\ C_c^{T_{fr}} \\ C_c^{TeMot} \\ C_c^{PeMot} \\ \mathbb{I}_{(n_{\bar{x}}+n_u^{con})} \end{pmatrix}$$

Note that equation (8.8) can be rewritten as:

$$C_T^{Z_d}.Z_d \leq b_{T1}^{Z_d} + b_{T2}^{Z_d}.u_{unc}(k) \tag{8.9}$$

Where: $C_T^{Z_d} = \begin{pmatrix} C_c^{Z_d} \\ -C_c^{Z_d} \end{pmatrix}$, $b_{T1}^{Z_d} = \begin{pmatrix} Y_{c,Z_d}^{max} - E_{Z_d} \\ -Y_{c,Z_d}^{min} + E_{Z_d} \end{pmatrix}$ and $b_{T2}^{Z_d} = \begin{pmatrix} -D_{Z_d} \\ D_{Z_d} \end{pmatrix}$

Finally, the extended steady state vector $\bar{X}_d$ and the steady state control u_{fd} are given by the steady desired vector $Z_d = \begin{pmatrix} \bar{X}_d \\ u_{fd} \end{pmatrix}$ which is the solution of the following Constrained Linear Programming (LP) problem:

$$\min_{Z_d} f^T.Z_d(k) \tag{8.10}$$

under the following equality and inequality constraints:

$$C_T^{Z_d}.Z_d(k) \leq b_{T1}^{Z_d} + b_{T2}^{Z_d}.u_{unc}(k)$$
$$A_c.Z_d(k) = B_c.y_d - B_c^{unc}.u_{unc}(k) - E_c$$

where $f = 1_{(n_{\bar{x}}+n_u^{con})}$ is a weighting vector.

The LP problem (8.10) that enables to derive the admissible extended steady vector $\bar{X}_d$ and its corresponding steady control vector u_{fd} obviously needs to be fed with the desired steady vector y_d whose only a priori known component is the desired electrical power P_{elec}^{ref}. Since this LP problem might be quite heavy to solve online due to the important size of its associated matrices (for the considered application $Z_d \in \mathbb{R}^{62}$ and $C_T^{Z_d} \in \mathbb{R}^{130\times 62}$) and since we

will have additionally to solve online a QP problem corresponding to our constrained optimal controller (as it will be explaines in Section 8.2), we proposed another alternative based on an offline computed cartography to determine the desired admissible steady state vectors as it is explained hereafter.

First of all, note that if the A_c matrix is invertible (full ranked square matrix) and one can determine an admissible (leading to the respect of the ORC system constraints) desired steady vector y_d, the desired admissible steady vector $\bar{X}_d$ and its corresponding steady control vector u_{fd} will be derived using the following equation: (see (8.4)):

$$Z_d(k) = \begin{pmatrix} \bar{X}_d \\ u_{fd} \end{pmatrix} = A_c^{-1}.(B_c.y_d - B_c^{unc}.u_{unc}(k) - E_c) \tag{8.11}$$

In order to make the A_c matrix invertible, the size of y_d (and therefore the size of $y_r(k)$) must be equal to $n_u^{con} = 4$. Then, we have to choose in addition of P_{elec} three more critical variables to add to the vector $y_r(k)$. In this case, it would be judicious according to the degree of importance of the constrained variables to choose ΔT_{vap}, T_{vap} and $PeMot$ as additional variables in $y_r(k)$. This leads to the definition of the following matrices:

$$y_r(k) = \begin{pmatrix} P_{elec}(k) \\ \Delta T_{vap}(k) \\ T_{vap}(k) \\ PeMot(k) \end{pmatrix}, \; y_d = \begin{pmatrix} P_{elec}^{ref} \\ \Delta T_{vap}^{d} \\ T_{vap}^{d} \\ PeMot^{d} \end{pmatrix} \text{ and } \bar{C}^{y_r} = \begin{pmatrix} \bar{C}^{P_{elec}} \\ \bar{C}^{\Delta T_{vap}} \\ \bar{C}^{T_{vap}} \\ \bar{C}^{PeMot} \end{pmatrix}$$

Then, a cartography $carto^{ORC}(TaCh^{vect}, T_{amb}^{vect}, P_{elec}^{vect}, \Delta T_{vap}^{vect}, T_{vap}^{vect}, PeMot^{vect})$ is built offline. This cartography is associated to a set of vectors of interpolation points corresponding to the operational uncontrolled variables namely $TaCh$ and T_{amb} and the set of regulated variables namely P_{elec}^{vect}, ΔT_{vap}^{vect}, T_{vap}^{vect} and $PeMot^{vect}$. The bounds of the vectors of interpolation points have to be chosen such that they entirely define all the admissible domain for the operational (exogenous) and regulated variables.

By scanning all the possible values of the vectors of interpolation points, the LP problem (8.10) is solved offline for each of the values $TaCh(i)$, $T_{amb}(j)$, $P_{elec}^{vect}(k)$, $\Delta T_{vap}^{vect}(l)$, $T_{vap}^{vect}(m)$ and $PeMot^{vect}(n)$ (where i, j, k, l, m and n are the indices of the vectors of interpolation points corresponding to some scanned value). If the LP problem has a solution, then the value 1 is put in the cartography at the indice (i, j, k, l, m, n) otherwise a 0 is put instead.

Then, by measuring the operational variables $TaCh$ and T_{amb} and knowing the reference electrical power P_{elec}^{ref} (power consumed by the off-grid loads), one has to extract in real time from $carto^{ORC}(.)$ the admissible reference vector y_d according to the diagram depicted in Figure 8.1. Note in this diagram that a minimum admissible value of $\Delta T_{vap}^{vect}(l)$, $T_{vap}^{vect}(m)$ and $PeMot^{vect}(n)$ is chosen in order to maximize the motor efficiency.

Finally, knowing y_d, the desired admissible steady vector $\bar{X}_d$ and its corresponding steady control vector u_{fd} are derived using (8.11).

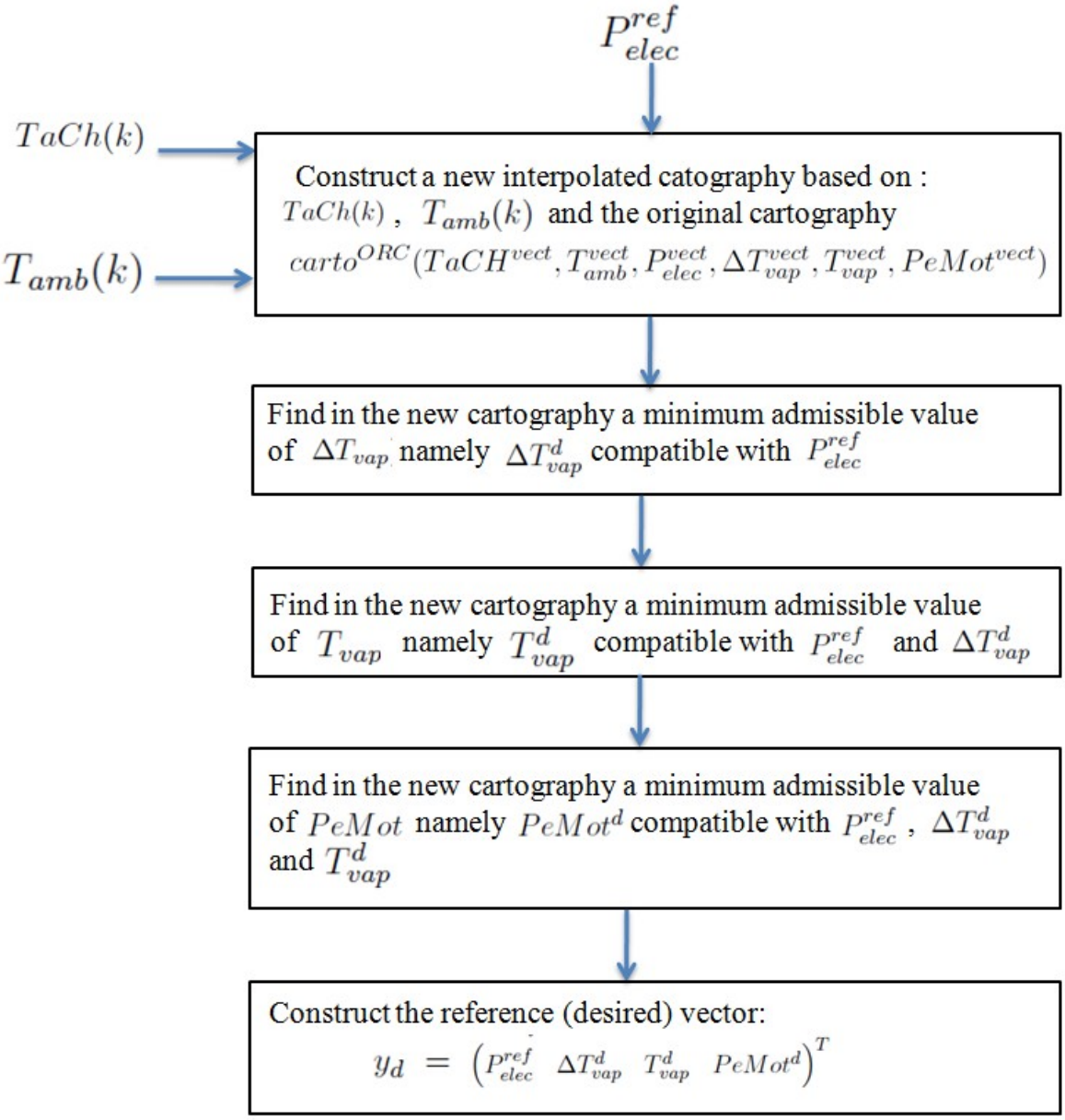

Figure 8.1: Principle diagram for extracting y_d from $carto^{ORC}(TaCH^{vect}, T_{amb}^{vect}, P_{elec}^{vect}, \Delta T_{vap}^{vect}, T_{vap}^{vect}, PeMot^{vect})$ based on the knowlege of P_{elec}^{ref}.

8.2 Constrained Model Predictive Control of the ORC power plant

Now that we have defined the control-oriented mathematical model for the ORC power plant in Section 7.5 and translated mathematically in Section 8.1 the control objectives and system constraints in terms of the admissible desired steady states, the last task is to design a control strategy that optimally tracks some desired reference electrical power P_{elec}^{ref} while respecting the system constraints. In this work and according to the system model structure, an MPC (Model Predictive Control) controller is the best suited option to achieve the control objectives since it handles explicitly the system constraints while insuring an optimal behavior.

The principle of an MPC controller is to solve online a finite horizon open-loop constrained optimization problem that depends on the current system state (rather than determining an off-line feedback law that holds for all the states) to derive at each sampling period an optimal control sequence from which the first control is applied to the system and the procedure is repeated at each sampling time to cope with the system disturbances.

MPC controllers rely on the use of a model for the system to be controlled. When the model of the plant is linear, the optimization problem consists in solving online a classical Quadratic Programming (QP) problem at each sampling time (refer to [Mayne et al., 2000] where a large literature review on MPC is presented).

Among the numerous advantages of Model Predictive Control:

- The possibility to handle explicitly the system constraints regardless their nature: control saturation, states and output limitations...etc.
- It is well adapted to control multi-variable coupled dynamical systems.
- The fact that MPC design relies on solving an optimization problem endows the methodology by some intuitiveness .

All these advantages made the MPC design widely used in the industry with thousands of succesful implementations (see [Qin and Badgwell, 2003] for some examples of industrial applications of MPC controllers).

In Section 8.2.1, the ORC power plant model is reformulated to handle the system disturbances, then the mathematical formulation of the MPC control problem is presented in Section 8.2.2. Simulation results of the resulting closed loop system will be discussed in Section 8.2.3.

8.2.1 Measured uncontrolled signals handling

If we suppose that the vector of operational variables remains constant during the whole prediction horizon (which is a good assumption since the dynamic of $TaCh$ and T_{amb} is very

slow compared to the dynamics of the other variables), the state space equations for the ORC power plant (7.49) become:

$$\bar{X}(k+1) = \bar{A}.\bar{X}(k) + \bar{B}_{con}.u_f(k) + \bar{B}_{unc}.u_{unc}(k) \tag{8.12a}$$
$$u_{unc}(k+1) = u_{unc}(k) \tag{8.12b}$$
$$y_r(k) = \bar{C}^{y_r}.\bar{X}(k) + D^{y_r}_{unc}.u_{unc}(k) + E^{y_r} \tag{8.12c}$$

By extending the state vector with the vector of the uncontrolled variables $u_{unc}(k)$ as follow:

$$\bar{X}_a(k) = \begin{pmatrix} \bar{X}(k) \\ u_{unc}(k) \end{pmatrix} \in \mathbb{R}^{n_{\bar{x}_a}} \text{ where } n_{\bar{x}_a} = n_{\bar{x}} + n_u^{unc}$$

the new state space equations become:

$$\bar{X}_a(k+1) = \bar{A}_a.\bar{X}_a(k) + \bar{B}^a_{con}.u_f(k) \tag{8.13a}$$
$$y(k) = \bar{C}^y_a.\bar{X}(k) + E^y \tag{8.13b}$$

where $\bar{A}_a = \begin{pmatrix} \bar{A} & \bar{B}_{unc} \\ \mathbb{O} & \mathbb{I} \end{pmatrix}$, $\bar{B}^a_{con} = \begin{pmatrix} \bar{B}_{con} \\ \mathbb{O} \end{pmatrix}$ and $\bar{C}^y_a = \begin{pmatrix} \bar{C}^y & D^y_{unc} \end{pmatrix}$

8.2.2 MPC controller design

Based on the extended model (8.13) for the ORC power plant, an MPC controller is designed to track the reference electrical power P^{ref}_{elec} (that will serve to define y_d according to Figure 8.1) while respecting the system constraints.

The objective function to be minimized is given by:

$$\min_p V(\bar{X}_a(k), p) = \sum_{i=1}^{N_p} \Big(\|y_r(k+i,p) - y_d\|^2_Q + \|u_f(k+i,p) - u_{fd}\|^2_R \Big) \tag{8.14}$$

under the constraints defined by:

$$y_c^{min} \leq y_c \leq y_c^{max} \tag{8.15}$$
$$u_f^{min} \leq u_f \leq u_f^{max} \tag{8.16}$$

where $y_c = \begin{pmatrix} P_{vap} & T_{vap} & \Delta T_{vap} & T_{fr} & TeMot & PeMot \end{pmatrix}^T \in \mathbb{R}^6$ is the vector of constrained variables. Q and R are the weighting matrices of the MPC controller, N_p is the prediction horizon and $p = \begin{pmatrix} u_f(k) & u_f(k+1) & \cdots & u_f(k+N_p-1) \end{pmatrix}^T$ is the decision variable from which we extract $u_f(k)$ the reference of the first order filter (7.47b) whose output defines the control vector $u_{con}(k)$ applied to the system.

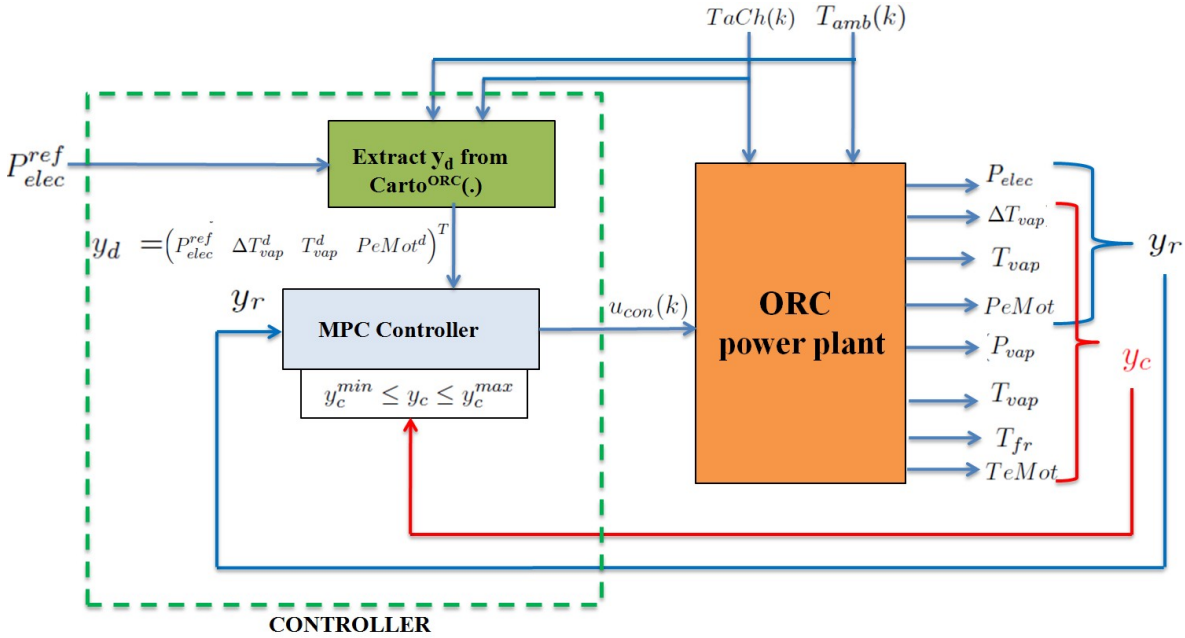

Figure 8.2: Diagram of the ORC control System.

The values of the weighting matrices Q and R are given for the system under consideration by:

$$Q = \begin{pmatrix} 5 & 0 & 0 & 0 \\ 0 & 5 \times 10^7 & 0 & 0 \\ 0 & 0 & 4000 & 0 \\ 0 & 0 & 0 & 3000 \end{pmatrix} \quad , \quad R = \begin{pmatrix} 0.1 & 0 & 0 & 0 \\ 0 & 150 & 0 & 0 \\ 0 & 0 & 1 & 0 \\ 0 & 0 & 0 & 1 \end{pmatrix}$$

These matrices are determined by tuning giving more importance (and hence more weight) to the regulation respectively of the superheating ΔT_{vap}, T_{vap}, $PeMot$ and finally P_{elec} in order to let the constrained variables, that intervene in the definition of y_r, converge rapidly towards their calculated references. The fact there is a great dispersion in the values of the matrices Q and R is due to a normalization effect.

Note that since some of the constraints in (8.15) are hard, constraints softening methods are used to soften the remaining constraints to guarantee the feasibility of the optimization problem.

The control architecture of the ORC power plant is depicted in Figure 8.2.

8.2.3 Simulation Results

In order to assess the performance of the proposed control architecture (Figure 8.2), a simulation scenario is proposed in which we vary in time the operating conditions (with time constants close to the reality) in term of the hot source temperature profile $TaCh$ and the

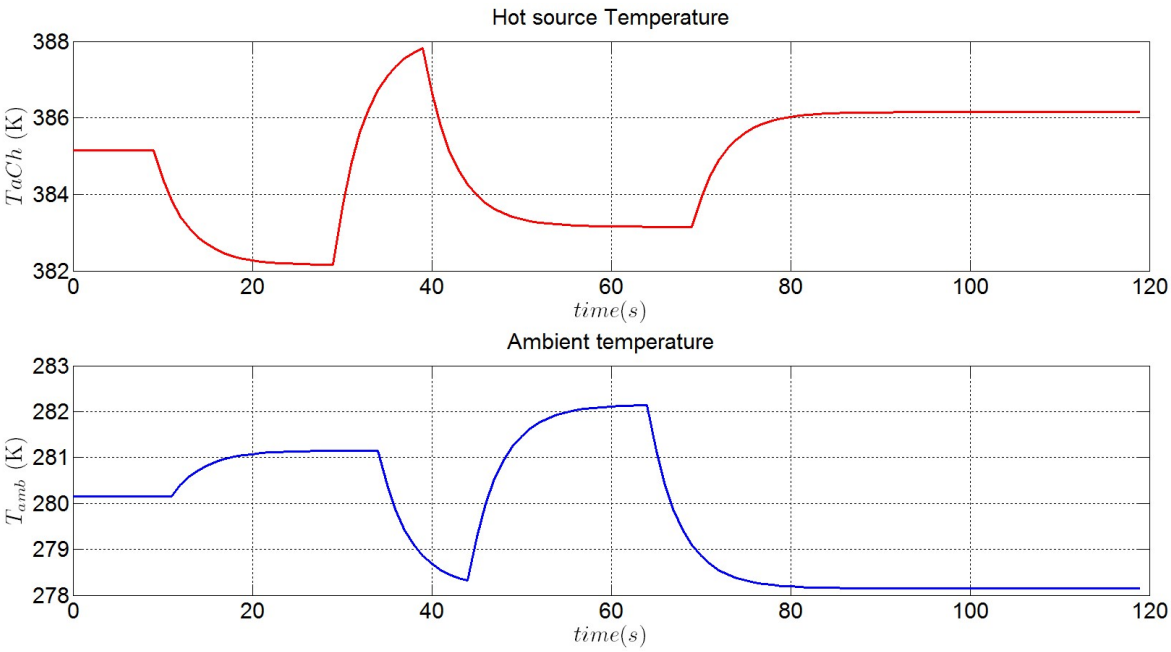

(a) Temperature profile of the measured uncontrolled signals $TaCH$ and T_{amb}.

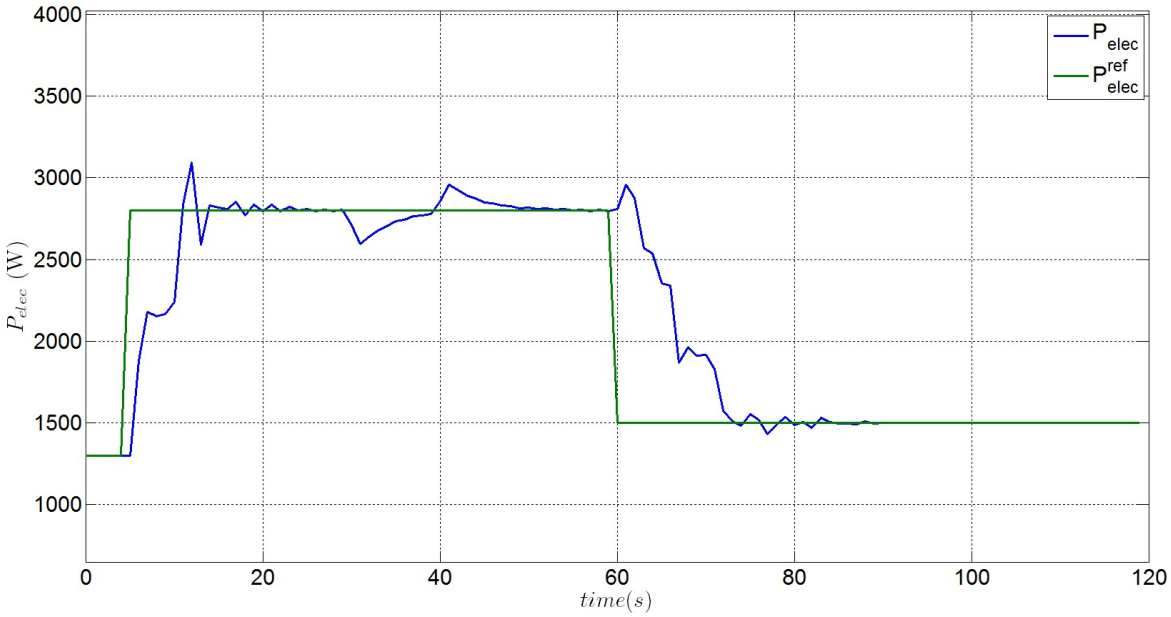

(b) ORC turbine output electrical power P_{elec} and its reference signal P_{elec}^{ref}.

Figure 8.3: Tracking results and disturbance rejection for the ORC turbine output electrical power P_{elec}.

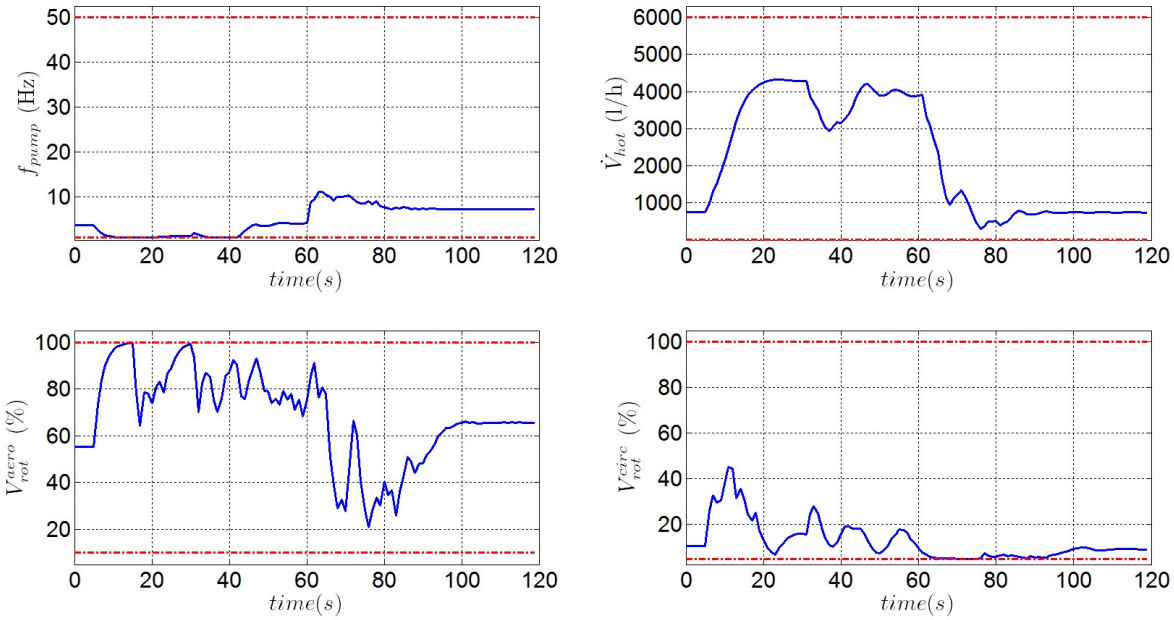

Figure 8.4: ORC system actuators: f_{pump}, $\dot{V}_{hot}$, V_{rot}^{aero} and V_{rot}^{circ}. The red dashed lines indicate the minimum and maximum admissible values.

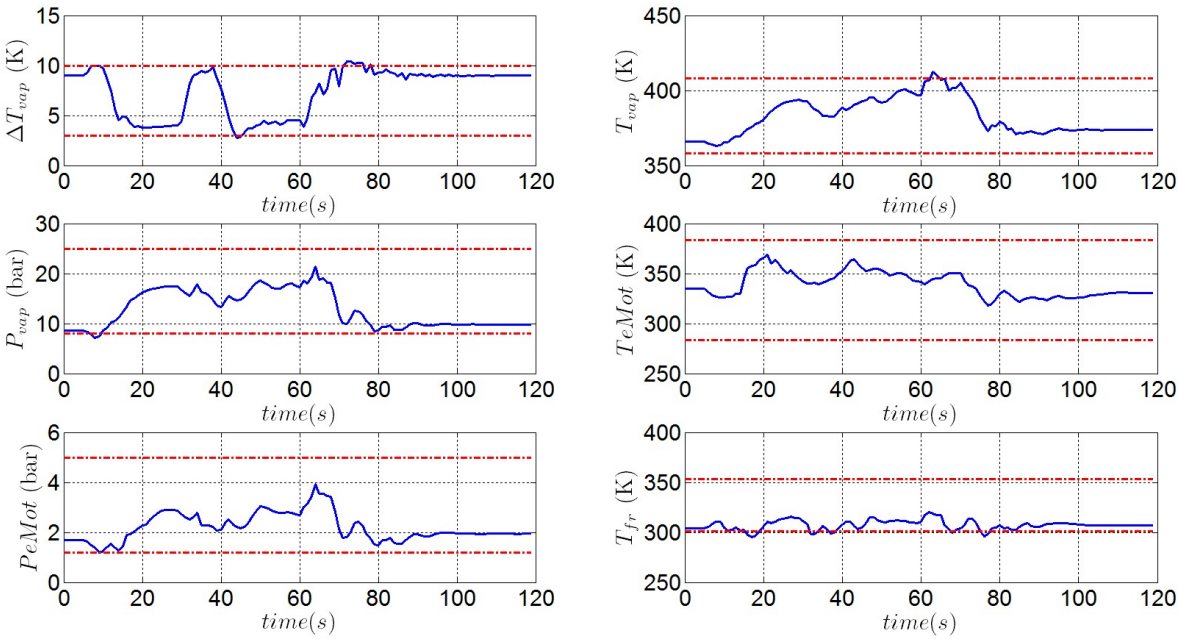

Figure 8.5: ORC system constrained variables. The red dashed lines indicate the minimum and maximum admissible values.

ambient temperature T_{amb} as depicted in Figure 8.3a. Figure 8.3b gives the tracking results for a reference electrical power P_{elec}^{ref} profile consumed by the off-grid loads. One can appreciate from Figure 8.3b the performances in term of settling time and disturbance (measured uncontrolled signals) rejection of the proposed controller since the latter one makes the ORC system converge rapidly toward the desired reference power with time responses reduced by more than half compared to the time responses obtained by EXOES (one of the MICROSOL project partners) using their PI-based control methodology (indeed, EXOES announced a time response of 30s to respond to a 1kW electrical power demand). The time responses obtained with the proposed control methodology suggest that a significant reduction in the battery bank size can be performed. Figure 8.4 gives the time profile of the controlled variables (output of the controller) and their corresponding maximum and minimum admissible values that are perfectly respected. The time profiles of the constrained thermodynamic variables of the ORC system are depicted in Figure 8.5 together with their maximum and minimum admissible values (according to Section 7.2). One can observe that these constraints are respected (and sometimes active) even though at some time instants some of the constraints slightly overshoot their limitations due to the application of the constraint softening techniques that enable the MPC solver convergence.

8.3 Conclusion

In this chapter, the global state space model of the ORC power plant was used to design a constrained optimal control strategy to reach the system objectives while respecting its constraints. The predictive controller is real time implementable and shows very good performances in simulation. Future works will focus on implementing this controller on a real time target and assess experimentally the global performance of the proposed solution.

General Conclusion and Perspectives

This thesis, prepared within the Gipsa-lab laboratory in partnership with Schneider Electric, is concerned with the modeling, simulation and control of two kinds of solar thermodynamic micro power plants that were considered as candidate power generation systems within the framework of the MICROSOL project led by Schneider Electric.

In the case of the first solar thermodynamic micro power plant, which is based on a Stirling thermodynamic engine linked to a dedicated energy conversion system developed within Schneider Electric laboratories, a nonlinear static model of the Stirling engine has been derived and its unknown parameters identified using experimental data gathered on the prototype. This model has been used to simulate the behavior of the Stirling engine with its power conversion system and to develop a cartography-based torque controller for the engine that maximizes the net thermoelectric efficiency of the system. Then, a state space model of the energy conversion system associated to the Stirling engine has been derived and used to develop a first control strategy, for the hybrid Stirling engine/supercapacitor power plant, that was validated experimentally first on a dedicated electrical motor testbed and then on the real Stirling based power system. This control strategy in addition of necessitating few design parameters endows the closed-loop system with near-to-optimal behavior in terms of settling time thus reducing the size of the supercapacitor needed as energy buffer to palliate the load power demand fast transients. Even if this developed control strategy was efficient and offers the expected performances, it does not handle explicitly the system constraints. For this reason, a second control strategy for the energy conversion system, that holds for a family of power circuits, has been developed. In addition of handling explicitly the saturation on control variables as well as on the component of the state vector, it also endows the closed-loop system with near to optimal performances in term of settling time.

In a second part, the problem of controlling optimally the energy of the second solar thermodynamic micro power plant, which is based on Organic Rankine Cycle (ORC) machines, has been addressed and solved. Prior to the control design step, one of the hurdles consisting in deriving nonlinear models for this engine has been solved using a recently developed nonlinear identification framework. Then based on linearized version of the identified model for the ORC machine, a model predictive controller has been developed that drives the system in a fast manner during load power demand transients, while respecting the physical system constraints, which enables the size reduction (at least by half) of the energy buffer consisting in the battery banks associated to the power plant. Preliminary tests on implementing the developed control strategy on a real time controller have proved the real time compatibility of the control algorithm.

The experimental data used to identify nonlinear models of the ORC power plant under consideration represent some specific operating range corresponding to tuning and calibration tests performed on the prototype. When exploring other operating ranges of the plant, one may obtain nonlinear models with a higher degree of nonlinearity. In this situation, either we

decide to apply the same control methodology, developed during this thesis, using a linearized model representing all the operating ranges and accepting some degradation of the closed loop system performances and less margins on the system constraints (however this approach has the advantage of resulting in an MPC controller whose implementablity on a real time target has been validated), or we decide to apply constrained nonlinear controllers (like NMPC controllers) that has to be validated and that will necessitate more computation resources to be implementable. This constitutes a very interesting research perspective to be investigated.

As other perspectives following the work done during this thesis, the experimental validation, on the real prototype, of the developed control strategy for the ORC based power generation system first using a fast real time target to prove the concept of the developed methodology and then implementing the control algorithms on the PLC (Programmable Logic Controller) that currently controls the ORC power plant prototype. Another interesting perspective for the present work is the investigation of ORC based power systems functioning with a variable speed turbine. Indeed, by using the speed reference of the turbine as an additional control variable, we will be able to design control strategies that make the ORC based power plant tracks some electrical reference power in a faster manner,compared to the constant speed case, thus reducing further the size of the battery bank associated to the power plant.

Since the proposed methodology for controlling the ORC based power system is quite generic and can be applied to several kinds of thermodynamic engines, it would be also interesting to investigate the applicability of this methodology to other thermal power generation systems like WHR (Waste Heat Recovery) systems which is currently the focus of many researches.

Appendix A

Résumé en français

Cette partie est un résumé en français du manuscrit de thèse. Etant donné que ce résumé n'est pas exhaustif, le lecteur est cordialement prié de se reporter à la version anglaise pour plus de détails techniques.

A.1 Introduction

Aujourd'hui, plus de 1.4 milliards de personnes n'ont pas accès à l'énergie. Ces populations, qui gagnent moins de 2 dollars par jours et dépensent plus de 15 dollars par mois et par famille pour avoir accès à l'électricité, vivent essentiellement en Inde, Indonésie, Bangladesh, Nigéria et dans certaines régions de l'Afrique sub-saharienne.

Afin d'apporter une solution pour ce problème d'accès à l'énergie pour ces populations, Schneider Electric a lancé un projet collaboratif appelé MICROSOL qui œuvre pour le développement de micros centrales solaires thermodynamiques utilisant l'énergie thermique du soleil pour produire de l'électricité. Le marché visé par le projet MICROSOL étant celui de l'électrification rurale pour des sites "isolés" qui ne sont pas connectés au réseau électrique ou bien qui disposent d'un réseau électrique très peu fiable. Ces centrales solaires doivent fournir au minimum $150kWh_{elec}$ par jour et fonctionner 24h/24 grâce à un stockage d'énergie thermique approprié. De plus, ces centrales doivent être fiables, respectueuses de l'environnement et accessibles à des populations ne disposant pas de beaucoup de ressources financières mais qui sont situés dans des zones ayant un fort potentiel d'ensoleillement.

La Figure A.1 donne le schéma d'une micro centrale solaire thermodynamique typique. L'un de ses principaux éléments est le champ de collecteurs solaires qui utilise l'énergie thermique du soleil pour chauffer un fluide caloporteur qui, dans le cadre du projet MICROSOL, est simplement de l'eau pressurisée afin d'être respectueux de l'environnement. Cette eau ainsi chauffée sera par la suite stockée dans une cuve qui doit assurer un minimum de pertes thermiques. La centrale solaire se compose également d'une boucle de refroidissement qui permet de refroidir un autre fluide caloporteur. Les deux fluides, chaud et froid, entrent à l'intérieur d'une machine thermodynamique qui utilise le gradient de température (entre la source chaude et la source froide) pour fournir un travail mécanique en effectuant un cycle thermodynamique adéquat. Ce travail mécanique généré sert à entrainer une génératrice électrique produisant de l'électricité qui sera conditionnée grâce à un système de conversion d'énergie adéquat qui s'interface entre la génératrice électrique et la charge électrique isolée que l'on veut alimenter.

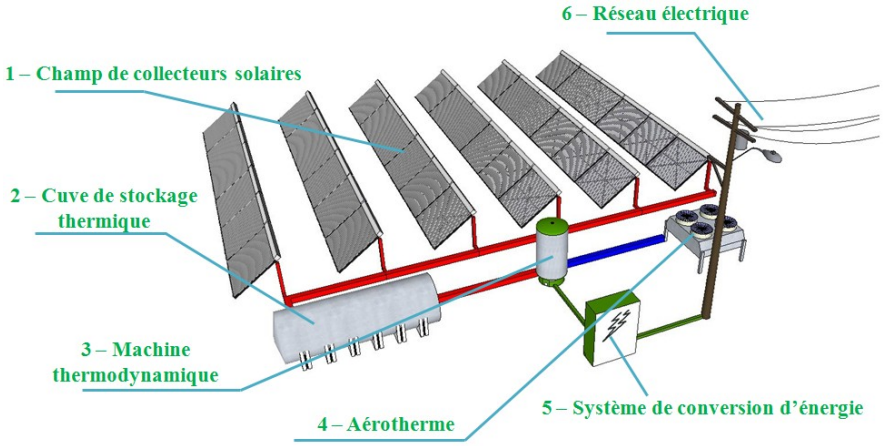

Figure A.1: Schéma global d'une micro centrale solaire thermodynamique

Dans le cadre du projet MICROSOL deux variantes de cette centrale solaire thermodynamique ont été considéré suivant les niveaux de température et pression de la source chaude:

- La première variante utilise des collecteurs solaires à base de tubes sous vide fixes qui chauffent de l'eau, pressurisée à un maximum de 10 bars, entre $110°C$ et $150°C$. Pour cette variante, une machine thermodynamique à cycle de Stirling est utilisée pour produire de l'électricité.
- La deuxième variante utilise des collecteurs solaires à base de miroirs cylindro-paraboliques, avec un système de suivi solaire, qui chauffent de l'eau, pressurisée à un maximum de 15 bars, entre $140°C$ et $180°C$. Pour cette variante, une machine thermodynamique à Cycle de Rankine Organique (ORC) est utilisée pour produire de l'électricité.

L'objectif de cette thèse étant l'élaboration de lois de commande performantes pour la gestion de l'énergie électrique de ces deux types de micro centrales solaire thermodynamiques.

A.2 Micro Centrale solaire thermodynamique à base d'une machine Stirling

Cette section résume les principaux résultats de la *Partie I* du manuscrit de thèse qui porte sur la gestion de l'énergie électrique d'une centrale solaire thermodynamique utilisant une machine à cycle de Stirling associée à un système de conversion d'énergie approprié. Le schéma d'une telle centrale est illustré à la Figure A.2

Lorsque la charge électrique varie, le moteur Stirling doit adapter sa puissance produite afin de compenser celle consommée par la charge électrique mais étant donné que la machine Stirling adapte sa puissance lentement vu son inertie mécanique et thermique, l'hybridation

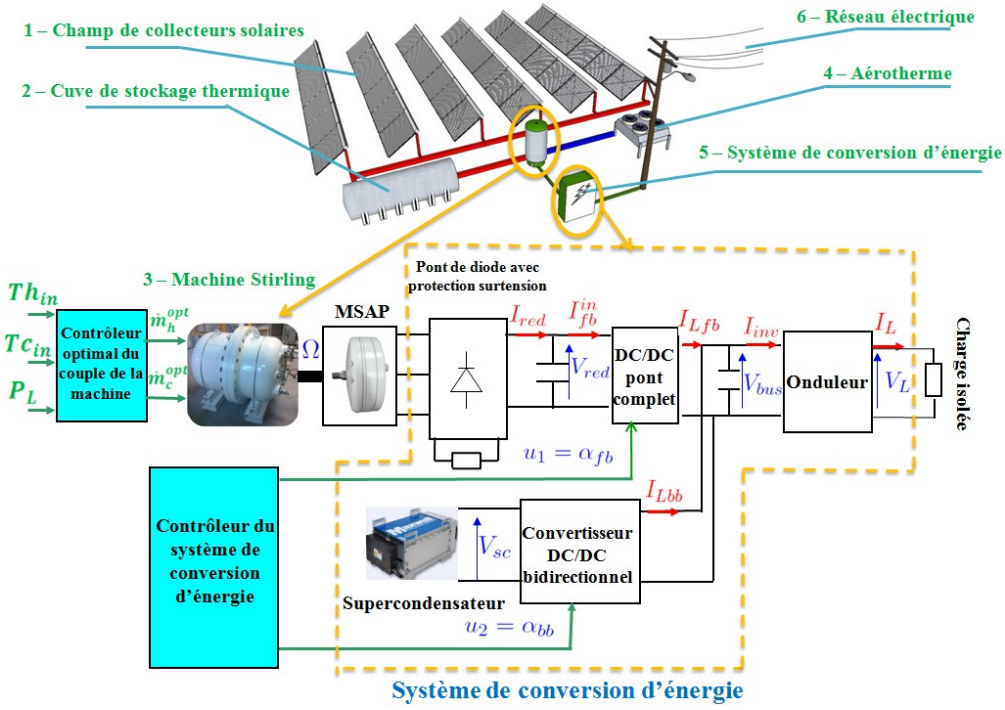

Figure A.2: Schéma global d'une micro centrale solaire thermodynamique à base d'un moteur Stirling

avec un dispositif de stockage électrique est nécessaire, d'où l'ajout du supercondensateur associé au système de conversion de l'énergie (Figure A.2). Ce supercondensateur sert à répondre aux transitoires rapides des appels de puissances de la charge électrique pendant que la machine Stirling adapte sa puissance d'une manière plus lente. L'objectif de contrôle étant de faire passer la machine Stirling d'un point de fonctionnement en puissance à un autre le plus rapidement possible afin de diminuer la taille du supercondensateur.

Etant donné que la puissance fournie par la machine Stirling est égale à son couple moteur fois la vitesse de rotation de l'arbre moteur et que ces deux grandeurs évoluent dans deux échelles de temps différentes, la synthèse des deux contrôleurs pour ces 2 grandeurs d'une manière indépendante est justifiée. Ainsi un premier contrôleur du couple du moteur Stirling a été développé en se basant sur un modèle statique de la machine validé expérimentalement.

Pour réguler la vitesse de rotation de l'arbre moteur, on agit sur le système de conversion de l'énergie. Ainsi deux lois de commande ont été développées à cet effet. La première loi de commande qui a été développée et qui a été validée expérimentalement gère explicitement les saturations sur les variables de contrôle du système de conversion d'énergie et dote le système en boucle fermé de performances quasi optimales en terme de temps de réponse. Cependant, cette première loi de commande ne gère pas explicitement les contraintes sur tous les états du système. Pour pallier à cette limitation, une deuxième loi de commande a été développée en se basant sur le principe des modes glissants.

A.2.1 Modèle statique non linéaire d'une machine Stirling et contrôle de son couple moteur

La machine Stirling que nous avons à disposition et qui est étudiée dans le cadre de cette thèse est une machine de type alpha[1] qui est constituée d'un ensemble de 3 cycles liés mécaniquement à un arbre moteur. Chaque cycle est constitué d'un ensemble de deux cylindres-pistons connectés au travers d'un régénérateur. Un des cylindres est connecté grâce à un premier échangeur de chaleur à la source chaude tandis que l'autre cylindre est connecté à la source froide à travers un autre échangeur de chaleur. La machine Stirling fournit un travail mécanique, qui sert à entrainer une Génératrice Synchrone à Aimants Permanents (MSAP), en effectuant un cycle thermodynamique fermé (qui est subit par le gaz de travail dans les cylindres et le régénérateur) à chaque rotation complète de l'arbre moteur comme illustré à la Figure A.3 dans le plan Pression-Volume (P-V).

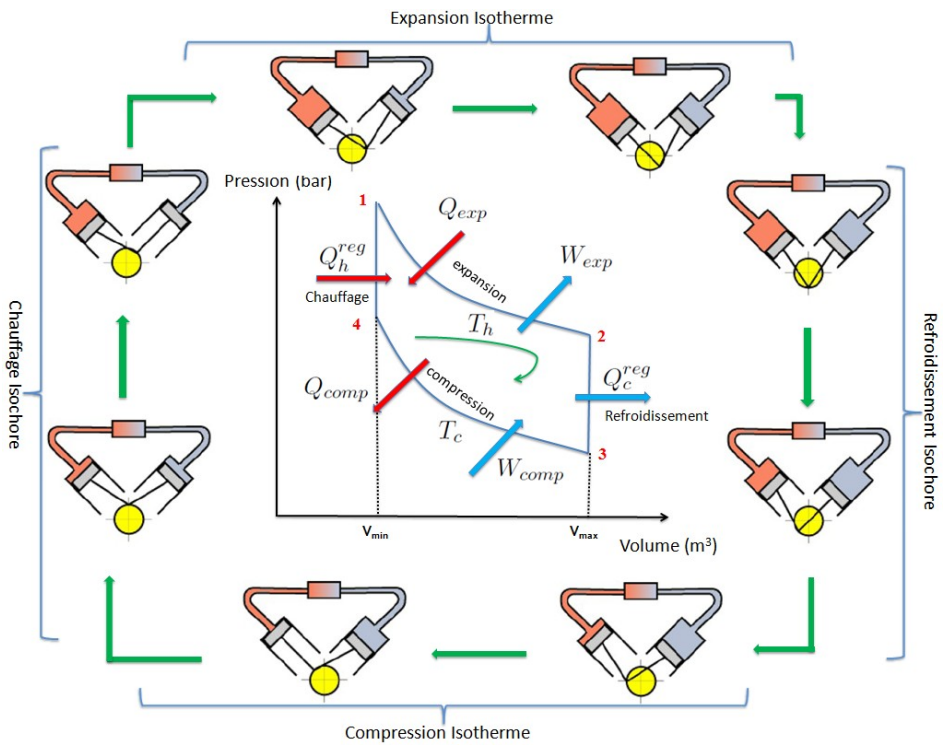

Figure A.3: diagramme Pression-Volume (P-V) du cycle de Stirling et position des pistons pour un moteur Stirling de type alpha pendant un cycle complet.

Pour modéliser en régime statique la machine Stirling, nous avons utilisé un modèle issu de la littérature qui se base sur l'analyse de Schmidt [Urieli and Berchowitz, 1984] qui établit un bilan de puissance parfait dans la machine et qui dépend des paramètres dimensionnant de

[1] http://www.ohio.edu/mechanical/stirling/

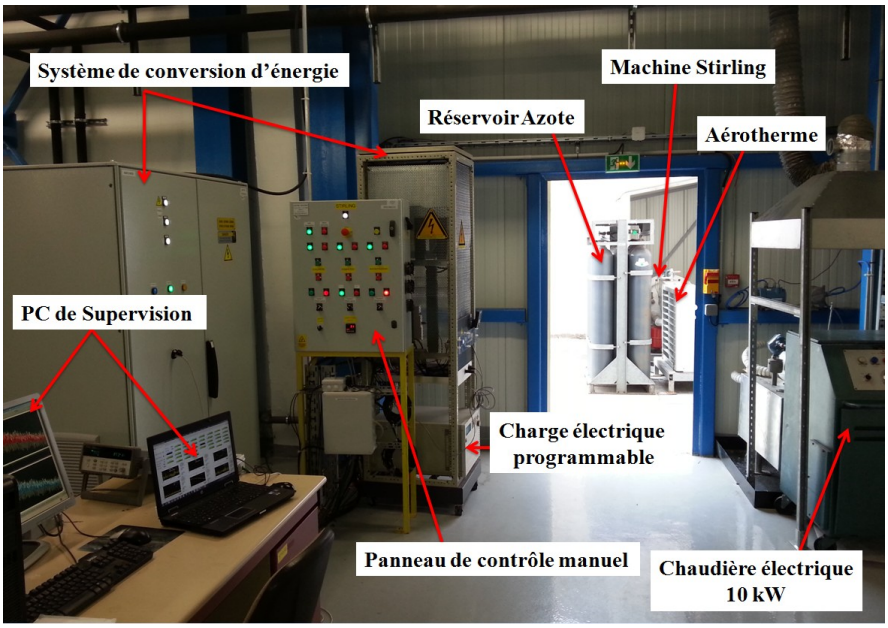

Figure A.4: Vue d'ensemble du système de production d'électricité à base de machine Stirling.

cette dernière. Cette analyse étant parfaite doit être augmenté par un ensemble d'équations qui décrivent les échanges thermique à travers les échangeurs de chaleur et le régénérateur et qui tiennent compte des pertes thermique. Il en résulte un modèle statique non linéaire (équations (3.30), (3.31) et (3.32) du manuscrit de thèse) avec 15 paramètres inconnus à identifier. Pour cela nous avons effectué une compagne de tests de caractérisation de la machine sur un prototype fonctionnel illustré à la Figure A.4 et recueillis des données expérimentales correspondantes à plusieurs points de fonctionnement qui ont été utilisé pour identifier les paramètres inconnus tel qu'illustré à la Figure A.5. Les Figures A.6 et A.7 donnent les résultats d'identification des paramètres inconnus où l'on compare certaines variables issues du modèle avec les variables mesurées correspondantes (La ligne verte étant la ligne identité). D'après les Figures A.6 et A.7, la plupart des points se situent autour de la courbe identité (en vert) ce qui nous amène à conclure que le modèle statique du Stirling que nous avons établi s'approche bien de la réalité.

Une fois que le modèle du Stirling établi, nous l'avons utilisé pour développer un contrôleur du couple de la machine qui doit établir, en fonction des températures chaudes et froides en entrées du Stirling (respectivement Th_{in} et Tc_{in}) et de la puissance électrique consommée P_L, les débits massiques optimaux du coté de la source chaude et du coté de la source froide (respectivement $\dot{m}_h^{opt}$ et $\dot{m}_c^{opt}$) qui maximisent le rendement thermoélectrique net (en excluant la puissance électrique consommée par les pompes P_{elec}^{pumps}) du Stirling. Ceci se traduit mathématiquement par:

$$(\dot{m}_h^{opt}, \dot{m}_c^{opt}) = \arg\max_{\dot{m}_h, \dot{m}_c} \eta_{thermoelectric}^{net} = \frac{P_{elec}^{load} - P_{elec}^{pumps}}{\dot{Q}_{exp}} \tag{A.1}$$

où $\dot{Q}_{exp}$ est la puissance thermique absorbée depuis la source chaude.

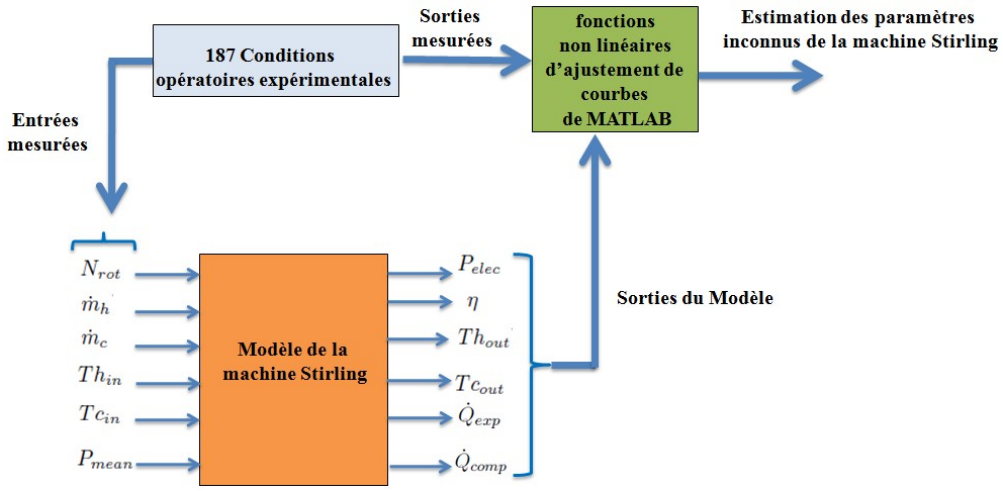

Figure A.5: Procédure d'identification des paramètres inconnus du modèle de la machine Stirling.

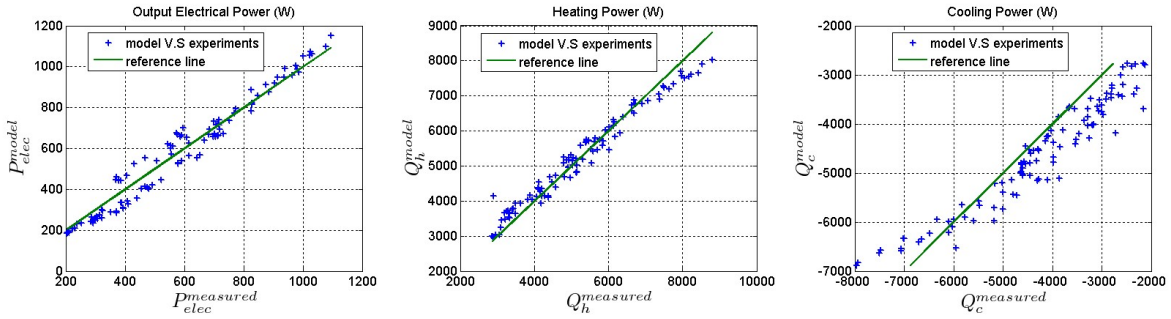

Figure A.6: Comparaison entre les valeurs mesurées et théoriques de: la puissance électrique produite, de la puissance thermiques absorbée et de la puissance thermique rejetée.

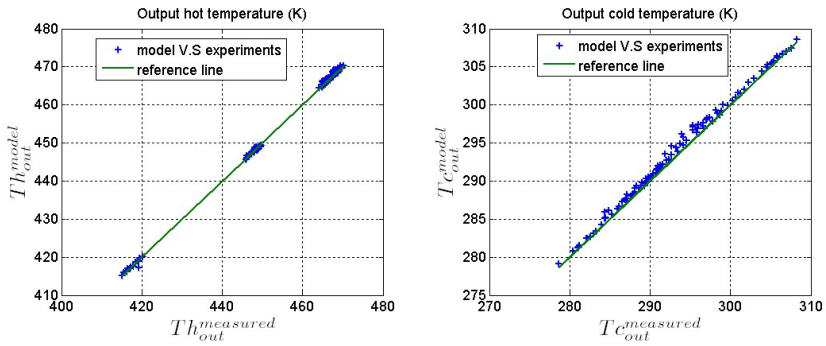

Figure A.7: Comparaison entre les valeurs mesurées et théoriques des températures chaude et froide en sortie de la machine Stirling.

Etant donné la complexité du modèle de la machine Stirling, nous avons préféré utiliser des cartographies calculées hors lignes résultantes du problème d'optimisation A.1 afin d'établir les débits optimaux en fonction des conditions opératoires.

A.2.2 Contrôle du système de conversion d'énergie associé à la machine Stirling

Une fois le contrôle du couple de la machine Stirling établi, nous nous sommes intéressé au contrôle de son système de conversion d'énergie associé dont l'architecture est illustrée à la Figure A.2. Ce système de conversion d'énergie se compose d'un pont de diodes connecté à la Machine Synchrone à Aimant Permanent (MSAP) et à un premier convertisseur DC/DC à pont complet contrôlable grâce à son rapport cyclique $u_1 = \alpha_{fb}$. Le convertisseur DC/DC à pont complet est lui même connecté à un bus continu. Un deuxième convertisseur DC/DC bidirectionnel en courant contrôlable grâce à son rapport cyclique $u_2 = \alpha_{bb}$ s'interface entre le bus continu et le supercondensateur. Le bus continu est ensuite connecté à un onduleur commercial autorégulé qui alimente la charge électrique isolée que l'on veut alimenter avec une tension AC 230V 50Hz.

La première étape pour contrôler ce système a consisté à établir son modèle dynamique qui est donné par les équations suivantes mises sous forme d'état:

$$\dot{x}_1 = a_1.x_1 - a_3.x_2 + a_2 \tag{A.2a}$$

$$\dot{x}_2 = -a_4.x_2 - a_5.x_1.x_2 + a_6.x_1 - a_7.x_3 \tag{A.2b}$$

$$\dot{x}_3 = a_8.x_2 - a_8.k.x_4.u_1 \tag{A.2c}$$

$$\dot{x}_4 = -a_9.x_5 + k.a_9.x_3.u_1 \tag{A.2d}$$

$$\dot{x}_5 = a_{10}.(x_4 + x_6) - \frac{a_{10}}{\eta_{inv}}.\frac{P_L}{x_5} \tag{A.2e}$$

$$\dot{x}_6 = -a_{11}.x_5 + a_{11}.x_7.u_2 \tag{A.2f}$$

$$\dot{x}_7 = -a_{12}.x_6.u_2 \tag{A.2g}$$

Où: $x_1 = \Omega$, $x_2 = I_{red}$, $x_3 = V_{red}$, $x_4 = I_{Lfb}$, $x_5 = V_{bus}$, $x_6 = I_{Lbb}$, $x_7 = V_{sc}$, $u_1 = \alpha_{fb}$ et $u_2 = \alpha_{bb}$ avec V dénotant une tension et I dénotant un courant (se référer à la Figure A.2). Les paramètres a_i dépendent de certaines grandeurs physiques du système (k et η_{inv} sont quand à eux des grandeurs physiques). En particulier a_1 et a_2 dépendent entre autre du couple moteur de la machine Stirling dont l'équation a été identifiée expérimentalement.

Les objectifs de contrôle pour ce système sont:

- La régulation d'une manière assez raide de la tension du bus continu x_5=V_{bus} autour de x_5^{st}=V_{bus}^{ref}=50V compatible avec un bon fonctionnement de l'onduleur commercial autorégulé.
- La régulation de la tension du supercondensateur x_7=V_{sc} autour de x_7^{st}=V_{sc}^{ref}, d'une manière plus lente, afin d'avoir une quantité d'énergie tampon adéquate.

Ce système est soumis aux contraintes suivantes:

✓ **Contraintes de positivité**: $x_i \geq 0$ à l'exception de x_6.

✓ **Fortes saturations sur les variables de contrôle**:

- $u_1 \in [0, 1]$: rapport cyclique du convertisseur DC/DC à pont complet.
- $u_2 \in [0, 1]$: rapport cyclique du convertisseur DC/DC bidirectionnel en courant.

De plus, le système de conversion d'énergie est sujet aux perturbations suivantes:

- P_L: Puissance électrique consommée par la charge isolée qui peut varier d'une manière très rapide.
- Th_{in} et Tc_{in}: Températures d'entrée du Stirling respectivement du coté de la source chaude et de la source froide. Ces températures qui entrent dans la définition des paramètres a_1 et a_2 dans (A.2a), ont une variation très lente comparée à la dynamique de la partie électrique.

A.2.2.1 Développement d'une première loi de commande pour le système de conversion d'énergie associé au moteur Stirling

Vu la structure du modèle du système de conversion d'énergie donné par (A.2a)-(A.2g), il est possible, en négligent le terme "$a_5.x_1.x_2$" correspondant à l'empiétement du pont de diodes, de décomposer le système en deux sous-systèmes qui évoluent dans deux échelles de temps différentes:

1) **Le premier sous-système (sous-système 1)** donné par (A.2a)-(A.2d) ne dépend que de u_1 comme variable de contrôle et de a_2 comme signal exogène qui dépend du couple moteur du Stirling. Ce premier sous système dépend également de x_5 qui est supposé parfaitement régulé autour de sa valeur désirée x_5^{st} en utilisant les équations du deuxième sous-système. Ainsi le sous-système 1 peut se récrire comme suit:

$$\dot{z} = A(u_1).z + B.\begin{pmatrix} a_2 \\ x_5^{st} \end{pmatrix} \tag{A.3}$$

où $z = \begin{pmatrix} x_1 & x_2 & x_3 & x_4 \end{pmatrix}^T$ est un vecteur d'état réduit.

2) **Le deuxième sous-système (sous-système 2)** correspond aux équations (A.2e)-(A.2g) qui ne dépendent que de u_2 comme variable de commande.

Les deux sous-systèmes sont liés grâce à la variable d'état x_4. La Figure A.8 donne l'architecture de la première loi de commande développée pour le système de conversion d'énergie associé à la machine Stirling.

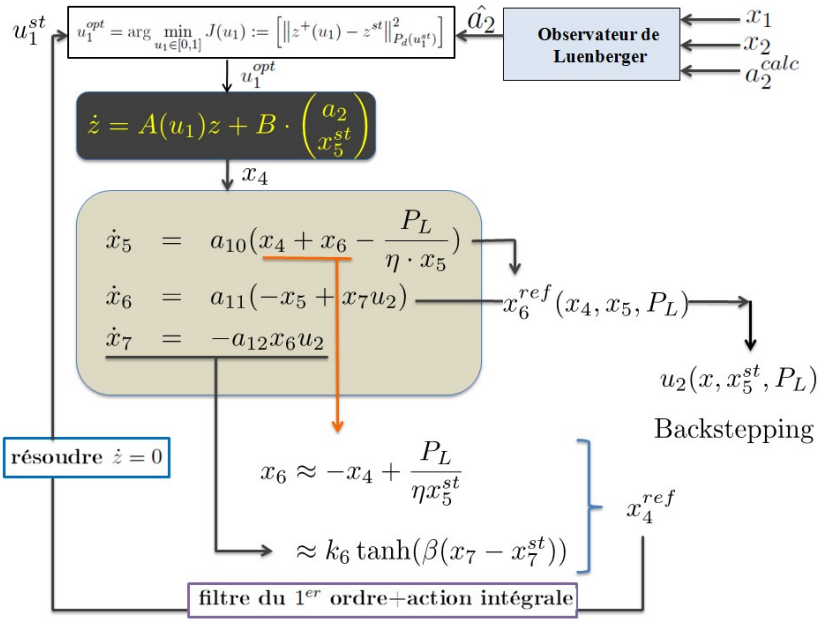

Figure A.8: Architecture de la première loi de commande pour le système de conversion d'énergie associé à la machine Stirling.

Ainsi un contrôleur par backstepping (voir [Khalil, 1996]) sert à réguler x_5 autour de x_5^{st} d'une manière assez raide en utilisant les équations du sous-système 2. Pour réguler la tension du supercondensateur x_7 autour de sa valeur stationnaire x_7^{st}, on impose à x_6 en régime stationnaire la valeur suivante:

$$x_6^{st} = k_6 . \tanh(\beta.(x_7 - x_7^{st})) \tag{A.4}$$

où k_6 and β sont des paramètres de réglage.

On aboutit ainsi à la définition de la valeur de référence x_4^{ref} ci-dessous qui devra être suivie en utilisant les équations du sous-système 1:

$$x_4^{ref} = -k_6 . \tanh(\beta.(x_7 - x_7^{st})) + \frac{P_L}{\eta_{inv}.x_5^{st}} \tag{A.5}$$

Pour cela connaissant x_4^{ref} on définit une nouvelle valeur de référence $\bar{x_4}^{st}$ issue du filtrage de x_4 (pour lisser certains effets d'undershoot et d'overshoot) et de l'ajout d'un intégrateur lent (pour corriger certaines erreurs du modèle) et on résout les équations correspondantes à $\dot{z} = 0$ pour déterminer le vecteur z^{st} qui sera régulé en utilisant un contrôleur prédictif à un pas appliqué aux équations du sous-système 1 (Figure A.8). Il est à noter, d'après la Figure A.8, l'ajout d'un observateur de Luenberger (voir [Besançon, 2007]) qui sert à estimer les erreurs d'identification du couple de la machine Stirling intervenant dans le paramètre a_2 de l'équation d'état (A.2a).

Avant de valider cette première loi de commande sur le prototype à base de moteur Stirling (Figure A.4), nous l'avons d'abord validé sur un banc moteur électrique illustré à la Figure

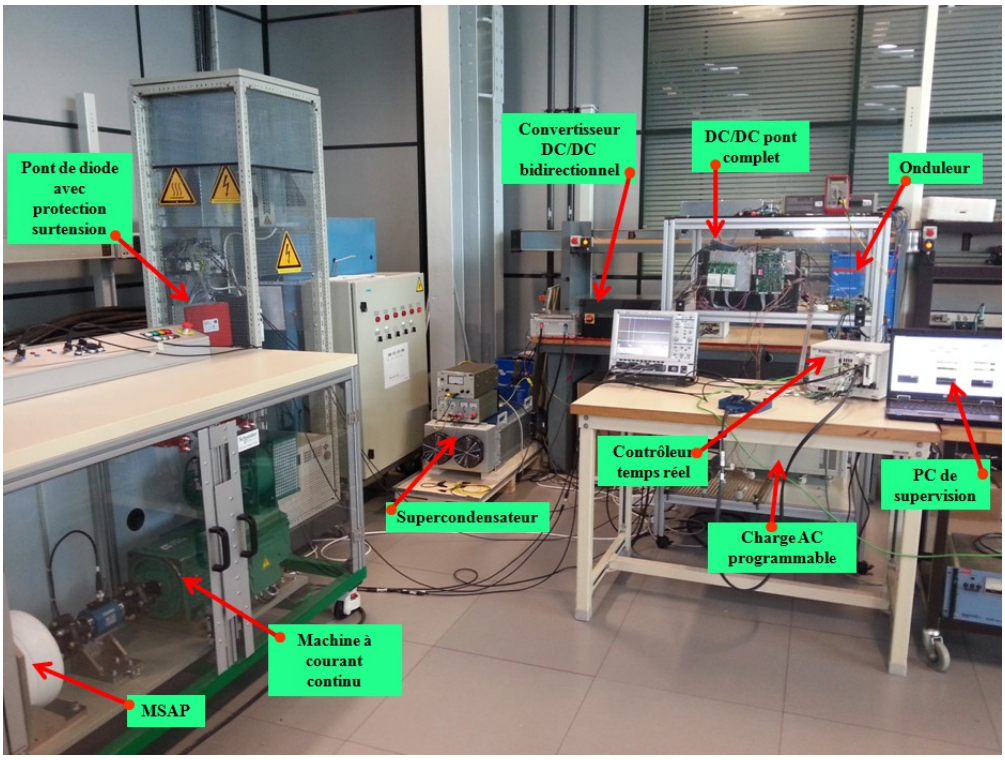

Figure A.9: Banc moteur électrique utilisé pour la validation expérimentale de la première loi de commande pour le système de conversion d'énergie associé au moteur Stirling.

A.9 où l'on reproduit le fonctionnement de la machine Stirling grâce à une machine à courant continu pilotée en couple (grâce à un variateur de couple commercial). Une fois que la loi de commande a été validé sur ce banc moteur électrique, nous l'avons par la suite validé sur le prototype de la Figure A.4 qui utilise une machine Stirling.

Ainsi, la Figure A.10 donne les résultats expérimentaux qui valident cette première loi de commande (sur le prototype de la Figure A.4) pour le système de conversion d'énergie associé à la machine Stirling. Ainsi on peut voir d'après la Figure A.10 que malgré les appels de puissance de la charge électrique P_L, le bus continu $x_5 = V_{bus}$ est bien régulé autour de sa valeur désirée de même que la tension du supercondensateur $x_7 = V_{sc}$. Les autres variables d'état x_1, x_2, x_3 et x_4 convergent eux aussi vers leurs valeurs de références calculées. Il est à noter d'après la Figure A.10 qu'entre $t = 24$s et $t = 27$s, la charge électrique a été déconnectée alors qu'il y a un couple moteur appliqué ce qui conduit à la saturation de $u_1 = \alpha_{fb}$ entrainant les états x_1, x_2, x_3 et x_4 à ne plus suivre leurs états désirés et la tension du supercondensateur à augmenter jusqu'à la reconnexion de la charge électrique.

Parmi les avantages de cette première loi de commande développée pour le système de conversion d'énergie:

- La géstion explicite les saturations sur les variables de contrôle.

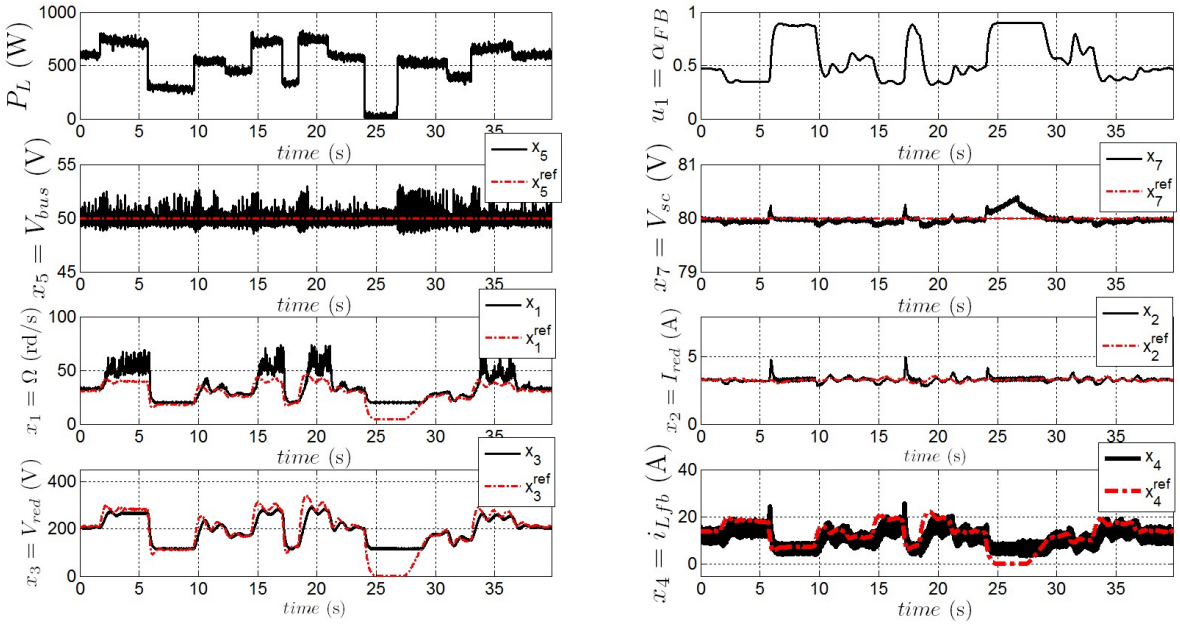

Figure A.10: Résultats expérimentaux validant la validation de la première loi de commande pour le système de conversion d'énergie associé au moteur Stirling.

- Le fait qu'elle nécessite peu de paramètres de réglage.
- Le fait qu'elle est compatible temps réel.

Cependant cette loi de commande ne gère pas explicitement les contraintes sur les variables d'état du système, à la place, un filtre ad-hoc a été introduit pour élargir le domaine de validité de la loi de commande ce qui conduit à ralentir inconditionnellement le système. Pour pallier à cette limitation une deuxième loi de commande a été développée en se basant sur le principe des modes glissants.

A.2.2.2 Développement d'une deuxième loi de commande sous contrainte pour le système de conversion d'énergie associé au moteur Stirling

D'une manière similaire à la première loi de commande développée, les équations du sous-système 2 servent à réguler x_5 autour de x_5^{st} et à générer une valeur de référence pour x4, soit x_4^{ref} donnée par (A.5) qui sert à réguler la tension du supercondensateur x_7 autour de sa valeur de référence x_7^{st}. Par la suite x_4^{ref} sera régulée en utilisant les équations du premier sous système.

Préalablement à cela, des limitations dynamique sur x_3, qui tiennent compte des valeurs minimum et maximum admissibles pour x_2 et x_3, ont été établi d'une manière explicite (Se référer au Chapitre 6 pour plus de détails concernant la définition de ces limitations dy-

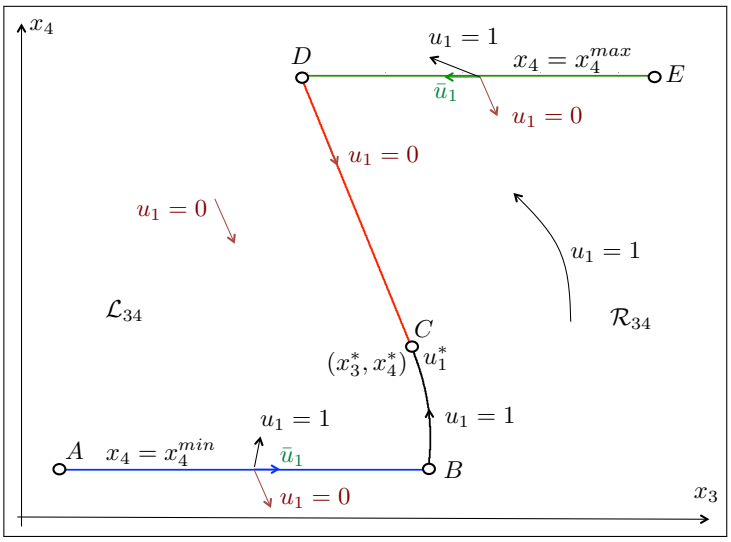

Figure A.11: Disposition typique des champs de vecteurs pour le système dynamique (A.2c)-(A.2d) quand $x_2 = x_2^{st}(x_3^*)$ et $x_5 = x_5^r$ sont supposés constants.

namiques):

$$x_3(t) \in \left[\underline{x}_3\big(x_1, x_2, x_3^{min}, x_2^{max}\big), \bar{x}_3\big(x_1, x_2, x_3^{max}, x_2^{min}\big)\right]$$

Grâce à ces limitations dynamiques et à la connaissance de x_4^{ref}, une nouvelle paire de variables de référence (x_3^*, x_4^*) est calculée et sous certaines conditions adéquates et validées une analyse graphique des champs de vecteurs de (A.2c)-(A.2d) dans le plan de phase (x_3, x_4) peut etre effectuée pour atteindre la paire désirée comme illustré à la Figure A.11. Ainsi on peut déterminer une surface de glissement ABCDE (Figure A.11) qui passe par la paire désirée (x_3^*, x_4^*) et qui respecte les limitations sur x_4. Cette surface de glissement a les propriétés suivantes:

- Si un point dans le plan de phase (x_3, x_4) se situe sur la surface de glissement, en appliquant la commande appropriée u_1, on atteint en un minimum de temps la paire désirée (x_3^*, x_4^*).
- La surface de glissement ABCDE est attractive.

Pour atteindre une paire désirée (x_5^{st}, x_6^r), la même analyse graphique dans le plan de phase (x_5, x_6) peut être effectuée.

Afin d'illustrer les performances de cette deuxième loi de commande développée pour le système de conversion d'énergie associé à la machine Stirling, des simulations ont été effectuées. La Figure A.12 donne quelques résultats de simulation du contrôle du premier sous-système (découplé du second). Ainsi, d'après cette figure, pour atteindre une valeur désirée x_4^d, des limitations dynamiques sur x_3 ($\underline{x}_3(.)$ et $\bar{x}_3(.)$) sont calculés en tenant compte de l'état actuel et de x_2^{min}, x_2^{max}, x_3^{min} et x_3^{max}. Connaissant ces limitations dynamiques ainsi que x_4^d une

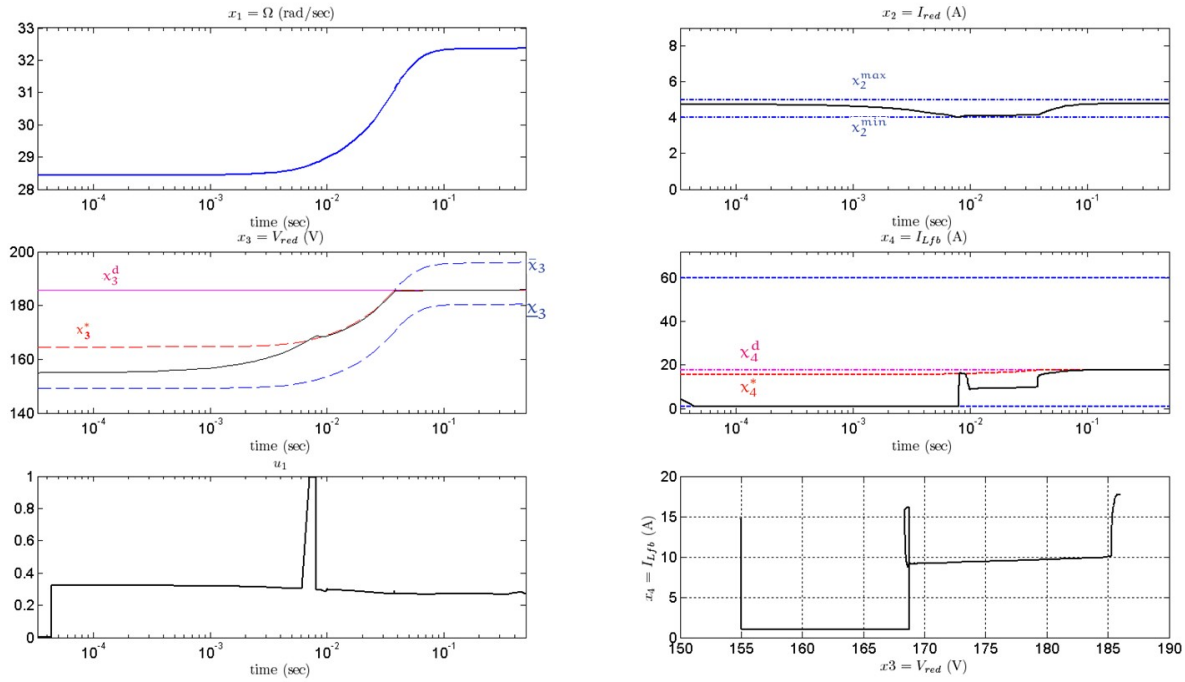

Figure A.12: Contrôle du système (x_3, x_4) sous $x_5 = x_5^d$ après un changement de +20% pour la valeur désirée x_4^d. Il est à remarquer que les limitations sur x_3 ralentissent le temps de réponse du système afin de garantir le respect des contraintes sur x_2.

nouvelle paire désirée (x_3^*, x_4^*) est recalculée et suivie tout en respectant les contraintes du système.

A.3 Micro Centrale solaire thermodynamique à base d'une machine ORC

Cette section résume les principaux résultats de la *Partie II* du manuscrit de thèse qui porte sur la gestion de l'énergie électrique d'une centrale solaire thermodynamique utilisant une machine à Cycle de Rankine Organique (ORC) associé à un système de conversion d'énergie commercial autorégulé. Le schéma d'une telle centrale est illustré à la Figure A.13

A.3.1 Présentation de la machine ORC considérée

La Figure A.14 illustre le schéma de la machine ORC seule. Cette dernière se compose d'une première boucle d'eau chaude qui permet faire circuler l'eau stockée dans la cuve thermique. L'eau chaude transmet sa chaleur à une boucle de travail interne à travers deux évaporateurs. Cette boucle de travail, dans laquelle circule un fluide organique, se compose d'une pompe

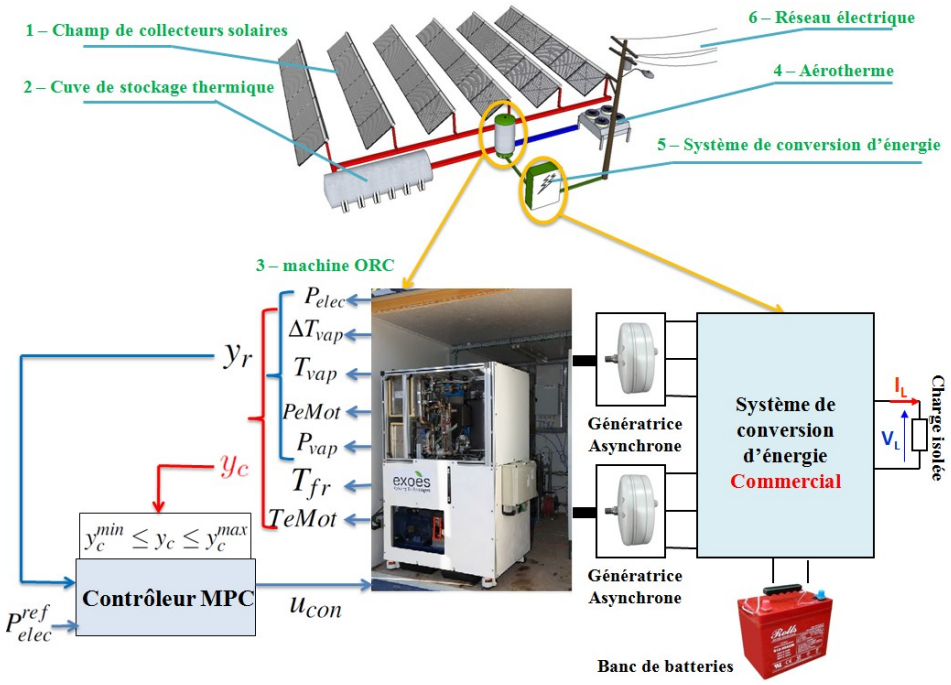

Figure A.13: Schéma global d'une micro centrale solaire thermodynamique à base d'une machine ORC

volumétrique, d'un récupérateur de chaleur et de deux turbines scroll (voir [Quoilin, 2011]) entrainant deux génératrices électriques asynchrones connectées électriquement à un système de conversion d'énergie, à base de produits commerciaux, qui s'interface avec la charge électrique que le veux alimenter. La machine ORC se compose également d'une boucle de refroidissement, constituée d'une pompe de circulation et d'un aérotherme, permettant d'absorber de la chaleur depuis la boucle de travail interne à travers deux condenseurs.

La machine ORC utilise un cycle thermodynamique de Rankine fermé illustré à la Figure A.15 dans le plan Température-Entropie (T-S). Il es résulte de cycle thermodynamique un couple moteur positif qui sert à entrainer les génératrices électriques couplées aux deux turbines.

Dans le cas de la machine ORC considérée dans cette thèse, la vitesse de rotation des turbines est fixe. Ainsi, pour modifier la puissance fournie par la machine ORC, on ne peut agir que sur son couple moteur produit à travers la partie thermo-hydraulique. Là encore, l'objectif de contrôle pour ce système est de faire passer la machine ORC d'un point de fonctionnement à un autre le plus rapidement possible tout en respectant ses contraintes physiques afin de diminuer la taille des batteries (source d'énergie tampon) associées à la machine ORC et pour cela des lois de commande performantes doivent être développées. Pour ce faire, nous avons au préalable identifié des modèles dynamiques de la machine ORC en utilisant des données expérimentales recueillis sur un prototype fonctionnel illustré à la Figure A.16, puis nous avons

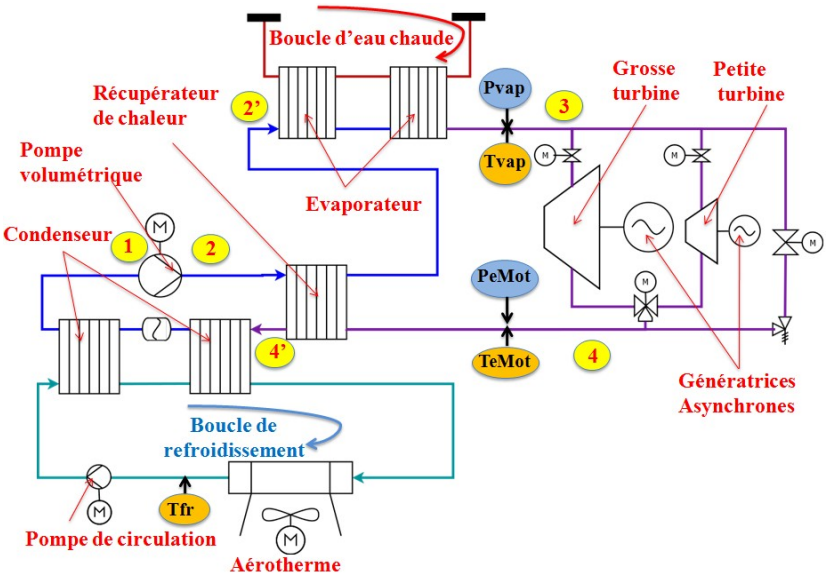

Figure A.14: Schéma du système de production d'électricité à base d'une machine à cycle de Rankine organique (ORC).

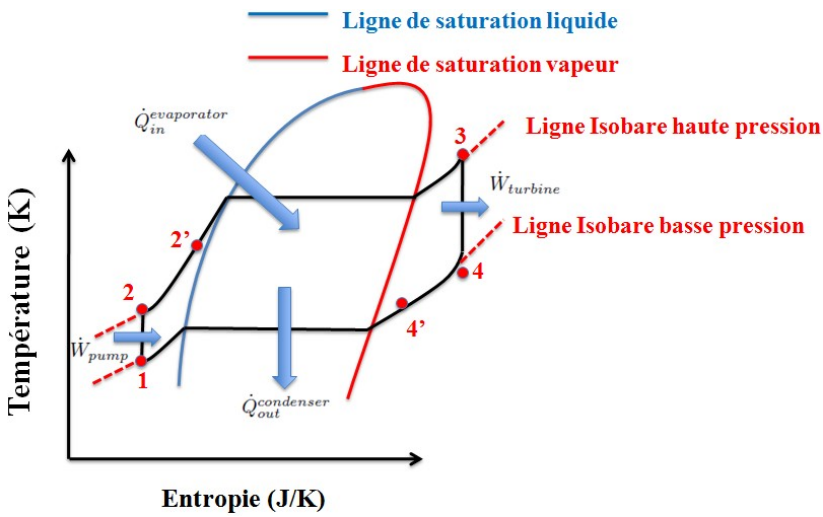

Figure A.15: diagramme Température-Entropie (T-S) du système de production d'électricité à base d'une machine à cycle de Rankine organique (ORC).

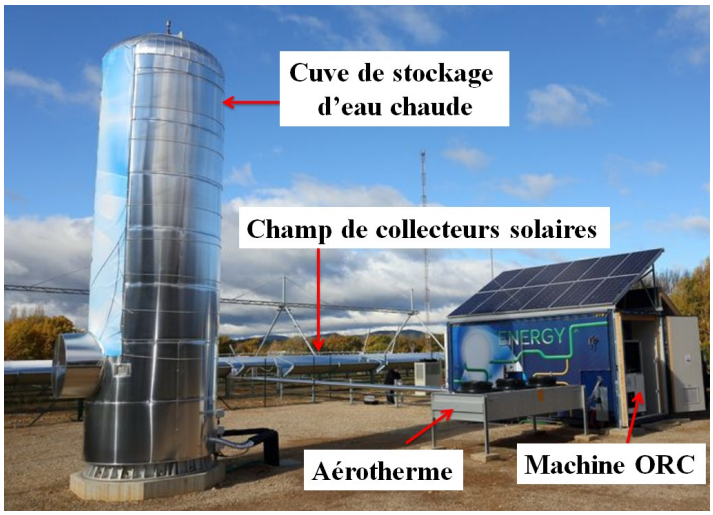

Figure A.16: Prototype du système de production d'électricité à base de machine ORC

utilisé ces modèles pour synthétiser un contrôleur prédictif MPC[2] de la machine qui régule la puissance fournie par cette dernière tout en respectant ses contraintes physiques (Figure A.13). Nous avons par la suite validé l'implémentabilité du contrôleur MPC développé sur une cible temps réel National Instrument en utilisant le solveur open source QPOASES[3] pour la résolution du problème d'optimisation quadratique QP[4] associé au contrôleur MPC.

A.3.2 Objectifs de controle et contraintes du système

D'après les discutions de la Section A.3.1, l'objectif de contrôle pour la machine ORC considérée est de réguler sa puissance électrique produite P_{elec} pour qu'elle soit égale à celle consommée par la charge électrique que l'on veut alimenter P_{elec}^{ref} et ceci le rapidement possible, afin de diminuer le nombre de batteries nécessaires comme source d'énergie tampon, tout en respectant les contraintes physiques du système qui sont comme suit (se référer à la Figure

[2]Model Predictive Control
[3]`http://www.coin-or.org/qpOASES/doc/3.0/manual.pdf`
[4]Quadratic Programming

A.14):

$$3°C \leq \Delta T_{vap} \leq 15°C \tag{A.6a}$$
$$85°C \leq T_{vap} \leq 135°C \tag{A.6b}$$
$$8bar \leq P_{vap} \leq 25bar \tag{A.6c}$$
$$TeMot \leq 110°C \tag{A.6d}$$
$$1.7bar \leq PeMot \leq 7bar \tag{A.6e}$$
$$30°C \leq T_{fr} \leq 80°C \tag{A.6f}$$
$$1 \leq f_{pump} \leq 50Hz \tag{A.6g}$$
$$0 \leq \dot{V}_{hot} \leq 6000l/h \tag{A.6h}$$
$$10\% \leq V_{rot}^{aero} \leq 100\% \tag{A.6i}$$
$$10\% \leq V_{rot}^{circ} \leq 100\% \tag{A.6j}$$

où ΔT_{vap} est la valeur de la surchauffe en entrée de la turbine donnée par:

$$\Delta T_{vap} = T_{vap} - T_{sat}(P_{vap}) \tag{A.7}$$

avec T_{sat} la température de saturation du fluide de travail.

f_{pump}, $\dot{V}_{hot}$, V_{rot}^{aero}, et V_{rot}^{circ} sont les 4 variables de contrôle du système et représentent respectivement la fréquence de rotation du moteur de la pompe volumétrique de la boucle interne, le débit volumique de la pompe de la boucle d'eau chaude, la vitesse de rotation relative de l'aérotherme et la vitesse de rotation relative du moteur de la pompe de circulation de la boucle froide.

De plus la machine ORC est soumise aux perturbations (variables exogènes non controlables) mesurables suivantes:

- $TaCh$: température en Kelvin de l'eau chaude en entrée de l'évaporateur.
- T_{amb}: température ambiante en Kelvin.

A.3.3 Identification d'un modèle dynamique pour la machine ORC

Le problème d'identification consiste à trouver une fonction non linéaire F_y qui lie chaque variable d'intérêt $y(k.\tau_s) = y(k)$ (où τ_s est la période d'échantillonnage des signaux), qui peut être la puissance électrique régulée P_{elec} ou bien l'une des variables sous contraintes (ΔT_{vap}, T_{vap}, P_{vap}, $TeMot$, $PeMot$ et T_{fr}), à un régresseur associé $Z_y(k)$ défini par:

$$Z_y(k) = \begin{pmatrix} u^y(k) \\ u^y(k-1) \\ \vdots \\ u^y(k-(N^y-1)) \end{pmatrix} \in \mathbb{R}^{n_z^y} \quad ; \quad n_z^y = N^y.n_u^y \tag{A.8}$$

où n_u^y est la dimension du vecteur d'entré $u^y(k)$ (qui peut contenir aussi bien des variables de contrôle que des variables non contrôlables mais mesurables) et N^y est la profondeur du régresseur. La fonction non linéaire $F_y(Z)$ a été restreinte à avoir la forme suivante:

$$F_y(Z) = \Gamma_y^{-1}(Z_y^T.L_y); \quad \Gamma_y(.) \ \textit{strictement croissante} \tag{A.9}$$

où L_y est un vecteur à identifier. Le lecteur pourra trouver l'allure des fonctions non linéaires Γ_y utilisées en se référant au manuscrit de thèse.

La procédure d'identification s'éffectue sur un ensemble de données d'apprentissage

$$\Big\{(y(k), Z_y(k))\Big\}_{k=1}^{k=N_{data}} \qquad ; \qquad \mathbb{K} = \{1, \ldots, N_{data}\}$$

et le problème d'identification revient à trouver la fonction non linéaire $F_y : \mathbb{R}^{n_z^y} \to \mathbb{R}$ qui lie au sens des moindres carrés Z_y à y:

$$\min_{F_y} \sum_{k \in \mathbb{K}} \|y(k) - F_y(Z_y(k))\|^2 \tag{A.10}$$

La Figure A.17a donne un exemple des résultats d'identification obtenus où l'on compare la sortie du modèle identifiée (courbe verte) de la puissance électrique P_{elec} avec sa valeur mesurée (courbe bleue). La courbe en couleur rouge représente les données utilisées pour l'apprentissage. La Figure A.17b donne l'allure de la fonction non linéaire $\Gamma^{P_{elec}}$ ainsi que son gradient pour juger du degré de non linéarité nécessaire pour l'identification du modèle de la puissance électrique.

Une que fois les modèles dynamique pour chaque variable d'intérêt y ont été identifié, il est possible après un certain nombre d'opérations (se reporter au manuscrit de thèse pour plus de détails) d'aboutir à un modèle linéarisé au sens des moindre carré pour chacune des variables d'intérêt sous la forme suivante:

$$\bar{X}(k+1) = \bar{A}.\bar{X}(k) + \bar{B}_{con}.u_f(k) + \bar{B}_{unc}.u_{unc}(k) \tag{A.11a}$$

$$y(k) = \bar{C}^y.\bar{X}(k) + D_{unc}^y.u_{unc}(k) + E^y \tag{A.11b}$$

où:

$$\bar{X}(k) = \begin{pmatrix} x^T(k) & u_{con}^T(k) \end{pmatrix}^T$$

$$x(k) = \begin{pmatrix} u^T(k-1) & \cdots & u^T(k-(N-1)) \end{pmatrix}^T$$

$$\begin{aligned} u &= \begin{pmatrix} f_{pump} & \dot{V}_{hot} & V_{rot}^{aero} & V_{rot}^{circ} & TaCh & T_{amb} \end{pmatrix}^T \\ &= \begin{pmatrix} u_{con}^T(k) & u_{unc}^T(k) \end{pmatrix} \end{aligned}$$

où $\bar{X}$ est un vecteur d'état augmenté qui contient le vecteur d'état d'origine x ainsi que le vecteur de contrôle filtré u_{con}. Le paramètre N est le maximum des profondeurs des régresseurs pour toutes les variables thermodynamiques d'intérêt.

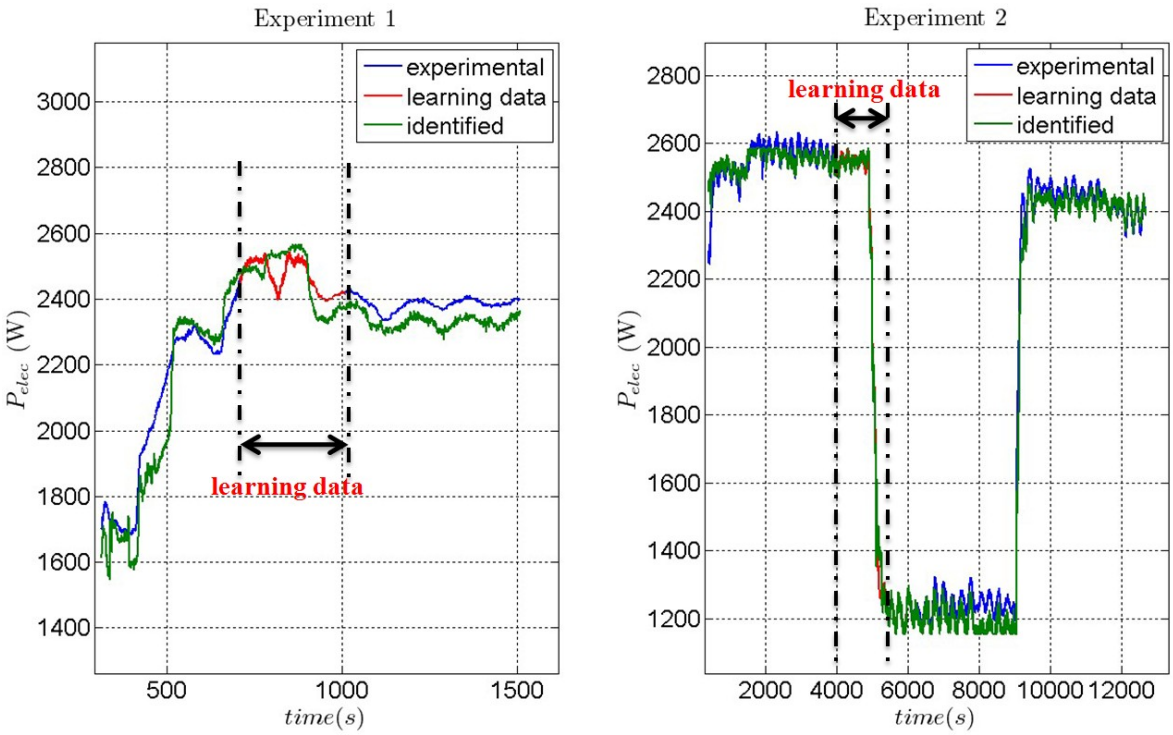

(a) Profiles temporels des puissance électrique P_{elec} mesurée et identifiée sur l'ensemble des données d'apprentissage et de validation.

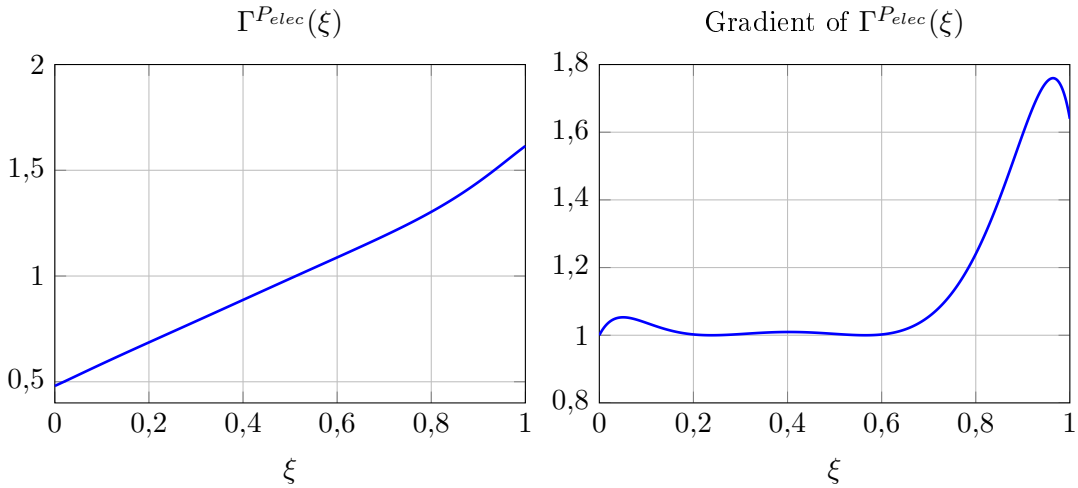

(b) Fonction non linéaire et son gradient pour l'identification de P_{elec}.

Figure A.17: Résultats d'identification pour P_{elec}.

A.3.4 Etude des états stationnaires désirés admissibles

Avant de développer le contrôleur optimal sous contrainte pour la machine ORC, il est intéressant d'étudier tous les états stationnaires admissibles (c'est-à-dire qui respectent les contraintes du système) et qui sont compatibles avec une certaine puissance électrique désirée P_{elec}^{ref}. Pour cela, partant des équations d'état linéarisées (A.11) du système, si on prend comme seule sortie régulée la puissance électrique, et vu qu'on a 4 actionneurs, alors pour chaque puissance électrique désirée il peu y avoir plusieurs états stationnaires compatibles mais qui ne respectent pas forcément tous les contraintes du système. Pour ne converger vers qu'un seul régime stationnaire que l'on maîtrise, on augmente le vecteur de sortie régulé y_r avec 3 autres variables thermodynamiques qui sont critiques pour le système: ΔT_{vap}, T_{vap} et $PeMot$. On aboutit aux équations d'état suivantes:

$$\bar{X}(k+1) = \bar{A}.\bar{X}(k) + \bar{B}_{con}.u_f(k) + \bar{B}_{unc}.u_{unc}(k) \tag{A.12a}$$

$$y_r(k) = \bar{C}^{y_r}.\bar{X}(k) + D_{unc}^{y_r}.u_{unc}(k) + E^{y_r} \tag{A.12b}$$

où: $y_r(k) = \begin{pmatrix} P_{elec}(k) & \Delta T_{vap}(k) & T_{vap}(k) & PeMot(k) \end{pmatrix}^T$

Ainsi, il est possible de reformuler le problème qui consiste à trouver les états stationnaires admissible $\bar{X}_d$ et le vecteur de commande associé en régime stationnaire u_{fd} sous la forme problème d'optimisation LP[5] où l'on cherche à trouver le vecteur d'état augmenté $Z_d = \begin{pmatrix} \bar{X}_d(k) \\ u_{fd}(k) \end{pmatrix}$ solution du problème suivant:

$$\min_{Z_d} f^T.Z_d(k) \tag{A.13}$$

sous les contraintes suivantes:

$$A_c.Z_d(k) = B_c.y_d - B_c^{unc}.u_{unc}(k) - E_c \tag{A.14}$$

$$C_T^{Z_d}.Z_d(k) \leq b_{T1}^{Z_d} + b_{T2}^{Z_d}.u_{unc}(k) \tag{A.15}$$

où $f = 1_{(n_{\bar{x}}+n_u^{con})}$ est un vecteur de pondération.

L'équation (A.14) correspond à l'équation d'état stationnaire et à l'équation de sortie stationnaire ou y_d est la vecteur désiré correspondant à y_r. L'inégalité (A.15) reflète quand à elle le fait que tous les états stationnaires doivent respecter les contraintes du système.

Etant donné que ce problème d'optimisation LP est assez lourd pour être résolu en ligne vu la taille des matrices associés et vu qu'on ne connait pas à priori les valeurs des autres composantes du vecteur désiré y_d compatibles avec P_{elec}^{ref}, on a préféré utiliser une cartographie calculée hors ligne (dénotée $Carto^{ORC}$) qui balaye toutes les valeurs admissibles de y_d ainsi que toutes les valeurs admissibles des variables exogènes et qui contient des 0 et des 1 suivant la faisabilité du problème LP. On extrait par la suite en ligne à partir de la cartographie et de ses vecteurs d'appui associés le vecteur y_d correspondant à une puissance électrique désirée et à une certaine valeur des conditions opératoires (variables exogènes mesurées) en

[5] Linear Programming

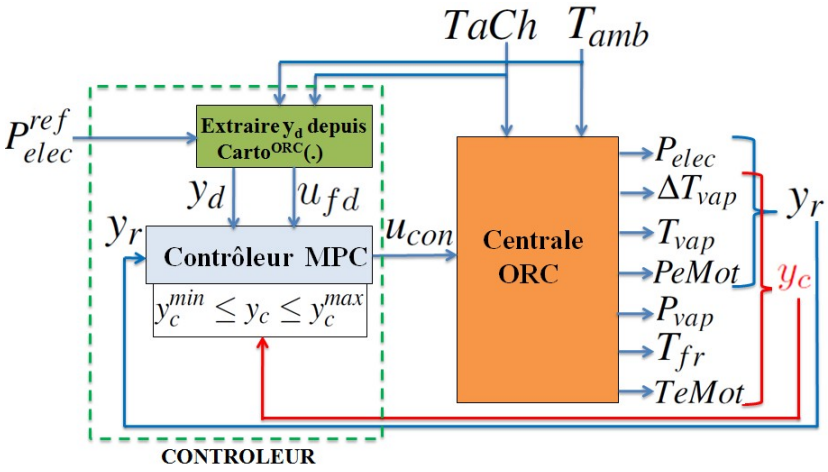

Figure A.18: Architecture de contrôle du système ORC.

prenant toujours le minimum de ΔT_{vap}, T_{vap} et $PeMot$ dans le cas ou plusieurs solutions des états stationnaires admissibles existent et ceci pour augmenter le rendement de la machine ORC. Une fois y_d déterminé, $\bar{X}_d$ et u_{fd}, qui sont les composantes du vecteur Z_d, peuvent être déterminé à partir de (A.14).

A.3.5 Contrôle MPC de la machine ORC

Connaissant maintenant les états stationnaires désirés, admissibles et compatibles avec une puissance électrique de référence P_{elec}^{ref}, on applique un contrôleur MPC pour atteindre ces états le plus rapidement possible tout en respectant les contraintes physiques du système. La Figure A.18 illustre l'architecture de contrôle utilisé où l'on voit bien que la cartographie calculée hors ligne, suivant les discutions de la Section A.3.4, utilise la puissance électrique désirée et la mesure des variables exogènes pour fournir au contrôleur MPC les états stationnaires désirés à atteindre.

Pour illustrer en simulations les performances du contrôleur développé pour la machine ORC, on fait varier dans le temps les signaux exogènes mesurables tels qu'illustré à la Figure A.19a. La Figure A.19b donne les résultats de régulation de la puissance électrique produite. Ainsi, on peut apprécier au vu de la Figure A.19b et les performances du système en boucle fermée en terme de temps de réponse et de rejet des perturbations. Les Figure A.20 et A.21 donnent les variables de contrôle utilisés et les variables thermodynamiques sous contraintes qui restent bien dans leur domaine admissible.

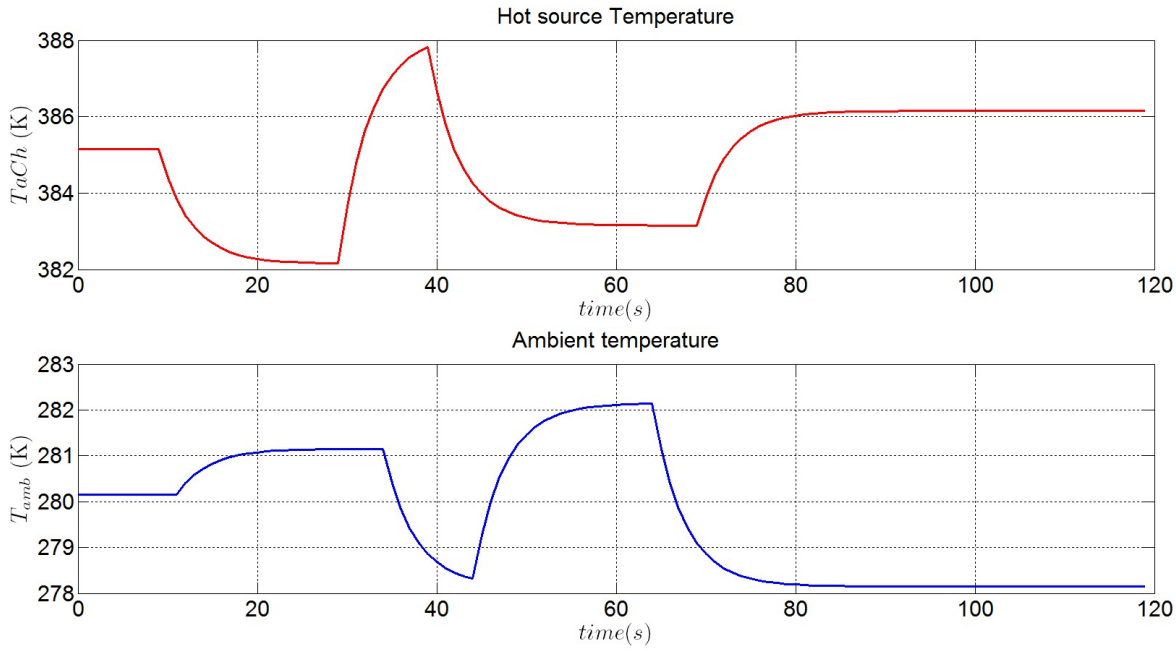

(a) Profil de température pour les signaux exogènes mesurés: $TaCH$ et T_{amb}.

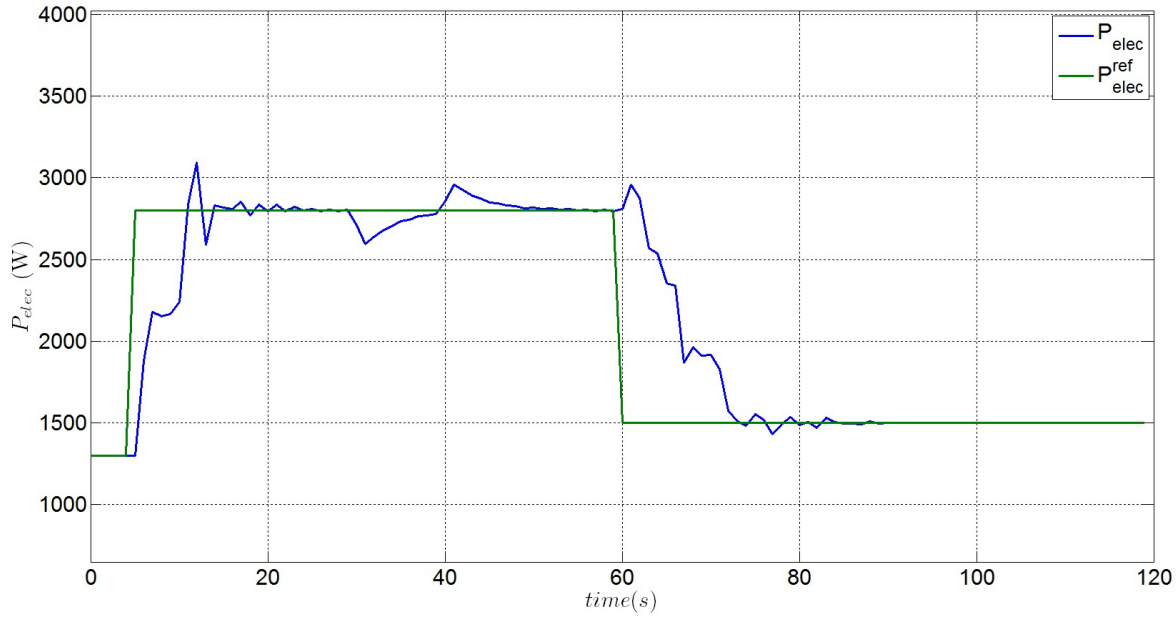

(b) Puissance électrique P_{elec} en sortie de la turbine du système ORC ainsi que sa valeur de référence P_{elec}^{ref}.

Figure A.19: Résultats de la régulation et du rejet de perturbations pour la puissance électrique P_{elec} en sortie de la turbine du système ORC.

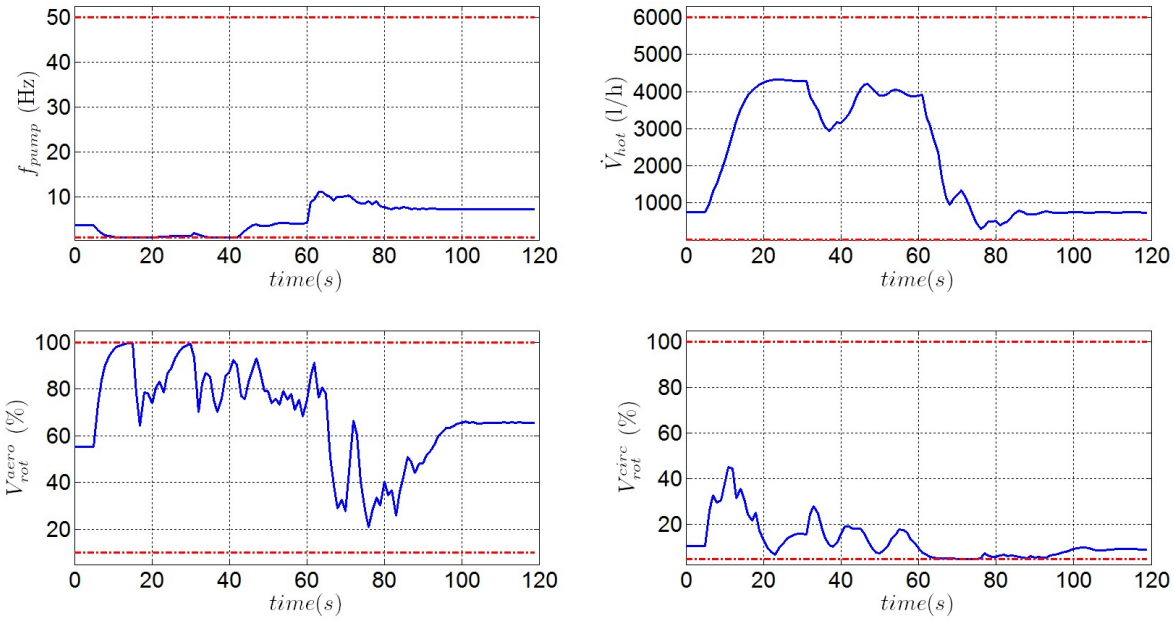

Figure A.20: Actionneurs du système ORC: f_{pump}, $\dot{V}_{hot}$, V_{rot}^{aero} and V_{rot}^{circ}. Les lignes en pointillés rouge représentent les valeurs minimum et maximum admissibles.

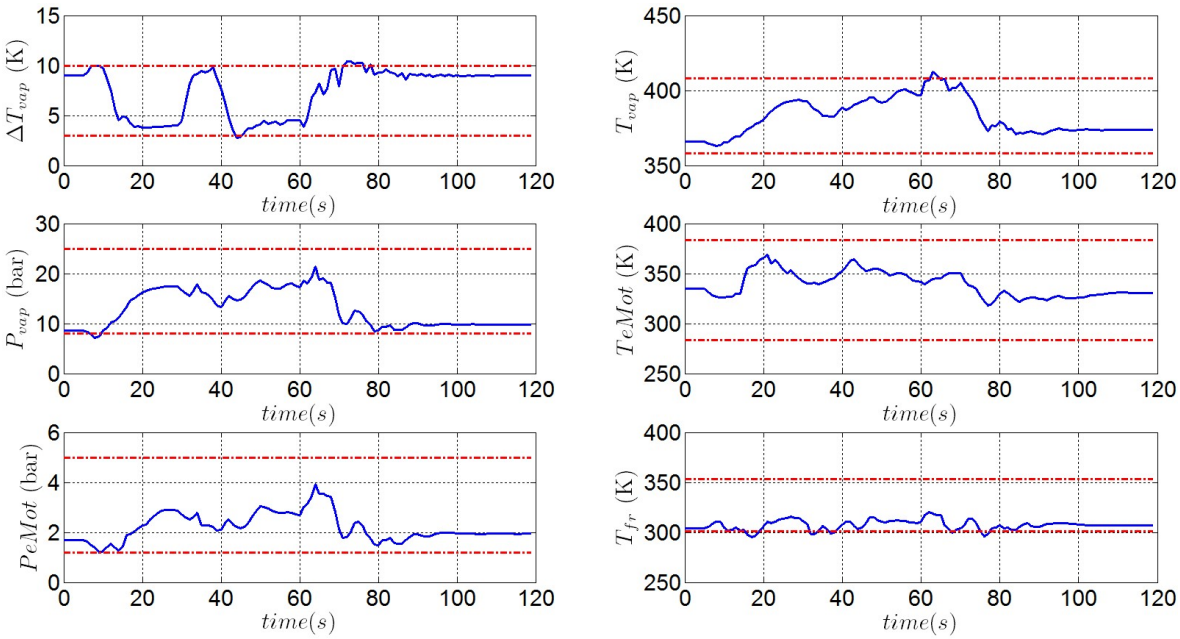

Figure A.21: Variables sous contrainte du système ORC. Les lignes en pointillés rouge représentent les valeurs minimum et maximum admissibles.

A.4 Conclusion générale

Cette thèse a été dédiée au développement de lois de commande performantes pour deux types de micros centrales solaires thermodynamiques considérées dans le cadre du projet MICROSOL.

La première centrale solaire étudiée utilise une machine thermodynamique à cycle de Stirling associée à un système de conversion d'énergie adéquat. Un premier contrôleur optimal du couple de la machine Stirling a été développé en se basant sur un modèle validé expérimentalement. Pour le contrôle du système de conversion d'énergie, deux lois de commandes ont été développées à cet effet. La première loi de commande développée gère explicitement les contraintes sur les saturations des variables de contrôle tout en étant simple à régler. Elle a été validée expérimentalement sur un prototype fonctionnel à base de machine Stirling et offre les performances attendues. La seconde loi de commande développée gère explicitement les contraintes sur tous les états du système de conversion d'énergie tout en dotant le système en boucle fermé de performances optimales en termes de temps de réponse.

Par la suite, le problème du contrôle optimal sous contraintes d'une micro centrale solaire utilisant une machine ORC a été abordé et résolu en ayant une approche qui part des données expérimentales recueillis sur un prototype fonctionnel afin d'identifier des modèles dynamiques de la centrale. Ces modèles nous ont par la suite servis à élaborer un contrôleur MPC qui fait passer la machine ORC d'un point de fonctionnement à un autre en puissance le plus rapidement possible tout en respectant les contraintes physiques du système Les temps de réponse obtenus en simulation avec notre approche suggèrent qu'une réduction significative du nombre de batteries, nécessaires comme source d'énergie tampon, pourrait être envisagée.

Appendix B

Average modeling of the DC/DC converters of the energy conversion system associated to the Stirling based power plant

Here we present the methodology for deriving mean models for the controlled DC/DC full bridge and the bidirectional DC/DC converters which constitute a part of the energy conversion system associated to the Stirling based solar power plant.

B.1 Average modeling of the DC/DC full bridge converter

The DC/DC full bridge converter depicted in Figure 4.4 is controlled acting on its associated IGBTs namely Tr_1, Tr_2, Tr_3 and Tr_4 in such a way that during a cutting period T_{sw} of this converter, the two IGBT pairs (Tr_1, Tr_3) and (Tr_2, Tr_4) are activated during the same controllable period t_f but 180° out of phase according to the the diagram of Figure B.1 where t_m denotes some dead time during witch all the IGBTs are disabled. Figure B.1 gives also the shapes for the signals of interest (see Figure 4.4 for the notations) according to the IGBTs state. By defining the duty ratio of this converter as follow:

$$\alpha_{fb} = \frac{2.t_f}{T_{sw}} \tag{B.1}$$

one can set its corresponding electrical equations during a cutting frequency as follow:

When $\mathbf{0 < t < t_f = \alpha_{fb}.\frac{T_{sw}}{2}}$: Tr_1=Tr_3=ON and Tr_2=Tr_4=OFF

According to Figure 4.4 and the state of the IGBTs, the equations of the converter are:

$$L_{fb}.\frac{\mathrm{d}I_{Lfb}}{\mathrm{d}t} = k.V_{red} - V_{bus} \tag{B.2a}$$

$$C_f.\frac{\mathrm{d}V_{red}}{\mathrm{d}t} = I_{red} - I_{fb}^{in} \tag{B.2b}$$

$$I_{fb}^{in} = k.I_{Lfb} \tag{B.2c}$$

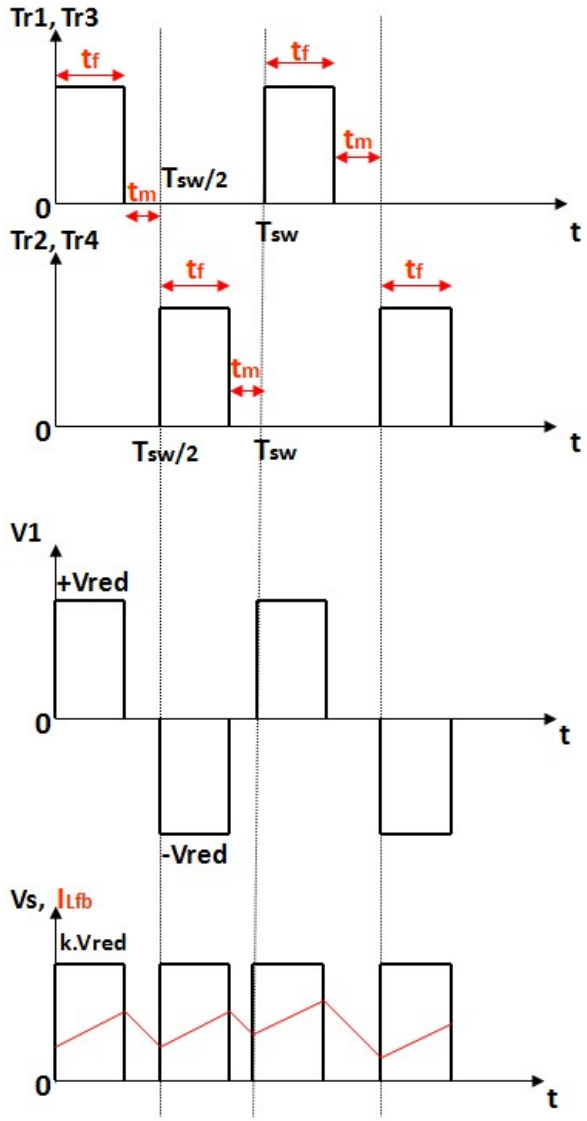

Figure B.1: temporal diagram of the DC/DC Full Bridge.

When $\alpha_{\mathbf{fb}}.\frac{\mathbf{T_{sw}}}{\mathbf{2}} < \mathbf{t} < \frac{\mathbf{T_{sw}}}{\mathbf{2}}$: Tr_1=Tr_2=Tr_3=Tr_4=OFF

According to Figure 4.4 and the state of the IGBTs, the equations of the converter are:

$$L_{fb}.\frac{\mathrm{d}I_{Lfb}}{\mathrm{d}t} = -V_{bus} \tag{B.3a}$$

$$C_f.\frac{\mathrm{d}V_{red}}{\mathrm{d}t} = I_{red} - I_{fb}^{in} \tag{B.3b}$$

$$I_{fb}^{in} = 0 \tag{B.3c}$$

When $\frac{\mathbf{T_{sw}}}{\mathbf{2}} < \mathbf{t} < \frac{\mathbf{T_{sw}}}{\mathbf{2}} + \alpha_{\mathbf{fb}}.\frac{\mathbf{T_{sw}}}{\mathbf{2}}$: Tr_1=Tr_3=OFF and Tr_2=Tr_4=ON

One obtains the same equations as (B.2)

When $\frac{\mathbf{T_{sw}}}{\mathbf{2}} + \alpha_{\mathbf{fb}}.\frac{\mathbf{T_{sw}}}{\mathbf{2}} < \mathbf{t} < \mathbf{T_{sw}}$: Tr_1=Tr_2=Tr_3=Tr_4=OFF

One obtains the same equations as (B.3)

By defining the following control variable $u_{fb}(t)$ over the cutting frequency:

$$u_{fb}(t) := \begin{cases} 1 & \text{if} \quad 0 < t < \alpha_{fb}.\frac{T_{sw}}{2} \quad or \quad \frac{T_{sw}}{2} < t < \frac{T_{sw}}{2} + \alpha_{fb}.\frac{T_{sw}}{2} \\ 0 & \text{if} \quad \alpha_{fb}.\frac{T_{sw}}{2} < t < \frac{T_{sw}}{2} \quad or \quad \frac{Tsw}{2} + \alpha_{fb}.\frac{T_{sw}}{2} < t < T_{sw} \end{cases}$$

The DC/DC full bridge converter equations become:

$$L_{fb}.\frac{\mathrm{d}I_{Lfb}}{\mathrm{d}t} = k.V_{red}.u_{fb} - V_{bus} \tag{B.4a}$$

$$C_f.\frac{\mathrm{d}V_{red}}{\mathrm{d}t} = Ired - I_{fb}^{in} \tag{B.4b}$$

$$I_{fb}^{in} = k.I_{Lfb}.u_{fb} \tag{B.4c}$$

In order to get the average model of the DC/DC full bridge converter that will be used during the control design, we apply the following moving average formula over a cutting period T_{sw} to equations B.4:

$$\bar{x}(t) = \int_{t-T_{sw}}^{t} x(\tau)\,\mathrm{d}\tau \tag{B.5}$$

This leads to the following mean model for the converter (the upper bar symbol representing the mean value is omitted here for convenience)

$$L_{fb}.\frac{\mathrm{d}I_{Lfb}}{\mathrm{d}t} = k.V_{red}.\alpha_{fb} - V_{bus} \tag{B.6a}$$

$$C_f.\frac{\mathrm{d}V_{red}}{\mathrm{d}t} = Ired - I_{fb}^{in} \tag{B.6b}$$

$$I_{fb}^{in} = k.I_{Lfb}.\alpha_{fb} \tag{B.6c}$$

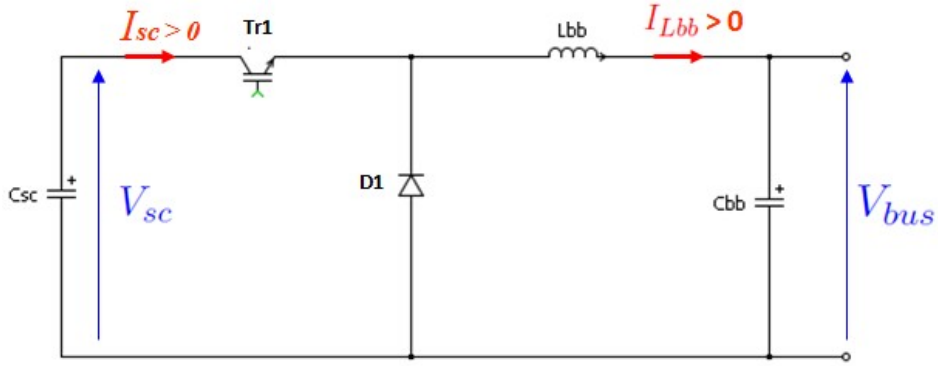

(a) Buck mode of the bidirectional DC/DC converter.

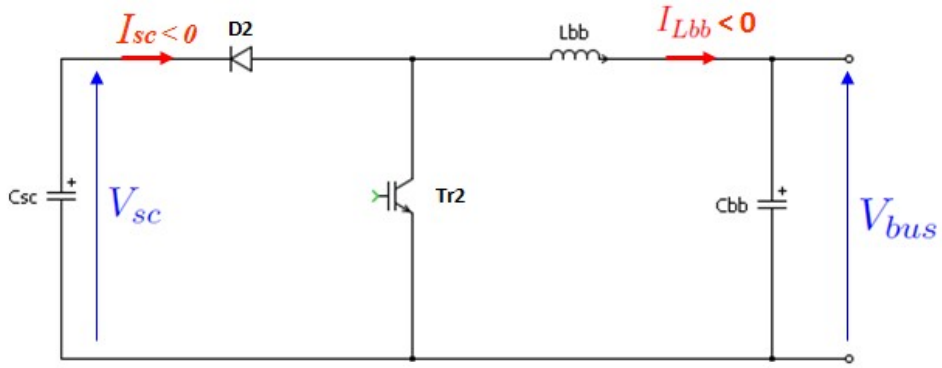

(b) Boost mode of the bidirectional DC/DC converter.

Figure B.2: Operational modes of the bidirectional DC/DC converter according to the current flow

B.2 Average modeling of the bidirectional DC/DC converter

The bidirectional DC/DC converter illustrated in Figure 4.5 is a current reversible converter that can work in a buck mode (Figure B.2a) when the output current I_{Lbb} (see the notations of Figure 4.5) is positive and in a boost mode (Figure B.2b) when I_{Lbb} is negative. In the buck mode, the switching pair is (Tr_1,D_1), which means that only Tr_1 is activated during a part of the cutting period corresponding to $\alpha_{bb}^{buck}.T_{sw}$ where $\alpha_{bb}^{buck} \in [0,1]$ is the duty ratio of the converter in the buck mode. In the boost mode, the switching pair becomes (Tr_2,D_2) where Tr_2 is active during a period $\alpha_{bb}^{boost}.T_{sw}$ where $\alpha_{bb}^{boost} \in [0,1]$ is the duty ratio of the converter in the boost mode.

B.2.0.1 Buck mode: positive current direction ($I_{Lbb} > 0$)

In this mode of operation, the switching pair is (Tr_1,D_1) as illustrated in Figure B.2a and Tr_2 is always disabled.

When $\mathbf{0 < t < \alpha_{bb}^{buck}.T_{sw}}$: Tr_1=ON and D_1=OFF

$$L_{bb}.\frac{dI_{Lbb}}{dt} = V_{sc} - V_{bus}$$
$$C_{sc}.\frac{dV_{sc}}{dt} = -I_{Lbb}$$

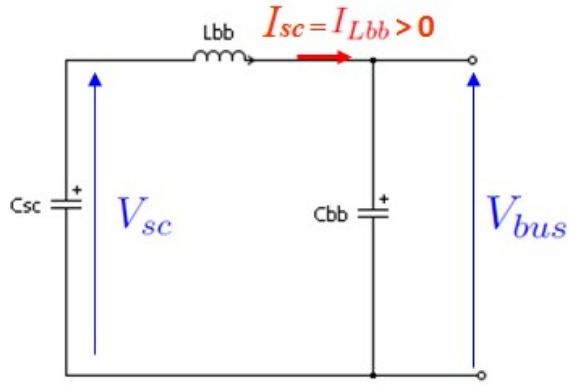

When $\mathbf{\alpha_{bb}^{buck}.T_{sw} < t < Tsw}$: Tr_1=OFF and D_1=ON

$$L_{bb}.\frac{dI_{Lbb}}{dt} = -V_{bus}$$
$$C_{sc}.\frac{dV_{sc}}{dt} = 0$$

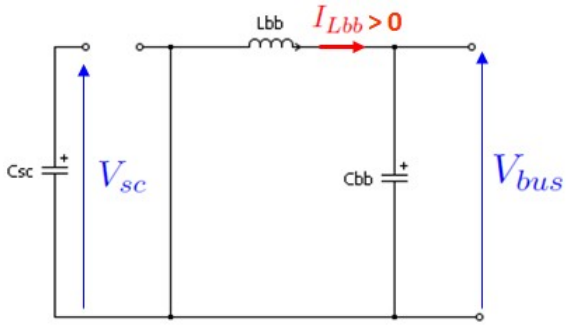

B.2.0.2 Boost mode: negative current direction ($I_{Lbb} < 0$)

In this mode of operation, the switching pair is (Tr_2,D_2) as illustrated in Figure B.2b and Tr_1 is always disabled.

When $\mathbf{0 < t < \alpha_{bb}^{boost}.T_{sw}}$: Tr_2=ON and D_2=OFF

$$L_{bb}.\frac{dI_{Lbb}}{dt} = -V_{bus}$$
$$C_{sc}.\frac{dV_{sc}}{dt} = 0$$

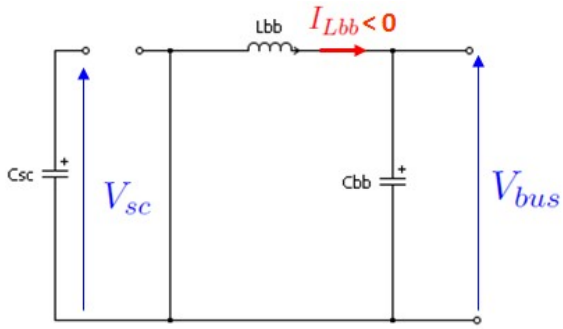

When $\mathbf{\alpha_{bb}^{boost}.T_{sw} < t < Tsw}$: Tr_2=OFF and D_2=ON

$$L_{bb}.\frac{dI_{Lbb}}{dt} = V_{sc} - V_{bus}$$
$$C_{sc}.\frac{dV_{sc}}{dt} = -I_{Lbb}$$

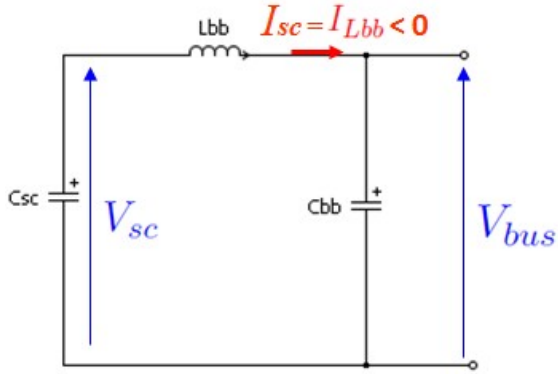

B.2.1 Complementary mode

In order to get a continuous conduction mode of the bidirectional DC/DC converter when the output current I_{Lbb} is close to zero, it is interesting to control this converter in the complementary mode in which Tr_1 is activated (while Tr_2 is disabled) during a period $\alpha_{bb}.T_{sw}$, where $\alpha_{bb} \in [0, 1]$ is the new duty ratio of the converter, and Tr_2 is activated (while Tr_1 is disabled) during the rest of the cutting period T_{sw}. The equations governing this mode are as follow:

When $\mathbf{0 < t < \alpha_{bb}.T_{sw}}$: Tr_1=ON (D_2=ON if $I_{Lbb} < 0$) and Tr_2=OFF

$$L_{bb}.\frac{\mathrm{d}I_{Lbb}}{\mathrm{d}t} = V_{sc} - V_{bus} \quad \text{(B.7a)}$$

$$C_{sc}.\frac{\mathrm{d}V_{sc}}{\mathrm{d}t} = -I_{Lbb} \quad \text{(B.7b)}$$

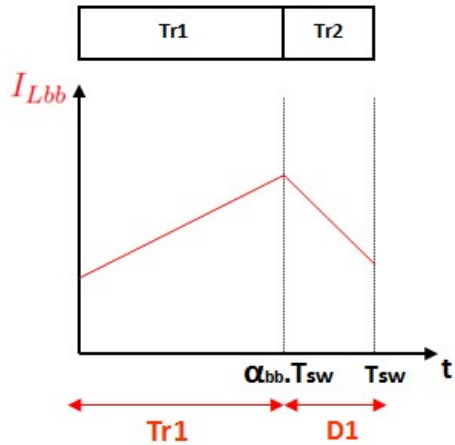

When $\mathbf{\alpha_{bb}.T_{sw} < t < T_{sw}}$: Tr_2=ON (D_1=ON if $I_{Lbb} > 0$) and Tr_1=OFF

$$L_{bb}.\frac{\mathrm{d}I_{Lbb}}{\mathrm{d}t} = -V_{bus} \quad \text{(B.8a)}$$

$$C_{sc}.\frac{\mathrm{d}V_{sc}}{\mathrm{d}t} = 0 \quad \text{(B.8b)}$$

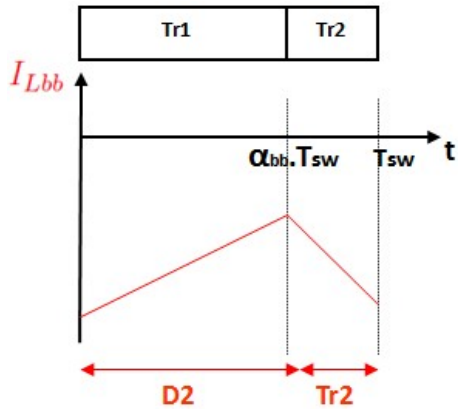

Hence, if the output current I_{Lbb} changes its sign during a cutting period T_{sw} it remains always continuous as illustrated in Figure B.3.

In order to use the bidirectional DC/DC converter in a complementary control mode, we switch from the structure corresponding to $Tr_1 = ON$ and $Tr_2 = OFF$, for which we associate a control $u_{bb} = 1$, to a structure corresponding to $Tr_2 = ON$ and $Tr_1 = OFF$, for which we associate a control $u_{bb} = 0$. Then, one can combine equations (B.7) and (B.8) into the following equations:

$$L_{bb}.\frac{\mathrm{d}I_{Lbb}}{\mathrm{d}t} = V_{sc}.u_{bb} - V_{bus} \quad \text{(B.9a)}$$

$$C_{sc}.\frac{\mathrm{d}V_{sc}}{\mathrm{d}t} = -I_{Lbb}.u_{bb} \quad \text{(B.9b)}$$

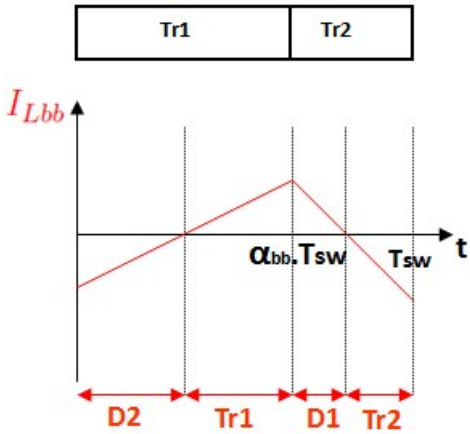

Figure B.3: Output current I_{Lbb} of the bidirectional DC/DC converter in the complementary control mode.

where:

$$u_{bb} := \begin{cases} 1 & \text{if} \quad 0 < t < \alpha_{bb}.T_{sw} \\ 0 & \text{if} \quad \alpha_{bb}.T_{sw} < t < T_{sw} \end{cases}$$

In order to get the mean model of the bidirectional DC/DC converter used during the control design, we apply the same moving average equation (B.5) to the set of equations (B.9) leading to the following average model of the converter:

$$L_{bb}.\frac{\mathrm{d}I_{Lbb}}{\mathrm{d}t} = V_{sc}.\alpha_{bb} - V_{bus} \tag{B.10a}$$

$$C_{sc}.\frac{\mathrm{d}V_{sc}}{\mathrm{d}t} = -I_{Lbb}.\alpha_{bb} \tag{B.10b}$$

Appendix C

Starting procedure for the Stirling based power system prototype

Hereafter, we present the starting procedure that brings the Stirling based power plant prototype depicted in Figure 3.7 to its nominal operating mode in which the control strategy developed in Chapter 5 holds. The presented starting procedure holds also for the dedicated motor testbed depicted in Figure 5.11 with some slight modifications.

As mentioned in Section 5.3.1, the Stirling based power plant illustrated in Figure 3.7 contains an ATV32[1] speed drive (not represented in Figure 4.1 because this figure concerns the nominal operating mode of the prototype in which the speed drive is disconnected) in addition of the energy conversion system as illustrated in Figure C.1 This speed drive enables to bring the Stirling shaft to some preset speed value Ω^{start} to initially enable the movement of the Stirling engine pistons hence creating some motor torque (when the temperature of the heat source is high enough and the valves inside the Stirling engine between the cylinders and the pressure vessel are closed).

Figure C.2 gives the starting procedure flowchart of the Stirling based power system prototype. In this figure the variable "start_system" takes the value 1 when the user pushes a "start system" button on the supervisor (supervision PC of Figure 3.7). In this flowchart, the "Switch" corresponds to the one in Figure C.1 which is initially closed to enable the speed drive to control the shaft speed of the PMSG. The variable "Mode_Regule_FB" indicates the regulation mode of the DC/DC full bridge converter as explained hereafter.

C.1 Case where (Mode_Regule_FB)=1

This case happens when the supercapacitor voltage V_{sc} is greater than the bus voltage V_{bus}. In this case, the DC/DC full bridge converter regulates the DC bus voltage V_{bus} to its reference value V_{bus}^{ref}=50V compatible with the good functioning of the inverter.

The regulation is performed using standard PI based cascaded current-voltage loops using

[1] http://www.schneider-electric.com/download/hk/en/details/2619521-Altivar-32-variable-speed-drives-catalog?showAsIframe=false&reference=DIA2ED2100401EN

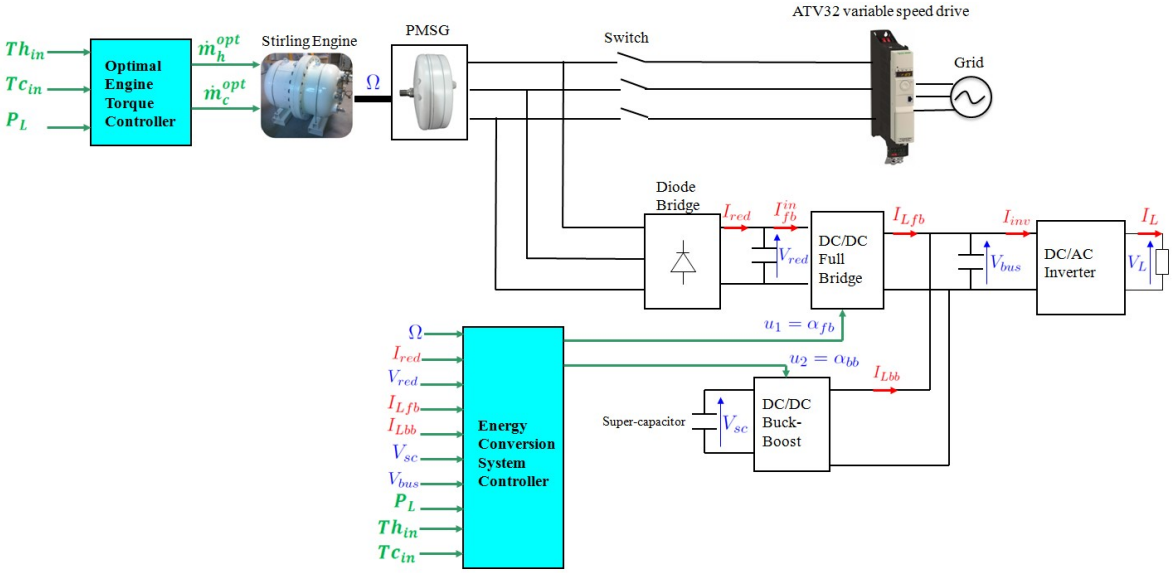

Figure C.1: Overview of the Stirling based power plant and its associated power conversion system including the ATV32 variable speed drive

equations (4.9d) and (4.9e) that are recalled thereafter for convenience:

$$C_{tot}.\frac{dV_{bus}}{dt} = I_{Lfb} + I_{Lbb} - I_{inv} \tag{C.1a}$$

$$L_{fb}.\frac{\mathrm{d}I_{Lfb}}{\mathrm{d}t} = k.V_{red}.\alpha_{fb} - V_{bus} \tag{C.1b}$$

Using (C.1a) a reference value for I_{Lfb} namely I_{Lfb}^{ref} is derived to impose the following stable dynamics for V_{bus} (that stabilizes V_{bus} around V_{bus}^{ref}):

$$\frac{dV_{bus}}{dt} = K_{bus1}.(V_{bus}^{ref} - V_{bus})$$

where K_{bus1} is some design parameter. This leads to:

$$I_{Lfb}^{ref} = -I_{Lbb} + I_{inv} + C_{tot}.K_{bus1}.(V_{bus}^{ref} - V_{bus}) \tag{C.2}$$

To overcome some model errors, measurements errors and undesirable sharp transients during starting procedure, I_{Lfb}^{ref} is filtered using a first order filter and a corrective term is added to I_{Lfb}^{ref} leading to the following modified reference value for I_{Lfb} namely $I_{Lfb}^{\star}$ in the discrete form:

$$I_{Lfb}^{\star}(k+1) = \alpha_f^{bus1}.(I_{Lfb}^{ref}(k) + \epsilon_{bus1}(k)) + (1 - \alpha_f^{bus1}).I_{Lfb}^{\star}(k) \tag{C.3a}$$

$$\epsilon_{bus1}(k+1) = k_{aw}^{bus1}.\epsilon_{bus1}(k) + \eta_{corr}^{bus1}.(I_{Lfb}^{ref}(k) - I_{Lfb}(k)) \tag{C.3b}$$

where α_f^{bus1} is a filtering parameter, η_{corr}^{bus1} is an integrator gain and k_{aw}^{bus1} is an anti windup gain.

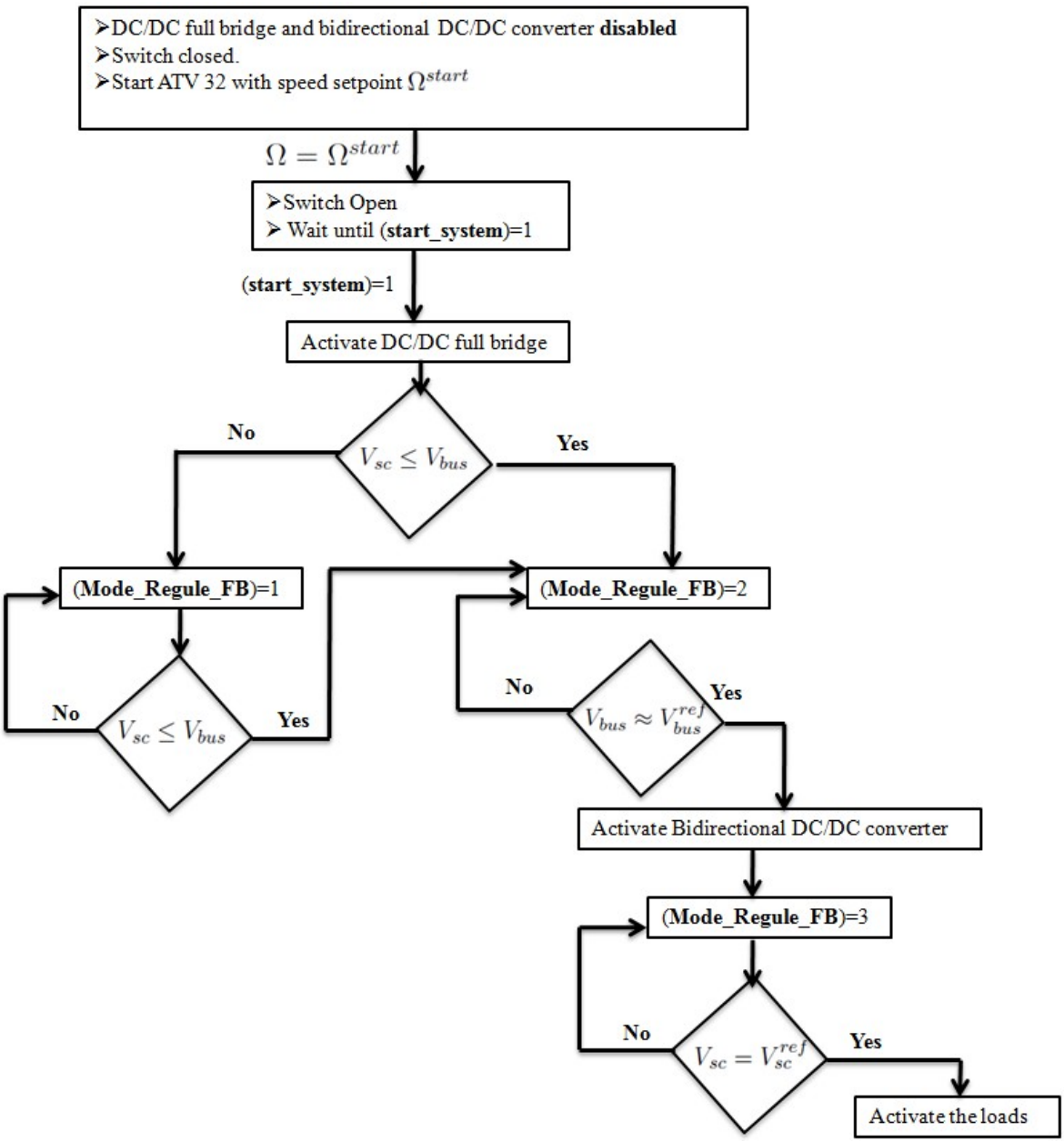

Figure C.2: Starting procedure flowchart

Then using (C.1b), the control variable α_{fb} is used to control I_{Lfb} to the reference value $I^{\star}_{Lfb}$ by imposing the following stable dynamics to I_{Lfb}:

$$\frac{dI_{Lfb}}{dt} = K_{fb1}.(I^{\star}_{Lfb} - I_{Lfb})$$

where K_{fb1} is some design parameter. This leads to the following equation for the control variable α_{fb}:

$$\alpha_{FB} = \frac{1}{k.V_{red}}.\Big(V_{bus} + K_{fb1}.(I^{\star}_{Lfb} - I_{Lfb})\Big) \tag{C.4}$$

C.2 Case where (Mode_Regule_FB)=2

This case happens when the supercapacitor voltage V_{sc} is less than or equal to the bus voltage V_{bus}. In this situation the diode $D2$ of the bidirectional DC/DC converter (see Figure 4.5) becomes conductive and then, the supercapacitor C_{sc} becomes in parallel with the DC bus capacitors C_{tot} resulting in greater DC bus total capacitor $C^{\star}_{tot} = C_{sc} + C_{tot}$. In this mode the DC/DC full bridge converter regulates also the DC bus voltage V_{bus} to its reference value V^{ref}_{bus}=50V using the same equations developed in Section C.1 (for the reference value of I_{Lfb} and the control α_{fb}) but replacing C_{tot} by $C^{\star}_{tot}$.

C.3 Case where (Mode_Regule_FB)=3

This mode corresponds to the nominal operational mode in which both converters are enabled and for which the control equations were developed in Chapter 5.

Appendix D

Proofs related to chapter 6

In this appendix, we present the proofs of: Lemma 6.1, some items of Assumption 6.5 and Proposition 6.1 all of them used during the design step of the constrained sliding mode controller for the energy conversion system associated to the Stirling engine.

D.1 Proof of Lemma 6.1

According to Assumption 6.1, the linear subsystem in (x_1, x_2) defined by (6.1a)-(6.1b) steered by the exogenous signal x_3 shows two eigen-modes: a fast one denoted by z_f and a slow one denoted by z_s. The output we are interested in for this subsystem is $y = x_2$ and is given, according to the definition of the eigen-modes, by:

$$y(t) = \alpha_f z_f(t) + \alpha_s z_s(t)$$

The objective of this proof is to characterize all constant profiles on x_3 leading to the respect of the saturation constraints (6.2) on x_2 starting from an admissible initial condition.

To do this, consider the temporal generic structure of the trajectory $y(\cdot)$ depicted in Figure D.1 where the first order behaviors of the eigen-modes are approximated by straight lines. According to this figure, the position in time of the singular point (zero time-derivative) is close to the settling time (t^*) of the fastest modes and this regardless of the value of the constant steering signal x_3. This is because after this value t^*, the derivative of y becomes monotonic and cannot change its sign anymore.

Now for this once-for-all fixed value t^*, the expression of the output $y(t^*) = x_2(t^*)$ can be given in terms of the current value of (x_1, x_2) and the input x_3 using constant and off-line computable matrices M^*, N^* and K^* according to:

$$x_2(t^*) := M^* \cdot \begin{pmatrix} x_1 \\ x_2 \end{pmatrix} + N^* a_2 + K^* x_3 \tag{D.1}$$

This obviously leads to the following expressions for $\underline{x}_3$ and $\bar{x}_3$:

$$\underline{x}_3(x_1, x_2) := \max\Big\{x_3^{min}, \frac{1}{K^*}\Big[x_2^{max} - M^* \begin{pmatrix} x_1 \\ x_2 \end{pmatrix} - N^* a_2\Big]\Big\} \tag{D.2}$$

$$\bar{x}_3(x_1, x_2) := \min\Big\{x_3^{max}, \frac{1}{K^*}\Big[x_2^{min} - M^* \begin{pmatrix} x_1 \\ x_2 \end{pmatrix} - N^* a_2\Big]\Big\} \tag{D.3}$$

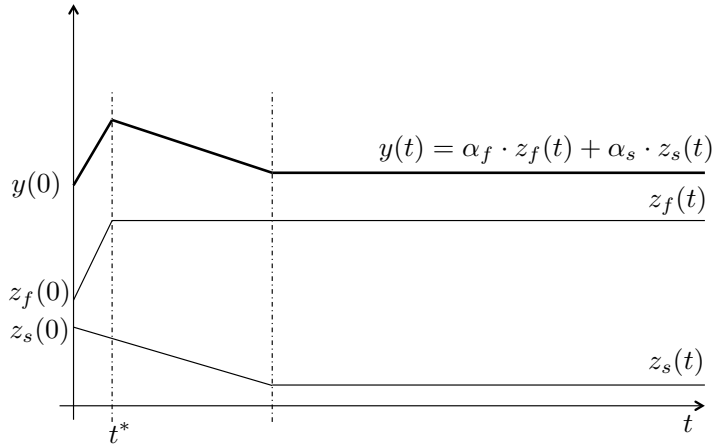

Figure D.1: Illustration of the proof of Lemma 6.1: Under the conditions of the Lemma, the position of the *pic* of $y = x_2$ is almost independent of x_3.

Now if x_3 is not constant but satisfies at each instant the constraint (6.5), the result can be proved by obvious receding-horizon way by looking at the first order two eigen-systems. This obviously ends the proof of Lemma 6.1.

D.2 Mathematical conditions to check items 5), 6) and 7) of Assumption 6.5

The Item 5) of Assumption 6.5 can be checked through the following conditions that can be checked by scalar optimization in the decision variable x_3:

$$\min_{(x_3, x_4^{min}) \in AB} \left[x_2^{st}(x_3^*) - \frac{x_4^{min} x_5^r}{x_3} \right] > 0 \tag{D.4}$$

$$\max_{(x_3, x_4^{max}) \in DE} \left[x_2^{st}(x_3^*) - \frac{x_4^{max} x_5^r}{x_3} \right] < 0 \tag{D.5}$$

since the analyzed expression is nothing but the resulting derivative of x_3 when x_2, x_4 and x_5 take the appropriate values.

As for the items 6) and 7) regarding the atractivity of the set BCD, it can be checked through the following conditions (in which the notation $p = (x_3, x_4)^T$ is used for compactness):

$$\min_{(t, p^0) \in [0, t_f] \times \mathcal{R}_{34}} d\Big(p(t, p^0, u_1 = 1), \text{ABCDE}\Big) = 0 \tag{D.6}$$

$$\min_{(t, p^0) \in [0, t_f] \times \mathcal{L}_{34}} d\Big(p(t, p^0, u_1 = 0), \text{ABCDE}\Big) = 0 \tag{D.7}$$

where the subsets $\mathcal{R} \in \mathbb{R}^2$ and $\mathcal{L} \in \mathbb{R}^2$ are the sets that denote the values of (x_3, x_4) that lie to the right and to the left of BCD respectively. $p(t, p^0, u_1 = 1)$ denotes the trajectories of

(6.1c)-(6.1d) starting from p^0 under the control $u_1 = 1$ and when $x_5 = x_5^r$ and $x_2 = x_2^{st}(x_3^*)$ are used. Similar definitions hold for $p(t, p^0, u_1 = 0)$ except that the control $u_1 = 0$ is used. The notation $d(p, \text{ABCDE})$ denotes the distance between p and the curves ABCDE. Finally, the final time t_f is some sufficiently long computation time in order for the trajectory to cross the curve ABCDE.

D.3 Proof of proposition 6.1

Note that by definition of the interpolated feedback laws $K_1(x, P_L)$ and $K_2(x, P_L)$, the resulting closed-loop trajectories passes through neighborhoods $\mathcal{V}_{34}(x_3^*, x_4^*)$ and $\mathcal{V}_{56}(x_5 r, x_6^r)$ of the targeted pairs (x_3^*, x_4^*) and (x_5^r, x_6^r) of size $O(1/\lambda)$ after a finite time.

Let first $\gamma_{34} > 0$ and $\gamma_{56} > 0$ be taken sufficiently small to guarantee that the corresponding level sets belong to the regions of attraction of the local controls $u_1^{st}(x_3^*(x, P_L))$ and $u_2^*(x, P_L)$. Once this is done, take $\lambda > 0$ sufficiently high to guarantee that each of the conditions $d_{34}(x, P_L) < \gamma_{34}$ and $d_{56}(x, P_L) < \gamma_{56}$ will be reached in finite time so that the local controllers can be fired.

Now since the switching conditions in (6.27)-(6.28) are defined using the Lyapunov level sets associated to the local stabilizing control laws, no chattering behavior occurs and the state is asymptotically steered to the stationary state x^{st} defined by:

$$x_i^{st}(x_4^d) \quad \text{i=1,...,4} \tag{D.8}$$

$$x_5^{st} = x_5^r \tag{D.9}$$

$$x_6^{st} = 0 \tag{D.10}$$

$$x_7^{st} = x_7^r \tag{D.11}$$

where x_4^d is given by:

$$x_4^d := \frac{P_L}{\eta_{inv} x_5^r} \tag{D.12}$$

Indeed, this last equation comes from (6.8) because of the asymptotic convergence of x_7 towards x_7^r that results from (6.9). This with (6.7) shows that x_6 converges to 0. This obviously ends the proof.

Bibliography

[Abdelli, 2007] Abdelli, A. (2007). *Optimisation multicritère d'une chaine éolienne passive.* PhD thesis, Institut National Polytechnique de Toulouse.

[Ahmed et al., 2011] Ahmed, N., Al-Othman, A., and Alrashidi, M. (2011). Development of an efficient utility interactive combined wind/photovoltaic/fuel cell power system with mppt and dc bus voltage regulation. *Electric Power Systems Research*, 81:1096–1106.

[Alamir, 2013] Alamir, M. (2013). A new identification framework for off-line computation of moving-horizon-observers. *IEEE Transactions on Automatic Control*, 58:1877–1882.

[Alamir et al., 2014a] Alamir, M., Alberer, D., and Del Re, L. (2014a). Identification of a class of nonlinear dynamic relationships: Application to the identification of emission models in diesel engines. *To appear in International Journal of Engine Research.*

[Alamir et al., 2014b] Alamir, M., Rahmani, M., and Gualino, D. (2014b). Constrained control framework for a stand-alone hybrid (stirling engine)/supercapacitor power generation system. *Applied Energy*, 118:192–206.

[Alamir et al., 2014c] Alamir, M., Rahmani, M., and Gualino, D. (2014c). Generic model identification structure for thermodynamic engines for use in hybrid power stations control and simulation. *Journal of Process Control*, 24:966–974.

[Barakat et al., 2010] Barakat, A., Tnani, S., Champenois, G., and Mouni, E. (2010). Analysis of synchronous machine modeling for simulation and industrial applications. *Simulation Modelling Practice and Theory*, 18:1382–1396.

[Besançon, 2007] Besançon, G. (2007). *Nonlinear Observers and Applications.* Springer.

[Bonnet, 2005] Bonnet, S. (2005). *Moteurs thermiques à apport de chaleur externe : étude d'un moteur Stirling et d'un moteur Ericsson.* PhD thesis, L'Université de Pau et des Pays de l'Adour.

[Bracikowski, 2012] Bracikowski, N. (2012). *Modélisation multi-physique par modèles à constantes localisées ; Application à une machine synchrone à aimants permanents en vue de son dimensionnement.* PhD thesis, Ecole Centrale de Lille.

[Chatelain, 1983] Chatelain, J. (1983). *Machines Electriques.* Edition Georgi.

[Doyle et al., 2001] Doyle, F., Pearson, R., and Ogunnaike, B. (2001). *Identification and Control Using Volterra Models.* Springer-Verlag.

[Feru et al., 2013] Feru, E., Willems, F., Rojer, C., de Jager, B., and Steinbuch, M. (2013). Heat exchanger modeling and identification for control of waste heat recovery systems in diesel engines. In *Proceedings of IEEE American Control Conference (ACC)*, pages 2860–2865.

[Foch et al., 1992] Foch, H., Arches, R., Escaut, B., Marty, P., and Metz, M. (1992). Convertisseurs continu-continu isolées. Techniques de l'ingénieur.

[Haque et al., 2010] Haque, M., Negnevitsky, M., and Muttaqui, K. (2010). A novel control strategy for a variable speed wind turbine with a permanent magnet synchronous generator. *IEEE transactions on industry applications*, 46(1):331–339.

[Haruni et al., 2010] Haruni, A.M.O. Gargoom, A., Haque, M., and Negnevitsky, M. (2010). Dynamic operation and control of a hybrid wind-diesel stand alone power systems. In *Proceedings of Applied Power Electronics Conference and Exposition (APEC)*, pages 162–169.

[Kalantar and Mousavi, 2010] Kalantar, M. and Mousavi, S. (2010). Dynamic behaviour of stand-alone hybrid power generation system of wind turbine, microturbine, solar array and battery storage. *Applied Energy*, 87:3051–3064.

[Khalil, 1996] Khalil, H. (1996). *Non Linear Systems*. Michigan: Prentice Hall.

[Langlois, 2006] Langlois, O. (2006). *Conception d'un réseau de secours électrique pour l'aéronautique*. PhD thesis, Institut National Polytechnique de Toulouse.

[Mathieu, 2012] Mathieu, A. (2012). *Contribution à la conception et à l'optimisation thermodynamique d'une Micro-Centrale Solaire Thermoélectrique*. PhD thesis, Université de Lorraine, Nancy.

[Mayne et al., 2000] Mayne, D., Rawlings, J., Rao, C., and Scokaert, P. (2000). Constrained model predictive control:stability and optimality. *Automatica*, 36:789–814.

[McKinley and Alleyne, 2008] McKinley, T. L. and Alleyne, A. (2008). A switched system model for heat exchangers using a moving boundary method. In *Proceedings of 2008 American Control Conference*, pages 1455–1462, Seattle, Washington, USA.

[Mendis et al., 2011] Mendis, N., Muttaqui, K., Perera, S., and Uddin, M. (2011). A novel control strategy for stand-alone operation of a wind dominated raps system. In *Proceedings of the Industry Applications Society Annual Meeting (IAS)*, pages 1–8.

[Meyer, 2011] Meyer, D. (2011). Modélisation et controle commande d'un moteur stirling pour une micro centrale solaire thermodynamique (micst). Master's thesis, Institut National Polytechnique de Grenoble.

[Mouni et al., 2008] Mouni, E., Tnani, S., and Champenois, G. (2008). Synchronous generator modelling and parameters estimation using least squares method. *Simulation Modelling Practice and Theory*, 16:1678–689.

[Peralez et al., 2012] Peralez, J., Tona, P., Sciarretta, A., Dufour, P., and Nadri, M. (2012). Towards model-based control of a steam rankine process for engine waste heat recovery. In *Proceedings of 2012 IEEE Vehicle Power and Propulsion Conference (VPPC)*, pages 289–294.

[Qi et al., 2011a] Qi, W., Liu, J., Chen, X., and Christofides, P. (2011a). Supervisory predictive control of standalone wind/solar energy generation systems. *IEEE transactions on control systems technology*, 19(1):199–207.

[Qi et al., 2011b] Qi, W., Liu, J., and Christofides, P. (2011b). A two-time-scale framework to supervisory predictive control of an integrated wind/solar energy generation and water desalination system. In *Proceedings of 2011 American Control Conference*, pages 2677–2682.

[Qin and Badgwell, 2003] Qin, S. J. and Badgwell, T. A. (2003). A survey of industrial model predictive control technology. *Control Engineering Practice*, 11:733–764.

[Quoilin, 2011] Quoilin, S. (2011). *Sustainable Energy Conversion Through the Use of Organic Rankine Cycles for Waste Heat Recovery and Solar Applications.* PhD thesis, Liège University.

[Quoilin et al., 2011a] Quoilin, S., Aumann, R., Grill, A., Schuster, A., Lemort, V., and Splieethoff, H. (2011a). Dynamic modeling and optimal control strategy of waste heat recovery organic rankine cycles. *Applied Energy*, 88:2183–2190.

[Quoilin et al., 2011b] Quoilin, S., Orosz, M., Hemond, H., and Lemort, V. (2011b). Performance and design optimization of a low-cost solar organic rankine cycle for remote power generation. *Solar Energy*, 85:955–966.

[Rasmussen and Alleyne, 2006] Rasmussen, B. P. and Alleyne, A. (2006). Dynamic Modeling and Advanced Control of Air Conditioning an Refrigeration Systems. Project report, University of Illinois, USA.

[Schmidt and Lipson, 2009] Schmidt, M. and Lipson, H. (2009). Distilling free-form natural laws from experimental data. *Science*, 324(5923):81–85.

[Shah et al., 2003] Shah, R., Alleyne, A., Bullard, C., Rasmussen, B., and Hrnjak, P. (2003). Dynamic Modeling And Control of Single and Multi-Evaporator Subcritical Vapor Compression Systems. Project report, University of Illinois, USA.

[Skvarenina, 2002] Skvarenina, T. (2002). *The power electronics handbook.* Indiana: Purdue University.

[Sun et al., 2006] Sun, J., Mitchell, D., Greuel, M., Krein, P., and Bass, R. (2006). Averaged modeling of pwm converters operating in discontinuous conduction mode. *IEEE Transactions on power electronics*, 16(4):482–492.

[Twomey et al., 2013] Twomey, B., Jacobs, P., and Gurgenci, H. (2013). Dynamic performance estimation of small-scale solar cogeneration with organic rankine cycle using a scroll expander. *Applied Thermal Engineering*, 51:1307–1316.

[Urieli and Berchowitz, 1984] Urieli, I. and Berchowitz, D. (1984). *Stirling Cycle Engine Analysis.* Institute of Physics Publishing.

[Valenciaga and Puleston, 2005] Valenciaga, F. and Puleston, P. (2005). Supervisor control for a stand-alone hybrid generation system using wind and photovoltaic energy. *IEEE Transactions on Energy Conversion*, 20(2):398–405.

[Valenciaga and Puleston, 2008] Valenciaga, F. and Puleston, P. (2008). High-order sliding control for a wind energy conversion system based on a permanent magnet synchronous generator. *IEEE transactions on energy conversion*, 23(3):860–867.

[Valenciaga et al., 2004] Valenciaga, F., Puleston, P., and Battaiotto, P. (2004). Variable structure system control design method based on a differential geometric approach: application to a wind energy conversion subsystem. In *Proceedings of IEE Control Theory Application*, volume 151, pages 6–12.

[Valenciaga et al., 2000] Valenciaga, F., Puleston, P., Battaiotto, P., and Mantz, R. (2000). Passivity/sliding mode control of a stand-alone hybrid generation system. In *Proceedings of IEE Control Theory Application*, volume 147, pages 680–686.